2011

The effects of galaxy interactions on star formation

Bradley W. Peterson
Iowa State University

The effects of galaxy interactions on star formation

by

Bradley Wayne Peterson

A dissertation submitted to the graduate faculty

in partial fulfillment of the requirements for the degree of

DOCTOR OF PHILOSOPHY

Major: Astrophysics

Program of Study Committee:
Curtis Struck, Major Professor
Charles Kerton
Lee Anne Willson
Craig Ogilvie
Diane Cook

Iowa State University

Ames, Iowa

2011

TABLE OF CONTENTS

LIST OF TABLES

LIST OF FIGURES

ACKNOWLEDGEMENTS

I would like to take this opportunity to express my thanks to those who helped me with the research that has gone into this dissertation. First, my advisor Curt Struck has provided invaluable direction, suggestions, and feedback over the course of the all the projects that are collected here. I am also increasingly grateful for the timeliness of his advice.

For assistance on the star cluster projects, I wish to thank Bev Smith (East Tennessee State University), who has been an enormous help with data reduction and analysis. I also thank Mark Hancock (ETSU; University of California, Riverside) for providing essential advice on the use of STARBURST99 models for the star cluster projects.

I also wish to thank the IPAC Visiting Graduate Student Fellowship program for providing the opportunity to work at Caltech on what became the Taffy project. I thank my IPAC advisor Phil Appleton for making possible my *Spitzer* spectroscopy work. I also wish to thank Tom Jarrett for use of his IRS bad pixel cleaning software; Michelle Cluver for instructing me in the use of CUBISM, as well as assistance with MAPPINGS models; Pierre Guillard for (quickly) running PDR models; Patrick Ogle, George Helou, and Francois Boulanger (Institut d'Astrophysique Spatiale) for general advise on the Taffy project.

ABSTRACT

This dissertation explores the effects of galaxy interactions on star formation through three separate projects. In the first two projects, we examine enhanced star formation by studying the star cluster populations of the interacting galaxies Arp 284 (NGC 7714/5) and Arp 261, using data from the *Hubble Space Telescope* along with ancillary data from the *Spitzer Space Telescope* and *Galaxy Evolution Explorer* to obtain broader wavelength coverage. Combined with STARBURST99 evolutionary synthesis models, we estimate the ages and masses of the clusters. The mass and luminosity distributions are found to be in good agreement with other systems from the literature.

The clusters in Arp 284 are predominantly young, with ages less than 20 Myr, though observational limits make the significance of this result uncertain. Older clusters, though not numerous, have nearly the same spatial distribution within the imaged portion of NGC 7714 as young clusters. The cluster population in the bridge connecting the galaxies appears to be older, though the data in this part of the system are too limited to draw firm conclusions. The ages of the giant H II regions in NGC 7714 are generally older than those of their constituent clusters, possibly indicating that the young clusters we detect are surrounded by their dispersed predecessors. We call this the "jewels in the crown" effect.

The age distribution of the Arp 261 cluster population is more difficult to interpret because the metallicity of the galaxies is currently unknown, making the ages highly uncertain. Despite these uncertainties, it is clear that the majority of the clusters have ages $\sim$20 Myr or less. We also find more evidence of the jewels in the crown effect in this system. The cluster age distributions in the features of this system have significant implications for its dynamical history. Radio data from the NVSS already indicates that the Taffy-like collision scenario

suggested by the optical morphology may not be correct. Analysis of optical spectra, which have already been obtained, will allow us to determine the metallicity of the galaxies and improve our estimates of the cluster ages.

In the final project, we examine the suppression of star formation in the bridge between the Taffy galaxies using strong, resolved emission from warm H_2. Relative to the continuum and faint PAH emission, the H_2 emission in the system is the strongest in the bridge, where the purely rotational lines of H_2 dominate the mid-infrared spectrum in a way very reminiscent of the group-wide shock in the strongly interacting group Stephan's Quintet. We use excitation diagrams to characterize the warm molecular gas, finding an average surface mass of $\sim$5 $M_\odot$ pc^{-2} and typical excitation temperatures of 150–175 K. H_2 emission is also seen in the galaxy disks, although there the emission is more consistent with that seen in normal star forming galaxies. We investigate several possible heating mechanisms for the bridge gas, but favor the conversion of mechanical energy from the head-on collision via turbulence and shocks as the main heating source. Since the cooling time for the warm H_2 is short, shocks must be permeating the bridge region in order to continue heating the molecular hydrogen.

CHAPTER 1. Introduction

1.1 Galaxy Interactions

In astronomy, many significant breakthroughs have begun with a catalogue. In the case of galaxy interactions, the relevant catalogue was *The Hubble Atlas of Galaxies*, first published in 1936, in which Hubble introduced a simple galaxy classification scheme, which is still in use today. Hubble believed that the"tuning fork" arrangement, shown in Figure 1.1, depicted an evolutionary sequence, with elliptical galaxies increasing in eccentricity before becoming spiral galaxies, either with or without a central bar. Over time, the size of the central bulge relative to the disk would decrease, while the arms became less tightly wound but increasingly clumpy. While this evolutionary sequence ultimately proved to be incorrect, the classifications have remained useful, with elliptical galaxies still described according to their axial ratio and spirals by the relative size of the bulge and winding of the arms.

Interest in interacting galaxies begins outside of Hubble's tuning fork, where galaxies with morphologies not fitting into the main categories were set aside and designated as irregulars. The existence of a"miscellaneous" bin in Hubble's classification scheme would inspire additional work. Early catalogues of irregular galaxies include the *Atlas and Catalogue of Interacting Galaxies* by Vorontsov-Velyaminov in 1959 (an updated and expanded version may be found in Vorontsov-Velyaminov 1977) and the *Atlas of Peculiar Galaxies* (Arp, 1966).

Although the seminal works in the field of galaxy interactions would be published in the 1970's, one particularly pioneering effort bears special mention. Holmberg (1941) performed the first simulation of galaxy interactions. Assuming the dynamics were dominated by gravity, he used the fact that both the gravitational force and the intensity of light from a spherical source have a $1/r^2$ dependence. This allowed him to use an arrangement of light bulbs as

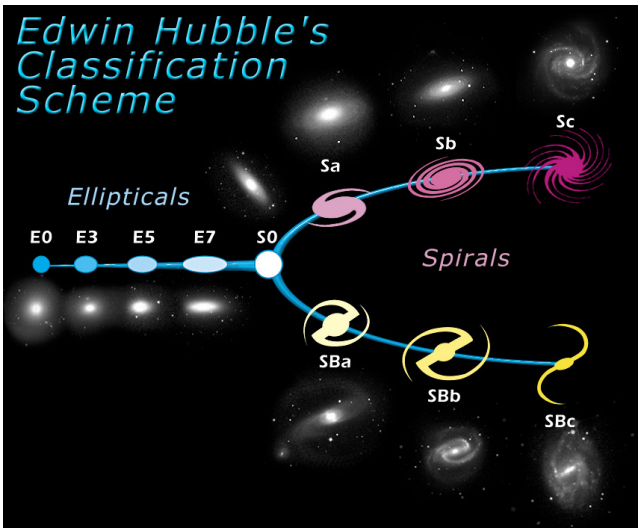

Figure 1.1 The Hubble "tuning fork." On the left are elliptical galaxies, with axis ratios increasing to the right. The "tines" of the fork are disk galaxies with and without central bars. Moving right, the size of the bulge decreases, the arms become less tightly wound, and more "clumps" appear along the arms. Figure from Sloan Digital Sky Survey website.

"masses", with the intensity on each bulb serving as a proxy for gravity. The simulation was remarkably successful in producing the basic morphological deformations resulting from the tidal interactions.

Despite the work of Holmberg and a few others, the idea that gravity, and tidal forces in particular, was responsible for morphological peculiarities was met with some resistance until the work of Toomre & Toomre (1972), which demonstrated that both intergalactic bridges and extended tails could result from tidal forces. It is beyond the scope of this thesis to give a complete discussion of morphologies resulting from interactions of various types, so the interested reader is referred to the review of Struck (1999). We shall direct our attention instead to a small subsection at the end of Toomre & Toomre (1972), entitled "Stoking the Furnace?"

1.2 Induced Star Formation

In their investigation of the relationship between the dynamics of an interaction and the effect on the morphologies of the galaxies, Toomre & Toomre (1972) found evidence suggesting that, were two galaxies to be in very close proximity, and enough gas flung out into long tidal tails to remove angular momentum, the galaxies could merge. They further speculated that, in less extreme circumstances, clouds of gas could be dislodged from one galaxy and fall toward the nucleus of the other, increasing the gas density and thereby fueling a burst of star formation activity.

Observational evidence that interactions led to enhanced star formation had been available for some time. Holmberg (1958) found a correlation in the colors of paired galaxies, in which the colors of the two galaxies tended to be close together. This effect is partially the result of star formation triggered by the interaction, although there is also a tendency for similar galaxy types to form together.

Further evidence of interaction-induced star formation came with the work of Larson & Tinsley (1978), in which the authors compared star formation in a sample of peculiar galaxies taken from the Arp (1966) atlas to a sample of normal galaxies from the Hubble atlas (Sandage, 1961). Star formation was gauged using the $U-B$ and $B-V$ colors. Young stellar populations are dominated by bright, blue O and B stars, so these color indices will tend toward smaller values for younger populations, though it should be noted that this simple relation can be complicated by additional factors such as reddening, metallicity, and the stellar initial mass function. This will be discussed further in Section 1.4.1.

The observational results from Larson & Tinsley (1978) are shown in Figure 1.2. First, galaxies from the Arp sample tended to be somewhat bluer in the $U-B$ and $B-V$ color indices. Second, the Arp galaxies showed a much greater scatter in both colors than the Hubble galaxies. Moreover, within the Arp sample, most of the scatter resulted from galaxies that showed signs of tidal interactions. Arp galaxies that, while morphologically peculiar, did not appear to be interacting, showed only slightly more scatter than the sample drawn from the Hubble atlas.

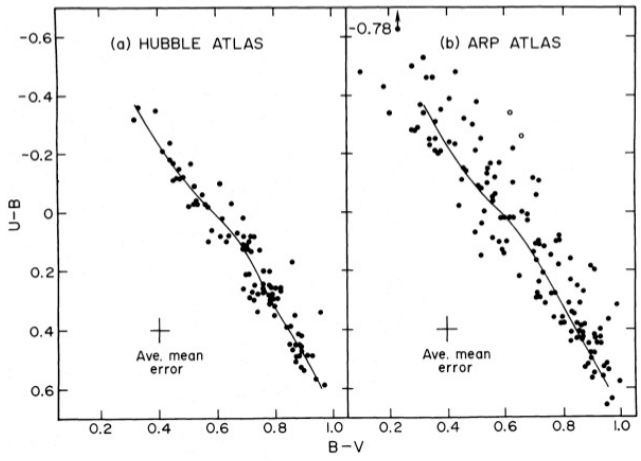

Figure 1.2 Color-color plots showing (a) normal spirals from the Hubble atlas and (b) morphologically peculiar galaxies from the Arp atlas. The solid curve is the estimated mean for the Hubble atlas sample. The Arp atlas sample shows slightly bluer colors, and also shows higher scatter. From Larson & Tinsley (1978).

These results were interpreted using a series of model galaxies constructed using evolutionary synthesis techniques (see Section 1.4.1). The models indicated that the colors of a galaxy depended most strongly on the star formation rate (SFR). In particular, the more extreme colors of the Arp sample were best fit by models in which a strong burst of star formation, lasting as little as 20 Myr, was superposed over an older stellar population. In contrast, the colors of the Hubble galaxies were consistent with models in which the SFR had not varied significantly over a time period shorter than 500 Myr. It seems, then, that one of the effects of galaxy interactions is to trigger bursts of star formation.

The enhanced SFR in interacting galaxies observed by Larson & Tinsley (1978) has been confirmed in numerous subsequent studies. Recent examples include Barton et al. (2000), who used optical spectra of 502 galaxies in close pairs and N-tuples to measure Hα equivalent widths [EW(Hα)], which are an indicator of star formation. They found that galaxies in near proximity tended to have higher EW(Hα) values. When these values were fit to evolutionary synthesis models (see Section 1.4.1), it was found that interaction-induced star formation could plausibly explain the elevated Hα emission.

Smith et al. (2007) conducted mid-IR observations in the 3.6, 4.5, 5.8, and 8.0 μm bands of

the Infrared Array Camera (IRAC) and the 24 μm band of the Multiband Imaging Photometer for *Spitzer* (MIPS) instruments on board the *Spitzer Space Telescope*. In this study, *Spitzer* colors for 35 pairs of interacting galaxies exhibiting strong tidal features were compared to colors from a set of 26 normal spiral galaxies from the *Spitzer* Infrared Nearby Galaxies Survey (SINGS; Kennicutt et al. 2003; Dale et al. 2005). Several of the colors differed significantly from the spirals, although some did not. Most notably, the [3.6]$-$[24] colors of the interacting sample were found to be be 0.8 mag redder on average than in the spirals, consistent with an enhancement to the SFR of a factor ~ 2 per unit mass.

A recent study by Smith & Struck (2010) combined UV data from *Galaxy Evolution Explorer* (*GALEX*) with optical data from the Sloan Digital Sky Survey (SDSS). The interacting galaxy sample consisted of 42 interacting pairs showing strong tidal features from the Spirals, Bridges, and Tails *GALEX* atlas (Smith et al., 2010), while the control sample was made up of 121 spirals selected from the *GALEX* Ultraviolet Atlas of Nearby Galaxies (Gil de Paz et al., 2007). In most of the colors, including all those with one of the *GALEX* UV bands, the interacting sample showed larger scatter than the sample of normal galaxies, likely due to enhanced star formation accompanied by high extinction at UV wavelengths.

1.3 Physics of Star Formation

Understanding interaction-induced star formation is crucial to understanding the star formation history of the universe. In addition to the "isolated" pairs of galaxies that will be the subjects of Chapters 2–4, most galaxies reside in clusters where interactions with both other galaxies and the intercluster medium occur frequently (see Section 1.5.2). Interactions were also more important in the early universe when the density of galaxies was higher and interactions more frequent.

With the goal of improving our understanding of star formation in interacting systems, we will give a brief overview of the physics which drive the formation of stars.

1.3.1 Star Formation on Small Scales

Star formation begins in the dense cores of molecular clouds. These regions are normally near hydrostatic equilibrium; that is, pressure gradients (often turbulent pressure) approximately support them against gravitational collapse. However, cloud cores also have exceptionally low temperatures ($T \sim 10$ K) and high densities ($\geq 10^4$ cm^{-3}, compared to a typical value of $n \sim 200$ cm^{-3} throughout the cloud; Tielens 2005), which allows a sufficiently large density perturbation to overcome hydrostatic equilibrium and cause the cloud to collapse and form stars.

To get a very rough sense of how star formation occurs, we will follow the treatment of the text of Ryden & Peterson (2010). Suppose we have a spherically symmetric molecular cloud of mass M and initial radius r_0. For the moment, we will assume the cloud is not rotating. For a molecule orbiting in the cloud at radius r, Kepler's Third Law gives

$$P^2 = \frac{4\pi^2 a^3}{GM_r}, \tag{1.1}$$

where P is the orbital period, a is the semi-major axis of the orbit, and M_r is the mass interior to r. For a molecule at the outer edge of the cloud, we have $M_r = M$. This will hold even when the cloud collapses, since all particles on smaller orbits will also be falling toward the cloud center and will therefore remain interior to a molecule at the outer edge of the cloud.

Since the cloud has no angular momentum, the molecule will effectively be in free-fall, so its orbit will have a very high eccentricity, $e \approx 1$. It will also have $a = r_0/2$ and its orbital period will be twice the free-fall time, $t_{ff} = 2P$. Substituting into Equation 1.1,

$$t_{ff}^2 = \frac{\pi^2 r_0^3}{8GM}. \tag{1.2}$$

In terms of the mass density $\rho = M/(4/3\pi r^3)$,

$$t_{ff}^2 = \frac{3\pi}{32G\rho} \tag{1.3}$$

For a typical molecular cloud core we take $n = 10^6$ cm^{-3}, so $\rho = 3 \times 10^{-15}$ kg m^{-3} and

$$t_{ff} = 4 \times 10^4 \text{ yr} \left(\frac{3 \times 10^{-15} \text{ kg m}^{-3}}{\rho} \right)^{1/2}. \tag{1.4}$$

For this rapid collapse to occur, the cloud must experience a perturbation that causes self-gravity to overwhelm the pressure gradients that normally support the cloud. Hydrostatic equilibrium will be restored if these pressure gradients change on a time scale smaller than the free-fall time. The pressure changes on a time scale

$$t_{pres} = \frac{r_0}{c_s}, \tag{1.5}$$

where c_s is the sound speed in the cloud, given by

$$c_s = \left(\frac{\gamma kT}{\mu m_H}\right)^{1/2}, \tag{1.6}$$

where T is the temperature, γ is the adiabatic index, μ is the mean molecular mass, and m_H is the mass of the hydrogen atom. The collapse condition is then

$$t_{ff} < t_{pres}. \tag{1.7}$$

Finally, we obtain the Jeans condition,

$$\left(\frac{3\pi}{32G\rho}\right)^{1/2} < r_0 \left(\frac{\mu m_H}{\gamma kT}\right)^{1/2}. \tag{1.8}$$

The critical value of r_0 is called the Jeans radius, given by

$$r_J = \left(\frac{3\pi\gamma kT}{32G\rho\mu m_H}\right)^{1/2}. \tag{1.9}$$

Cloud cores larger than the Jeans radius are unstable against collapse.

It is worth noting that the Jeans radius decreases with $\rho^{-1/2}$. As a large cloud collapses and its density increases, the size scale for further collapse also decreases, so that the collapse of a single molecular cloud can result in the formation of numerous stars. This fragmentation process does not fully describe the physics involved in the formation of multiple stars, which uses much less of the available gas than implied by the above analysis (Carroll & Ostlie, 2006). A proper analysis must consider factors such as turbulence, rotation, and magnetic fields (Carroll & Ostlie, 2006). While the detailed physics of multiple star formation remain unclear, observations indicate that most stars form in clusters (Lada & Lada, 2003).

It should be noted that by assuming the cloud core has no initial angular momentum, we have ignored a significant problem. If the cloud is rotating before it collapses, a great deal

of angular momentum will need to be removed. Assuming a typical cloud core forms a single star, we take the rotation velocity to be $v_0 \sim 0.1$ km s^{-1} (Ryden & Peterson, 2010) and the radius to be $r_0 \sim 1$ pc (Tielens, 2005). Taking the final stellar radius $r_f \sim 10^{10}$ m for an O star, the final rotational velocity of the star would be $v_f \sim 10^8$ m s^{-1} – highly relativistic, and well in excess of the values ~ 10 km s^{-1} observed in rapidly rotating stars (e.g., Palla, 2002).

The problem of angular momentum dissipation has not been entirely solved. One possibility is that mass is ejected when the cloud core has formed a large protostellar disk. A similar possibility is loss to magneto-centrigugal jets. An alternative is that the formation of a single, high-mass planet in the protostellar disk at a significant distance from the star could hold a significant amount of angular momentum (Ryden & Peterson, 2010).

The Jeans criterion is still frequently used in large-scale models to trigger star formation, so it is useful to discuss. Nevertheless, the preceding treatment represents a significant over-simplification of an enormously complex subject. Among its lesser offenses is the assumption of uniform density, which observations and numerical modeling both suggest is not the case (e.g., Elmegreen, 2000; Gittins et al., 2003). More importantly, the treatment omits turbulent instabilities and magnetic fields. Here we shall provide a brief outline of the star formation process, orchestrated on cloud scales, as it is currently understood. Readers seeking a more complete treatment are directed to the reviews of Vázquez-Semadeni (2010) and McKee & Ostriker (2007).

The star formation cycle begins when a giant molecular cloud is formed from the diffuse interstellar medium (ISM), driven by a spiral density wave, large-scale turbulence, or supernova shock wave (Vázquez-Semadeni, 2010). The turbulence within the ISM from which the cloud forms remains in the cloud (McKee & Ostriker, 2007). This turbulence seems to vanish rapidly, but leaves a mark on the cloud by causing the dense cores to be clustered (McKee & Ostriker, 2007). At this stage, self-gravity and magnetic fields are in near equilibrium, but eventually the growth of the cloud and local density variations will cause the gravitational potential energy low-mass clusters of cores to exceed the magnetic energy supporting the core. At this point the cloud is said to be magnetically supercritical, and collapse begins (McKee & Ostriker, 2007;

Vázquez-Semadeni, 2010). The low-mass cores have shorter free-fall times, and will form stars before the more massive cores (Vázquez-Semadeni, 2010).

Each collapsing core forms an accretion disk, which must transport angular momentum outward, partly in the form of protostellar winds (McKee & Ostriker, 2007). The winds cause more turbulence in the cloud, temporarily impeding the collapse and delaying the bulk of the star formation (Vázquez-Semadeni, 2010). Eventually, winds from protostars in the more massive cores disperse the remainder of the cloud into the ISM, where the star formation cycle will start again (McKee & Ostriker, 2007; Vázquez-Semadeni, 2010).

1.3.2 Star Formation on Galaxy Scales

The enhancements in the star formation rate of a galaxy caused by tidal interactions are often global, involving the movement of large quantities of gas both within and between galaxies. A more global treatment of star formation than that of the preceding section is therefore desirable.

A simple model of the SFR $\psi(t)$ is the Schmidt (1959) law, which assumes the SFR has a power law dependence on the gas density:

$$\psi(t) \propto \frac{\mathrm{d}\rho_g}{\mathrm{d}t} \propto \rho_g^n, \tag{1.10}$$

where ρ_g is the gas density. If the gas is compressed by a factor A, the density is enhanced by

$$\rho_g^n \propto \left(\frac{M}{r^3/A}\right)^n = A^n \rho_0^n$$

per unit volume. Since the volume has decreased by a factor A, the total SFR is enhanced by a factor A^{n-1} (Kennicutt, 1998a). From an observational standpoint, this formulation is not ideal, since only surface densities, and not volume densities, are directly observable. The Schmidt law was reformulated by Kennicutt (1989) in terms of surface densities, and the power law index was constrained by observations. The result is sometimes called the Kennicutt-Schmidt (K-S) law,

$$\Sigma_{\mathrm{SFR}} = \Sigma_{\mathrm{g}}^N = (\Sigma_{\mathrm{HI}} + \Sigma_{\mathrm{H_2}})^N, \tag{1.11}$$

where the Σ's correspond to surface densities. Note that we have used an upper-case N to distinguish the power-law index from that of the volume-density Schmidt law, n, although for an approximately linear star formation law with $n \approx 1$, $N \approx n$ (Kennicutt, 1989).

Kennicutt (1998b) estimated $N = 1.4 \pm 0.15$ from an exceptionally large sample of 61 normal spirals and 36 IR-selected starbursts, covering 5 orders of magnitude in ρ_g and 6 in SFR. It should however be noted that there was significant scatter, roughly half of which could be accounted for by extinction and uncertainties in the molecular gas mass (Kennicutt, 1998b).

Although the Kennicutt-Schmidt law is approximately valid over wide ranges of gas density, it has no cutoff at low gas density. This is problematic, as there are observations showing that the K-S law does not hold at low densities. For example, Hα, H I, and CO observations of M51 show a drop in star formation between spiral arms in excess of that expected based on the decrease in gas density (Knapen et al., 1992). Abrupt drops in the radial SFR are also found in many spirals, as shown in Figure 1.3 (Kennicutt, 1998b). The decrease can be explained as the result of a gas density threshold that must be reached for gravity to overcome pressure and shear and allow large molecular clouds to build up (e.g., Kennicutt, 1998b; Struck, 1999).

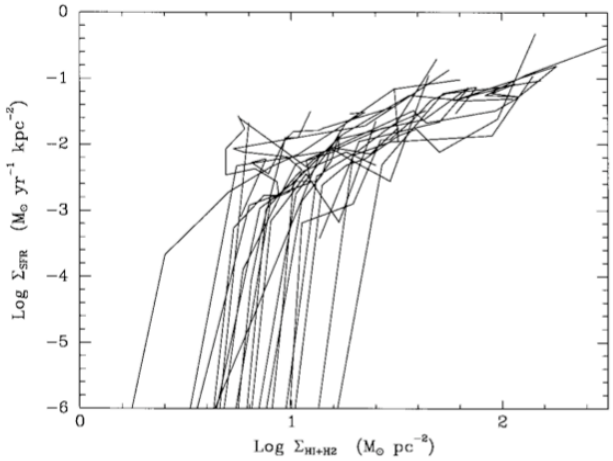

Figure 1.3 Azimuthally averaged SFR profiles per unit area are plotted against gas density for 21 normal spiral galaxies. The SFRs were estimated using Hα data. While the SFR is approximately linear at high densities in most of the galaxies, it drops off abruptly at low densities, illustrating threshold effects. From Kennicutt (1998b).

The threshold surface density Σ_c, developed by Toomre (1964), is commonly given as

$$\Sigma_c = \alpha \frac{\kappa c}{\pi G}, \tag{1.12}$$

where κ is the radial epicyclic frequency, c is the velocity dispersion of the clouds, and α is a dimensionless constant ~ 1 (e.g., Struck, 1999; Kennicutt, 1998a). The ratio of the critical to measured gas density is given by the Toomre Q parameter,

$$Q = \frac{\Sigma_c}{\Sigma_{\rm g}}. \tag{1.13}$$

The value of c is roughly constant with radius. The gas density profile typically has the form $\Sigma_g \propto 1/r$ (Struck-Marcell, 1991), and $\kappa \propto 1/r$ as long as the rotation curve is flat (Struck, 1999). Thus, the value of Q changes little with radius over a disk. Typical threshold densities are $\sim$ 1–20$M_\odot$ pc^{-2} (Kennicutt, 1998a).

The value of Q determines whether star formation is possible. If $Q \gg 1$, star formation should be suppressed due to the inability of the gas to form large, gravitationally unstable clouds. If instead $Q \sim 1$, the growth of unstable clouds will be suppressed in most of the disk, but local variations may allow for some star formation (Kennicutt, 1998a).

Gas density threshold arguments have been successful in accounting for nonlinear changes in the SFR with gas density. Rand (1993) showed that the SFR in M51 could be explained by a threshold density mechanism, with the spiral arms above the threshold and the interarm regions below it. Kennicutt (1989) found that drops in the radial SFR in late-type spirals could be reproduced by a Toomre-style instability criterion with a reasonable choice of parameters. These results were expanded using a larger sample by Kennicutt (1998b). However, recent studies based on UV data have shown extended star formation well beyond the optical disks (see Bigiel et al. 2010b, and references therein).

Improving data quality, especially in the UV due to *GALEX*, has changed our understanding of the K-S law dramatically in recent years. While the UV suffers from extinction to a far greater degree than Hα, it also traces a much wider segment of a young stellar population, since strong UV emitters typically have masses $> 3M_\odot$, much lower than the $M > 17M_\odot$ required for strong Hα emission (Lee et al., 2009). Since the lifetimes of lower mass stars are

longer, the UV also allows star formation to be traced over a much longer time period $\sim 10^8$ yr, rather than $\sim$ few Myr.

One of the main questions to emerge from the recent UV work has been what role the two gas components, H I and H_2, play in determining the star formation rate. Various authors have claimed that one or the other of the components is more significant than the other (see Bigiel et al. 2010a, and references therein). Bigiel et al. (2008) addressed this question using a sample of 7 nearby spiral galaxies with high-resolution data in H I and H_2 (from CO). The SFR was measured using a combination of *GALEX* FUV and *Spitzer* 24 μm data. They found that the SFR was generally uncorrelated with $\Sigma_{\rm HI}$, but was strongly correlated with with $\Sigma_{\rm H2}$, with a power law index $N = 1.0 \pm 0.2$. A study of the inner regions of M51 similarly indicated that the SFR depended only on the molecular gas density (Blanc et al., 2009).

Although these studies seem to reduce the role of H I in directly fueling star formation, the amount of H I available may be the most important factor in outer disks. Bigiel et al. (2010b) estimated the SFR in outer disks using *GALEX* FUV and determined that it correlated well with $\Sigma_{\rm HI}$. This may be because outer disks are deficient in H_2 compared to inner disks, so the formation of H_2 from H I becomes the slowest part of the star formation process, and thus its primary regulator.

Shruba et al. (2010) explored the length scales over which the K-S law holds in M33 using CO to measure $\Sigma_{\rm H2}$ and Hα to measure the SFR. On kpc scales, they found an K-S type dependence of SFR on $\Sigma_{\rm H2}$, with $N = 1.1$–1.5, independent whether the targeted star formation region was centered on a CO or Hα peak. On smaller spatial scales, the CO-to-Hα ratio showed a great deal more variation, and the large-scale star formation law is no longer useful at scales ≤ 300 pc, at which point the evolutionary state of individual gas clouds becomes a dominant factor.

Although the application of the K-S law is becoming increasingly complex, it is still useful for roughly describing the level of star formation exhibited by a particular system. Star formation levels that can be accounted for by the Kennicutt-Schmidt law fall into the linear regime. The dynamical models of Wallin (1990) showed that tidal forces resulting from the passage of

a companion galaxy at approximately the disk radius of the primary galaxy typically produce density enhancements of a factor 2–5 in the emerging tidal tails, with the local SFR increasing by a factor ≤ 10 for values of $n \approx 1.5$. Evolutionary synthesis models (see Section 1.4.1) indicated that the color changes associated with this SFR change were consistent with observations (Wallin, 1990).

Enhancements requiring more extreme parameters in the K-S law fall into the nonlinear regime. In these systems, the global SFR is up to 30 times higher than in normal disk galaxies, and can be still higher locally, with fractions $\geq 10\%$ of the global stellar population formed on a time scale less than $\sim 10^8$ yr (Kennicutt, 1998a). Starburst nuclei are a particularly relevant example of nonlinear star formation enhancements.

At the limit of physically possible SFRs is the catastrophic regime, which includes ultraluminous infrared galaxies (ULIRGs). In these galaxies the star formation is highly concentrated in the nucleus, but occurs at such a rate that nearly all of the nuclear gas must be converted into stars in $\sim 10^8$ yr. Paradoxically, the small spatial scales of the nuclei in which catastrophic star formation occurs are sufficiently small that the K-S law may be able to explain the observed SFR, provided the star formation efficiency is high enough (Kennicutt, 1998a).

1.3.2.1 Cloud Collision Models

To effect the rate of star formation, interactions must alter the interstellar media (ISM) of galaxies. This can be accomplished in a number of ways. Here, we consider the effect of collisions between clouds in the ISM of one or more of the galaxies involved in a collision.

The most direct approach to cloud collisions is for a giant molecular cloud (GMC) from one of the galaxies to pass through the disk of the other galaxy. Tenorio-Tagle (1981) found that infalling clouds with relative velocities ≤ 250 km s^{-1} would coalesce with high-density regions of the disk, namely GMCs. The passage of the cloud through the disk was accompanied by shocks, which became gravitationally unstable and collapsed into star-forming regions according to a Jeans-like criterion. However, it was noted that GMCs are not sufficiently common that this mechanism could account for starburst-level activity.

In a less direct approach, the two galaxies do not collide, but the cloud collision rate within a single disk is increased by the tidal forces from the companion. Olson & Kwan (1990) ran several sets of 3-dimensional models of gas clouds in a perturbed gravitational potential. They found that stronger interactions resulted in a broader velocity range for cloud-cloud collisions, with an increasing fraction of the collisions leading to disruption rather than merging of the clouds. However, if the overlap regions between clouds in glancing collisions became gravitationally unstable, then cloud collisions could reasonably account for some of the observed enhancement to the SFR, though it should be noted that these models did not explicitly include star formation.

Jog & Solomon (1992) found that in order to induce star formation of the type seen in starburst galaxies, collisions between molecular clouds would be far too rare. Instead, they found that collisions between far more common H I clouds could produce a high-pressure medium to compress GMCs. The resulting pressure would produce shocks in the outer cloud layers, which in turn became gravitationally unstable, leading to star formation. An existing high-pressure medium acting on GMCs that have fallen towards the central regions of a galaxy could be responsible for nuclear starbursts (Jog & Das, 1992).

The recurring problem of infrequent collisions between molecular clouds may be due in part to model assumptions. Tan (2000) showed that the Kennicutt-Schmidt law could be reproduced in a differentially rotating disk where all star formation was caused by cloud collisions. The clouds were assumed to be bound and found to be long-lived, which may not be realistic (see Dobbs et al. 2011, and references therein). The number of collisions was increased over that in previous studies partly because collisions in a differentially rotating disk are much more frequent than collisions between "particles in a box," particularly where shear velocities are high. The small vertical scale height of the GMC's also lends itself to a nearly 2-dimensional treatment of the problem, which further increases the collision rate. More recent work by Tasker & Tan (2009) confirmed these results, and also reproduced many other properties of molecular clouds in the Galaxy.

Much of the recent work on cloud collisions has focussed on the triggering of star formation

in individual cloud collisions, even to the point of modeling specific star forming regions (e.g., Duarte-Cabral et al., 2011). Models have consistently shown that the clouds form a shocked layer or slab, which then becomes gravitationally unstable and leads to successive fragmentation of the cloud into star forming regions (Kitsionas & Whitworth, 2007; Anathpindika, 2009a,b), though under certain conditions hydrodynamic instabilities in the gas prevent the growth of gravitational instabilities (Anathpindika, 2009a).

1.3.2.2 Radial Gas Transport

Nuclear starbursts are observed to involve tremendous quantities of gas $\sim 10^{10}$–$10^{11} M_{\odot}$ (Kennicutt, 1998a). Much of this gas is transported to the central regions of the galaxy from farther out in the disk as a result of dynamical torques on molecular clouds.[1]

Barnes & Hernquist (1996) showed in a series of models of parabolic encounters between disks that the torques on gas that ended up in the central regions of a perturbed disk had a gravitational origin. Although gas-dynamical torques did not transport a significant amount of angular momentum away from this gas, collisionless models were unable to radially transport gas, implying that gravitational torques operate via a gas-dynamic mechanism. At early stages of the encounter, these torques come from the companion galaxy, with the angular momentum of the gas transported to the spin of the companion disk. At later times, the torques come from induced bars. These results are summarized in Figure 1.4.

The gas and stellar bars produced in the models of Barnes & Hernquist (1996) were typically out of phase by 5–10°. This phase difference results from the fact that the stars are collisionless, while the gas is not. Intersections between gas orbits then produce radiative shocks, reducing the kinetic energy of the gas and putting the gas bar on a slightly different orbit. Torques between the two bars transport angular momentum away from the gas, moving it radially inward.

[1] Dynamical torques on the the clouds result from the fact that, while gravity is a central force, the clouds are spatially extended rather than point sources. Tidal friction within the Earth-moon system has a similar origin.

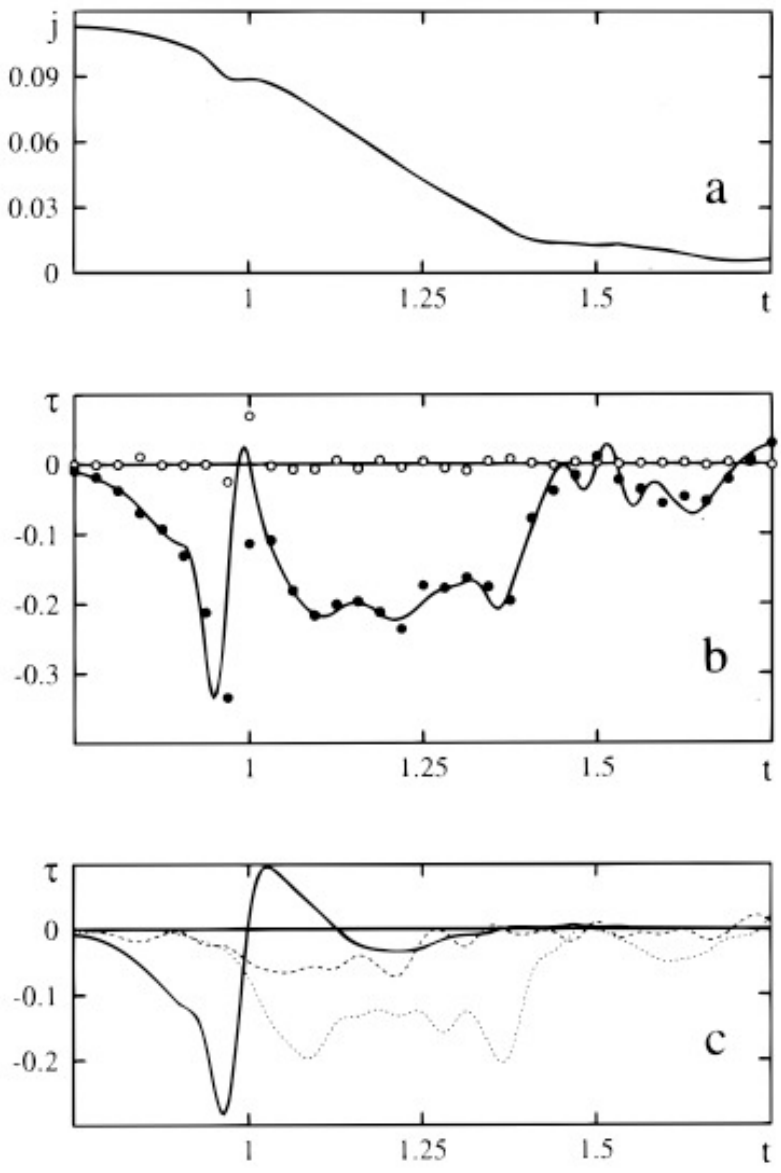

Figure 1.4 (a) Specific angular momentum of the gas that ends the simulation in the center of the perturbed disk. (b) Specific torques on the gas. Filled circles represent gravitational torques, while open circles show hydrodynamic torques. The smooth curve was obtained by numerical differentiation of the data from (a). (c) Gravitational torque components. The solids curve is the gravitational torque due to the companion galaxy, the dashed line is due to the halo, and the dotted line is due to the bar. From Barnes & Hernquist (1996).

1.3.2.3 Cross-Fueling

Star formation can also be induced by the transfer of gas from one galaxy to another. This cross-fueling can be accomplished in two different ways: hydrodynamic interactions and tidal interactions.

Hydrodynamic interactions involve a direct collision between disks or halo gas leading to supersonic collisions between gas clouds (Struck, 1999). The effects of these interactions on star formation are complex, since the cloud collisions create shocks that heat the gas and temporarily suppress star formation (Struck, 1999). It is also possible for large quantities of gas to be "splashed" out of one or more of the galaxies. The mass ejected by the splash, and which galaxy (if any) it returns to, are heavily influenced by the relative inclination of the disks.

Star formation resulting from a splash collision is typically delayed until the gas falls back onto one of the galaxies. If the gas falls back onto the companion, it will often reform the disrupted disk (Struck, 1997). Regardless of which disk the gas returns to, it ultimately moves toward the galactic center. Initially, the accretion process will heat the gas and inhibit star formation, though once it has cooled star formation may be enhanced in the galaxy center (Struck, 1997). Situations in which star formation is suppressed will be further discussed in Section 1.5.

Unlike hydrodynamic effects, tidal interactions have comparable effects on both the stars and the gas (Struck, 1999). Mass transfer resulting from tidal forces was first demonstrated by Toomre & Toomre (1972). A particularly thorough follow-up effort was made by Wallin & Stuart (1992), who created a grid of over 1000 models using restricted three-body methods. The models indicated that the three most important parameters in determining mass transfer are the mass ratio of the disks, the impact parameter of the collision, and the relative inclination of the disks, but the dependences are usually complex. Generally, prograde encounters (in which the orbital angular momentum of the companion has the same direction as the rotational angular momentum of the galaxy) with low inclinations produce the strongest tidal features. The prograde nature of the encounter increases the length of time over which the same parts

of the disks are near one another. Low inclinations enhance the tidal features because the disk particles prefer to remain in the plane of their original orbit.

There is a wealth of observational evidence for enhanced star formation in tidal features (e.g., Bastian et al., 2005b; Smith et al., 2008; Mullan et al., 2011), though it is much more difficult to identify cross-fueling. Marziani et al. (2003) give three conditions required to establish cross-fueling: (1) gas must be stripped from one of the galaxies; (2) the gas must be falling toward the other galaxy; (3) the infalling gas must be associated with a starburst.

Marziani et al. (2003) observationally demonstrate cross-fueling in Arp 194 using a combination of morphological and kinematic observations. The stripping of gas from A194N is indicated by its morphology and by the trail of gas "blobs" leading to the southern galaxy, and the redshift of the blob nearest A194S shows that it is falling toward that galaxy. The presence of vigorous star formation in A194S is inferred from its Hα luminosity, which indicates a star formation rate of 4.5 $M_\odot$ yr^{-1}.

The combination of observations with dynamical modeling is also a good method of identifying cross-fueling. In models of the Arp 284 system (NGC 7714/5; see Chapter 2), Struck & Smith (2003) found that NGC 7715 had transferred a significant amount of mass to NGC 7714, up to 2/3 of its original gas. The gas transferred to the southwest tail of NGC 7714 likely triggered star formation there, as the gas was compressed by the low angular momentum of the transfer material. Smith et al. (2008) made dynamical models of the Arp 285 interaction, finding that a significant amount of material was removed from the primary (NGC 2854) by the nearby passage of the companion (NGC 2856). Some of this gas eventually fell onto the companion, where it was compressed, leading to star formation.

As noted in the cross-fueling criteria of Marziani et al. (2003), mass transfer is a necessary but not sufficient condition to demonstrate cross-fueling, and there have been observations of systems in which mass transfer has not (so far) lead to star formation. An example is the work of Keel (2004) on the interacting system NGC 1409/10. Two-band *HST* Space Telescope Imaging Spectrograph (STIS) imaging was used to estimate extinction across a dust stream stretched between the two galaxies, while WIYN data provided kinematic information. From

these data, the dust feature is estimated to contain 3×10^8 $M_\odot$ of gas, which is transferring to NGC 1409 at a rate of 1 $M_\odot$ yr^{-1}. However, NGC 1409 does not appear to be experiencing enhanced star formation.

Not all collisions involve mass transfer. Cullen et al. (2006) searched for molecular gas in the early-type galaxy (either elliptical or S0) in eight interacting pairs from the Arp atlas using IRAM observations of CO emission lines. They were unable to detect molecular gas in any of the galaxies, indicating that no significant transfer of molecular gas had taken place.

1.4 Deciphering Star Formation Histories

1.4.1 Evolutionary Synthesis Models

The characterization of a stellar population ideally begins with the study of individual stars. In the Galaxy, it is generally possible to obtain photometric or spectroscopic measurements of individual stars down to some limiting luminosity. From the properties of those stars, characteristics of a the population can be inferred. For example, the color indices of a large number of stars in a globular cluster can be used to find the main sequence turnoff and thus the age of the cluster, assuming all of the stars formed at the same time.

In extragalactic astronomy, attempts to study stellar populations are complicated by the fact that the populations cannot usually be resolved into stars, so that the only spectra available are integrated over the entire population. It is the goal of evolutionary synthesis models to use these integrated spectra to characterize the stellar population.

1.4.1.1 Evolutionary Synthesis Technique

Evolutionary synthesis has its roots in population synthesis, a technique dating from the 1930s. In population (or spectral) synthesis, individual stellar spectra taken from empirical libraries are summed so as to match the spectrum of an observed stellar population. While useful in determining the distribution of spectral types in a stellar population, population synthesis provides no direct information about the star formation history, which involves parameters including the stellar initial mass function (IMF; see Section 1.4.1.2), metallicity, and

age. Reliable models of stellar atmospheres are also required for these parameters to yield spectra that can be compared with observations. Evolutionary synthesis may be broken into three main steps (Leitherer & Heckman, 1995):

1. Star formation occurs at a specified rate; stars are placed in the HR diagram along the zero-age main sequence (ZAMS) according to the selected IMF.

2. Stellar evolutionary models provide the metallicity, $Z(t)$; mass, $M(t)$; luminosity, $L(t)$; effective temperature, $T_{eff}(t)$.

3. Number densities in the HR diagram are determined and each star is assigned a spectral type based on its position. The integrated spectrum is obtained by summing over the population.

Statistical methods such as chi-square minimization are generally used to compare the integrated population spectrum (or broadband colors) to observations and find the best fit to the free parameters.

Evolutionary synthesis is a very powerful technique for studying stellar populations, but it suffers from the significant shortcoming that many of the free parameters are degenerate with one another: reddening, age, metallicity, and the IMF can all produce similar changes, especially to broadband optical colors (Kennicutt, 1998a).

Due to these degeneracies, the integrated colors of a stellar population can result from a number of factors. Increasing the metallicity will generally redden the integrated colors, mimicking an older population. Interstellar extinction also results in reddening of the intrinsic spectrum, and can therefore mask the presence of a young population. The assumed form of the stellar initial mass function (see Section 1.4.1.2) is also significant. An IMF that gives more weight to high mass stars is difficult to distinguish from a recent increase in star formation (Kennicutt, 1998a). Older background populations can contaminate photometric apertures and dilute the light of young populations, particularly if individual star clusters are not fully resolved (see Section 2.7.3).

1.4.1.2 Initial Mass Function

A stellar population such as a star cluster forms with a mass distribution called the initial mass function (IMF), $\xi(M)$. The IMF gives the number of stars $\mathrm{d}N$ in the mass interval $(M,\, M + \mathrm{d}M)$ by

$$\mathrm{d}N = N_0 \xi(M) \mathrm{d}M, \tag{1.14}$$

where N_0 is a normalization constant. The IMF is often taken to have the form of a power law, such that

$$\xi(M) \propto M^{-\alpha}. \tag{1.15}$$

The form of the IMF is difficult to determine observationally, and it remains unclear if there is a universal form for the IMF or if the IMF has been constant through time (e.g., Bastian et al., 2010). The main difficulty in observational determination of the IMF is stellar evolution, since the mass distribution of a sample field stars will not directly yield the IMF because high-mass stars will have evolved off the main sequence (Bastian et al., 2010). Further, the field population is unlikely to be coeval, meaning the stars did not all form at the same time. While the measured distribution can be corrected for stellar evolution, doing so tacitly assumes that the IMF is time-independent (Bastian et al., 2010).

Some of the difficulties posed by stellar evolution can be surmounted by using a coeval population such as a star cluster, which ensures that the population formed simultaneously and with similar composition. However, open clusters may not have enough stars to properly sample the high-mass end of the IMF, while richer globular clusters will have much more evolved populations in which high-mass stars have evolved far beyond the main sequence.

Despite these difficulties, measurements of the IMF are broadly consistent. The first IMF came from Salpeter (1955), who found $\alpha = 2.35$, a value which is still often used today. More recently, Kroupa (2002) defined a piecewise form of the IMF, with $\alpha = 1.3$ for $M/M_\odot = 0.1$–0.5 and $\alpha = 2.3$ for $M/M_\odot = 0.5$–100.

1.4.2 Super Star Clusters

Prior to the launch of the *Hubble Space Telescope* (*HST*), limitations in angular resolution limited the study of extragalactic stellar populations. For all but the most nearby galaxies (e.g., the Magellanic Clouds), the star formation rate could be determined only on global or near-global (i.e., inner vs. outer disk) scales. *HST* has made it possible to resolve individual star clusters at significant distances, and in so doing has completely changed the study of extragalactic star formation.

The first observation of super star clusters was made by Holtzman et al. (1992) using the *HST* Planetary Camera. Several bright, blue, point-like sources were found near the nucleus of the peculiar elliptical galaxy NGC 1275 ($d \approx 70$ Mpc; NED) with absolute magnitudes $M_V \sim -10$ to -12 and the brightest having $M_V \sim -14$. Typical globular clusters in the Galaxy have $M_V \sim -7$, with the brightest having $M_V \sim -10$. Along with the blue colors, this suggested that the sources represented a population of young globular clusters. Evolutionary synthesis models indicated ages ≤ 300 Myr, with masses of 10^5–$10^8 M_\odot$. The observations also revealed new morphological peculiarities in the galaxy which suggested a merger $\sim$ few $\times 10^8$ Myr ago, which could have led to the formation of the clusters.

Whitmore et al. (1993), also using the *HST* Planetary Camera, found 40 blue pointlike objects in NGC 7252, a merger remnant resulting from a collision of two disks ~ 1 Gyr ago. Like the Holtzman et al. (1992) sources, the objects were too bright to be individual stars, implying that they were clusters. The ages were estimated to be 34–500 Myr, suggesting that these were also young globular clusters.

Additional evidence that the clusters were young was provided by their association with young emission regions. Conti & Vacca (1994) resolved the two starburst regions of the Wolf-Rayet (W-R) galaxy He 2-10 into clusters. The W-R emission from one of the starburst regions indicates the presence of short-lived W-R stars, constraining the age of the emission region to a few Myr. Clusters were also found in strong Hα emission regions (Hunter et al., 1994; Barth et al., 1995).

Although massive, super star clusters are also highly compact. Scheepmaker et al. (2007)

found that clusters in M51 had typical radii of 1–10 pc, with a peak in the radius distribution near 1.5 pc. The largest cluster had a radius of 21.6 pc.

In systems where clusters were particularly numerous, it became possible to study the demographics of star cluster populations. Whitmore & Schwiezer (1995) detected over 700 clusters in the NGC 4038/9 merger, also known as "the Antennae." The cluster luminosity function was defined by a power law, $\phi(L)\mathrm{d}L \propto L^{-\beta}\mathrm{d}L$, with $\beta = 1.78 \pm 0.05$. Subsequent measurements have generally found steeper luminosity functions ($\beta \approx 2$) and a steeper slope at high luminosities (e.g., Whitmore et al., 1999; Gieles et al., 2006; Hwang & Lee, 2008).

Of greater interest than the cluster luminosity function is to derive the more fundamental initial cluster mass function (ICMF). The ICMF is typically determined by combining the cluster luminosities with age estimates obtained using evolutionary synthesis techniques. The models provide a mass-to-light ratio as a function of the cluster age, so once the age of a cluster has been determined its luminosity can be used to determine the mass. To avoid the selection effect of evolutionary fading, only young clusters are used, so that the measured mass function reflects the ICMF.

To a simple approximation, the ICMF has the same power law form as the cluster luminosity function, with a power law index $\alpha = 2$ measured in the Large and Small Magellanic Clouds (Hunter et al., 2003; de Grijs & Anders, 2006; de Grijs & Goodwin, 2008), M51 (Bik et al., 2003), M82 (de Grijs et al., 2003), and the Antennae (Zhang & Fall, 1999). The high mass end of ICMF may however be truncated. Gieles (2009) uses a Schechter function of the form

$$\frac{\mathrm{d}N}{\mathrm{d}M} = AM^{-2}\exp(-M/M_*), \tag{1.16}$$

where A is a constant that depends on the cluster formation rate. The cutoff mass $M_* = (1.9 \pm 0.5) \times 10^5 M_\odot$ (Gieles, 2009).

In addition to the luminosity and mass distributions, systems with abundant cluster populations also provide information about the spatial distribution of clusters. Conti & Vacca (1994) found that the 2 starburst regions of the dwarf galaxy He 2-10 each contained numerous star clusters. On a larger scale, Whitmore & Schwiezer (1995) found in the Antennae that clusters were themselves clustered into larger groups of ~ 10 clusters, which had been seen as

unresolved "giant HII regions" with sizes $\sim$ 100 pc in ground-based observations (Kennicutt, 1984). A detailed description of the fractal nature of hierarchical star formation is beyond the scope of this thesis. The interested reader is directed to Cartwright & Whitworth (2004), Bastian et al. (2007), and Scheepmaker et al. (2009) as starting points.

1.4.2.1 Disruption of SSCs

The possibility that SSCs represent young, metal-rich progenitors of globular clusters has made them objects of considerable interest. However, recent studies have revealed that many SSCs do not survive to become globular clusters – in fact, the majority may dissolve after only 10–20 Myr. This early-stage dissolution, morbidly dubbed "infant mortality" by Lada & Lada (2003), has added a rich new dimension to the field of extragalactic star formation.

Early evidence of this effect was found by Tremonti et al. (2001) in a study of the dwarf starburst galaxy NGC 5253. UV spectra from 8 bright star clusters generally showed the features of O stars, which were absent in the diffuse field. Evolutionary synthesis models indicated that the clusters were very young, 1–8 Myr old. This could be explained if O stars typically formed in clusters, which then dissolved into the field after $\sim$10 Myr.

Evidence of cluster disruption comes primarily from cluster age distributions. The most significant studies have been of the Antennae (NGC 4038/9; Fall et al. 2005) and M51 (Bastian et al., 2005a), which led to competing models of cluster disruption mechanisms.

Fall et al. (2005) obtained images of the Antennae in 5 bands with the *HST* Wide Field and Planetary Camera 2 (WFPC2) and estimated cluster ages using evolutionary synthesis models. The completeness limit of the sample was determined based on mass estimates to avoid the problem of evolutionary fading, in which clusters become dimmer and thus harder to detect as they age. When the cluster ages were binned ($\mathrm{d}N/\mathrm{d}\tau$) and plotted against $\log(\tau/\mathrm{yr})$, the number of clusters in each age bin was found to decrease linearly over an age range of 10^6–10^9 yr, shown in Figure 1.5. It was estimated that 90% of clusters dissolve over each age dex in this range, regardless of mass.

The originators of the mass independent disruption model were based out of the Space

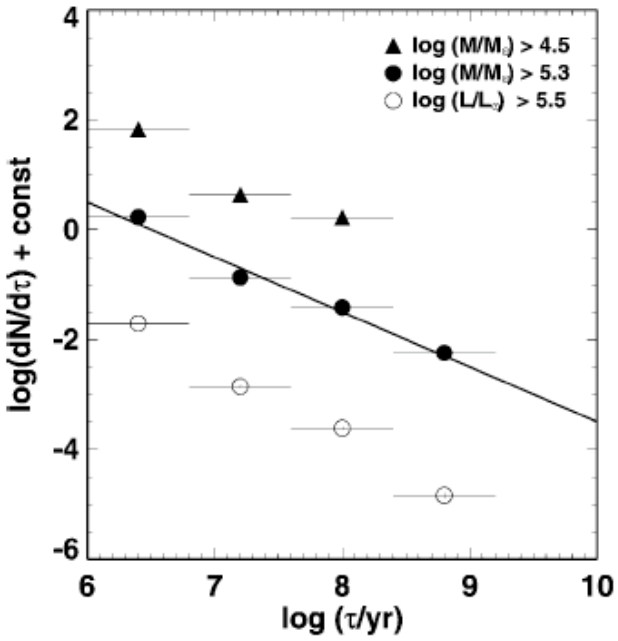

Figure 1.5 Age distribution of clusters from the Antennae, with samples based on three different selection criteria: $L_V > 3{\times}10^5 L_\odot$ (open circles), $M > 3 \times 10^4 M_\odot$ (filled triangles), and $M > 2 \times 10^5 M_\odot$ (filled circles). The diagonal line indicates $\mathrm{d}N/\mathrm{d}\tau \propto \tau^{-1}$, corresponding to a cluster mortality rate of 90%. From Fall et al. (2005).

Telescope Science Institute, so the model is also called "the Baltimore Model" by Lamers (2009). Further studies supporting the model include a revisiting of the Antennae results by Whitmore et al. (2007), which confirmed the mass independent disruption of 90% of clusters per age dex was consistent with the data (but see Bastian et al. 2009). Chandar et al. (2006) found a similar age distribution in the Small Magellanic Cloud (SMC; but see Gieles 2006).

The mass independent cluster disruption is summarized by Lamers (2009) as follows. Clusters dissolve at a rate of 90% per age dex over an age range of 10^6–10^9 yr. These results are obtained using a mass-limited sample (but see Gieles 2006) in which a plot of the number of clusters N in an age bin of width τ, $\log(\mathrm{d}N/\mathrm{d}\tau)$, plotted against log(age/yr) produces a straight line with a slope of -1. A magnitude-limited sample, which has not yet been analyzed by the Baltimore group, would be expected to have a steep slope, between -1 and -2 (Lamers, 2009).

The competing cluster disruption model, originated by a group working out of Utrecht, involves the mass dependent disruption of clusters. The mass dependent disruption model (also called the "Utrecht model" by Lamers 2009) originated in Boutkoulos & Lamers (2003), but the most commonly cited work is the study of M51 by Bastian et al. (2005a). The main results of their analysis are shown in Figure 1.6. Age and mass estimates for the observed sample were obtained using evolutionary synthesis techniques. To remove the effects of binning and fitting methods, a simulated population was also created. The distribution in $\log(M/M_{\odot})$ versus log(age/yr) of the observed sample was then divided by the distribution of the simulated sample to produce a final distribution free of artifacts from the analysis. The resulting figure showed a decrease in the number density of clusters at high mass, which was interpreted as evidence of cluster disruption for ages $\sim$10 Myr. At early ages the disruption is independent of mass, but at older ages disruption is expected to be mass dependent.

Additional support for the mass dependent disruption comes from Gieles et al. (2005), who performed a more detailed analysis of disruption in M51. The model has also been found to be consistent with observations of the solar neighborhood (Lamers et al., 2005; Lamers & Gieles, 2006), SMC (Gieles et al., 2007b), and the Antennae (Bastian et al., 2009). The original work of Boutkoulos & Lamers (2003) was found to be consistent the numerous systems, including M51, M33, the SMC, and the solar neighborhood.

In summarizing the mass dependent disruption model, Lamers (2009) divides the process into three steps. The earliest stage of disruption lasts for roughly $\sim$20 Myr, and is mass independent. At this stage, the clusters dissolve mainly due to mass loss driven by stellar winds and massive star supernovae, which drops the escape velocity below the mean stellar velocity (e.g., Bastian & Goodwin, 2006; Goodwin & Bastian, 2006). In the second phase, lasting from 10^8–10^9 yr, the disruption of clusters is expected to be minimal, so that the cluster age distribution should be roughly flat over this range of ages. However, due to evolutionary fading, the number of clusters observed in each age bin in a magnitude-limited sample is expected to decrease, so $\log(\mathrm{d}N/\mathrm{d}t)$ is expected to have a negative slope.

Mass dependent disruption mechanisms enter in the last phase of the Utrecht model, which

typically begins around an age of 10^9 yr, although the exact age can vary considerably based on environmental factors. The dominant disruption mechanism is interactions with giant molecular clouds (Gieles, 2006). Clusters can also be disrupted by tidal forces (Takahashi & Portegies Zwart, 2000; Baumgardt & Makino, 2003), spiral arm passage (Gieles et al., 2007a), and shocks (Gnedin & Ostriker, 1999), all of which preferentially disrupt low mass clusters.

In the mass dependent disruption model, magnitude-limited observations of a cluster age distribution would thus have three segments. At very young ages, $\log(\mathrm{d}N/\mathrm{d}t)$ is expected to drop sharply as mass loss causes the clusters to become unbound. In the second phase, the decrease in $\log(\mathrm{d}N/\mathrm{d}t)$ is dominated by evolutionary fading, and the slope should be more shallow. In the mass dependent third phase, the slope is expected to steepen (Lamers, 2009).

A mass-limited sample would be similar. The first phase of disruption is mass independent, so the slope should be essentially the same as in a magnitude-limited sample. In the second phase, evolutionary fading effects are removed by the use of a mass-limited sample, so the distribution should be flat. The final phase will again show a steep slope.

The question of which model is correct remains controversial. The confirmation of the mass independent model by Chandar et al. (2006) was challenged by Gieles (2006). The latter authors asserted that the Baltimore group had made an error in determining their completeness limits due to "their erroneous assumption that the sample is limited by cluster mass, rather than luminosity." Evolutionary fading directly effects the luminosity limit of a sample rather than the mass, but the masses are derived based on the luminosities, so that the sample is in fact luminosity-limited.

The results of Whitmore et al. (2007) were challenged by Bastian et al. (2009), who corrected the observed age distribution based on a model of the star formation history of the Antennae. This resulted in an age distribution which did not require a mass independent disruption mechanism. The fact that the mass independent model lacks a clear mechanism to disrupt clusters over 10^6–10^9 yr, independent of the cluster mass, remains one of the major shortcomings of the model.

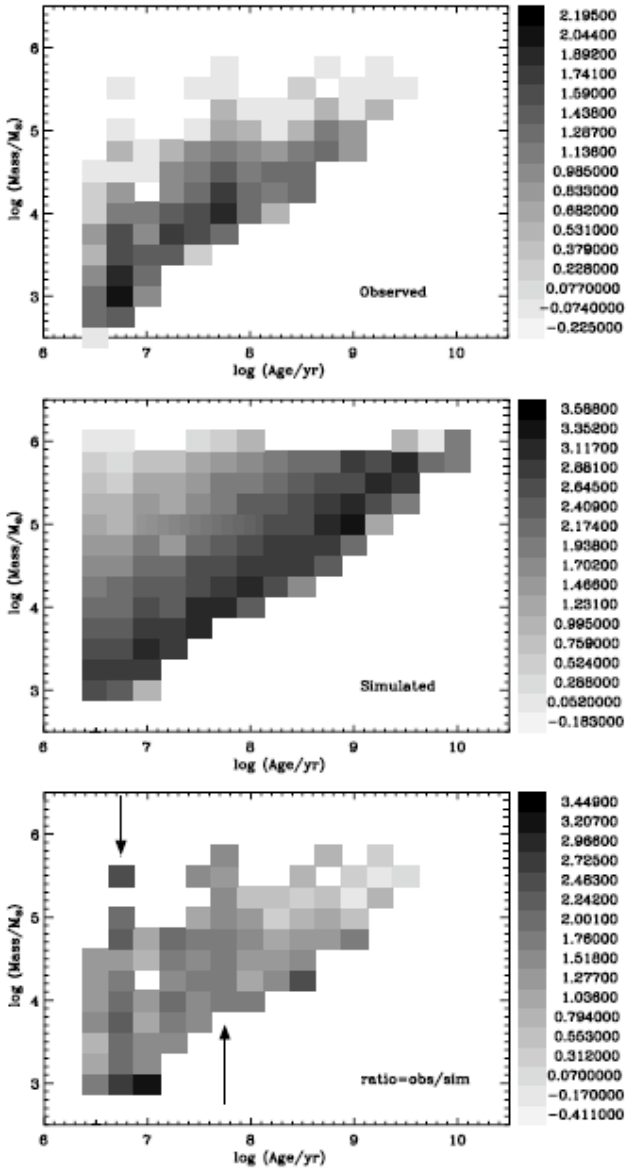

Figure 1.6 Mass as a function of age for clusters in M51. The number density of clusters in each bin is represented by grayscale shading. (a) The observed mass function. (b) A simulated mass function. (c) The observed mass function divided by the simulated one. This procedure removes artifacts due to binning and fitting. The arrows in (c) show ages with overdensities of clusters. From Bastian et al. (2005a).

Studies of cluster populations remain ongoing. Pellerin et al. (2009) examined the cluster population of the collisional ring galaxy NGC 922. To compare the disruption models, a dynamical model including star formation was used to determine the star formation history of the system. When this model was compared to the disruption models, the mass independent model was found to over-correct the age distribution for dissolution. The mass dependent model under-corrected for dissolution for ages between 10^7–10^8 yr.

In Chapters 2 and 3, we will examine the cluster populations of two different interacting systems, Arp 284 and Arp 261. We will determine current luminosity and mass functions for the clusters, as well as the age distributions across the systems. We will also attempt to address the question of early-stage cluster disruption.

1.5 Suppression of star formation

The majority of the work done on the effects of galaxy interactions on star formation has focused on the enhancement of the SFR. There are however cases in which star formation is, at least temporarily or locally, suppressed. In some cases, it is possible for enough gas to be removed from a galaxy that star formation is brought to a complete halt.

1.5.1 Temporary suppression

One way to suppress star formation is through hydrodynamic effects. Splash collisions remove considerable amounts of gas from one or both of the colliding galaxies, forming a bridge. These gas bridges are generally too warm for star formation due to heating from the collision. Unlike tidal interactions, hydrodynamic collisions have little effect on stars, due to the small fraction of the surface area covered by stars (the stellar filling factor) in comparison with gas. A particularly relevant example is the bridge between the Taffy galaxies (UGC 12914/5), which holds 25% of the system's H I gas (Condon et al., 1993) and significant molecular gas (Smith & Struck, 2001; Braine et al., 2003; Gao et al., 2003), but shows no evidence of star formation outside of a single large H II region (Bushouse & Werner, 1990; Gao et al., 2003). This system is the subject of Chapter 4, and a (possibly) similar system is the subject of

Chapter 3.

The removal of significant quantities of gas from a galaxy in a splash collision can result in star formation enhancements after the material falls toward one (or both) of the galaxies, where it forms an accretion disk and moves toward the central regions. The accretion process generally leads to heating of both the infalling material and the local ISM of the host galaxy. Effective star formation requires both high densities and low temperatures, so the heating in the accretion disk temporarily prevents star formation in the central regions of the galaxy (Struck, 1997).

Another relevant phenomenon is the delayed starburst. Strictly speaking, this is not a suppression of star formation, since there is no decrease in the SFR. Rather, one galaxy experiences a starburst before the other. Bernlöhr (1993) spectroscopically identified 12 starburst systems and 5 post-starburst galaxies in a sample of 30 interacting groups. The starbursts were found to start earlier in the smaller companion galaxies, and ended before the starburst in the primary galaxy began $\sim$ few $\times 10^8$ yr later. Starbursts were rarely observed in both galaxies simultaneously. This could be the result of several factors. Smaller companion galaxies have shorter dynamical time scales, potentially allowing a starburst to begin more rapidly. In addition, smaller galaxies typically have a higher gas fraction, and are more strongly disturbed than the larger primary galaxy in an interaction. Any of these factors could facilitate a starburst in the companion before the primary.

1.5.2 Ram pressure stripping

The best studied means of suppressing star formation involving the interaction of a galaxy with its environment is ram pressure stripping (RPS). This process is important in the cores of galaxy clusters, where the mean velocities of the galaxies are too high ($\sim 10^3$ km s^{-1}, compared to $\sim 10^2$ km s^{-1} in the field) to allow strong gravitational interactions (Struck, 2006). Hydrodynamic interactions, however, can be much stronger than in non-cluster galaxies.. In particular, the ISM of a galaxy can be partly stripped away as it passes through the dense intercluster medium (ICM) in the cluster core (Struck, 2006). Although long-time cluster

residents lost their gas long ago, small galaxy groups continue to fall into denser clusters, sending new galaxies through the dense central ICM for the first time (Struck, 2006).

As a disk galaxy makes its first trip through the dense ICM, the low density gas of the outer disk is stripped rapidly, most of which becomes unbound from the galaxy, though some may fall back (Schulz & Struck, 2001; Roediger & Hensler, 2005). After this first passage, the disk can continue to lose gas at a slower rate (Roediger & Hensler, 2005). The remaining gas disk can also be compressed and displaced relative to the galaxy center. The displaced disk may form spiral density waves, which can move angular momentum outward from the inner disk and lead to further compression. The resulting gas disk is somewhat fortified against further stripping (Schulz & Struck, 2001).

Observations indicate that RPS may have very important effects on galaxy morphology, acting to evolve late-type spirals with high SFRs into S0's with little or no star formation. For example, Dressler (1980) found a strong correlation between galaxy type and galaxy density in a sample of 55 rich clusters, with more S0 and elliptical galaxies where the density was highest. Dressler (1980) actually argued that RPS was probably not responsible for the lack of late-type spirals near cluster centers, for three reasons: (1) the bulge-to-disk ratio is different in S0's than in spirals; (2) S0 galaxies are found even where the ICM density is low; (3) similar relative numbers are found in clusters with densities low enough that RPS should not be important.

More direct observational evidence that late-type galaxies were changing to early-type galaxies was found by Dressler et al. (1999) in a survey of cluster galaxies. Optical spectra revealed a population of late-type spiral galaxies undergoing little or no star formation, possibly representing a transitional state from late- to early-type. These "passive spirals" were found only in clusters. Support for this interpretation was provided by Moran et al. (2006), who found that the *GALEX* FUV$-V$ colors and Hδ emission of passive spirals could be matched by models only if there was a rapid drop in the SFR. A numerical study by Shioya et al. (2004) found that spirals could evolve into S0's gradually via RPS, though a heavily obscured starburst can achieve a similar effect more rapidly. This latter result could be important in explaining why S0 galaxies are found where RPS should not be effective.

Evidence of the removal of outer disk gas has also been found. Koopmann & Kenney (2004) found in a study of spirals in the Virgo cluster that 50% have truncated Hα disks, compared to 12% of isolated galaxies. The truncated disks were also found in a higher concentration near the cluster center, where RPS would be most active. Further, galaxies with truncated Hα disks have normal stellar disks, indicating a hydrodynamic origin and consistent with RPS.

Crowl & Kenney (2008) studied truncated spirals with central star formation in the Virgo cluster. While many of these disks were likely stripped in the cluster core, several of the outer galaxies also showed signs of stripping within the last 500 Myr. This could indicate that the stripping occurred outside the core, implying that the ICM density profile is not as smooth as previously believed. It also provides another explanation for how apparently stripped disks are found far from cluster cores.

1.6 Summary

The effects of galaxy interactions on star formation are complex, involving numerous mechanisms for both the enhancement and suppression of star formation. Galaxies with enhanced star formation can form large systems of massive young clusters. While these clusters appear to be the progenitors of high-metallicity globular clusters, there is evidence to suggest that most of the clusters will not last for the $\sim$10 Gyr lifetime of Galactic globular clusters. The mechanism behind cluster disruption, particularly whether or not it depends on the cluster mass, remains controversial. We shall attempt to address this question as we characterize the cluster populations of the interacting systems Arp 284 and 261 in Chapters 2 and 3, respectively.

There are also conditions under which star formation can be suppressed, although this phenomenon has generally received much less attention than enhanced star formation. In Chapter 4, we will examine the Taffy galaxies (UGC 12914/5) using mid-IR spectroscopy and addressing the question of why the bridge between the two galaxies, which is extremely rich in both atomic and molecular gas, shows little evidence of star formation.

1.7 Dissertation Organization

Chapters 2 and 3 of this dissertation cover the subject of star cluster populations. Chapter 2 was published in *Monthly Notices of the Royal Astronomical Society* in 2009. My role in the paper was to obtain the photometric colors for the clusters, and for the larger clumps of clusters. The STARBURST99 evolutionary synthesis models were run and fit by collaborator Mark Hancock, who sent me the ages, extinctions, and masses. I then examined the age, mass, and luminosity distributions.

Chapter 3 will eventually be published as a journal paper, but is not quite complete. We have obtained optical spectra of Arp 261 from Lick Observatory which should allow us to determine the metallicity of the galaxies and bridge, providing much stronger constraints on the cluster ages than are available from photometry alone. The work I have done thus far is more or less the same as for the Arp 284 system in Chapter 2, except that this time I have run and fit the STARBURST99 models myself.

Chapter 4 has been submitted to *The Astrophysical Journal* based on work I completed while on a visiting graduate student fellowship at the Caltech Infrared Processing and Analysis Center (IPAC), and we have incorporated most of the referee's comments into this version. Here I extracted all of the spectra and measured the line fluxes. I also performed the supplemental photometry. Most of the modeling work was contributed by collaborators. Phil Appleton ran an excitation diagram fitting code, Michelle Cluver made the figure for the MAPPINGS shock models, and Pierre Guillard ran the photodissociation region code.

CHAPTER 2. Star Clusters in the Interacting Galaxy System Arp 284

A paper published in *Monthly Notices of the Royal Astronomical Society*[1]

Bradley W. Peterson, Curtis Struck, Beverly J. Smith, Mark Hancock

2.1 Abstract

We present results from a study of proto-globular cluster candidates in the interacting galaxy system Arp 284 (NGC 7714/5) using data from the *Hubble Space Telescope*. Previous studies of the Antennae and M51 have suggested that the majority of young massive star clusters dissolve within 20 Myr due to mass loss. We use the evolutionary synthesis code STARBURST99 to estimate ages and extinctions for approximately 175 clusters visible with *HST*. We also use lower-resolution *GALEX* and ground-based Hα data to estimate the ages of the giant H II regions in which these clusters are found, and compare the *Spitzer* colors of these H II regions to those of star forming regions in other interacting systems. The ages are also used to aid in the interpretation of *Chandra* X-ray data.

Clusters in the tidal tails of NGC 7714 are generally found to have ages less than 20 Myr, though observational limits make the significance of this result uncertain. Older clusters, though not numerous, have nearly the same spatial distribution within the imaged portion of NGC 7714 as young clusters. The cluster population in the bridge connecting the two galaxies appears to be older, but the data in this part of the system is too limited to draw firm conclusions. The ages of the giant H II regions in NGC 7714 are generally older than those of their constituent clusters, possibly indicating that the young clusters we detect are surrounded by their dispersed predecessors.

[1]Peterson, B. W., Struck, C., Smith, B. J., Hancock, H. (2009). *Monthly Notices of the Royal Astronomical Society*, 400, 1208.

2.2 Introduction

The study of star formation in interacting galaxies has been revolutionized by the *Hubble Space Telescope*. One of the early results to emerge from *HST* was the discovery of a class of bright, blue clusters ∼300 Myr old in the peculiar elliptical galaxy NGC 1275 (Holtzman et al., 1992). These young massive clusters (YMCs) were also found in the prototypical merger remnant NGC 7252, with ages ranging from 34–500 Myr, consistent with the age of the merger (Whitmore et al., 1993). Many more examples soon followed, in which it was found that the properties of these YMCs implied that they might be young globular clusters, though with higher abundances (Conti & Vacca, 1994; Hunter et al., 1994).

In interacting galaxy systems, in which star forming regions are abundant, the high resolution of *HST* has allowed the study of star cluster demographics. Among the results to emerge from such studies is the apparent dissolution of young star clusters, also known as infant mortality. Fall et al. (2005) used evolutionary synthesis models to estimate the ages of clusters in the Antennae and found that 90% of clusters vanish over each age dex from 10^6 up to 10^9 yr, suggesting that cluster dissolution continues over very long time scales. In contrast, Bastian et al. (2005a) found in M51 that 70% of clusters dissolve in the first 20 Myr, indicating that disruption is concentrated on short time scales. Recent spectroscopic observations of star clusters in the Antennae, combined with more careful modeling of the star formation history of the system, does not show the long-term cluster mortality previously claimed (Bastian et al., 2009), thus this issue is still controversial.

Additional evidence for a short dissolution time scale has been found in comparisons of cluster and field populations. Tremonti et al. (2001) obtained UV spectra and evolutionary synthesis models of both clusters and diffuse regions of the dwarf starburst galaxy NGC 5253. Unlike the clusters, the diffuse region spectra lacked indications of O-type stars. It was suggested that stars form entirely within clusters, which dissolve on ∼10 Myr time scales, preventing short-lived O stars from ever entering the field population.

Early-stage disruption has been ascribed largely to the loss of gas left over from star formation, which is swept out of the cluster by stellar winds and massive star supernovae. The

resulting mass loss drops the escape velocity below the stellar velocities, causing the cluster to expand and decrease in surface brightness. The departing stars disperse into the field population in ∼few 10^7 yr (Bastian & Goodwin, 2006; Goodwin & Bastian, 2006). On longer time scales (∼10^8 yr and longer), interactions with giant molecular clouds (Gieles, 2006) and tidal effects are expected to become significant disruption mechanisms.

If YMCs are progenitors of globular clusters, some of them must survive their most massive stars, as well as external effects that may lead to dissolution (de Grijs & Parmentier, 2007). Interacting galaxy systems have high numbers of YMCs, making them ideal targets for cluster population studies. To date, too few interacting systems have been observed to definitively determine how rapidly and by what mechanism massive clusters dissolve. Further, both the Antennae and M51 are advanced interactions with complex star formation histories. It is necessary to confirm infant mortality in early-stage interactions where the star formation history is simpler, with a particular emphasis on covering a wide range of tidal environments.

In this chapter we focus on the early-stage interacting system Arp 284, which at a distance of 38.6±2.7 Mpc ($1'' = 190$ pc) according NED[2] has nearly 175 detected star forming regions in archival *HST* images. We use *HST* colors and the evolutionary synthesis code STARBURST99 (SB99) to obtain age and reddening estimates for star forming regions. We also use lower-resolution UV data from the *Galaxy Evolution Explorer* (*GALEX*; Martin et al. 2005) and ground-based Hα to obtain age estimates for larger H II regions, and mid-IR colors from the Infrared Array Camera (IRAC; Fazio et al. 2004) on board the *Spitzer Space Telescope* (Werner et al., 2004) to compare the H II regions to IR emission clumps found in other interacting systems. These age results are used to aid in the interpretation of the X-ray data of Smith et al. (2005a),which was obtained using *Chandra* (Weisskopf et al., 2002).

[2]This research has made use of the NASA/IPAC Extragalactic Database (NED) which is operated by the Jet Propulsion Laboratory, California Institute of Technology, under contract with the National Aeronautics and Space Administration.

2.3 Tidal Star Forming Environments of Arp 284

The peculiar morphology of the Arp 284 system results from an off-centre collision between two disk galaxies, with the primary (NGC 7714) having roughly three times the mass of the companion (NGC 7715). The time of closest approach was ∼100 Myr ago. For a discussion of the interaction history of the system, the reader is directed to the models of Struck & Smith (2003). In this section we summarize previous observations of the Arp 284 system that relate to its star formation history. Most of the tidal features are labelled in Figure 2.1, while the H II region complexes in the primary disk are labelled in Figure 2.2.

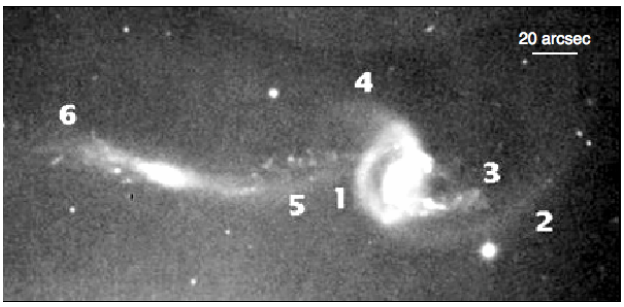

Figure 2.1 Optical photograph of Arp 284 from Arp (1966), with numbers labeling the prominent tidal features. North is up and east to the left. The field of view is $4.5' \times 2.2'$.

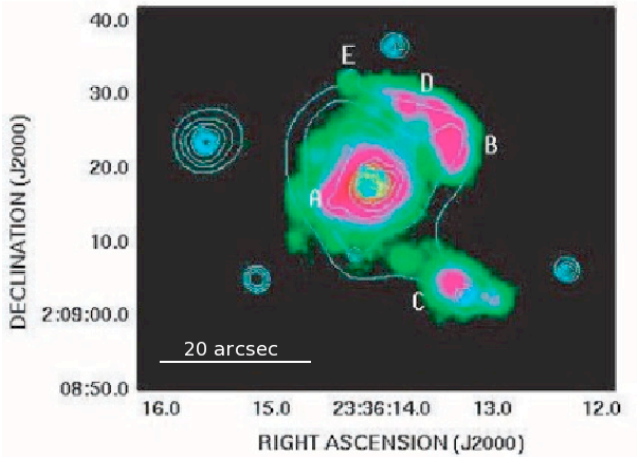

Figure 2.2 NGC 7714 disk indicating H II regions from Smith et al. (2005a). The color scale shows Hα. The contours are a Chandra 0.3–8 keV X-ray map

2.3.1 Nucleus of NGC 7714

The NGC 7714 nucleus was the first object to be described using the term "starburst," although there are earlier references in the literature to "bursts of star formation" (Weedman et al., 1981). Strong Hα emission indicates a large nuclear H II region and ongoing star formation (González Delgado et al., 1995; Smith et al., 1997). O and B stars are required to fit the UV spectrum, with a best fitting age $\sim$5 Myr and a burst of star formation favored over continuous star formation (González Delgado et al., 1999).

Lançon et al. (2001) found that a second, older nuclear population is suggested by strong absorption bands of CO in the near-IR. In particular, the K-band spectrum is compatible with a combination of red supergiants, AGB stars, and RGB stars. They concluded that a two-component model is probably an oversimplification of the nuclear star formation history, preferring a star formation rate that has decreased over several 10^8 yr, either through a smooth exponential decrease or a series of successively smaller bursts. The burst model best fits the observed supernova rate with a burst 15–50 Myr ago, in addition to the most recent burst 5 Myr ago.

Infrared Space Observatory (*ISO*) and *Spitzer* mid-IR spectra of the nuclear region show strong features from polycyclic aromatic hydrocarbons (PAHs) as well as bright forbidden lines (O'Halloran et al., 2000; Brandl et al., 2004). The metallicity of NGC 7714 peaks in the nucleus, with a value near $0.5Z_{\odot}$, and generally decreases with distance from the nucleus (González Delgado et al., 1995).

2.3.2 Stellar Ring of NGC 7714 (Feature 1)

NGC 7714 has a partial ring-like structure to the east. This feature does not show prominent Hα emission, reflecting a lack of ongoing star formation, while the red continuum suggests an old stellar population (González Delgado et al., 1995; Smith et al., 1997). Low levels of H I emission indicate that there is little hydrogen gas (Smith et al., 1997).

2.3.3 Southern Tails of NGC 7714 (Features 2 and 3)

Two parallel tidal tails lie to the southwest of the NGC 7714 nucleus. The outer southern tail, faintly visible in optical images, is revealed by 21 cm maps to be part of a large H I loop which reconnects with the galaxy in the northern tail (Smith & Wallin, 1992; Smith et al., 1997). The loop is also visible in *GALEX* FUV, which is shown smoothed with overlaid H I contours in Figure 2.3. This gas loop is an entirely separate structure from the inner southern tail, which hosts significant ongoing star formation.

The base of the inner southern tail just south of the nucleus contains H II region A (Smith et al., 2005a). This region is visible in 20 cm radio continuum (González Delgado et al., 1995; Smith et al., 1997). The *HST* images reveal numerous bright clusters along this structure, with another large H II region at the edge of the field (region C; González Delgado et al. 1995), coincident with a bright X-ray source (Smith et al., 2005a). The ages of regions A and C have been estimated by García-Vargas et al. (1997) at 5.0 ± 0.5 and 4.5 ± 0.5 Myr based on photoionization models. These regions also appear in *Spitzer* images (Smith et al., 2007), to be discussed below.

González Delgado et al. (1995) found Hα region A to have a metallicity comparable to the nucleus, about $0.5Z_{\odot}$. Region C, at a larger distance from the nucleus, shows a lower metallicity of $0.25Z_{\odot}$.

2.3.4 Northern Tail of NGC 7714 (Feature 4)

The northern tail of the primary galaxy is visible but not particularly prominent in optical photographs. Near the base of the tail, to the northwest of the nucleus, are Hα regions B, D, and E. These regions are also detected in 21 cm H I emission and red continuum (Smith et al., 1997). *HST* resolves these regions into several smaller groups of clusters. The age of region D has been estimated at 3.5 ± 0.5 Myr using photoionisation modeling (García-Vargas et al., 1997).

Hα region B has been found to have lower metallicty than the nucleus, about $0.25Z_{\odot}$ (González Delgado et al., 1995).

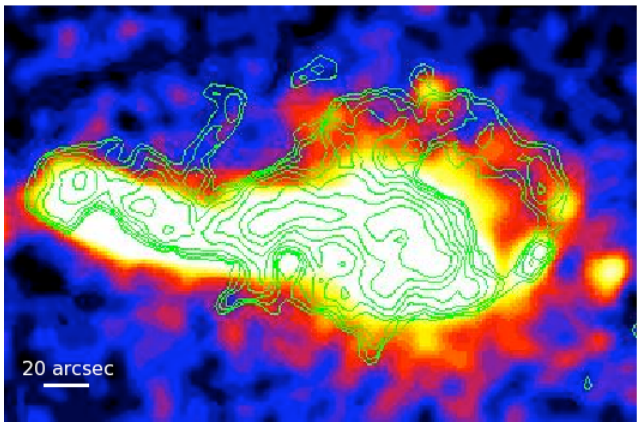

Figure 2.3 Smoothed *GALEX* FUV (color) overlaid with VLA H I (contours). Note that the western tail loops back to the main galaxy, and this ring-like feature is present in both H I and UV. The field of view is $5.1' \times 3.5'$.

2.3.5 Bridge (Feature 5)

The bridge consists of a northern and a southern component. The northern bridge shows "clumpy" emission from H I gas, and several Hα peaks are also found, offset slightly to the south, indicating ongoing star formation. The southern component lacks H I gas and Hα emission, but is readily seen in the red continuum, likely indicating an older stellar population (Smith et al., 1997). No metallicity data is currently available for the bridge.

2.3.6 Nucleus of NGC 7715

The lack of significant Hα emission in the NGC 7715 nucleus indicates that there is no ongoing massive star formation (González Delgado et al., 1995; Smith et al., 1997). Emission from the 21 cm H I radio line is also minimal, and offset to the north of the optical galaxy. The nucleus is comparatively bright in the red continuum, suggesting an aged stellar population (Smith et al., 1997). Spectral studies of the nucleus show a post-starburst spectrum, again confirming the lack of ongoing star formation (Bernlöhr, 1993).

2.3.7 Eastern Tail of NGC 7715 (Feature 6)

The eastern tail of NGC 7715 is faintly seen in optical images. Radio maps show an H I counterpart, offset slightly to the north (Smith & Wallin, 1992; Smith et al., 1997). Massive star formation is thought to be weak based on the lack of Hα emission. This feature has not been studied in detail, and it falls outside the field of the *HST* images. This poor coverage is unfortunate, because the models suggest that this tail curves behind the NGC 7715 disk, passes behind the bridge, and comes back into view as the faint outer southern tail of NGC 7714 (Struck & Smith, 2003). In this scenario, the tail contains a significant fraction of the original mass from the NGC 7715 disk (Struck & Smith, 2003).

2.4 Observations

2.4.1 *HST* observations

The *HST* Wide Field and Planetary Camera 2 (WFPC2) has observed the Arp 284 system through several observing programs between 1995 May 13 and 2001 July 10. These programs targeted either the starburst nucleus or SN 1999dn in the disk of NGC 7714. The disparate nature of the observations means that many of the bright clusters are not visible in all filters, and in some cases the clusters were not found on the same chip across all filters. The field of view is $36'' \times 36''$ on the PC chip and $80'' \times 80''$ for the WF chips, with pixel sizes of $0.05''$ pixel^{-1} on the PC chip and $0.1''$ pixel^{-1} on the WF chips. The images and exposure times are summarized in Table 2.1. Note that the number in the filter name approximately corresponds to the central wavelength of the filter in nanometers. The available filters were F380W ($\sim U$), F555W ($\sim V$), F606W ($\sim R$), and F814W ($\sim I$).

The NGC 7714 nucleus and most of the inner southern tail are visible on the PC chip in all filters. One image in both F380W and F814W had to be discarded due to excessive cosmic ray contamination. This left three good images in the F380W filter, two in F555W, one in F606W, and three in F814W. In F814W, H II region C was visible in two images on the WF4 chip.

The entire northern tail was visible on the PC chip in the F380W and F606W filters. In F555W and F814W, only 12 clusters were visible on the PC chip, with the remainder visible on WF4 in F814W.

The bridge was on the seam between the WF3 and WF4 chips in all four F380W images, so some of the clusters could not be measured in this band. In the other filters, it was always on the WF3 chip, with two images in F555W, one in F606W, and two in F814W.

Table 2.1 *HST* WFPC2 imaging of NGC 7714/5

Dataset	Exposure (sec)	Filter	H II Regions in PC chip	H II Regions in WF chip	Comment
U3GQ0201R	500	F380W	nucleus,A,B,part C,D,E	bridge	bridge split WF3/4
U3GQ0202R	500	F380W	nucleus,A,B,part C,D,E	bridge	bridge split WF3/4
U3GQ0203R	400	F380W	nucleus,A,B,part C,D,E	bridge	CR on PC chip bridge split WF3/4
U3GQ0204M	400	F380W	nucleus,A,B,part C,D,E	bridge	bridge split WF3/4
U6A01601R	350	F555W	nucleus,A,E	bridge	
U6A01602R	350	F555W	nucleus,A,E	bridge	
U2E68801T	500	F606W	nucleus,A,B,part C,D,E	bridge	
U6A01701R	350	F814W	nucleus,A	B,C,part D	
U6A01702R	350	F814W	nucleus,A	B,C,part D	
U6A01801R	350	F814W	nucleus,A, E	bridge	
U6A01802R	350	F814W	nucleus,A, E	bridge	CR on PC chip

2.4.2 H II region observations

Archival *GALEX* and *Spitzer* IRAC data are available for the Arp 284 system. The *GALEX* images increase the number of colors that can be fit with SB99 models, while *Spitzer* colors can be compared to those of star forming regions in other interacting systems. These instruments have significantly lower resolution than *HST*, but still allow the H II regions A–E to be resolved, as shown in Figure 2.4. Each of these regions contains numerous star clusters resolved by *HST*. For clarity, the point-like sources in the *HST* data will be called "clusters" while these larger structures will be called "H II regions." With Hα luminosities of $10^{39} - 10^{41}$ erg s^{-1} (Smith et al., 2005a), these are properly classified as "giant H II regions" (e.g., Kennicutt, 1984).

The H II regions were located in an Hα map, which was then registered to the other images.

The Hα and accompanying R-band images were obtained using the 1.8 m Perkins Telescope of the Ohio State University, using a CCD with a pixel size of $0.49''$ pixel^{-1}. These data were published previously in Smith et al. (1997).

GALEX observations are available in both the FUV and NUV bands, with effective wavelengths of 1516 and 2267 Å. The pixel size is $1.5''$ pixel^{-1}, which makes even these relatively large H II regions difficult to identify. The integration times are 4736 s in FUV and 520 s in NUV.

IR data from *Spitzer* are available for both the IRAC and Multiband Imaging Photometer for Spitzer (MIPS) instruments. The resolution in the MIPS bands is far too low for cluster studies, and there are pronounced artifacts due to the point spread function because of the brightness of the nucleus, so only the broadband IRAC bands (3.6, 4.5, 5.8, and 8.0 μm) were used. The data reduction and mosaicing for the *Spitzer* data are described in Smith et al. (2007).

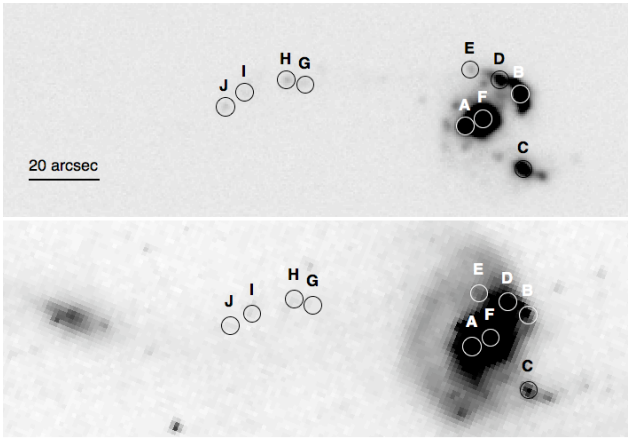

Figure 2.4 H II regions in Hα (top) and *Spitzer* 3.6 μm (bottom). The aperture radii have an angular size of $2.45''$, and are also shown on the *HST* images in Figures 2.7–2.12. The field of view is $2.4' \times 0.9'$.

2.5 *HST* Data Analysis

2.5.1 Data Reduction

All of the images were processed by the standard Hubble pipeline. The small number of exposures available in some data sets made cosmic ray removal a non-trivial task, since median combining two images is ineffective. First, we used the IRAF[3] task *cosmicrays* to remove events a few pixels in size that were well above background. Next, images were blinked to identify remaining cosmic rays, which were removed manually using the *fixpix* task. Finally, images were combined using the *imcombine* task. For F606W, only one image was available, so other filters were used for comparison.

2.5.2 Cluster Selection

Clusters were selected using the IRAF task *daofind*. The background level σ was determined using *imstat* in a relatively dark part of the image. The nuclear region is much brighter than the rest of the disk, so it was necessary to use a higher background for cluster detection, measured at the outer edge of the nucleus. We used *daofind* in each filter and then merged the lists to obtain the final sample. Clusters detected in only two filters were not included in the sample.

We detected 16 clusters in the nucleus at the 5σ level. The nucleus is quite crowded, so no attempt was made to push the detection threshold any lower. The lowest detected flux was 2.28×10^{-17} erg s^{-1} cm^{-2} Å^{-1} in F814W.

In the southern tail, 60 clusters were detected at the 5σ level and another 34 were detected at the 3σ level. These levels correspond to fluxes of 2.17 and 1.32×10^{-19} erg s^{-1} cm^{-2} Å^{-1}, respectively, in F814W. Before using the software, clusters in this part of the system were selected by eye. The 3σ set matched well with the results of the visual inspection, and were retained for the analysis.

[3]IRAF is distributed by the National Optical Astronomy Observatories, which are operated by the Association of Universities for Research in Astronomy, Inc., under cooperative agreement with the National Science Foundation.

In the northern tail, *daofind* detected 60 clusters at the 5σ level, with no additional clusters detected at the 3σ level. This is probably due to crowding in the major complexes, which resulted in multiple detections on single clusters at lower detection thresholds. These clusters may in fact represent multiple unresolved star clusters. In a few cases, multiple resolved clusters had to be measured in a single aperture because they were too close together to measure without aperture overlap.

Cluster selection was difficult in the bridge due to the higher background level in this part of the system and the lower resolution of the WF3 chip compared to the PC chip. For these reasons, it was necessary to lower the detection threshold in the bridge to 2σ, allowing the detection of 34 clusters. The faintest flux detected in F814W was 2.17×10^{-19} erg s^{-1} cm^{-2} Å^{-1}. Note that this is higher than the 3σ level on the PC chip. Only 23 of the clusters could be measured in F380W.

2.5.3 Photometry of clusters

Photometry was performed using the IRAF task *phot* in the DAOPHOT package, with magnitudes calibrated to the Vega magnitude system using the zero point values given in the WFPC2 Data Handbook. The magnitudes and ages for the cluster sample are given in Table A.1, while the extinctions and mass estimates are given in Table A.2. The determination of the ages and extinctions will be discussed in Section 2.6.2. The mass determination will be discussed in Section 2.7.2.

The tidal tails generally fell on the PC chip. For these clusters, we used aperture radii of 3 or 4 pixels for single clusters, depending on crowding, and 6 pixels in six cases when barely-resolved clusters had to be measured in a single aperture. Sky brightness for background subtraction was determined by the mode of the pixel values in an annulus of 10–15 pixels, centered on the cluster. In F814W, most of the northern tail was on the WF4 chip. These were measured using apertures with 2-pixel radii, or 3-pixel apertures for the poorly resolved groups, with sky subtraction determined by the mode in a 5–8 pixel annulus. These sizes were chosen because the WF chips have approximately twice the angular size of the PC chip, so

the same area of sky was measured regardless of which chip a cluster fell on. Very little of the northern tail was visible in F555W.

The nucleus was always on the PC chip, but required the use of smaller apertures with radii of 2 or 3 pixels due to crowding. Background levels were determined by the mode in a 10–15 pixel annulus.

The bridge was generally on the WF3 chip. In F380W, the bridge unfortunately straddled the WF3 and WF4 chips, so a few clusters could not be observed in this filter. The aperture radius was 3 pixels, with background determined by the median in an 8–13 pixel annulus. This aperture size was selected because bridge clusters are often isolated, but there are several areas where multiple emission sources are packed closely together. In such cases, *daofind* generally detected only one or two of the brightest sources, which were always sufficiently separated to be measured individually.

Aperture corrections could not be determined on the images. It was therefore necessary to use the standard corrections prescribed by Holtzman et al. (1995). The corrections for WF3 were used for all of the wide field chips. Standard corrections are not given for the F380W or F606W filters, so corrections for the F336W and F555W, respectively, were used. The corrections were typically ≤ 0.3 mag.

2.5.4 H II region photometry

In addition to the five regions A–E, we measured the nucleus (designated region F) and four regions (G–I) in the northern part of the bridge, shown in Hα and *Spitzer* 3.6 μm in Figure 2.4. The *GALEX* and *Spitzer* images were registered to the *HST* data so that age estimates could be obtained using the total flux in the *HST* bands. This also allowed identification of the clusters making up the H II regions. Most of region C was off frame in all of the *HST* bands except F814W. Region G could not be measured at 4.5 μm because of a cosmic ray.

The aperture radius was selected as 2.45″ (5 pixels on the Hα image) in all instruments to ensure that the same area of sky was represented at all wavelengths. The sky annulus widths were 1.82″ in *HST*, 2.45″ in Hα, 4.5″ in *GALEX*, and 3.6″ in *Spitzer*. The measurements

were not aperture-corrected because the *HST* apertures were largely empty, and the emission regions were highly pixelated in *GALEX* and *Spitzer*.

Table A.3 summarizes the photometric measurements. The Hα and R bands were calibrated to standard units using the results of James et al. (2004). The ratio of the Hα flux to R flux density provided an estimate of the equivalent width of the Hα line, EW(Hα). This equivalent width is included in the SB99 models and provides another method for determining the ages of the emission regions. Ages are presented in Table A.4 and extinctions in Table A.5. These will be discussed in Section 2.7.3.

2.6 *HST* Results

2.6.1 Cluster colors

Color-color diagrams are shown in Figure 2.5. In the top left panel, we plot the magnitude in the F555W filter minus the magnitude in the F606W filter (F555W−F606W) versus (F606W−F814W) for all detected clusters for which these colors were available. The curves show SB99 instantaneous star formation models with $0.2Z_{\odot}$ metallicity for $E(B-V) = 0$ (solid curve), 0.24 (dashed curve), and 0.5 (dot-dashed curve) for ages from 10^6–10^{10} yr. The youngest ages are at the lowest values of (F606W−F814W). The models are shown to give a sense of the effect of reddening, and it should be noted that $0.2Z_{\odot}$ is not the observed metallicity for the nucleus and parts of the southern tail. The bridge population is generally bluer in (F555W−F606W) and redder in (F606W−F814W) than the populations of the other regions. The southern tail has the opposite tendency, leaning red in (F555W−F606W) and blue in (F606W−F814W). Only a few clusters in the northern tail were on frame in F555W; those that were tend toward more intermediate values in both colors. The nuclear population is similar.

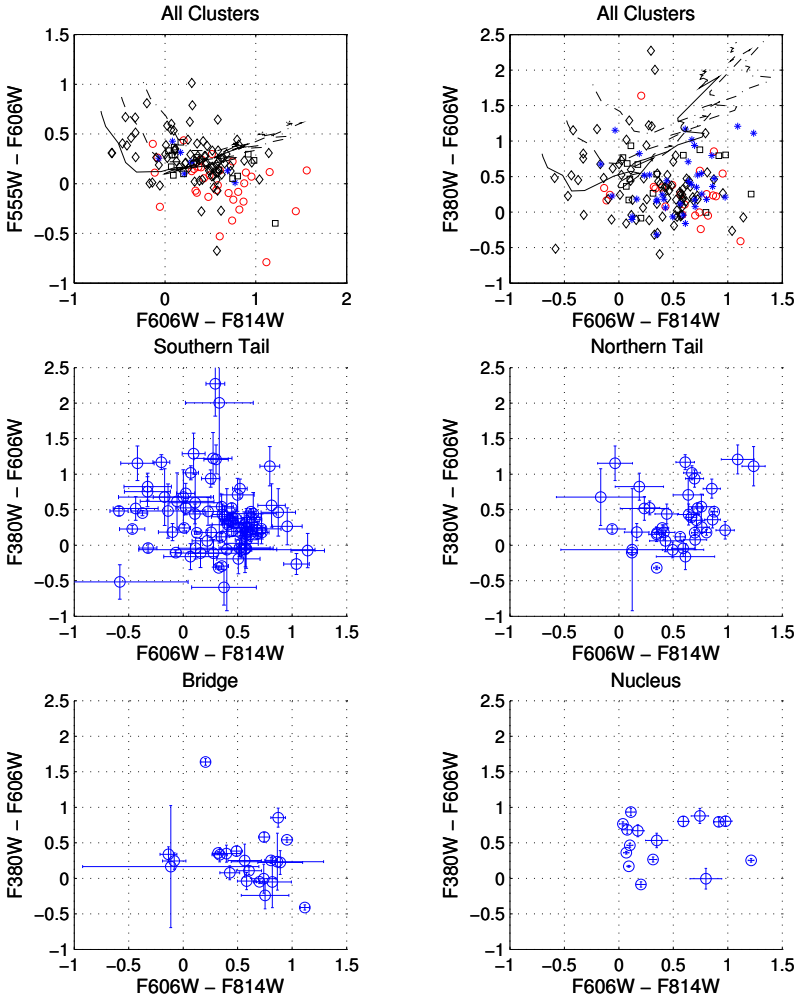

Figure 2.5 In the top panels, red circles represent clusters from the bridge, black diamonds the southern tail, blue asterisks the northern tail, and black squares the nucleus. The curves show SB99 instantaneous star formation models with $0.2Z_{\odot}$ metallicity for $E(B-V) = 0$ (solid curve), 0.24 (dashed curve), and 0.5 (dot–dashed curve). These curves give a sense of the effect of reddening, but the metallicity is not representative of the nucleus or parts of the southern tail. The middle and bottom four panels show the same colors as the upper right panel separated by region, with error bars.

The top right panel shows all detected clusters in (F380W−F606W) versus (F606W−F814W), along with SB99 models. The youngest ages on the curves appear at the lowest values of (F606W−F814W). The middle and bottom panels show the same colors, with the different regions plotted separately and error bars shown. The differences between the populations are less striking in this color combination than the one discussed above, and arise primarily in (F606W−F814W).

The median statistical uncertainties in the northern tail are 0.081 and 0.095 mag for (F380W−F606W) and (F606W−F814W), respectively. In the southern tail, the median uncertainties are 0.153 and 0.107 mag; in the nucleus, 0.050 and 0.040 mag; and in the bridge, 0.167 and 0.123 mag. The uncertainties are large in the southern tail in part because it includes clumps detected at the 3σ level. If only 5σ level clumps are included, the median uncertainties are 0.114 in (F380W−F606W) and 0.088 in (F606W−F814W).

2.6.2 Age determination

Age and reddening estimates were obtained using the STARBURST99 v5.1 evolutionary synthesis code (Leitherer et al., 1999; Vázquez & Leitherer, 2005). We modeled the colors of the clusters assuming a single, instantaneous burst of star formation with a Kroupa (2002) initial mass function over the range 0.1–100$M_{\odot}$. Spectral energy distributions (SEDs) were calculated for cluster ages of 1 Myr to 10 Gyr and included contributions from Hα emission. The SEDs were reddened from 0–2 mag of $E(B-V)$ using the reddening law of Calzetti et al. (1994). These model spectra were convolved with the bandpasses of the four *HST* filters. The model age and extinction providing the best fit to the observations was determined using χ^2 minimization.

Uncertainties in both the ages and extinctions were determined as in Smith et al. (2008), and are driven largely by the degeneracy between age and reddening. Breaking this degeneracy is particularly difficult for clusters with coverage in only three filters. Such clusters generally have larger age uncertainties than those with that were covered in all four filters.

Models were run for three different metallicities: $Z_{\odot}$, $0.4Z_{\odot}$, and $0.2Z_{\odot}$. The $0.4Z_{\odot}$ model

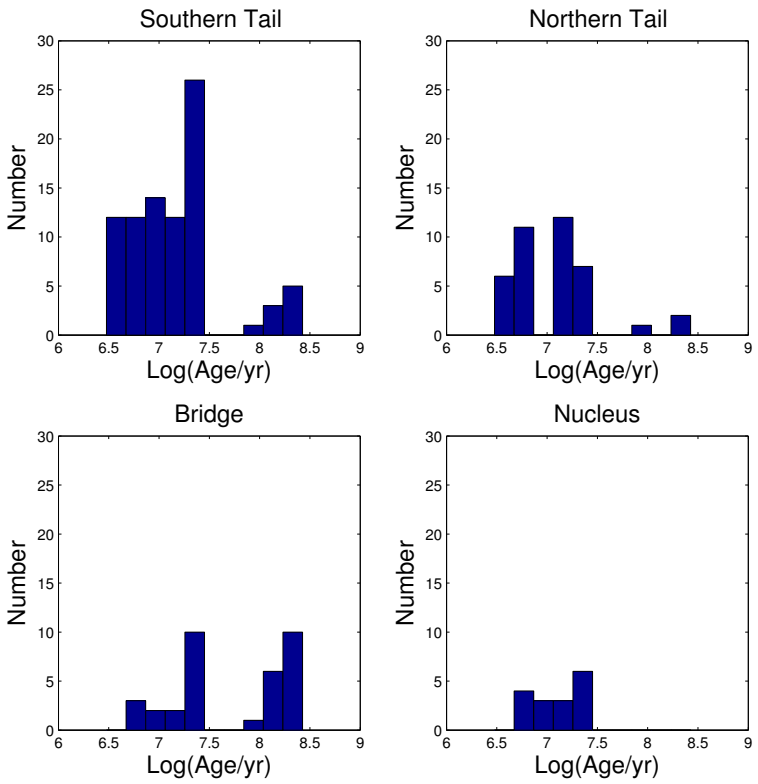

Figure 2.6 Histograms of cluster ages from $0.2Z_{\odot}$ models in the southern tail (top left panel), northern tail (top right panel), and bridge (bottom left panel), and from the $0.4Z_{\odot}$ model in the nucleus (bottom right panel).

is representative of the spectroscopically measured abundances in the nucleus and H II region A, while the $0.2Z_{\odot}$ model is close to that of H II regions B and C. The solar composition models were used primarily for comparison.

Several color combinations were used because not all clusters were available in all colors. Age estimates obtained from SB99 have been found to be most reliable when (1) large numbers of colors are used and (2) the bluest available combination of colors are used. U coverage is particularly important (e.g., Hancock et al., 2008). We adhered to these results in determining which of the available color combinations would provide the best age estimate for each cluster at each metallicity.

Our best-fitting ages for the clusters are given in Table A.1, while $E(B-V)$ and masses

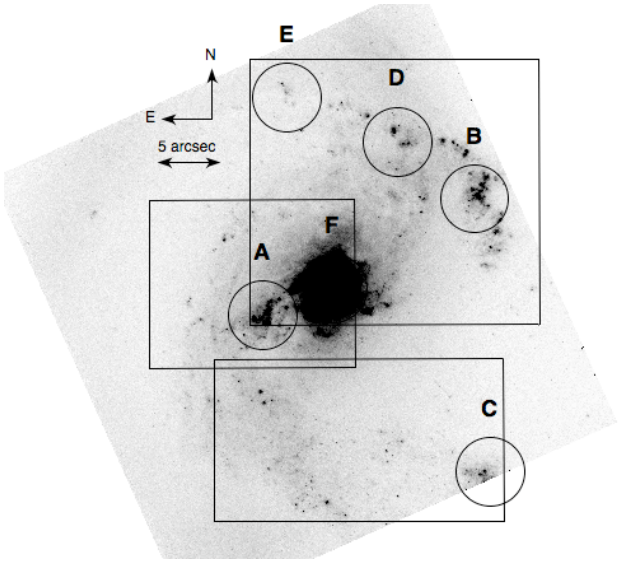

Figure 2.7 F606W image of NGC 7714 with northern, central, and southern areas indicated. These areas are examined more closely in Figures 2.8–2.12. Several H II regions identified in lower-resolution data are also indicated. Note that region C is partially off frame toward the bottom right of the box indicating the southern area.

are shown in Table A.2. The age distributions within the features of the system are shown in Figure 2.6. Finding charts showing the locations of the clusters are given in Figures 2.7–2.12, with circles indicating ages $\leq$ 10 Myr, diamonds 11–22 Myr, and squares $>$ 22 Myr. The apertures used for photometry of the large H II regions are also shown. The clusters are generally very young, occupying the two younger age bins (1–10 and 11–22 Myr). Very few clusters older than 22 Myr are found in the tidal tails.

Ages determined by evolutionary synthesis techniques generally have large uncertainties. In our sample, the uncertainties are typically very close to the ages. The median age is 14 Myr, with a median negative uncertainty of 5 Myr and a positive uncertainty of 10 Myr.

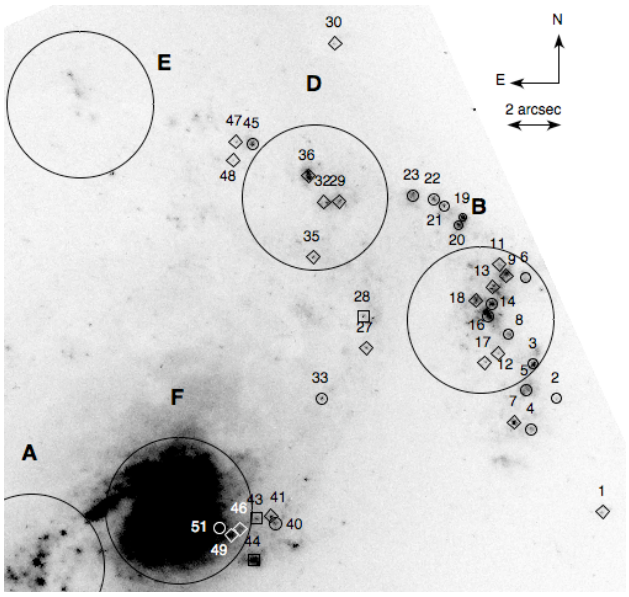

Figure 2.8 F606W image of the northern tail of NGC 7714, with ages indicated for all detected clusters for the $0.2Z_{\odot}$ models. Circles represent ages 1–10 Myr, diamonds 11–22 Myr, squares $\geq$ 23 Myr. The metallicities of H II regions B and D have been measured at $0.25Z_{\odot}$, while the nucleus has metallicity $0.5Z_{\odot}$. All clusters shown are considered part of the northern tail.

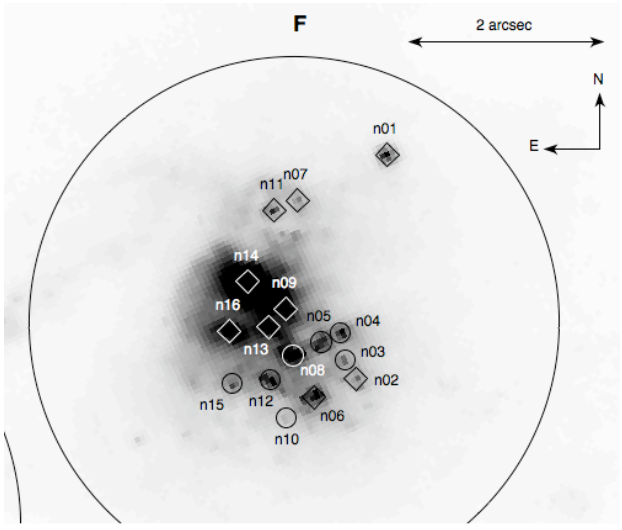

Figure 2.9 F606W image of the NGC 7714 nucleus with ages from the $0.4Z_{\odot}$ model indicated for all detected clusters. Circles represent ages 1–10 Myr, diamonds 11–22 Myr, squares $\geq$ 23 Myr. The metallicity has been measured at $0.5Z_{\odot}$.

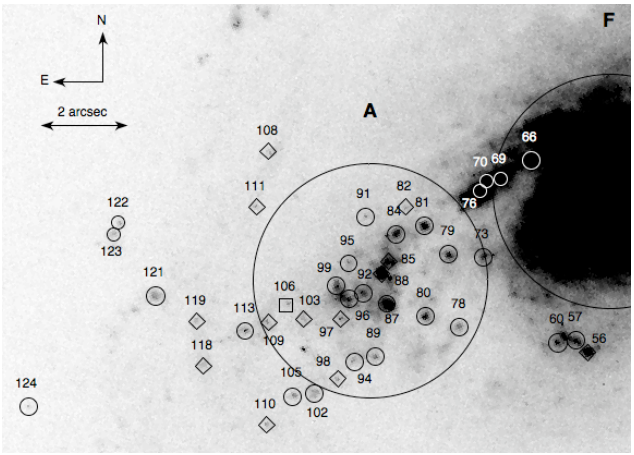

Figure 2.10 F606W image of the central region of NGC 7714 with ages from the $0.4Z_{\odot}$ model indicated for all detected clusters. Circles represent ages 1–10 Myr, diamonds 11–22 Myr, squares $\geq$ 23 Myr. The nucleus has a measured metallicity of $0.5Z_{\odot}$, so this model should give the best age estimates. These clusters are considered to be part of the southern tail.

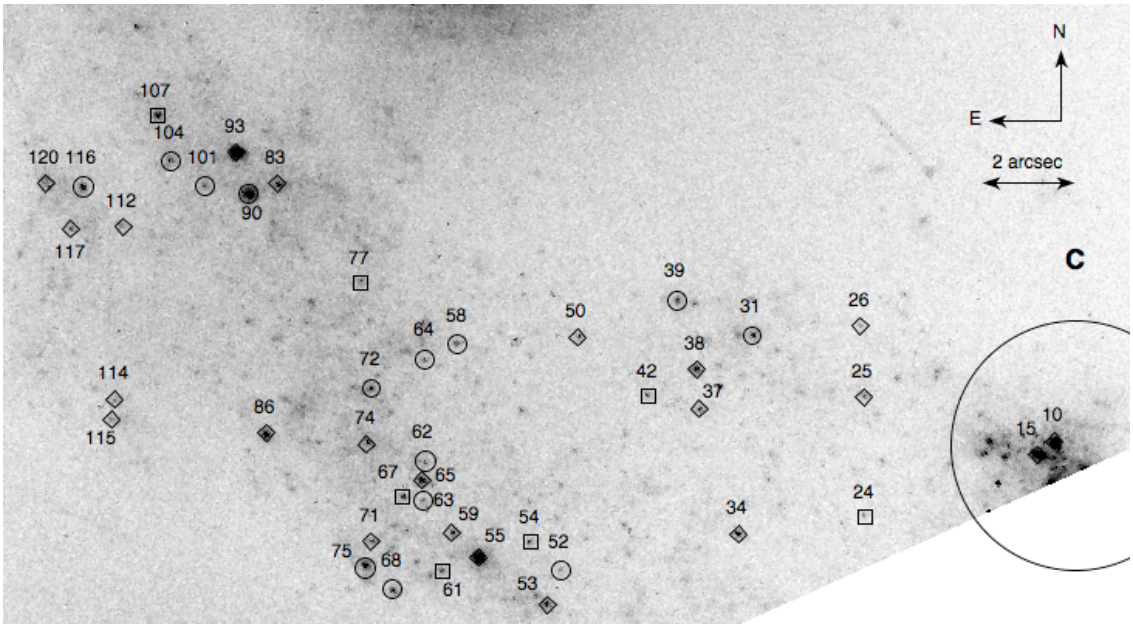

Figure 2.11 F606W image of the southern tail of NGC 7714 with ages from the $0.2Z_{\odot}$ models indicated for all detected clusters. Circles represent ages 1–10 Myr, diamonds 11–22 Myr, squares $\geq$ 23 Myr. Clusters 10 and 15 are inside H II region C, which has a measured metallicity of $0.25Z_{\odot}$

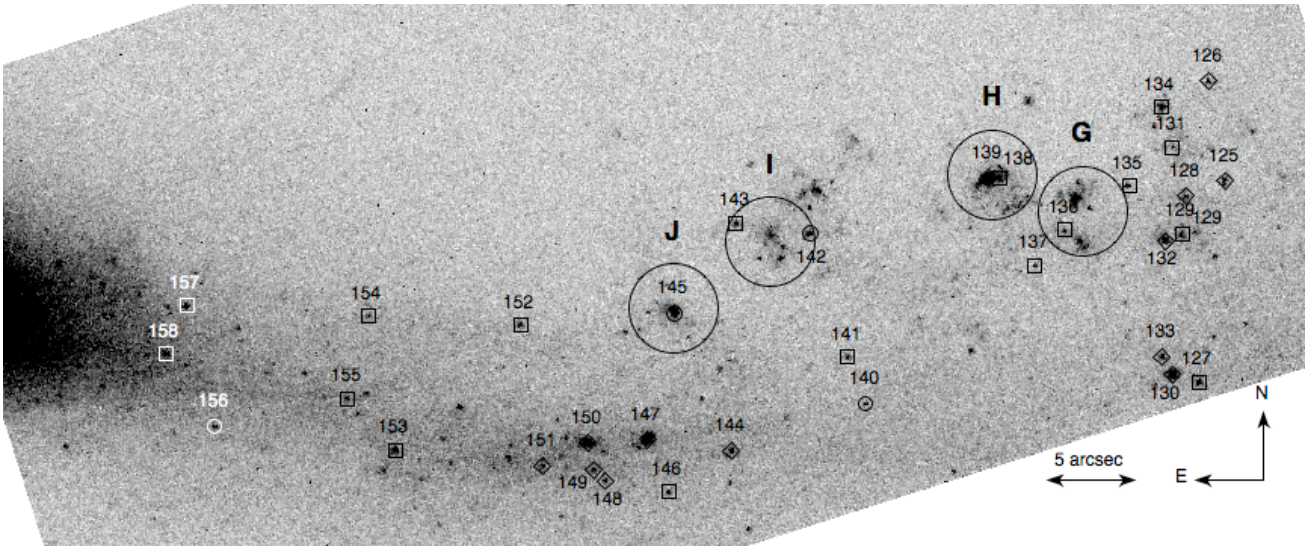

Figure 2.12 F555W image with all detected clumps in the bridge with ages from the $0.2Z_{\odot}$ models. Circles represent ages 1–10 Myr, diamonds 11–22 Myr, squares $\geq$ 23 Myr. The metallicity of the bridge has not been measured, but is likely to be low.

2.6.3 Luminosity function

The luminosities in the F814W band for the clusters $\Delta\nu L(\nu)$ were calculated using a distance of 39 Mpc (NED), using a bandwidth of 7.2×10^{13} Hz. The luminosity distribution, excluding the extremely luminous nuclear population, is shown in Figure 2.13, and provides one estimate of our sample completeness. We assume a simple power law form for the luminosity function, defined by $n(L)dL \propto L^{-\alpha}dL$. A best-fitting line is determined after the distribution turns over, giving a slope of -1.3 with a completeness limit of $10^{5.1}L_{\odot}$.

The uncertainty in the slope may be estimated as follows. The distribution has a flat top, so there are two reasonable possibilities for the turnover point. Selecting as the completeness limit $10^{4.9}L_{\odot}$, we obtain a slope of slope -1.1. Our best estimate for the slope is -1.3 ± 0.2. Cluster luminosity functions typically have $\alpha = -2$ (e.g., Whitmore et al., 1999), which gives a slope of -1 when binned logarithmically. Our luminosity function is consistent with this trend to within the uncertainties.

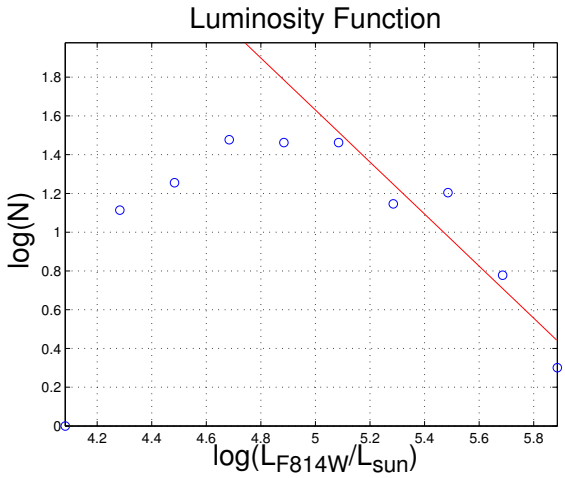

Figure 2.13 Luminosity distribution in F814W for all detected clusters outside the nucleus. The luminosity is defined as the luminosity in the F814W band $\Delta\nu L(\nu)$, where $\Delta\nu$ is the bandwidth of 7.2×10^{13} Hz. The solid red line is a power law fit to the distribution after the turnover with slope -1.3 ± 0.2, giving a completeness limit of approximately $(5.1 \pm 0.2) \times 10^{5}L_{\odot}$.

2.7 Discussion

2.7.1 *HST* cluster ages

The metallicities determined by González Delgado et al. (1995) aid in the interpretation of our evolutionary synthesis results. In the southern tail, H II region A has a measured metallicity $\sim 0.5Z_{\odot}$. The best age estimates should therefore come from our $0.4Z_{\odot}$ models, which show this region to be dominated by clusters with ages 10 Myr or less.

The metallicity of H II region C at the base of the southern tail is $\sim 0.25Z_{\odot}$ (González Delgado et al., 1995). Combined with the general metallicity gradient observed in the galaxy, we are led to favor the $0.2Z_{\odot}$ model in the western part of the southern tail, which shows more clusters older than 22 Myr than does the $0.4Z_{\odot}$ model. Note, however, that part of region C was off frame (Figure 2.11), so we only have age estimates for two of its constituent clusters.

In the northern tail, the dependence of derived age on metallicity is less pronounced. Only five clusters change age bins between the $0.2Z_{\odot}$ and $0.4Z_{\odot}$ models, all of which are near the nucleus. Most of the clusters are in H II regions B and D. These regions have measured abundances $\sim 0.25Z_{\odot}$, so our $0.2Z_{\odot}$ models should provide the best age estimates. The cluster ages are all less than 23 Myr in these models, with about half 10 Myr or younger. This is not unexpected, since this part of the northern tail is detected in Hα (Smith et al., 1997) and *Spitzer* 8.0 μm (Smith et al., 2007).

The metallicity of the nucleus has been measured at $\sim 0.5Z_{\odot}$, so the $0.4Z_{\odot}$ model is preferred here. Seven of the 16 clusters have ages $\leq$ 10 Myr, with the remainder between 14–21 Myr. The gap between these age populations is probably not significant, since the rapid evolution of red giants after 10 Myr makes exact age determination exceptionally difficult and often results in gaps between 10–15 Myr (e.g., Fall et al., 2005). The younger population fits well with the UV spectral results of González Delgado et al. (1999), while the older population fits with one of the bursts expected by Lançon et al. (2001).

Of the 124 clusters detected in the tidal tails of NGC 7714, those with ages $>$ 22 Myr number only five in the $0.4Z_{\odot}$ model and 12 in the $0.2Z_{\odot}$ model. If an age is assigned to each

cluster based on the measured or most likely metallicity, there are eight older than 22 Myr. The small sample of 16 clusters detected in the nucleus has no clusters older than 22 Myr. There is little evidence in NGC 7714 of a population older than ∼20 Myr, despite an interaction that had closest approach ∼100 Myr ago. We also find that the cluster age groups are evenly distributed over the galaxy. The lack of older clusters detected in the nucleus may be due to the difficulty in detecting such clusters amidst the high background caused by YMCs.

These results are similar to those obtained by Bastian et al. (2005b) for the interacting galaxy NGC 6872. Most of the clusters in NGC 6872 were found by color fitting to be younger than 30 Myr. These were spread throughout the galaxy, extending far out into the tidal tails. Clusters older than 30 Myr were concentrated in the central regions of the galaxy. However, the "central regions" of NGC 6872 have a spatial size ∼30 kpc, while the imaged portion of the NGC 7714 disk in our data is only ∼7 kpc. The age distribution within NGC 7714 is compatible with that found by Bastian et al. in NGC 6872, but a wider field will be required to determine if the concentration of old clusters is similar in the two galaxies.

The bridge ages are difficult to interpret because of the large color uncertainties, incomplete coverage in F380W, and lack of metallicity data. The metallicity in NGC 7714 generally decreases with distance from the nucleus. However, some of the bridge material may originate in NGC 7715, which has unknown metallicity. Nevertheless, a low metallicity is expected due to the abundances measured elsewhere in the system and because tidal features in interacting galaxies generally show low abundances.

Despite the large uncertainties, we note that the only evidence for a significant population with age ≥ 100 Myr is in the bridge. Out of 34 clusters, the numbers with ages > 22 Myr are 12 and 17 in the $0.4Z_{\odot}$ and $0.2Z_{\odot}$ models, respectively. However, only one of these clusters has F380W data available in the $0.4Z_{\odot}$ case, and nine in the $0.2Z_{\odot}$ case. The existence of an older population in the bridge is by no means certain, but if present could indicate that cluster dissolution mechanisms have acted more weakly here than in the tidal tails, which in this system are closer to the nucleus. Older clusters should survive more easily in the bridge because tidal forces are generally smaller there than in the tails. However, the gas expulsion

mechanisms thought to be responsible for infant mortality operate independently from the tidal forces, so the rate at which very young clusters dissolve is not expected to change.

To address the issue of sample completeness, we begin with the luminosity function (Figure 2.13). Cutting out clusters with luminosities below the completeness limit, we have 49 left in the tidal tails and only four in the bridge. The bridge sample is far too incomplete to permit any reliable analysis.

Only two clusters in the tidal tails that survive the luminosity cut have ages > 22 Myr, and those only in the $0.2Z_{\odot}$ model. It is unsurprising that older clusters would be preferentially cut from a luminosity-limited sample, since clusters get both redder and fainter as their stellar populations age.

2.7.2 *HST* cluster mass function

It is common practice in studies of cluster ages to use a mass cutoff rather than a luminosity cutoff. Due to evolutionary fading, clusters of a given age will remain above the luminosity limit only if they have a sufficiently high mass. Therefore, imposing a luminosity limit will generally under-sample old clusters.

Mass estimates are based on the assumption that clusters of a given age all have the same mass to light ratio, with luminosity values calculated for clusters with mass $10^6 M_{\odot}$. The luminosity of a cluster relative to a $10^6 M_{\odot}$ cluster of the same age then gives an estimate of the mass. The uncertainties in the masses are quite large, up to a factor $\sim$2. Mass estimates based on the best-fitting age and extinction are shown in Table A.2.

The lowest mass for which the sample is complete was determined assuming a simple power law form for the cluster mass distribution. For $0.4Z_{\odot}$, we obtain a reasonably good fit with a slope ≈ -1.4 and a limiting mass of $10^{5.0} M_{\odot}$. The quality of the fit is not high due to a lack of clusters in the mass bin centered at $10^{6.0} M_{\odot}$, which may reflect the high uncertainties in masses determined in this way. The mass estimates for the $0.2Z_{\odot}$ model produced a slope of -1.5, but with a lower mass limit at about $10^{4.8} M_{\odot}$. The mass distribution for the $0.2Z_{\odot}$ model is shown in Figure 2.14.

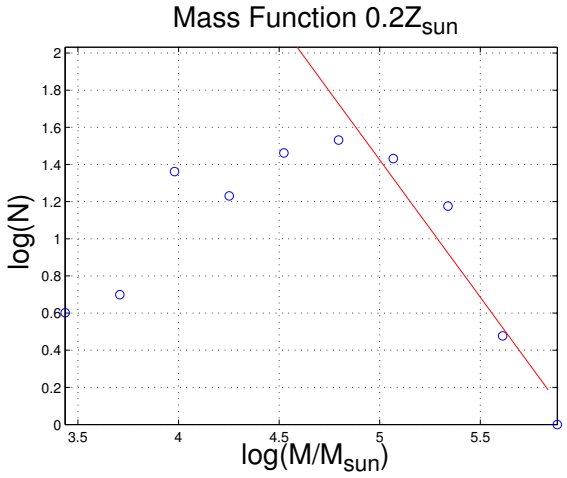

Figure 2.14 Cluster mass distributions for the $0.2Z_{\odot}$ model. The solid red line is a power law fit to the part of the distribution after the turnover. The fit has slope -1.5 ± 0.4 with a limiting mass $\sim 10^{4.8} M_{\odot}$.

The uncertainties for the mass function fits may be estimated using the same technique as was used for the luminosity function. For the $0.4Z_{\odot}$ model, the next best choice of limiting mass would be $10^{4.7} M_{\odot}$, which gives a slope of -1.0. In the $0.2Z_{\odot}$ model, both $10^{4.5} M_{\odot}$ and $10^{5.0} M_{\odot}$ are reasonable choices, producing slopes of -1.8 and -1.1, respectively. Using these alternate choices to estimate the uncertainties, the $0.4Z_{\odot}$ model has a slope -1.4 ± 0.4 , with smaller values being more likely. For the $0.2Z_{\odot}$ model, the slope is -1.5 ± 0.4. At the limits of the uncertainties, our mass functions agree with the typical power law index near $\alpha = -2$, found for example in the Antennae (Zhang & Fall, 1999) and Magellanic Clouds (Hunter et al., 2003). Due to the small size of our sample, we are unable to test the claim of Gieles (2009) that the cluster initial mass function is truncated at the high mass end.

The completeness limit in mass, unlike that in luminosity, is a function of age due to evolutionary fading. Thus the turn-over in Figure 2.14 gives an age-averaged completeness limit for mass. For younger systems, the mass completeness limit is lower than for older systems. The masses are plotted against the ages for the $0.2Z_{\odot}$ model in Figure 2.15, with the NGC 7714 disk clusters as blue circles and bridge clusters as red asterisks. The solid black curve shows the mass of a cluster with an F814W luminosity equal to our completeness limit

of $10^{5.1} L_{\odot}$, as a function of age. At lower ages, we are reaching less massive clusters, and are more deficient at older ages. For clusters less than 10 Myr old, we are complete to about $10^{4.3} M_{\odot}$, while for 10^9 yr we are complete only to $10^{5.5} M_{\odot}$. The dashed black line indicates the average completeness limit of $10^{4.8} M_{\odot}$. The significance of evolutionary fading is apparent, as all of the clusters with ages $\sim 10^8$ yr have masses $\geq 10^{4.5} M_{\odot}$.

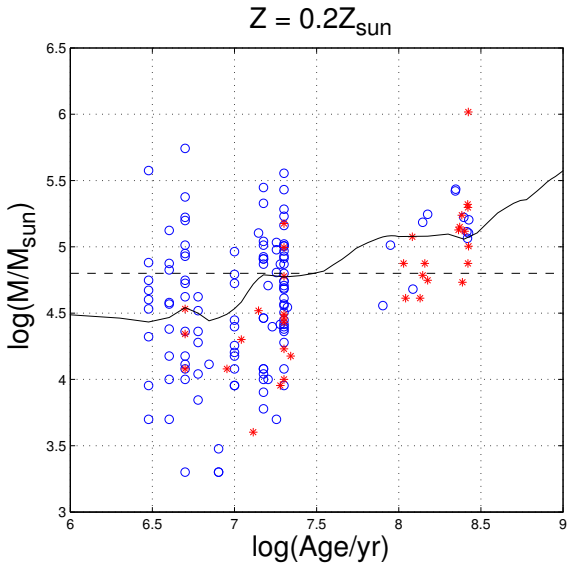

Figure 2.15 Mass vs. Age for the $0.2 Z_{\odot}$ model. Blue circles represent the NGC 7714 disk, while red asterisks are bridge clusters. The dashed black line represents the age-averaged mass completeness limit of $10^{4.8} M_{\odot}$ from Figure 2.14. The solid black curve shows the mass of a cluster with an F814W luminosity equal to our completeness limit of $10^{5.1} L_{\odot}$, as a function of age.

Mass cuts alter the age distributions considerably. In the $0.4 Z_{\odot}$ model, seven of the 27 clusters remaining after eliminating those with mass $< 10^{5.0} M_{\odot}$ are older than 22 Myr, with the youngest of these 111 Myr old. These account for six of the seven clusters remaining in the bridge (only one of which has F380W coverage) and one of six in the northern tail, but none of the 14 clusters in the southern tail.

Of the 63 clusters remaining after eliminating those with mass $< 10^{4.8} M_{\odot}$ in the $0.2 Z_{\odot}$ model, 31 are in the southern tail, 18 in the northern tail, and 14 in the bridge. There are 22 clusters with ages > 22 Myr, 12 of them in the bridge, of which five lacked coverage in F380W.

In the southern tail, seven of 31 clusters are older than 22 Myr (five of them detected at 3σ level), while the northern tail has two of 18 clusters older than 22 Myr. The youngest of these clusters has an age of 89 Myr.

The number of clusters falling into each age bin in the $0.2Z_{\odot}$ model is summarized in Table 2.2 for all measured clusters, clusters above the luminosity limit, and clusters above the average mass completeness limit. For comparison, we have included columns showing the expected numbers of clusters assuming a cluster formation rate of 1 cluster Myr^{-1}, and constant cluster formation for the last $10^{7.5}$ (CCF_{30}) and 10^{8} (CCF_{100}) yr, only including clusters above the mass limits. These are limiting cases, based on Figure 2.14. The observed number of clusters in the mass limit case fall between these two limits. Thus with the available data we cannot rule out constant cluster formation with no infant mortality. More sensitive data are needed to reduce the completeness limits and search for evidence of cluster destruction. With the current data set, the number of clusters is relatively small and the mass cut-off relatively high, thus the results on infant mortality are uncertain.

Table 2.2 Clusters by age bin for $Z = 0.2Z_{\odot}$

Age	All	Luminosity Cut	Mass Cut	CCF_{30}[a]	CCF_{100}[b]
1–10 Myr	59	23	13	10	10
11–22 Myr	70	28	28	12	12
23–100 Myr	2	0	1	8	78
>100 Myr	27	2	21	0	0
Total	158	53	63	30	100

[a]Expected numbers for constant cluster formation over the last 30 Myr at a rate of 1 cluster Myr^{-1}
[b]As above for 100 Myr

2.7.3 H II region age estimates

Ages for the H II regions were estimated in two ways. The colors obtained from large-aperture photometry in the *GALEX* and *HST* bands were fit to SB99 models, using the methods described in Section 2.6.2. In regions E and G–J, the FUV and NUV measurements provided only upper limits, so these bands were not fit to the models. The range of cluster ages within the H II regions suggests that the star formation histories are more complex than

the instantaneous starbursts used to model the individual clusters. We therefore used both instantaneous and continuous star formation models to estimate the ages of these regions. The true star formation history is likely to fall between these two extremes.

Ages were also estimated using the Hα equivalent widths, which were fit to instantaneous burst SB99 models. These data are shown in Table A.4, along with the median age of the *HST* clusters detected in each region. Note that the *HST* sample has no clusters in region E (four were detected but were covered in only two filters), only two clusters in region C, since it is at the edge of the WFPC2 field of view, and in the bridge (regions G–J) only one or two clusters were found in each region, so this indicator is only useful in regions A, B, D, and F. When possible, we also compare with published ages determined via photoionisation modeling.

The ages determined using EW(Hα) are generally consistent with the median age of clusters found in the region, with both showing cluster population ages ≤ 15 Myr. These estimates are somewhat higher than those in the literature (see Table A.4), but are within a factor of $\sim$3 in most of the large aperture photometry cases.

The ages determined by fitting SB99 models to the large aperture photometry of the H II regions are much higher than those determined by other methods in regions B, D, and F. The area within the apertures occupied by clusters is relatively small, so it is possible that faint sources outside the clusters are making significant contributions to the total luminosity of the H II regions. If these sources are older and redder, the age of the region as a whole could be quite different from that of its bright clusters. These sources could be older clusters below our detection threshold or the remnants of clusters that have already dissolved and entered the field population.

To quantify the possible influence of faint sources on the *HST* apertures, the fraction of luminosity in the F814W band for each of the H II regions f_c originating in the measured clusters was determined. The f_c values are similar throughout the NGC 7714 disk, with $\sim$80% of the light coming from outside the clusters. Unresolved objects could significantly impact the colors, which may explain the higher age estimates for regions B, D, and F.

All of the bridge H II regions had their lowest age estimates provided by color fitting, while

f_c varies. Regions G and I had the lowest f_c values in the system, while H and J have the highest. Visual inspection of regions G and I indicates several likely clusters that were not selected by *daofind*. Considering the relatively high noise and low resolution in *HST* bridge data, it is likely that these results are products of the data quality. Deeper imaging will be required to learn if the bridge hosts a cluster population that differs from that of the NGC 7714 disk.

Extinction estimates are shown in Table A.5, along with some values from the literature. The extinction estimates of González Delgado et al. (1995) come from the Balmer decrement, while the extinction in the nucleus found by González Delgado et al. (1999) was determined using evolutionary synthesis results for UV continuum flux distributions, and was smaller than that found using the Balmer decrement by a factor ∼3. Our extinction estimate for the nucleus is in good agreement with that of González Delgado et al. (1999), while our other estimates are higher than the literature values by a factor ∼2. This is not surprising, since the Balmer decrement tends to give higher extinction estimates than the continuum by a factor ∼2 (Fanelli et al., 1988; Storchi-Bergmann et al., 1994), possibly because dust in star forming regions with strong nebular emission is destroyed or removed by ionizing radiation, stellar winds, or supernovae (Fanelli et al., 1988). Another possibility is that the hot stars responsible for the Balmer lines are still associated with the dusty molecular clouds in which they formed, while the cooler stars that contribute to the continuum have drifted away from these regions and suffer less extinction (Calzetti et al., 1994).

2.7.4 *Spitzer* colors

Figures 2.16 and 2.17 show as red circles the *Spitzer* [4.5]−[5.8] vs. [3.6]−[4.5] and [5.8]−[8.0] vs. [4.5]−[5.8] colors of the H II regions. These were calculated from the flux densities as described in the IRAC Data Handbook. For comparison, we also show emission "clumps" from several other interacting systems, including Arp 24 (Cao & We, 2007), 82 (Hancock et al., 2007), 107 (Smith et al., 2005b), 285 (Smith et al., 2008) and NGC 2207/IC 2163 (Elmegreen et al., 2006), as green crosses. In the Arp 285 system, NGC 2856 tail clump 3 and disk clump 1

were unusual, and are marked in Figure 2.16 as a magenta open diamond and cyan limit, respectively. The unusually luminous clump 'i' in the eastern tail of NGC 2207 is also shown separately, as an open blue diamond. We also display the mean colors of field stars of Whitney et al. (2004) (magenta open triangle), M0III stars (M. Cohen 2005, private communication; open blue square), quasars (Hatziminaoglou et al. 2005; red squares), and diffuse galactic dust (Flagey et al. 2006; blue crosses).

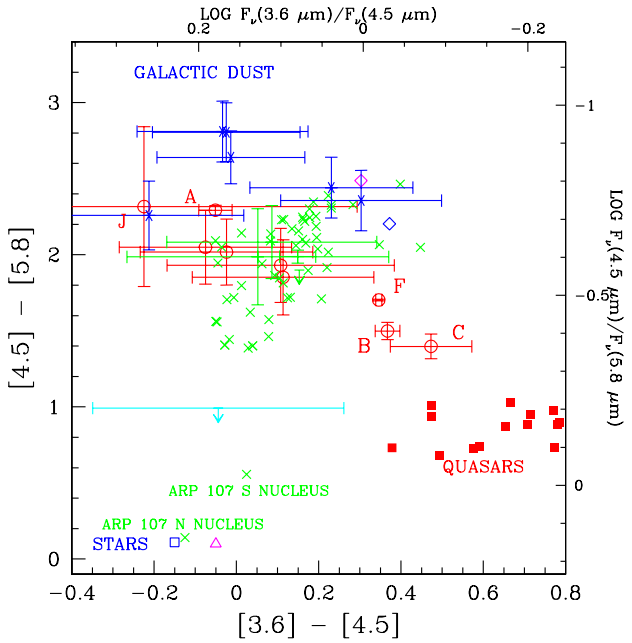

Figure 2.16 *Spitzer* [4.5]−[5.8] vs. [3.6]−[4.5] color-color plot. The Arp 284 H II regions (open red circles) are shown along with emission "clumps" from Arp 24 (Cao & We, 2007), 82 (Hancock et al., 2007), 107 (Smith et al., 2005b), 285 (Smith et al., 2008), and NGC 2207/IC 2163 (Elmegreen et al. 2006; green crosses). Shown separately are Arp 285 NGC 2856 tail clump 3 (magenta open diamond) and disk clump 1 (cyan limit), as well as NGC 2207/IC 2163 "clump i" shown separately (open blue diamond). Also shown are the mean colors of field stars of Whitney et al. (2004) (magenta open triangle), M0III stars (M. Cohen 2005, private communication; open blue square), quasars (Hatziminaoglou et al. 2005; red squares), and diffuse dust in the Milky Way (Flagey et al. 2006; blue crosses).

Most of the H II region *Spitzer* colors fit well with the clumps measured in other systems.

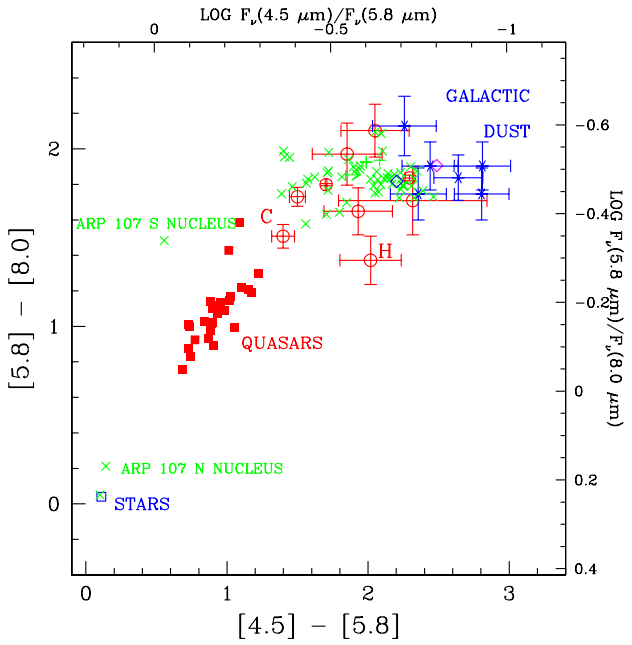

Figure 2.17 Same as Figure 2.16, but for [5.8]−[8.0] vs. [4.5]−[5.8].

This is important, since the selection criteria are somewhat different. The Arp 284 regions were selected based on Hα emission, whereas clumps in the other systems were selected based on *Spitzer* emission. While the Hα emission usually had a counterpart in *Spitzer* 8.0 μm, in some cases the aperture placement would have differed slightly if the 8.0 μm emission had been used for selection.

[4.5]−[5.8] is often used as a gauge of the star formation rate, with redder colors indicating higher rates of mass-normalized star formation (e.g., Smith et al., 2005b). The H II regions lie between interstellar matter and stars, indicating that, as in other interacting systems, they probably have contributions from both. However, none of the Arp 284 regions is quite as red as the Arp 285 tail clump. Smith et al. (2008) suggest that the exceptionally red color of this clump is due to strong emission from interstellar matter owing to the very young age of the clump, which was determined to be 4 Myr using optical colors. Region J has the same estimated age and is only slightly bluer in color, suggesting that it may also have numerous hot young stars.

The [5.8]−[8.0] colors generally fall close to those of interstellar matter, which is not sur-

prising since the 5.8 and 8.0 μm bands are expected to be dominated by interstellar dust.

A few of the regions are unusual. Regions B and C are unusually red in [3.6]−[4.5], but slightly blue in the other two colors. Region F is redder in [3.6]−[4.5] than clumps in other systems with similar [4.5]−[5.8] color. Region H is slightly blue in [5.8]−[8.0].

The colors of regions B and C suggest excess emission at 4.5 μm, perhaps with a slight deficiency at 5.8 and 8.0 μm, qualitatively similar to low-metallicity dwarf galaxies. In Figures 2.18 and 2.19, we compare the *Spitzer* colors of Arp 284 H II regions to those of the dwarf and spiral galaxies of Smith & Hancock (2009). Regions B and C are not as red in [3.6]−[4.5] as some the dwarfs, but are generally redder than the spirals. This may indicate that they are deficient in PAHs, though not extremely so, consistent with their moderately low metallicities.

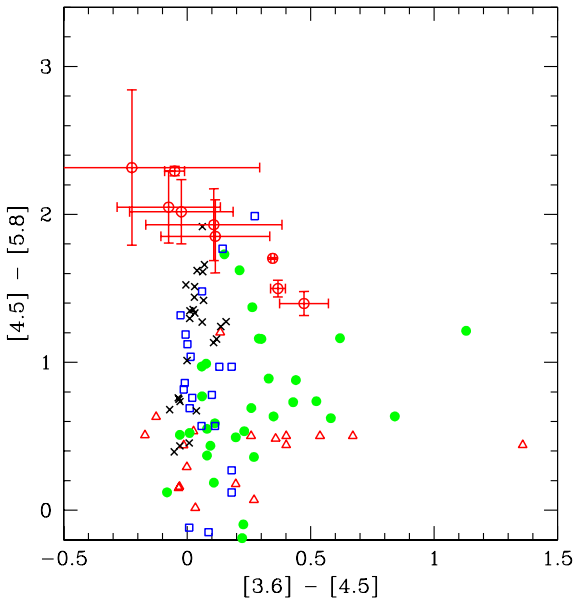

Figure 2.18 *Spitzer* [4.5]−[5.8] vs. [3.6]−[4.5] color-color plot showing Arp 284 H II regions (open red circles). The dwarf galaxies of Smith & Hancock (2009) are shown by metallicity, with $12 + \log(\mathrm{O/H}) < 7.9$ (red open triangles), $7.8 \leq 12 + \log(\mathrm{O/H}) \leq 7.9$ (green filled circles), and $12 + \log(\mathrm{O/H}) > 8.2$ (blue open squares), along with a sample of 'normal' spirals (black crosses).

It is interesting that regions B and C stand out in these plots, but the other regions do not.

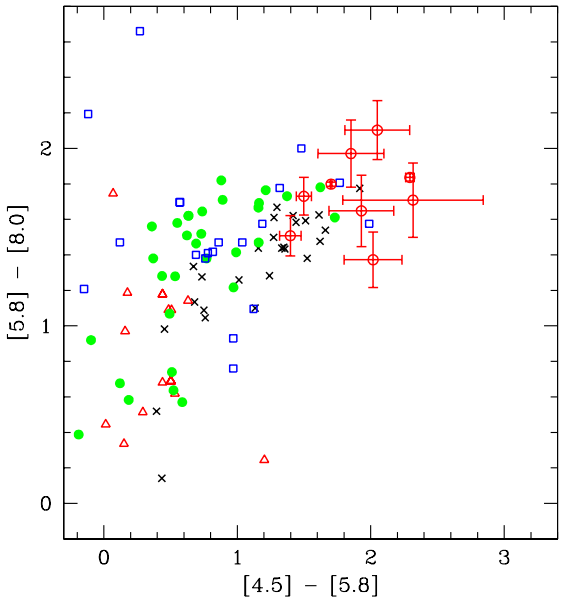

Figure 2.19 Same as Figure 2.16, but for [5.8]−[8.0] vs. [4.5]−[5.8].

Our color-based age estimate for region B is very similar to that of D, and our estimates based on EW(Hα) vary little between regions. García-Vargas et al. (1997), however, found regions B and C to be extremely young. This would imply more nebular continuum and Brα emission, which are two of the factors that appear to contribute to reddening [3.6]−[4.5] in the dwarfs (Smith & Hancock , 2009).

The SED for region B is plotted in Figure 2.20. We also show as black curves the best-fitting $0.2Z_{\odot}$ evolutionary synthesis models from SB99 for both continuous (top panel) and instantaneous burst (bottom panel) star formation models. The curves use the best-fitting ages for each model, which are 128^{+1272}_{-42} Myr for continuous star formation and 88^{+16}_{-18} Myr for the instantaneous star formation model. The models include both stellar and nebular emission. The solid green lines show the same models without nebular emission. The models corresponding to 1σ uncertainty (68% confidence) are also shown. All of the curves have been scaled to match the observations in F606W. The stellar and stellar+nebular emission models are nearly indistinguishable, indicating that nebular emission is relatively unimportant for these inferred ages. The large mid-IR excess could result from hot dust continuum emission,

PAH lines, or an older stellar population, either in clusters that have faded below our detection limits or in the field. The excess is diminished in the continuous star formation model, probably because it includes older stars.

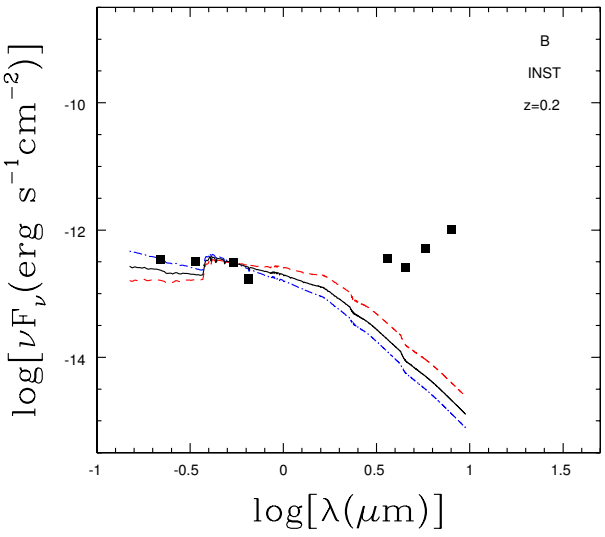

Figure 2.20 The FUV-mid-IR SED of region B. The black curves are the best-fitting $0.2Z_{\odot}$ evolutionary synthesis models including both stellar and nebular emission. The model in the top panel is for continuous star formation with an age of 128^{+1272}_{-42} Myr, while the bottom panel shows an instantaneous burst with an age of 88^{+16}_{-18} Myr. The solid green line plotted from 3–9.5 μm shows the models without nebular emission. The short-dashed red and dot-dashed blue curves correspond to the youngest and oldest models and the associated best-fitting extinctions. The models have been scaled to match the observations in F606W.

For comparison, the SED of the nucleus is shown in Figure 2.21. The top panel shows curves for a continuous star formation model with an age of 421^{+12}_{-11} Myr, while the bottom panel shows an instantaneous starburst with an age of 222^{+6}_{-6} Myr. In this plot we have also included the near-IR J, H, and K band fluxes from Lançon et al. (2001). The nucleus is known to have a complex star formation history, likely including stars older than ∼100 Myr. The mid-IR excess is greater in the instantaneous burst model, likely due older stars not included in this model.

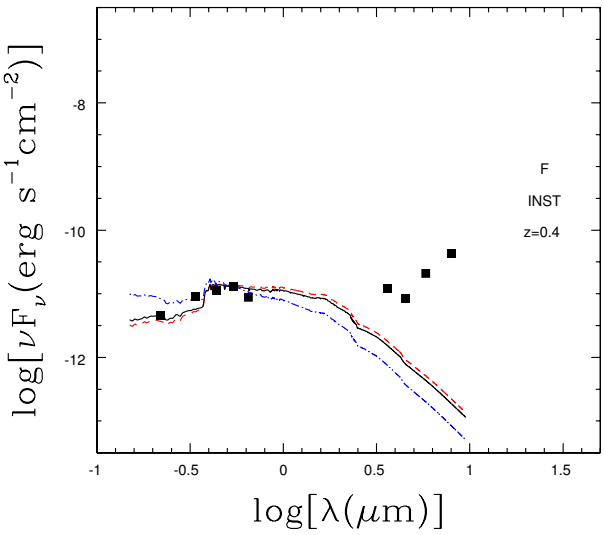

Figure 2.21 Same as Figure 2.20, but shows region F with $0.4Z_{\odot}$ models, with ages of 421^{+12}_{-11} Myr for the continuous star formation model and 222^{+6}_{-6} Myr for the instantaneous burst model.

2.7.5 Comparison with *Chandra*

2.7.5.1 Ultra-luminous X-ray sources (ULXs)

X-ray observations by Smith et al. (2005a) detected three non-nuclear point sources with $L_X > 10^{39}$ erg s^{-1}, the standard definition of an ultraluminous X-ray (ULX) source. Three other point sources lie just below this limit. The nature of ULXs is not presently understood. In one possible scenario, they could be intermediate mass ($100 - 1000 M_{\odot}$) black holes (IMBH; Colbert & Mushotzky 1999). Alternatively, they may be stellar mass black holes with beamed (King et al., 2001) or super-Eddington (Begelman, 2002) X-ray emission. IMBHs may preferentially form in massive star clusters (e.g., Portegies Zwart et al., 2004b). It takes at least 4 Myr for a stellar mass black hole/X-ray binary to form, and they are expected to be common in populations with ages up to ≈ 100 Myr (Rappaport et al., 2004b). In contrast, an IMBH may form in a YMC in ≤ 3 Myr (Portegies Zwart et al., 2004b). Evolutionary models of the predicted X-ray emission from IMBH+stellar companion mass-transfer binaries indicate

that such ULXs should generally have ages less than about 15–30 Myr (Portegies Zwart et al., 2004a).

As discussed in Smith et al. (2005a), the ULX candidates in NGC 7714/5 exist in a range of environments. A luminous X-ray point source is located 1.5″ away from the nucleus, near cluster n01, which has an estimated age of 14 Myr. If this association is correct, the young age is more consistent with the IMBH scenario. Another possibly young ULX candidate is found within H II region C, which has an age of 11 Myr based on EW(Hα) and a spectroscopically determined age of 4.5 Myr (García-Vargas et al., 1997). However, this second ULX cannot be associated with a specific star cluster, since there are several very close together in the area. Finally, one ULX is located in the outer western tail of NGC 7714, in an area that is undetected in Hα but is bright in *GALEX* images. Three other ULX candidates are neither located in H II regions nor are they close to optically-selected star clusters. Given the variety of environments, from this small sample we cannot make any strong conclusions about the nature of ULXs as a class.

2.7.5.2 Extended X-ray emission associated with star forming regions

In addition to point sources, the *Chandra* map revealed extended X-ray emission associated with some of the H II regions (Smith et al., 2005a). Figure 2.2 shows *Chandra* 0.3–8 keV X-ray contours over a color scale Hα image of NGC 7714. Extended X-ray emission is found associated with all of the disk H II regions except D. The bridge regions G–J also do not have observed diffuse X-ray emission.

The possible contributors to the extended X-ray emission include multiple unresolved high mass X-ray binaries (HMXBs), or hot gas from supernovae and stellar winds impacting the ambient interstellar medium. Based on Local Group studies, the HMXB component is expected to be too small to account for this emission in the NGC 7714/5 regions (Smith et al., 2005a), unless there is an excess above Local Group galaxies. For the hot gas component, using SB99 models and a constant X-ray production efficiency L_X/L_{mech}, where L_{mech} is the mechanical luminosity from the supernovae and winds, the ratio of the number of Lyman continuum

photons N_{LyC} to X-ray luminosity N_{LyC}/L_X is expected to drop off with age for a star forming region (Smith et al., 2005a). However, the one H II region complex in the NGC 7714 disk that is not detected in extended X-ray emission, region D, has an EW(Hα)-based age that is somewhat older than some of the other regions (Table A.4), in spite of having the highest N_{LyC}/L_X. In contrast, region E is bright in the X-rays, with a low N_{LyC}/L_X, but has a younger age from its EW(Hα). This suggests that the X-ray production efficiency may vary with time and/or from region to region, and/or the HMXB contribution may be larger than expected in some regions. This result is uncertain, however, due to the relatively large uncertainties on our age estimates and the small number of H II regions in our sample.

2.8 Conclusions

We have used broadband colors to obtain age estimates for 174 proto-globular cluster candidates in the Arp 284 system. The populations detected in the tidal features of NGC 7714 are generally quite young ($\leq$ 20 Myr old). However, when the sample is limited by a mass cut, the dominance of young clusters becomes unclear in the NGC 7714 disk and vanishes in the bridge. Due to the small number of clusters above the mass cut, this latter result is highly uncertain. Deeper imaging is required to better define the cluster mass function and push down the completeness limit, particularly in the bridge, which has higher photometric uncertainties and less F380W coverage than the rest of the system.

No substantial differences are found between the populations within NGC 7714. The clusters in the nucleus do not generally differ in age from those in the tidal structures. It therefore appears that the early-stage dissolution processes, if present, operate via internal processes, rather than local environmental effects, but we cannot rule out the possibility of weaker dissolution in the bridge.

Using larger apertures to study H II region complexes, we find in several cases that the region as a whole appears to be older than the clusters detected inside it. This suggests an older, redder population that is unresolved, possibly the remnants of star clusters that have already dissolved or which were not detected as discrete sources because of evolutionary fading.

The large aperture results suggest that star formation has been ongoing in H II regions B and D, located in the northern tail, for a dynamical time scale, like that in the nucleus. In both cases, the star formation history, whether continuous or in discrete bursts, is unknown. We also do not know if regions B and D are gravitationally bound, or simply regions where successive waves or infall events have triggered star formation. Region C is similar, but we have insufficient data to comment on its nature. If in the future these regions are found to be bound, they could be interpreted as nearby analogs to the high redshift disk clumps studied by Elmegreen et al. (2009).

The Arp 284 interaction has been in progress for over 100 Myr, yet we find little evidence for a significant cluster population older than 20 Myr. Thus it is possible that clusters are dissolving on a relatively short time scale. However, due to completeness issues, with the available data we cannot definitively confirm the possibility of infant mortality in this system. Further, more sensitive observations are needed to search for a deficiency of older clusters.

CHAPTER 3. The star cluster population of the interacting system Arp 261

3.1 Introduction

Arp 261 presents an interesting if poorly understood morphology. Its two parallel disks, separated by 7 kpc for a distance of 28 Mpc, suggest a Taffy-like collision (see Figure 3.1), in which the disks have collided face-on at high velocity in a predominantly hydrodynamic "splash" collision, with tidal forces relatively weak (see Struck 1997). However, several factors indicate that this scenario may not be correct.

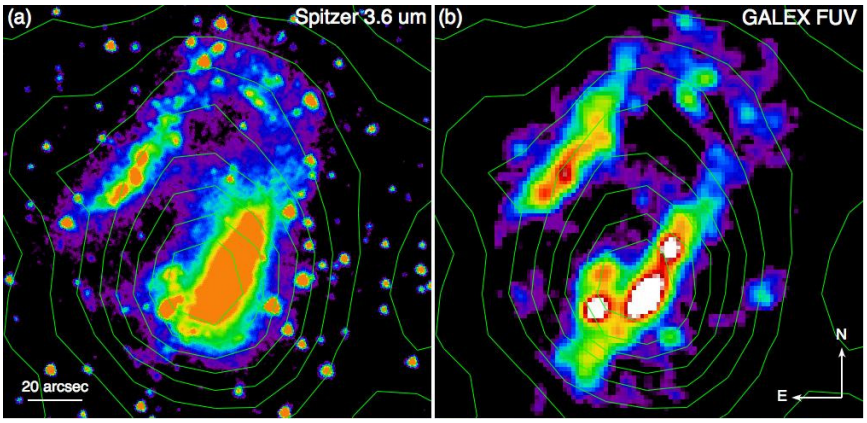

Figure 3.1 NVSS 1.4 GHz radio contours overlaid on (a) *Spitzer* 3.6 μm and (b) *GALEX* FUV image of Arp 261. The 3.6 μm image also shows several foreground stars. Note the emission regions in the northern bridge, and the presence of the diffuse central bridge in both images. The radio continuum emission is centered at the southern end of A261S, and may be associated with the hinge clumps.

One piece of conflicting evidence comes from 1.4 GHz radio continuum data from the NRAO

VLA Sky Survey (NVSS; Condon et al. 1998) is not stretched across both galaxies as in the Taffy galaxies (Condon et al. 1993; see also Chapter 4).

Detailed modeling is not possible because we lack 21 cm H I velocity data, but the *GALEX* NUV image, along Hα data from *HST*, indicate star formation is taking place in a bridge to the north of the galaxies. The origin of this northern bridge is not entirely clear. The gas bridge in the Taffy system is directly between the galaxies, not displaced to the north, though a modification of the angle of approach or inclination of the galaxies could rectify this discrepancy. More significantly, the Taffy bridge hosts no significant star formation (Bushouse & Werner 1990; Jarrett et al. 1999; Gao et al. 2003; see also Chapter 4).

Arp 261 seems to have a weak central bridge with a position more comparable to that of the gas bridge between the Taffy galaxies. However, the faint NUV emission from this area again suggests star formation. There are also a small number of star clusters detected in this central bridge, which requires either active star formation or a tidal component to the interaction, since purely hydrodynamic interactions do not displace stars.

It is clear from both the NUV and Hα images that both the northern (A261N) and southern (A261S) galaxies have significant star formation. A261S also has several "hinge" clumps of star clusters to the south, which are typically the result of tidal interactions (Hancock et al., 2009; Smith et al., 2010).

An alternative to a high-speed Taffy-like collision is a slower flyby. Since the time scale for the latter type of collision is significantly longer, the duration of enhanced star formation would also be longer, and we expect to see evidence of an intermediate age ($\geq$ 100 Myr) population.

3.2 Observations

3.2.1 *HST*

Observations of Arp 261 were obtained from the *Hubble* Legacy Archive (HLA). The data span 3 different observing programs, and utilize both the Wide Field and Planetary Camera 2 (WFPC2) and Advanced Camera for Surveys Wide Field Camera (ACS WFC) detectors. The coverage of the system is therefore not uniform across all filters. The data are summarized in

Table 3.1.

Table 3.1 *HST* imaging of Arp 261

Detector	Filter	Exposures	Total Duration (s)	Dataset
WFPC2	F300W	2	1000	hst_09124_42_wfpc2_f300w_wf
WFPC2	F555W	2	700	hst_08602_58_wfpc2_f555w_wf
WFPC2	F814W	2	700	hst_08602_59_wfpc2_f814w_wf
ACS	F625W	1	180	HST_9892_38_ACS_WFC_F625W
ACS	F658N	2	1500	HST_9892_38_ACS_WFC_F658N

Both galaxies appear in all filters. However, the gap between the chips of the ACS images in both F625W (∼R) and F658N (redshifted Hα) cut across a star forming region in the northern part of A261S. In the WFPC2 F555W (∼V) and F814W (∼I) filters, this same region falls at the intersection of all 4 chips. The F300W (∼U) filter has full coverage of A261S, but the seam between 2 of the WF chips runs through the length of the northeast galaxy. More significantly, the star forming bridge to the north of the galaxies is cut off in this filter. The F300W data also has considerably more noise than the other filters.

The pixel size of the ACS is approximately0.05″. The WFPC2 detector has pixel sizes of 0.10″ for the WF chips and 0.05″ for the PC chip. The HLA data products used in this analysis had already rebinned the PC data to the same resolution as the WF data. In addition, the images downloaded from the HLA had already been co-added where multiple images were available, and some cosmic rays removed by the processing pipeline. The cosmic ray removal was generally very effective in the WFPC2 images and required little additional cleaning. The pipeline cleaning was far less effective in the ACS images and required considerable manual cleaning using the IRAF[1] task fixpix.

3.2.2 *Spitzer*

Mid-infrared imaging of Arp 261 was obtained with the Infrared Array Camera (IRAC) on board the *Spitzer Space Telescope*, and were previously utilized in Smith et al. (2010). IRAC

[1]IRAF is distributed by the National Optical Astronomy Observatories, which are operated by the Association of Universities for Research in Astronomy, Inc., under cooperative agreement with the National Science foundation

has 4 imaging channels with effective wavelengths of 3.6, 4.5, 5.8, and 8.0 μm. The data were downloaded from the public archive using the *Spitzer* Science Center (SSC) software Spot[2]. The data had been processed using SSC pipeline version S18.7.0, and were of sufficiently high quality that additional processing was not necessary.

The IRAC detector has a native pixel size of 1.2″, but the pipeline-processed data products have been rebinned to a pixel size of 0.6". It is therefore not possible to resolve individual star clusters, but groups of clusters can still be studied and compared to the clusters they contain. For clarity, these large aperture regions will be called "clumps."

3.2.3 *GALEX*

Arp 261 has also been observed by the *Galaxy Evolution Explorer* (*GALEX*) far-UV (FUV) and near-UV (NUV) detectors. The total exposure times were 2157 s in FUV and 3844 s in NUV. The pixel size is 1.5″, so the *GALEX* data, like the *Spitzer*, is useful only for studying large groups of clusters.

The *GALEX* images were previously published as part of the Spirals, Bridges, and Tails (SB&T) UV atlas of interacting galaxies (Smith et al., 2010), and were also used in a study of the Larson-Tinsley effect using the SB&T sample (Smith & Struck, 2010). Photometry in these studies used much larger apertures than are appropriate for studying cluster groups, so we perform our own measurements.

3.3 Data Analysis

3.3.1 *HST* Photometry

Star clusters were selected using the HLA source lists, which corresponds to 5σ detections using the IRAF task daofind. The source lists for all of the filters were merged to form a single list. Faulty detections due to cosmic rays or multiple detections on a single source were removed from the list.

[2]There is now a web-based *Spitzer* Heritage Archive with an improved user interface available at http://archive.spitzer.caltech.edu/

To remove the effects of differing resolution between the WFPC2 and ACS detectors, the ACS data were blurred to match the WFPC2 resolution, which gave a FWHM = 0.19″. This was done using the IRAF task gauss, with a gaussian convolution kernel having FWHM = 0.15″.

Photometry was performed using the IRAF task phot with circular apertures of radius 0.15″–0.3″, depending on crowding and the apparent extent of the cluster. In some cases, aperture positions were offset slightly to prevent overlap with nearby clusters. Background subtraction was determined using the mode value in a circular sky annulus of inner radius 0.6″ and width 0.2″.

Photometric zero points in the Vega system for the ACS data were obtained from the Space Telescope Science Institute (STSci) web site[3], while those for the WFPC2 came from the WFPC2 Data Handbook. However, since the HLA WFPC2 images are in units of electron s^{-1}, rather than data number (DN) as assumed in the typical reduction pipeline used in the WFPC2 Data Handbook, the zero point must be adjusted for the gain. The average value of the gain over the three WF chips is 7.04, so the required correction is 2.5log(7.04) = 2.119 mag. This number was added to each of the zero points found in the WFPC2 Data Handbook.

Aperture corrections were determined using a set of isolated point sources in the images. For both detectors, the procedure is to determine corrections to an aperture of 0.5″, then apply an additional correction to infinite aperture. This final correction is −0.1 mag for all filters using WFPC2 (Holtzman et al., 1995). For the F625W ACS filters, the correction is −0.088 (Sirianni et al., 2005).

Photometric measurements of the F658N data were not converted to magnitudes, but were used to obtain the equivalent width of the Hα line, which can be used with the SB99 models to obtain an independent set of age estimates. Continuum subtraction was performed by subtracting a scaled F625W image from the F658N image. The F625W scaling was determined by assuming foreground stars in the image had no Hα line emission, and so when the scaled F625W image was subtracted from F658N, the stars were removed.

[3]http://www.stsci.edu/hst/acs/analysis/zeropoints; updated from Sirianni et al. (2005)

Fluxes in both F625W and continuum-subtracted F658N were measured in electron s^{-1} using the same set of apertures as for the other *HST* data, and the values were converted to erg s^{-1} cm^{-2} $Å^{-1}$ using conversion factors obtained from the STSci web site. The F658N numbers were then multiplied by the filter bandwidth of 37 Å, and finally divided by the F625W flux to obtain the Hα equivalent width, EW(Hα).

The magnitudes and equivalent widths for each sample cluster are listed in Table B.1. The colors of the clusters are presented in Figure 3.2. The panels on the left do not include error bars for clarity. The right panels show the same colors with error bars included.

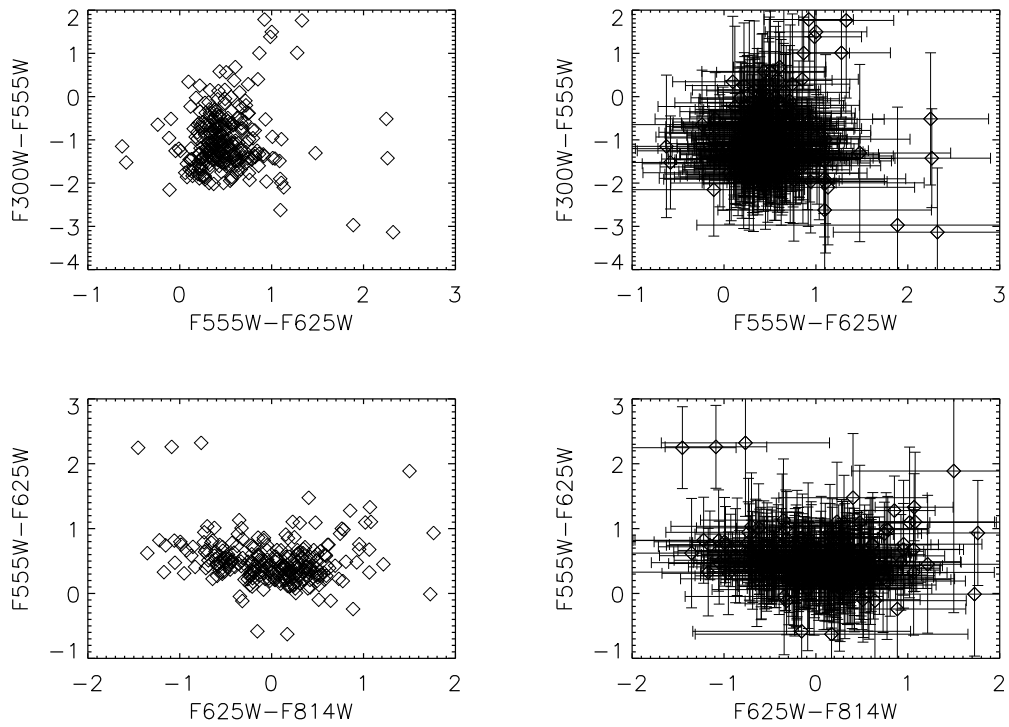

Figure 3.2 *HST* colors of Arp 261 clusters. The left panels show the colors without error bars for clarity, while the right panels include error bars to give a sense of the uncertainty in the measurements.

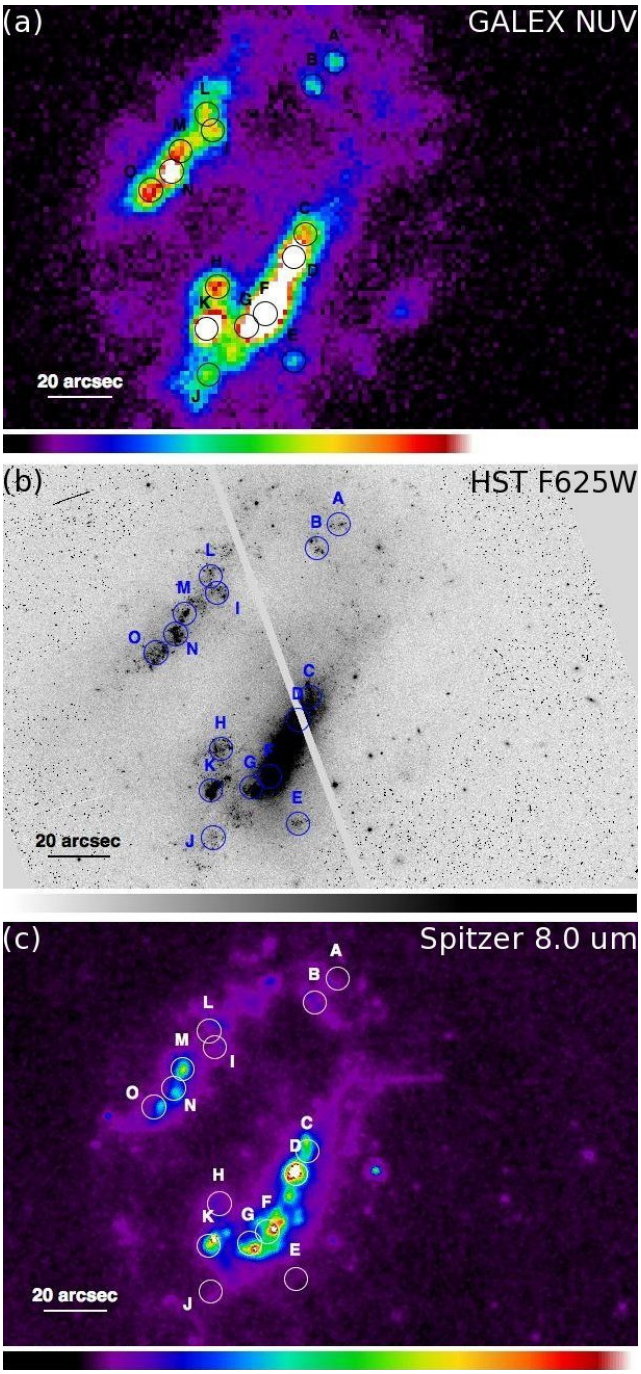

Figure 3.3 Arp 261 system in (a) *GALEX* NUV, (b) *HST* F625W, and (c) *Spitzer* 8.0 μm. The large-aperture photometry regions A–O are labeled in each panel. North is up and east to the left.

3.3.2 *Spitzer* and *GALEX* photometry

Photometry was performed on both the *Spitzer* IRAC and *GALEX* data using apertures that encompassed multiple star clusters. The regions were selected in *GALEX* NUV using the IRAF task daofind. The detections are at the 4σ level, where σ is the background level near the galaxies. These "clumps" are a good representation of what would be selected by eye in the *GALEX* images. When the *HST* images were blurred to approximately match the *GALEX* resolution, the same areas generally stood out. Figure 3.3 shows these regions in *GALEX* NUV, *HST* F625W, and *Spitzer* 8.0 μm, with the large aperture photometry regions labeled.

The *Spitzer* emission differed significantly in some areas. The difference between the *GALEX* and *Spitzer* emission is in many cases due to the comparatively poor resolution of *GALEX*. Clump B, for example, appears as a single source in *GALEX*, two bright clumps in *Spitzer*, and two groups of clusters in *HST*. One exception is clump E, which is clearly detected in *GALEX* and corresponds to a group of clusters in *HST*, but shows little emission in *Spitzer* except at 3.6 μm.

For the clump photometry, the measurements used an aperture radius of $3.75''$ in all instruments and filters, with background levels determined in a circular annulus with inner radius $4.75''$ and width $4''$. The IRAC fluxes were converted to *Spitzer* magnitudes using the prescription in the IRAC Data Handbook, while *GALEX* magnitudes in the ST mag system were obtained using conversions from the *GALEX* web site[4].

3.3.3 Age estimates

The cluster ages were estimated using the evolutionary synthesis code STARBURST99 version 6.0.2 (SB99; Leitherer et al. 1999; Vázquez & Leitherer 2005; Leitherer et al. 2010). We ran models for two different star formation histories, an instantaneous burst of $10^6 M_\odot$ and continuous star formation at a rate of 1 $M_\odot$ yr^{-1}. Each of these star formation histories was run at metallicities of 0.004 ($0.2Z_\odot$), 0.008 ($0.4Z_\odot$), and 0.020 ($Z_\odot$) with a Kroupa (2002)

[4]http://galex.stsci.edu/GR4/?page=faq

initial mass function (IMF). Hα line emission was also included.

Each of the six models produced a spectrum from 91 Å–160 μm at ages running from 10^6–1.4×10^{10} yr. The spectrum at each age point was reddened using the reddening law of Calzetti et al. (1994) for extinctions ranging from $E(B-V) = 0$–2 in increments of 0.02, so there were 100 different spectra corresponding to different extinctions at each age. All of the spectra were then convolved with filter bandpasses to produce a set of model colors. The best fitting combination of age and extinction $E(B-V)$, along with 1-σ uncertainties, were determined using χ^2 minimization (e.g., Press et al., 1986). For the *HST* data, either two or three colors were available for each cluster. Those with only 2 colors lack F300W−F555W. Coverage in the U band, which is close to F300W, is known to be particularly important for the determination of accurate cluster ages (e.g., Hancock et al., 2008). Therefore, the sample is subdivided into a primary, 3-color sample and a secondary sample which also includes clusters with only 2 measured colors. The age estimates, along with the number of colors used in fitting and whether or not the cluster was on frame in Hα, are listed in Table B.2.

The large-aperture clumps have much broader spectral coverage. Due to uncertainties in the transmission curves used to make the model colors, we did not create colors across instruments. There was therefore a maximum of seven colors available for age fitting.

3.4 Results

3.4.1 Cluster age distribution

Age estimates for each cluster, along with the number of colors fit N, are shown is Table B.2. For the clusters, we consider only instantaneous starburst models, assuming all stars in a cluster form at approximately the same time. The primary sample, which was fit using 3 colors, is predominantly young regardless of metallicity, though the relative size of the older population varies considerably with metallicity. The age distribution for each metallicity is shown in Figure 3.4. Since the metallicity of Arp 261 is unknown, we consider each case.

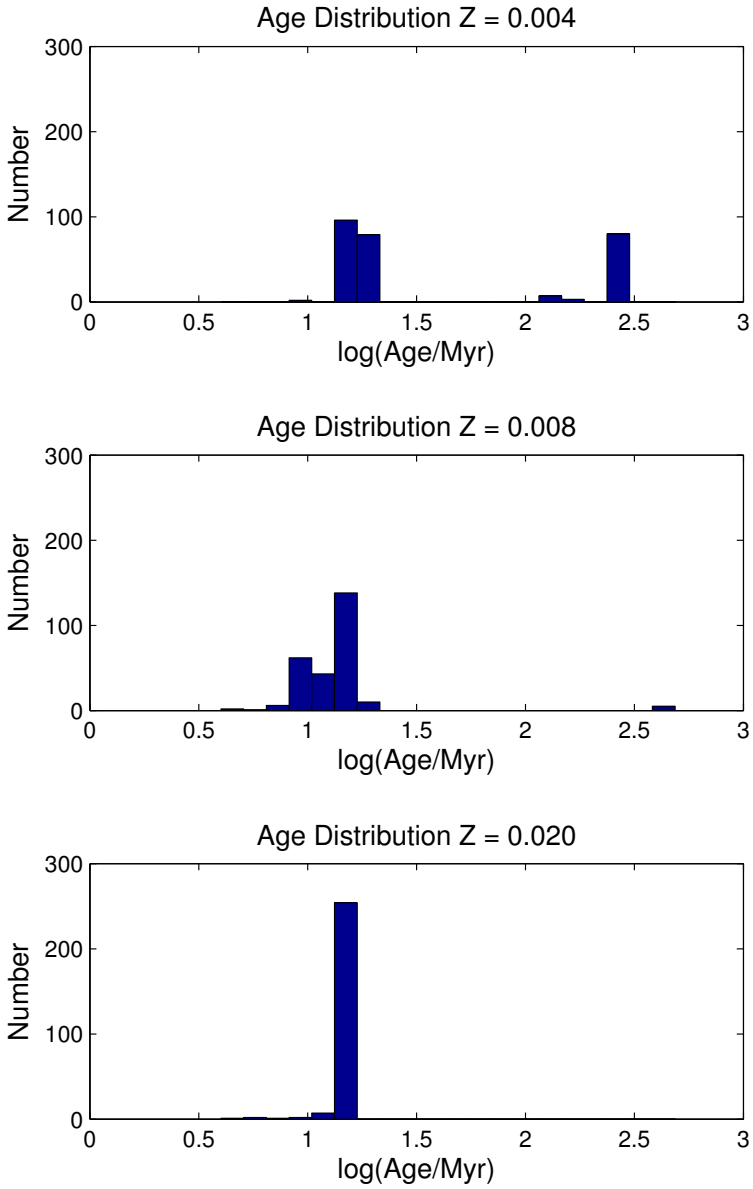

Figure 3.4 Histograms showing the best fitting age distribution of the primary sample at each of the 3 model metallicities. There are a total of 267 clusters in the primary sample, most with ages ∼20 Myr at each metallicity. The numbers older than ∼20 Myr are 90 at $Z = 0.004$, 5 at $Z = 0.008$, and 0 at $Z = 0.020$.

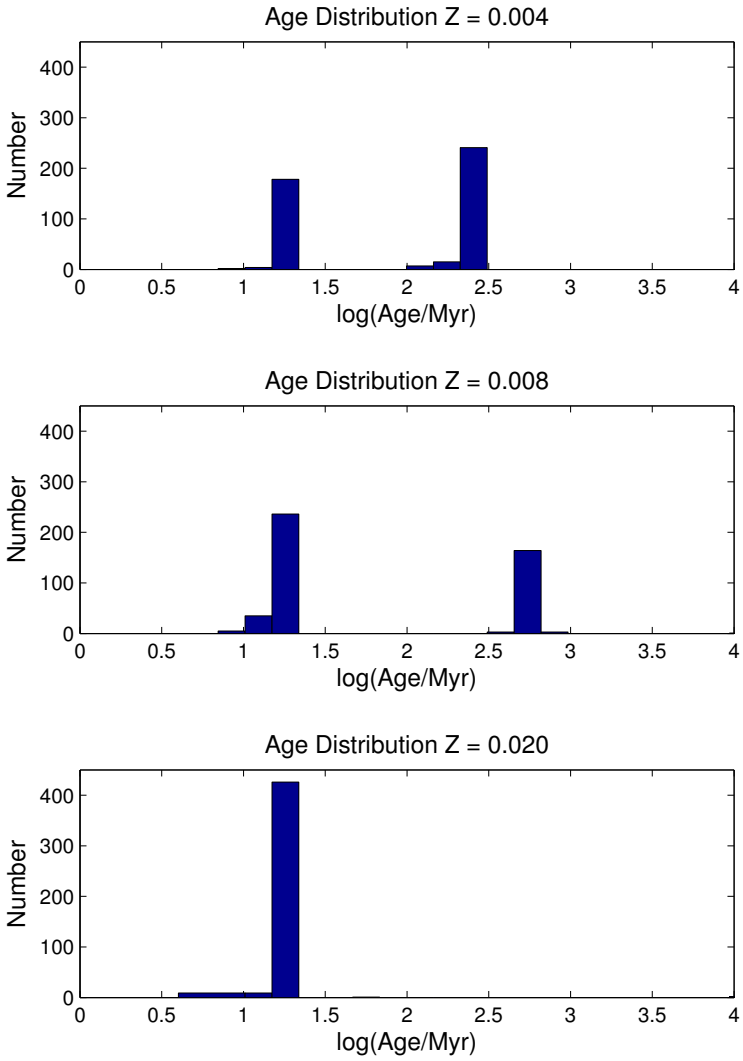

Figure 3.5 Histograms showing the best fitting age distribution of the primary and secondary samples at each of the 3 model metallicities.

The median age at $Z = 0.020$ is 16^{+131}_{-11} Myr, with none of the clusters having a median age >20 Myr. The next step down in metallicity is $Z = 0.008$, which has 5 intermediate age[5] clusters with median age 489^{+13610}_{-284} Myr, out of a total 267 clusters in the primary sample. The young population at this metallicity has a median age 20^{+321}_{-15} Myr. The highest number of intermediate age clusters appears at $Z = 0.004$, which has 90 such clusters with a median age 256^{+9940}_{-250} Myr. The young population at this metallicity has a median age 16^{+261}_{-11} Myr. The uncertainties in the age estimates are large for all 3 metallicities. This should be kept in mind, though we will focus primarily on the best fitting ages for the remainder of the discussion.

Despite the uncertainties, some trends are apparent. At $Z = 0.020$, the best fitting ages are entirely young, with early intermediate ages possible at the limits of the uncertainties. A few clusters with best fitting ages ∼500 Myr appear in the $Z = 0.008$ models, but most are still quite young, though the uncertainties are somewhat larger on the young sample. At $Z = 0.004$, there is a significant intermediate age population with best fitting ages ∼250 Myr, though given the uncertainties it is possible that there is only a single population.

The picture becomes far murkier when the secondary sample, fit by only 2 colors, is included. These clusters are almost exclusively old in the $Z = 0.004$ and $Z = 0.008$ models, with, respectively, only 7 and 14 out of 180 clusters younger than 20 Myr. This differs markedly from the distribution of the primary sample, and is also inconsistent with the Hα ages (discussed below). Moreover, the missing color is the only one that includes F300W, which is similar to the U filter that is known to be exceptionally important in obtaining accurate age estimates (Hancock et al., 2008). If the clusters from the primary sample are fit without F300W−F555W, the ages shift from predominantly young to predominantly old – very similar to the secondary sample. We therefore conclude that the age estimates for the secondary sample are of little use.

The age distribution determined using EW(Hα) is shown in Figure 3.6. The ages are all young, with very few older than ∼20 Myr. This is not surprising, since Hα emission comes predominantly from massive, young stars, so only young clusters are likely to be detected in

[5]We refer to clusters with ages < 100 Myr as young, 100–1000 Myr as intermediate age, and ages > 1 Gyr as old.

Hα. The agreement between the Hα ages and the 3-color ages is best at $Z = 0.020$, and worsens as the metallicity decreases and the number of old clusters increases.

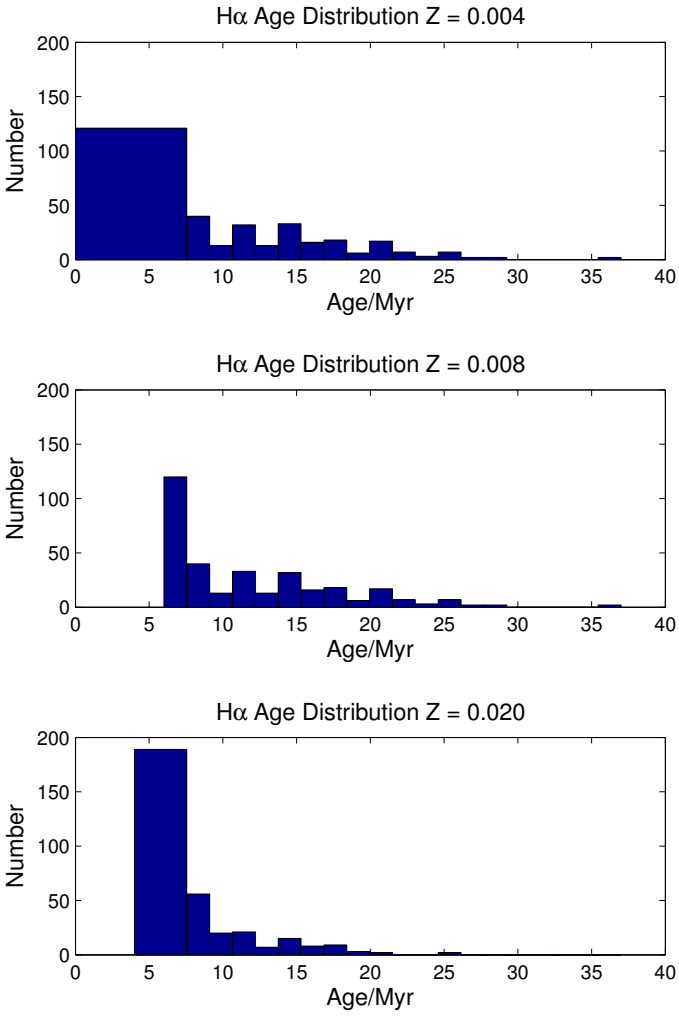

Figure 3.6 Histograms showing the best fitting age distribution of the primary and secondary samples based on EW(Hα). The clusters are all young, with few older than $\sim$20 Myr. This is expected, since Hα emission is strong only from massive young stars.

3.4.2 Cluster luminosity function

Because of evolutionary fading, clusters become less luminous as they age. This must be accounted for in determining the completeness of the sample. Assuming that the luminosity function (LF) has a linear form over the observed range, we find a limiting magnitude for the full cluster sample (primary and secondary) of 23.2 mag (Vega system) in F625W. This filter has been selected because of its good spatial coverage of the system, which includes the most clusters. It also has the advantage of being red, so it should not be as heavily affected by extinction as some of the bluer filters.

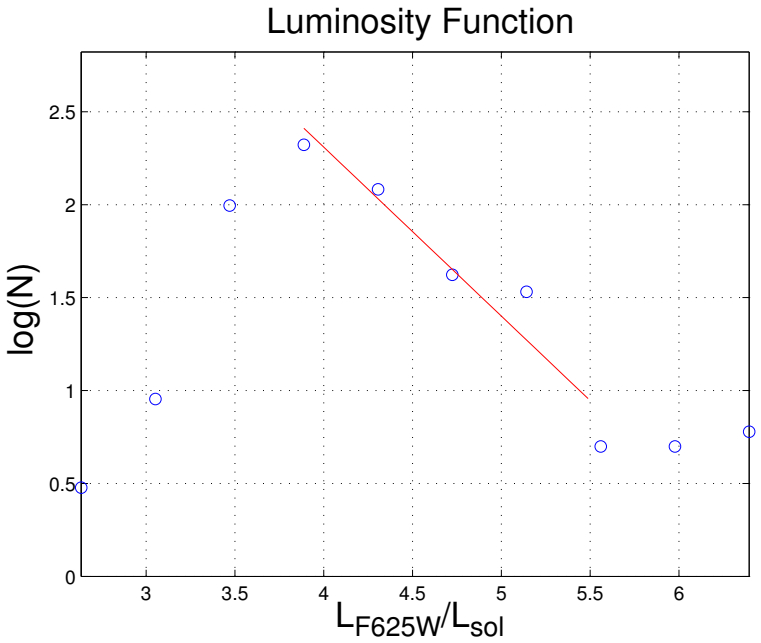

Figure 3.7 Luminosity distribution in F625W. The red line is a fit to the linear part of the distribution and has a slope of -0.91.

Above the completeness limit, we have 159 clusters in the primary sample. The magnitude-limited age distribution depends heavily on metallicity. At $Z = 0.004$, there are 108 clusters with ages $\leq$ 20 Myr; the remainder have ages $>$ 100 Myr. The $Z = 0.008$ ages are generally $\leq$ 20 Myr, with only 5 clusters older, all of which have ages $>$ 400 Myr. All of the clusters in the luminosity-limited $Z = 0.020$ are younger than $\sim$20 Myr, as they must be since the full sample also had no older clusters.

The luminosity function is shown in Figure 3.7. The slope is -0.91 for a 10-bin histogram and -0.85 for a 20-bin histogram. We thus estimate a slope -0.88 ± 0.03, so the power law index is $\beta \approx 1.88$ when the data are not binned logarithmically. This agrees well with the typical value $\beta \approx 2$ (e.g., Whitmore et al., 1999; Gieles, 2006; Hwang & Lee, 2008).

3.4.3 Cluster mass function

The cluster mass function is estimated using the age and $E(B-V)$ values from the SB99 models. Each age and extinction combination in the models has an associated luminosity in each of the filters. Since the models used for the cluster age estimates have a fixed mass of $10^6 M_\odot$, this corresponds to a mass-to-light ratio. The mass-to-light ratio is assumed to be the same for all clusters of the same age and metallicity. Under this assumption, we can use the measured luminosities relative the model values to obtain an estimate of the mass in units of $10^6 M_\odot$. Since older clusters are expected to have lower luminosities, they will generally be found to have higher masses. It should be noted that the uncertainties on masses determined in this way are quite large, at least a factor of 2, though we do not include formal uncertainties here.

The cluster mass distribution for the primary sample for each metallicity is shown in Figure 3.8. We assume a power law form and obtain fits to the linear parts of the distribution, with the lowest mass fit designated as the mass completeness limit. This is in fact an age-averaged value, since the masses depend on the ages and younger clusters are brighter and easier to detect. The mass limits for $Z = 0.004$, $Z = 0.008$, and $Z = 0.020$ are $10^{4.4}$, $10^{4.6}$, and $10^{4.4} M_\odot$, respectively. The slopes are -0.88, -0.96, and -1.13, so the power law indices are comparable to those found in other systems (Zhang & Fall 1999; Hunter et al. 2003; see also Section 2.7.2). The distributions are also surprisingly consistent with one another, considering how markedly the age distributions differ.

While the linear portion of the mass functions are in reasonable agreement with results from other systems, the high-mass end of the distribution is unusual in that it remains flat or even rises slightly, rather than either continuing the power law trend or truncating. This partly

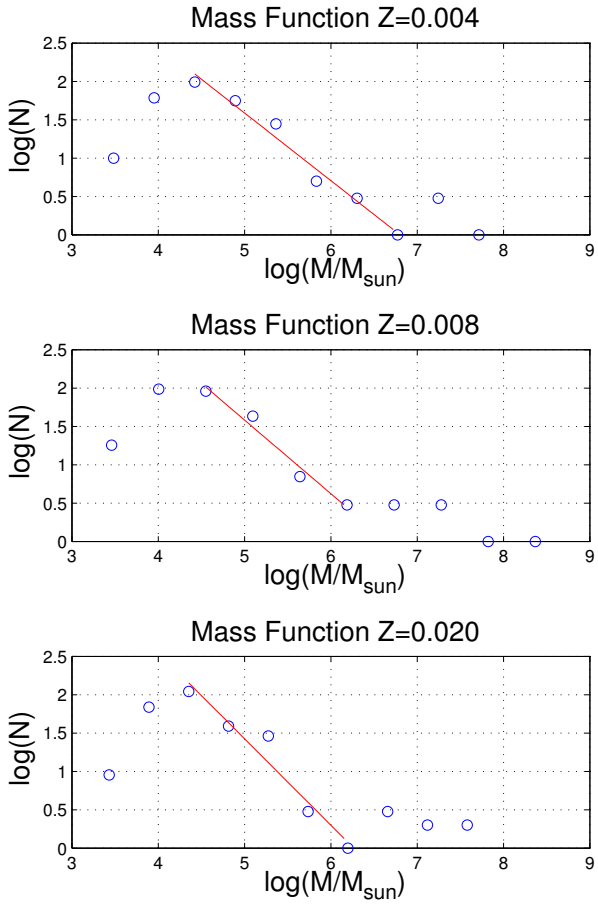

Figure 3.8 Mass distribution of clusters at all 3 model metallicities, based on 10-bin histograms. The red line is a fit to the linear part of the distribution. The masses are based on the luminosity in F625W; the mass estimation process is described in the text.

results from the presence of older clusters in the age estimates, which must be luminous and therefore massive in order to be detected. However, the entirely young $Z = 0.020$ distribution also shows no drop at the high mass end. This could be due to the presence of multiple unresolved compact clusters falling into a single photometric aperture.

3.4.4 Large aperture ages

Ages of large, *GALEX* NUV-selected clumps were determined using both continuous and instantaneous burst star formation histories. Ages based on EW(Hα) use only the instanta-

neous starburst, since the EW(Hα) values measured were in many cases outside the range predicted by the continuous star formation model. This is probably because both star formation histories represent limiting cases, and while each region has experienced star formation over an extended period of time, most are likely to have seen a significant increase in SFR resulting from the interaction. Thus all should have some Hα emission from young stellar populations, even if there is a significant older population.

For the case of continuous star formation, most of the clumps have ages well above 100 Myr, though there are several exceptions. Clumps A, C, and D have ages $\sim$2 Myr. These clumps had poor *HST* coverage, with C available only in F300W$-$F555W and A and D available in none of the *HST* colors. Unfortunately, the coverage makes the age estimates extremely uncertain. When all of the clumps are fit using only the colors available for A, C, or D, the ages are always $\sim$2 Myr. It thus seems likely that the unusually young ages for these clumps are artifacts of the wavelength coverage.

Clump B is the other exception, with an age $\sim$100 Myr regardless of metallicity. However, this clump was not covered in the important F300W$-$F555W color. We again tested the effects of the wavelength coverage by fitting the other clusters to this same set of colors. In this case, the clumps typically became older by a factor $\sim$2 over the ages obtained by fitting all 7 colors. It thus seems likely that clump B is, in fact, young.

The instantaneous star formation models generally predict very young ages $\sim$20 Myr, and the color-based estimates generally agree with the EW(Hα) ages to within a factor of 2. Clumps G, H, and O are exceptions, with ages $>$ 200 Myr at low metallicity. Clumps G and O both have all colors available for fitting, while H lacks only F300W$-$F555W, which may have the effect of making it appear older by a factor $\sim$2 compared to a 7-color age, as determined above for clump B. This makes the ages for region H very difficult to evaluate.

3.5 Discussion

3.5.1 Collision scenarios

The dynamics of the Arp 261 collision are not entirely clear, and detailed modeling is of limited use without H I velocities, but there are 3 basic scenarios that seem particularly likely.

The first collision scenario is a Taffy-like collision, in which two disks collide face-on with high relative velocities, forming a bridge of atomic and molecular gas between them in a hydrodynamic splash (Struck, 1997). Such a model reproduces the parallel disks, but the gas should be concentrated between the galaxies rather than to their north, though a slight inclination between the disks may displace the bridge. A larger drawback is that the bridge in a Taffy-like collision, while rich in gas, is not expected to form stars due to shocks in the gas (see Chapter 4). Also, the hinge clumps like those on the southern end of A261S are typically formed by tidal forces (Hancock et al., 2009; Smith et al., 2010), which are not expected to be particularly strong in this type of collision. Due to the high relative velocities and the direct nature of the collision, the collision timescale is fairly short in this scenario, $\sim$30 Myr. Because the bridge should be formed hydrodynamically, pre-collision stellar populations are not expected to have been displaced from the disks, so there should be no intermediate aged ($>$ 100 Myr) clusters in the bridge.

The second type of collision we consider is a flyby. Here, the galaxies move past one another without their disks overlapping, so that the interaction is almost purely tidal. Such encounters can produce strong bridges not unlike that seen in Arp 261, particularly if the encounter is prograde with respect to at least one of the galaxies and the galaxies have low inclinations (Wallin & Stuart, 1992). The bridge would contain both gas and stars from the disks, so an intermediate age or old stellar population may be present in the bridge, in addition to new star forming regions where the gas has become gravitationally unstable. The timescale for this type of encounter is much longer than that for a Taffy-like collision, $\sim$300 Myr.

The last collision scenario we consider is a hybrid of the first two in which the galaxies have only partial overlap during the collision. Such an interaction could have both splash and

tidal features and a timescale ∼100 Myr, but is otherwise difficult to distinguish from a pure flyby. A hybrid would look very much like Arp 107, viewed from an orthogonal perspective. Arp 107 is shown in *Spitzer* 8.0 μm in Figure 3.9; a dynamical model shown in an orthogonal perspective in shown in Figure 3.10.

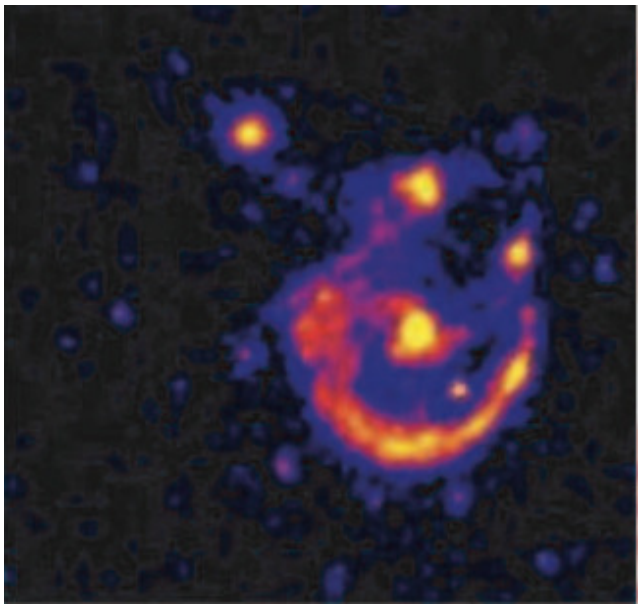

Figure 3.9 *Spitzer* 8.0 μm image of Arp 107. Arp 261 may resemble this system if it were viewed from the left or right in this figure. From Smith et al. (2005b).

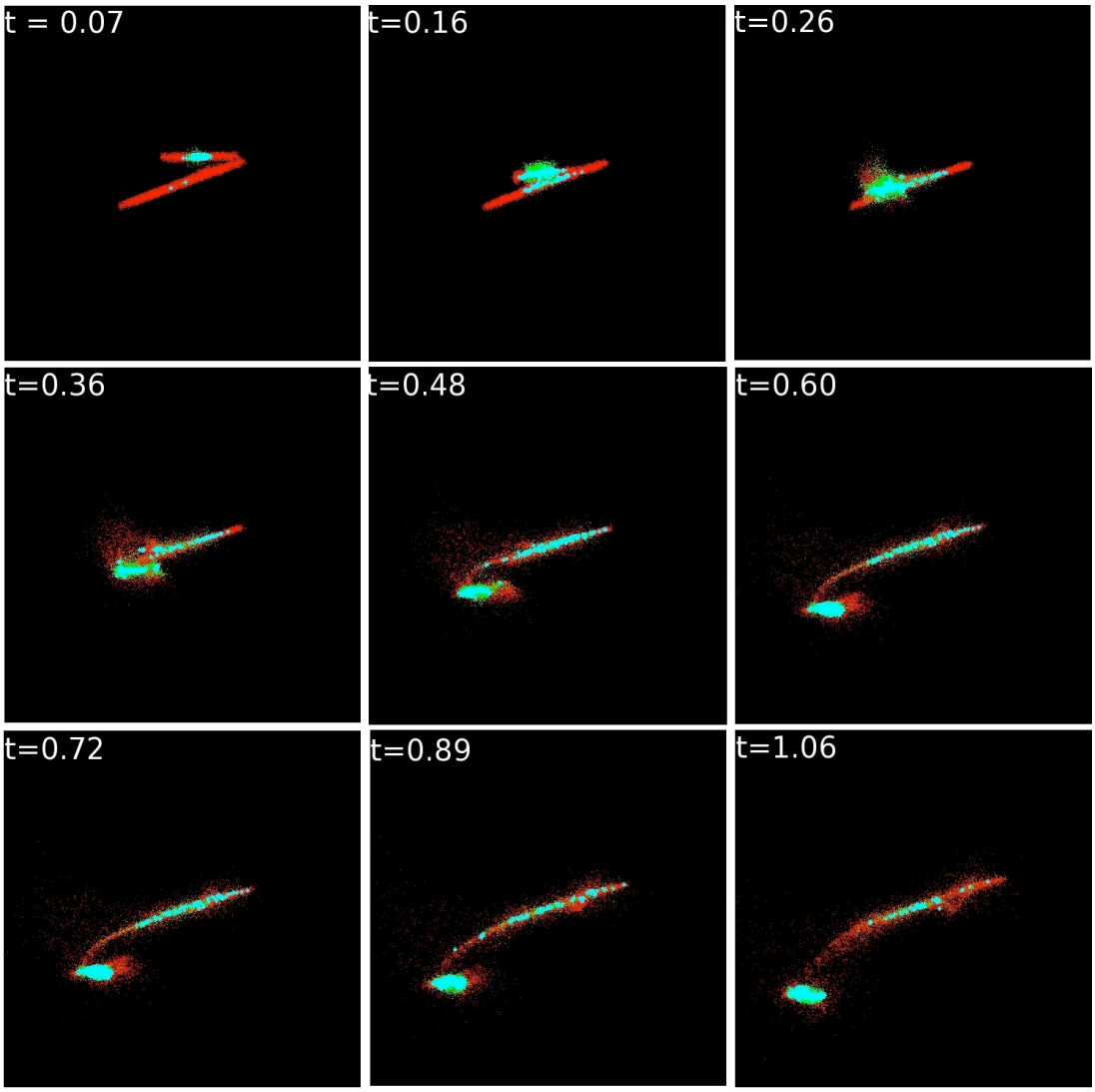

Figure 3.10 Dynamical models of Arp 107 collision, which is a hybrid of a Taffy-like collision and a flyby. Gas particles are shown in red, star particles in blue. This figure shows the model edge-on; Arp 107 is viewed face-on and would be seen from the top or bottom in this figure. The models are described in Smith et al. (2005b). If Arp 261 is similar, it would be viewed from the left or right in this figure.

3.5.2 Cluster age distribution in different regions

3.5.2.1 Full primary sample

We now consider the ages of the clusters across the system and their implications for the collision scenario. The boundaries between the components of the Arp 261 system are somewhat arbitrary (e.g., the transition from the galaxies to the northern bridge), but a broad census of the cluster populations in the features of the system is possible. The more important limiting factor is the nonuniform spatial coverage across different filters.

For purposes of distinguishing between collision scenarios, the most important clusters are those in the northern bridge. Unfortunately, the bridge has very little coverage in F300W, so only 8 of the 86 clusters are in the primary sample. The distribution of these ages based on color fitting varies considerably depending on the metallicity. The $Z = 0.004$ model indicates only 3 of the clusters have ages $\sim$20 Myr, while the $Z = 0.008$ model gives 7 at this age and the $Z = 0.020$ model estimates that all 8 of the clusters are $\sim$20 Myr old.

The Hα coverage is much better than the F300W coverage. Of the 86 bridge clusters, 82 are on frame in Hα, 61 of which are detected and have young ages irrespective of metallicity. Clusters not detected in Hα could be older, but it is also possible that they are young but not sufficiently luminous to be detected in these observations. Based on the available data, we can reasonably conclude that the cluster population in the bridge is generally quite young, but we cannot rule out the possibility of an older population.

The cluster population of the central bridge is very sparse, with only 8 clusters detected. The problem of the small population size is exacerbated by the *HST* coverage, which places only 3 clusters in the primary sample. These all have ages $\sim$20 Myr in the higher metallicity models, while 1 cluster has an age $\sim$250 Myr in the $Z = 0.004$ model. All 8 clusters are covered by Hα, with 5 detected. The cluster that was $\sim$250 Myr old in the $Z = 0.004$ model is not among those detected in Hα, so it could in fact be old provided this is the correct metallicity. The origin of this feature is not clear in the Arp 107 model, which is not surprising given how faint the structure is, but the Taffy-like model would not be expected to move older stellar populations outside of the disks, so the existence of old clusters would tend to favor the flyby

or hybrid models. However, with only one cluster that might be older than ∼20 Myr, firm conclusions are impossible in any case.

The clusters associated with the hinge on the southern end of A261S are also generally young. There are 55 clusters detected in and near the hinge clumps, 42 in the primary sample, all of which are on frame in Hα with 28 detected in Hα. Of the 18 clusters with color-based ages $>$ 100 Myr in the $Z = 0.004$ model, 10 are also detected in Hα and are thus probably young. Thus we have, for $Z = 0.004$, between 8 and 14 out of 42 clusters with ages $\sim$ 250 Myr. This would support a star formation enhancement duration more consistent with the flyby model than the hybrid. However, the $Z = 0.008$ and $Z = 0.020$ models have no clusters older than ∼20 Myr. This seems to be more in line with a Taffy-like collision, though it is possible that even with a flyby or hybrid collision this particular feature could have evolved more recently, so that the star formation was only recently triggered.

The southern tail of A261S has a total of 75 detected clusters, 49 of which had coverage in the three colors used for age determination. In the $Z = 0.004$ model, 30 have ages ∼20 Myr. Of the 19 estimated to have ages $>$ 100 Myr, 7 are detected in Hα. The Hα imaging covers 47 of the 49 clusters in the primary sample; 31 are detected. This leaves 12–16 clusters with ages ∼250 Myr, which would tend to support a flyby collision. However, like the hinge, the $Z = 0.008$ and $Z = 0.020$ models have, respectively, 1 and 0 old clusters, so we remain unable to eliminate either the flyby or hybrid scenario.

The cluster populations of the galaxies also have some implications for the collision type, in that star formation is expected to be enhanced starting at roughly the time of the collision. We detect 134 clusters in A261N, 93 in the primary sample. In the $Z = 0.004$ model, these clusters fall into two age groups, with 25 having ages $>$ 100 Myr and the rest ∼20 Myr. However, 18 of the 25 clusters for which old ages were obtained by color fitting are detected in Hα, strongly suggesting that they are in fact young. The Hα data covers 131 of the clusters, 93 of which are detected in Hα and have young ages. This gives a very wide range for the number of old clusters from 7–38. The higher metallicity models indicate much younger ages, with 1 cluster of age 480 Myr in the $Z = 0.008$ model and the rest ∼20 Myr. The $Z = 0.020$ model has no

clusters older than ∼20 Myr. Overall, the picture is much as it was in the previously discussed regions, with the possibility of an intermediate to old cluster population at low metallicity and much less evidence of such a population elsewhere.

The cluster population in A261S seems similar to that in A261N. There are a total of 83 clusters detected in the galaxy, 66 in the primary sample, all on frame in Hα with 47 detected. In the $Z = 0.004$ model, 16 have ages > 100 Myr (half of which have young Hα ages). The intermediate to old population is then 8–19 clusters. The higher metallicities again give no significant intermediate age populations.

Overall, the cluster population is almost entirely young unless $Z = 0.004$. Even in this latter case, many of the apparently older clusters are detected in Hα, strongly suggesting that the color-based age fits for these clusters are yielding erroneously high ages. It is interesting that, regardless of the metallicity, the color-based ages indicate that there are only a handful of clusters younger than 15 Myr in the entire system. The EW(Hα) ages however show a more even spread across young ages, so we cannot draw any firm conclusions about the star formation history based on this fact.

3.5.2.2 Luminosity-limited primary sample

Cutting out the clusters below the limiting luminosity (see Section 3.4.2) in the primary sample to obtain a "complete" sample, we are left with a total of 153 clusters in the Arp 261 system, only 2 of which are in the northern bridge. In the $Z = 0.008$ and $Z = 0.020$ models, there are essentially no clusters older than ∼20 Myr, so there is little to discuss regarding spatial variations in the sample.

The $Z = 0.004$ models show a broader range of ages, though many of the clusters which are apparently old based on color fitting are also detected in Hα, which makes interpretation difficult. Many of these clusters (and many of the young ones as well) have very low extinction values, many with $E(B - V) = 0$, which is certainly too low and would generally lead to an overestimate of the age. If we suppose that all of the clusters that color fitting determined to be old that were not detected in Hα are in fact old, some interesting patterns emerge. Ignoring

the northern bridge the highest percentage of old clusters is found in the hinge and southern tail. The galaxies themselves have significantly smaller fractions of old clusters.

The two galaxies should have had ongoing star formation before the interaction, so most of the old clusters in the system are expected to be found in or near the disks. One possible explanation for the lack of old clusters is that the tidal forces which may have produced the hinge and southern tail also disrupted many of the older clusters (e.g., Takahashi & Portegies Zwart, 2000; Baumgardt & Makino, 2003). A more likely explanation, alluded to above, is that the extinction estimates are not accurate. The fact that the oldest clusters tend to be found in the most disturbed parts of the system, where extinction may be highly variable, seems to support this interpretation.

3.5.3 Clump ages vs. cluster ages

For the continuous star formation models, the clumps are generally found to be much older than the clusters they contain. This is expected in the galaxies, since star formation should have been ongoing in these regions since the galaxies formed, even if the SFR has recently undergone a dramatic increase. There should then be a background of older stars which either reside in clusters that have fallen below our detection threshold due to evolutionary fading, or because the clusters have dissolved. The cluster disruption may be the result of either infant mortality or later stage disruption, due to mass dependent (e.g., Bastian et al., 2005a) or mass independent (e.g., Fall et al., 2005) disruption mechanisms. We have begun to refer to these young clusters embedded in older field star populations as "jewels in the crown."

The only clumps that have reliable ages < 200 Myr in the two higher metallicity models are B, I, J, L, and M. Clump B, along with A, is in the northern bridge.This part of the system is off frame in F300W, so the color-based age estimates for the clusters detected in these clumps are unreliable, but several clusters have EW(Hα) measurements indicating ongoing star formation. The intermediate age for B ($\sim$100 Myr) suggests some presence of older stars, and is consistent with the timescale for a hybrid collision. If the collision was similar to the Arp 107 interaction, then the northern bridge formed primary through a hydrodynamic splash, so there should be

few if any stars older than ∼100 Myr.

The star formation in clump J is probably the result of tidal forces which compressed the gas as hinge clumps H and K were pulled out from the disk. Only 2 of its 6 clusters are detected in Hα, which indicates the presence of intermediate aged clusters. The age of the clump itself ranges from 100–300 Myr depending on metallicity, and is therefore consistent with the flyby and hybrid collisions.

Clumps I, L, and M are all in A261N. I and L are the northernmost clumps in the galaxy and lie near the base of the bridge and so should have contained compressed gas at some point in the interaction, whether the bridge was splashed out of the disk or pulled out tidally. Neither clump has many clusters in the primary sample, but these are all young except at $Z = 0.004$, and even in this model the 2 clusters with intermediate ages from color fitting are both detected in Hα.

It is not clear why clump M would be atypically young, since it may be the nucleus of A261N and would thus be expected to have a significant old population.

The fraction of the light in each clump originating in detected clusters, f_c, is a useful measure of the level of clustering in each clump and filter. Note that not all clusters in any clump are detected by daofind, either because they fell below the flux threshold or had a point spread function (PSF) radius that differed significantly from the search criteria. The values of f_c in Table B.3 are therefore underestimates of the true cluster content of the clumps. These measurements show that 70–95% of the emission in the clumps is originating outside of detected clusters, supporting the idea that the clump ages are older than the cluster ages partly because of contributions from older, possibly diffuse populations.

We compare f_c in Hα and F625W, which respectively sample only the youngest stars and the more general stellar population. The number of clusters detected in Hα in the clumps is lower than the number detected in F625W, presumably because that not all of the clumps are young enough to have significant Hα emission, but since we are using the fraction of the total luminosity this should not be important. Clumps A, F, and G have $f_c(\mathrm{H}\alpha) < f_c(\mathrm{F625W})$, but some have comparable f_c values between the two filters, and in some cases the Hα emission is

significantly more clustered (clumps H, J, and M). The variability of f_c makes it difficult to draw a firm conclusion about the level of clustering at different ages.

3.5.4 *Spitzer* colors

We compare the *Spitzer* colors of the Arp 261 clumps to those of other interacting galaxies in Figures 3.11 and 3.12. The Arp 261 clumps are shown as black open circles. Clumps from Arp 24 (Cao & We, 2007), 82 (Hancock et al., 2007), 107 (Smith et al., 2005b), 285 (Smith et al., 2008), and NGC 2207/IC 2163 (Elmegreen et al., 2006) are shown as green crosses. The Arp 284 H II regions (Chapter 2) are shown as red open circles. We also show the mean colors of field stars (Whitney et al. 2004; magenta open triangle), M0III stars (Cohen, private communication; open blue square), quasars (Hatziminaoglou et al. 2005; red squares) and galactic dust (Flagey et al. 2006; blue crosses).

The [4.5]−[5.8] color typically becomes redder in regions with high SFRs (e.g. Smith et al., 2005b). The Arp 261 clumps are generally similar to the [4.5]−[5.8] colors of clumps from the other interacting systems. Clumps F, I, and L are unusually blue, suggesting that the SFR may be lower than in most comparable regions. However, their ages are not unusual. Clump E is exceptionally blue, similar to the Arp 107 nuclei. Although Arp 261 may be morphologically similar to Arp 107, the comparable [4.5]−[5.8] color in clump E is probably not significant, since E is a diffuse region outside the A261S disk. The color of clump E by itself would strongly suggest that clump E is a background elliptical galaxy; however, the *HST* data, shown in Figure 3.13, clearly resolve it into individual clusters, ruling out this possibility.

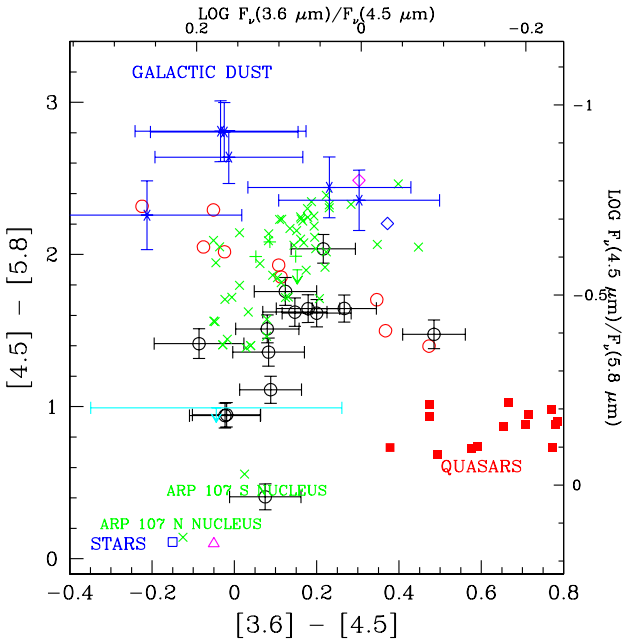

Figure 3.11 Color-color plot of *Spitzer* [4.5]−[5.8] vs. [3.6]−[4.5]. Arp 261 clumps are shown as black open circles. Also shown are the HII regions from Arp 284 (Chapter 2; red open circles) along with emission clumps from Arp 24 (Cao & We, 2007), 82 (Hancock et al., 2007), 107 (Smith et al., 2005b), 285 (Smith et al., 2008), and NGC 2207/IC 2163 (Elmegreen et al. 2006; green crosses). Shown separately are Arp 285 NGC 2856 tail clump 3 (magenta open diamond) and disc clump 1 (cyan limit), and NGC 2207/IC 2163 clump (open blue diamond). Also shown are the mean colours of field stars of Whitney et al. (2004) (magenta open triangle), M0III stars (M. Cohen 2005, private communication; open blue square), quasars (Hatziminaoglou et al. 2005; red squares), and diffuse dust in the Milky Way (Flagey et al. 2006; blue crosses).

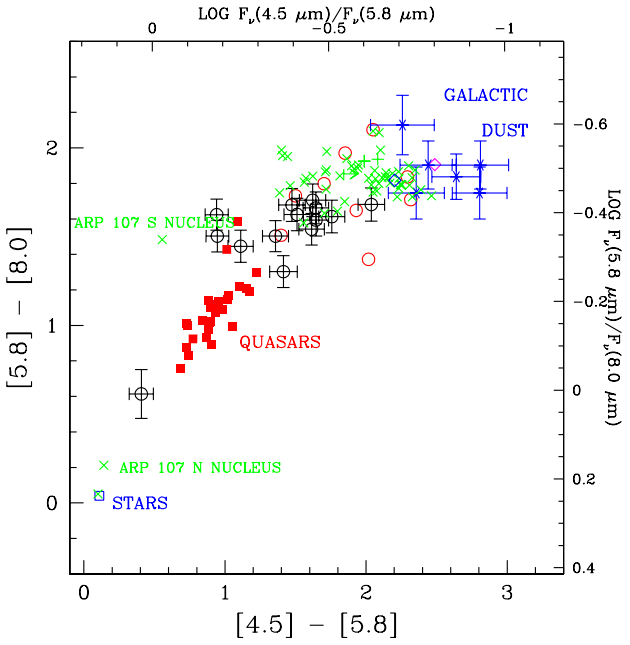

Figure 3.12 *Spitzer* [5.8]−[8.0] vs. [4.5]−[5.8]. Symbols are the same as in Figure 3.11.

It should be noted that the Arp 261 clumps were selected based on NUV emission, while most of the clumps in the other interacting galaxies were selected using mid-IR emission. The two are often similar, which was the case in Arp 284 (see Chapter 2). In Arp 261 however the difference is more significant. Clumps E and J outside the A261S disk would probably not have been selected based on the *Spitzer* data (see Figure 3.3). In A261N, the apertures for clumps N and O would have been positioned differently, as would I and L if they were selected at all. In A261S, clumps D, F, G, and K would have been placed differently; H would be either undetected or positioned differently. The same goes for clump A in the northern bridge.

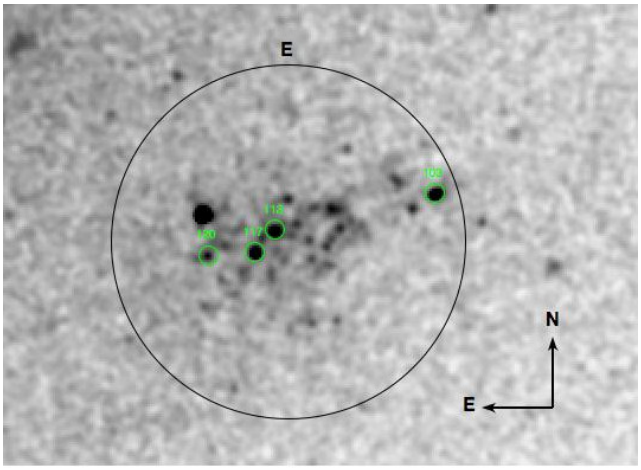

Figure 3.13 *HST* F625W image of clump E demonstrating that it consists of individual star forming regions and is not a background galaxy.

In [5.8]−[8.0], most of the Arp 261 clumps are again comparable to the clumps from other interacting systems, though again several of the bluer clumps fall outside the range typical of the other clumps. These clumps, F, I, J, and L, fall as close to the quasars as to the other clumps. Of these, only F would have been selected in the same position if the clumps were IR-selected, which may explain some of the difference.

Clump K is also approaching the quasar colors in [5.8]−[8.0], which is particularly notable since its [3.6]−[4.5] color was also closer than normal to the quasars. It is possible that one of the "clusters" in clump K is in fact a background quasar. Clump K is shown in Figure 3.14.

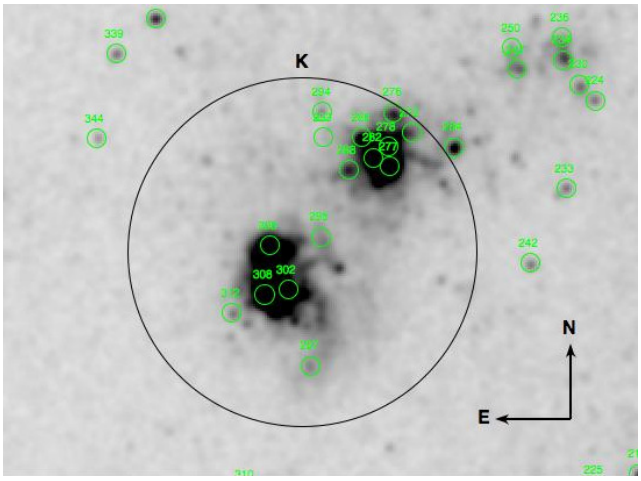

Figure 3.14 *HST* F625W image of clump K. It is possible that one of the clusters is a background quasar, particularly in the two knots of clusters. The field of view is $13.7'' \times 10.2''$.

3.6 Summary & Conclusions

We have examined the star cluster population of the Arp 261 system. We detected 447 cluster candidates. The luminosity and mass distributions of these clusters have slopes ≈ -2, in agreement with several other studies.

We obtained reliable age estimates for 267 clusters by fitting broadband colors to STARBURST99 evolutionary synthesis models. The clusters were generally found to be young, with ages $\sim$20 Myr. However, the $Z = 0.004$ models indicate a significant number of clusters $\sim$250 Myr. The interpretation is complicated by the fact that many of these apparently older clusters are also detected in Hα, implying that they are young.

Large clumps of clusters, which were fit with *GALEX* UV and *Spitzer* IR as well as *HST* optical colors, generally appear to be older than the clusters they contain, assuming continuous star formation over the entire history of the clump. This star formation history is an oversimplification, since the clusters that were the primary focus of this study formed instantaneously and thus represents a limiting case. However, most of the emission in the clumps does not originate in the detected sample clusters, so the older field population is contributing significantly, and may include emission from clusters that have already dissolved.

The unknown interaction dynamics of Arp 261 could potentially be constrained by cluster ages. Unfortunately, the most telling region in the system, the northern bridge, lacks coverage in the crucial F300W band, which severely limits our results. Nevertheless, the available ages, along with some of the morphological features of the system, suggest that the Arp 261 collision is not entirely Taffy-like, with at most partial disk overlap during the collision and a flyby with no disk overlap also possible.

Future work with optical spectra, which have already been obtained, will reveal the metallicity of the galaxies and greatly improve our results. Many additional observations would also be useful. *HST* data giving U-band coverage of the northern bridge would be extremely helpful. H I velocity data would also be helpful, in that it would allow for detailed dynamical modeling that would reveal more about the history of the interaction and expected star formation history.

CHAPTER 4. Detection of Powerful Mid-IR H_2 Emission in the Bridge Between the Taffy Galaxies

A paper submitted to *The Astrophysical Journal*

B. W. Peterson, P. N. Appleton, G. Helou, T. H. Jarrett, M. E. Cluver, P. Ogle, P. Guillard, C. Struck, F. Boulanger

4.1 Abstract

We report the detection of strong, resolved emission from warm H_2 in the Taffy galaxies. Relative to the continuum and faint PAH emission, the H_2 emission is the strongest in the connecting bridge, approaching $L(H_2)/L(\mathrm{PAH7.7}\mu\mathrm{m}) = 0.1$ between the two galaxies, where the purely rotational lines of H_2 dominate the mid-infrared spectrum in a way very reminiscent of the group-wide shock in the strongly interacting group Stephan's Quintet. Although there is variation from point to point in the bridge, the surface luminosity in the 0–0 S(0) and 0–0 S(1) lines is, on average, twice that observed in Stephan's Quintet, and the mass of warm H_2 is likely to be $> 9 \times 10^8 M_\odot$ if the gas fills the whole bridge region. We use excitation diagrams to characterize the warm molecular gas, finding an average surface mass of $\sim$5 $M_\odot$ pc^{-2} and typical excitation temperatures of 150–175 K. H_2 emission is also seen in the galaxy disks, although there the emission is more consistent with that seen in normal star forming galaxies. We investigate several possible heating mechanisms for the bridge gas, but favor the conversion of mechanical energy from the head-on collision via turbulence and shocks as the main heating source. Since the cooling time for the warm H_2 is short, shocks must be permeating the bridge region in order to continue heating the molecular hydrogen. We also find a larger shocked gas mass in the Taffy bridge over a smaller projected area compared with the Stephan's Quintet

intergroup shock, which may be a result of the larger available reservoir of gas through the head-on collision of two gas-rich systems.

4.2 Introduction

The *Spitzer Space Telescope* has led to tremendous advances in the study of galaxies and their interstellar media. Among the most notable discoveries was the detection by Appleton et al. (2006) of powerful emission from purely rotational H_2 lines in the group-wide shock of the strongly interacting group Stephan's Quintet (SQ). Spectral mapping reveals that the emission is distributed along the whole shock and outpowers the X-ray by a factor ≥ 3, indicating that these lines are probably a dominant cooling process in the post-shock region (Cluver et al., 2010).

Powerful H_2 emission has also been detected in many other environments, for example in luminous infrared galaxies (Lutz et al., 2003), radio galaxies (Ogle et al., 2007, 2010), AGNs (Roussel et al., 2007), and cool cluster core galaxies (Egami et al., 2006; Donahue et al., 2011). In another case powerful H_2 is detected in the apparent wake of a bow-shock in the cluster Abell 3627 (Sivanandam et al., 2009). The class of strong molecular hydrogen emission galaxies (called MOHEGs; Ogle et al. 2007) is defined by the strength of the H_2 0–0 S(0)–S(3) lines relative to that of polycyclic aromatic hydrocarbons (PAHs), with MOHEGs having $L(H_2)/L(\mathrm{PAH7.7}\mu\mathrm{m}) > 0.04$ (Ogle et al., 2010). The mechanism that powers the H_2 emission in MOHEGS is not fully understood, in part because the emission regions are usually unresolved, but in the case of the radio galaxies is likely to be jet-driven shocks (Ogle et al., 2010; Nesvadba et al., 2010). The SQ shock is a notable exception because it is well resolved spatially, and associated with a well-studied intergalactic shock within a compact group.

Here we report the detection of strong, resolved H_2 emission in the bridge between the interacting galaxies UGC 12914/5, also known as the "Taffy" galaxies because of the extended radio emission stretched between the two disks (Condon et al., 1993). The emission closely resembles that observed in SQ, with the H_2 lines featuring prominently in the mid-IR spectrum.

The Taffy system is believed to be the result of a nearly head-on collision between two disk

galaxies. The galaxies, UGC 12914 and 12915, have heliocentric velocities of 4371 ± 8 and 4336 ± 7 km s^{-1} respectively, and we assume a distance of 60 Mpc based on a Hubble constant of 72 km s^{-1} Mpc^{-1}. The disks are ~ 12 kpc apart and are believed to be separating mainly in the plane of the sky at a velocity of 450 km s^{-1} (Condon et al., 1993). This presumption is based on assumed masses and a parabolic orbit, and may be an upper limit since it does not take into account dynamical friction resulting from the overlapping dark matter halos. Among the notable features of the system is the gas-rich bridge, which contains about 25% of the H I gas in the system (Condon et al., 1993). The bridge is also host to a significant amount of molecular gas (Smith & Struck, 2001; Braine et al., 2003; Gao et al., 2003) and cold dust (Zhu et al., 2007). A warm dust component is apparently heated by UV radiation from the disks (Jarrett et al., 1999). Hα images reveal that the bridge has little star formation outside of a single large H II region (Bushouse & Werner, 1990).

When two galaxy disks collide nearly face-on at high velocity, we expect widespread collisions between diffuse atomic clouds, which have a large covering factor in galaxy disks (Leroy et al., 2008; Sánchez et al., 2010). While the Taffy disks as a whole collide face-on at $v \approx 450$ km s^{-1} (Condon et al., 1993), the clouds rotating at somewhat smaller velocities within the disks will collide with a range of angles of attack, and so lose various amounts of orbital angular momentum, as well as momentum transverse to the orbits. Dense molecular clouds are rare outside the centers of galaxy disks, so collisions between them will be rare (Leroy et al., 2008; Roman-Duval et al., 2010). In the collision, such clouds in one galaxy will have to ram their way through the more diffuse atomic gas of the second. However, given the much smaller column density of the latter compared to the former the effect will be small. If the molecular clouds are coupled to a larger region via magnetic fields the drag may be somewhat enhanced.

The net result of these processes is that the atomic gas will be splashed out into the bridge with a range of transverse velocities with values extending from that of one galaxy to that of the other (Struck, 1997). Some of this gas will fall promptly back into both disks, and some will be stretched between them. Large molecular clouds will tend to stay close to their parent

disks, helping us to understand the paucity of star formation in the bridge. The gas splashed into the bridge will also have a broad range of angular momenta, resulting in continuing cloud collisions, and the resulting shocks and turbulence, as the bridge develops. This picture is based on the observed structure of the interstellar medium in nearby galaxies, and general theoretical arguments.

4.3 Observations and Data Reduction

4.3.1 IRS spectra

We obtained spectra of the UGC 12914/5 system from the *Spitzer* public archives (Program ID: 21, PI: J. Houck). The observations were made with the Infrared Spectrograph (IRS; Houck et al. 2004) on board the *Spitzer Space Telescope* (Werner et al., 2004) on 2005 July 8 and 10 using the Short-Low (SL; 5.2–14.5 μm), Long-Low (LL; 14.0–28.0 μm), Short-High (SH; 9.9–19.6 μm), and Long-High (LH; 18.7–37.2 μm) modules. The positions of the slits for all four modules are shown in Figure 4.1. Although the original design of the astronomical observation requests (AORs) was to target the nuclei and some selected regions of the galaxies (not specifically the bridge) we were able to exploit the partially overlapping nature of the slits to make sparse maps of the region.

The spectra were initially processed by *Spitzer* Science Center (SSC) pipeline version S18.7.0. The starting point of our analysis were the Basic Calibrated Data (BCD) frames from the science pipeline. The BCD frames are a high-level calibrated data product which represent slope-fitted data values in electron s^{-1} derived from corrected data. Corrections include saturation, non-linearity, detector droop and stray-light corrections. BCD frames associated with each target position were coadded and background subtracted using dedicated off observations (in the SL and LL modules these were combined with spectral orders far from the galaxies) after removal of obvious glitches and other artifacts using custom software that allowed for interpolation via visual inspection of each dataset. Rogue pixels, especially common in the LH module (due to cosmic-ray activation of pixels), were removed by blinking the two nods against each other to determine which pixels were definitive artifacts and which were

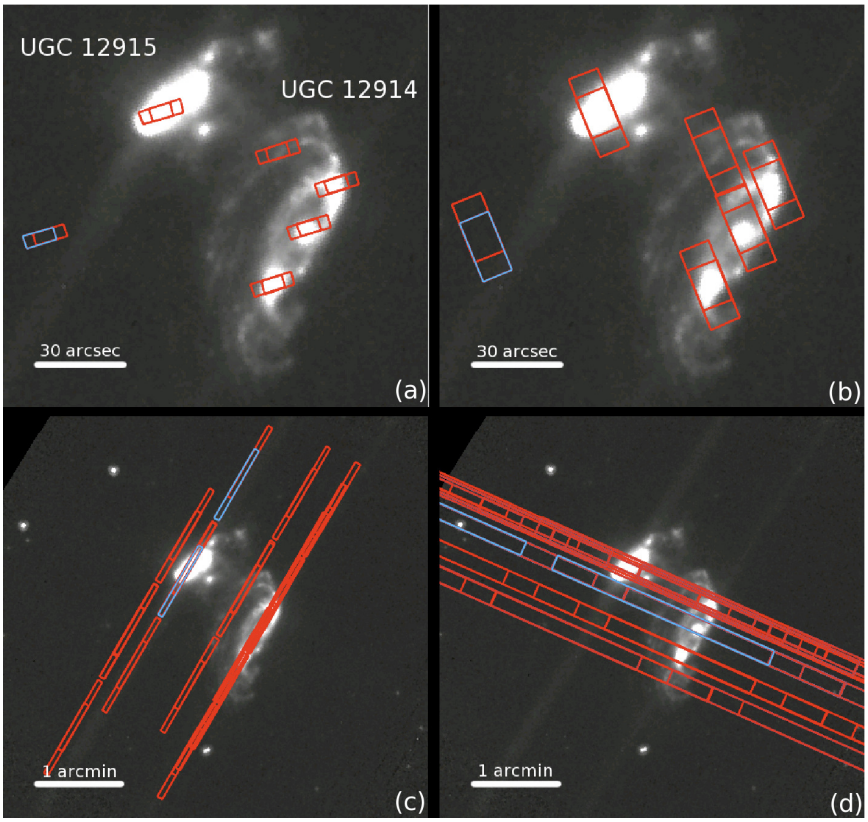

Figure 4.1 IRS SH (a), LH (b), SL (c), and LL (d) slit positions overlaid on IRAC 8.0 μm image. Each module was nodded between two positions at each target, with the target at the 1/3 and 2/3 positions in the slit. A single nod position for each module is shown in blue for clarity. For the SL and LL modules, both orders are shown. North is up and east to the left.

emission lines, which tend to move from one nod to the other.

Spectra were obtained at two nod positions for each target, with the target placed at the 1/3 and 2/3 positions in the slit. The CUBISM software (Smith et al., 2007a) was used to construct partial spectral maps along the LL slits, allowing extractions from numerous positions within the system, labeled A–U as shown in Figure 4.2. The extraction regions had angular size $10.15'' \times 10.15''$. The SL slits are oriented orthogonally and partially overlap in regions C and J. In both cases, the SL spectra covered about 1/3 of the area of the LL, and were initially scaled up to compensate for this difference.

The high-resolution spectra were extracted with the SSC software SPICE, using the point

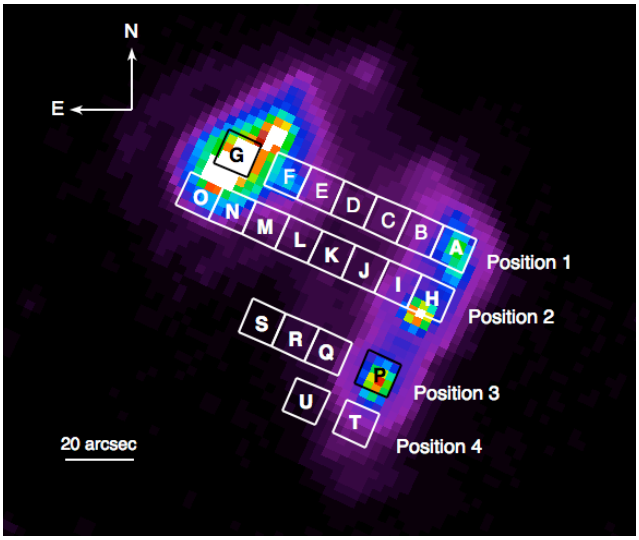

Figure 4.2 Spectral extraction regions A–U overlaid on MIPS 24 μm. The extraction regions are $10.15'' \times 10.15''$. Each row of extraction regions corresponds to one of the LL slit positions, which are labeled.

source calibration for the galaxies and extended source calibration for the bridge. The choice of calibrations involves some uncertainty, since the targets are neither fully unresolved point sources nor perfectly uniform extended sources. In extreme cases, differences between these two assumptions can lead to a maximum line flux uncertainty of $\sim$40%, with the point source calibration giving systematically higher fluxes.

Line fluxes in each extraction region were measured using the SMART software package (Higdon et al., 2004). In regions C and J, the partial overlap with the SL module expanded the wavelength coverage. In these cases we measured the line fluxes using both SMART and PAHFIT (Smith et al., 2007b). PAHFIT fits known lines, bands and dust contiuua to a stitched version of the SL and LL spectra. Similar line fluxes were obtained, and results from both methods are presented in Table C.1. We note a slight positive offset in the measured line fluxes at J by PAHFIT relative to SMART (but not for region C), but the differences are only at the 2σ level. The effect is more pronounced in the 28 μm line. As we point out in the footnote to Table C.1, the LL1 spectrum from which this was derived showed some inconsistency in its continuum level compared with LL2, and so this line is uncertain no matter how it is measured.

The high resolution line fluxes were measured by single Gaussian fitting using SMART. The SH slit covers a smaller area than the LH slit, so the SH spectra were rescaled at each nod position so that the continuum matched between the two modules. The scaling factors were similar for both nods. The line fluxes and mean of the scaling factors for the two nods are presented in Table C.1.

4.3.2 IRAC and MIPS images

Images of the system obtained with the Infrared Array Camera (IRAC; Fazio et al. 2004) and Multiband Imaging Photometer for *Spitzer* (MIPS; Rieke et al. 2004) were available from the *Spitzer* public archives (Program ID: 21, PI: J. Houck). The data were processed by SSC pipeline version S18.7.0, and were of sufficient quality that further processing was not required.

Photometric measurements were made in each of the LL bridge extraction regions using square apertures with the IRAF[1] task *polyphot*. The CUBISM spectral extractions use extended source calibration, so the photometric measurements were not aperture-corrected. The IRAC 3.6, 4.5, 5.8, and 8.0 μ images were Gaussian-convolved to match the resolution of the MIPS 24 μm image, which is comparable to the resolution at H_2 S(0) 28.22 μm.

For comparison with the high resolution spectra, we also measured the images using a set of boxes matched to each of the LH nod positions.

4.4 Results

4.4.1 Spectra

The high resolution spectra of the nuclei and the bridge are shown in Figure 4.3. The strength of the H_2 lines is very striking, especially in the bridge, where the S(0) and S(1) lines outpower all of the other lines except [SiII]34.82 μm. The S(1) line is similarly dominant in UGC 12914. The H_2 line fluxes are presented at the top of Table C.1, while the fine structure

[1]IRAF is distributed by the National Optical Astronomy Observatories, which are operated by the Association of Universities for Research in Astronomy, Inc., under cooperative agreement with the National Science Foundation.

line fluxes are shown in Table C.2. We will further quantify the strength of the H_2 emission in Section 4.5.1.

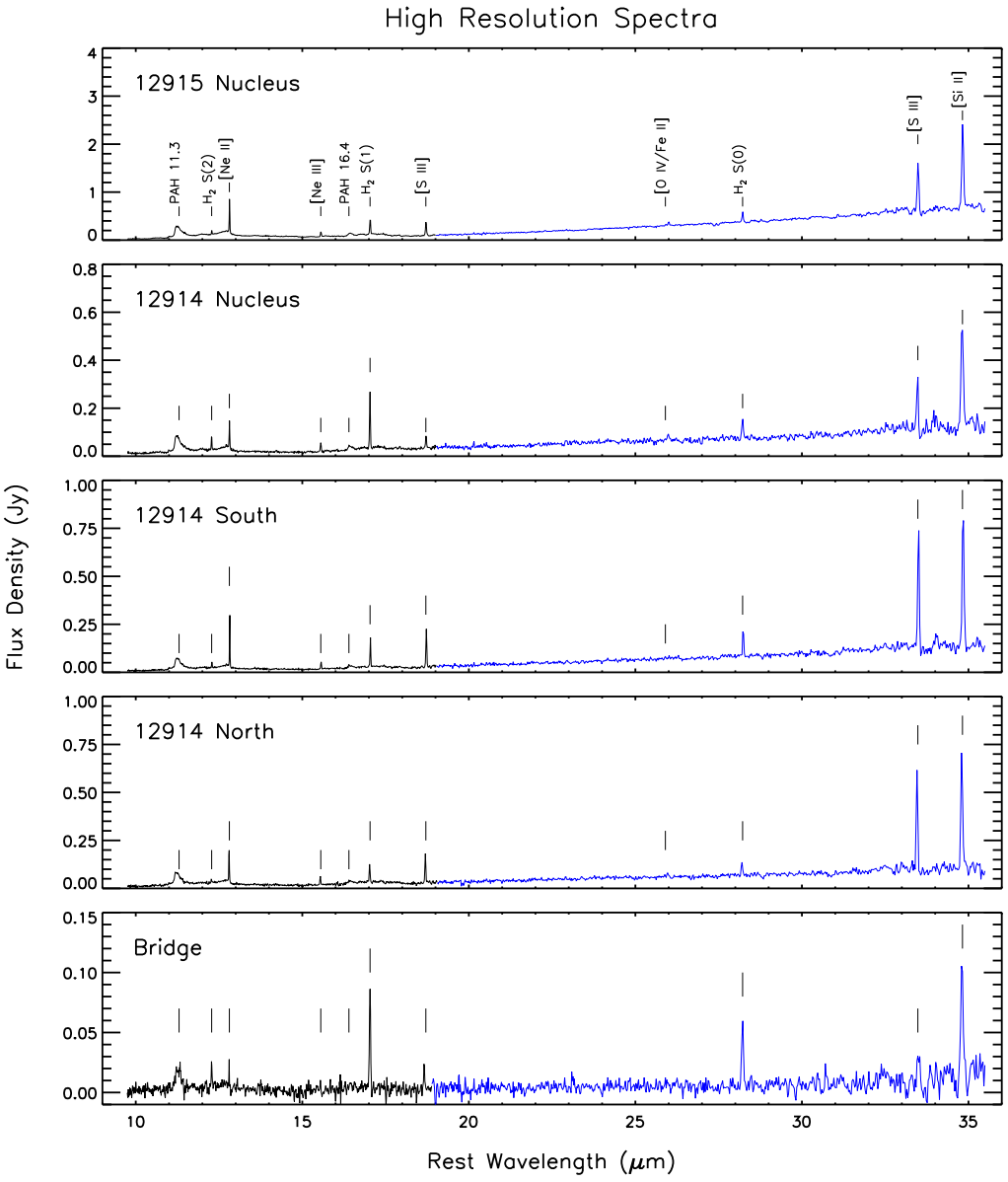

Figure 4.3 High resolution spectra from the IRS SH (black) and LH (blue) modules. The SH spectra were scaled up to match the LH continua. The mean scaling factors for the two nods, along with the measured line fluxes, are presented in Table C.1.

The low resolution spectra show that the emission in the bridge is not confined to the position of the high resolution slits, which also include the UGC 12914 ring. The H_2 S(1) line is clearly detected in most of the bridge regions, and marginally detected in the rest with the exceptions of regions S and T, which lie to the south of both galaxies. Spectra from these regions are shown in Figures 4.4 and 4.5.

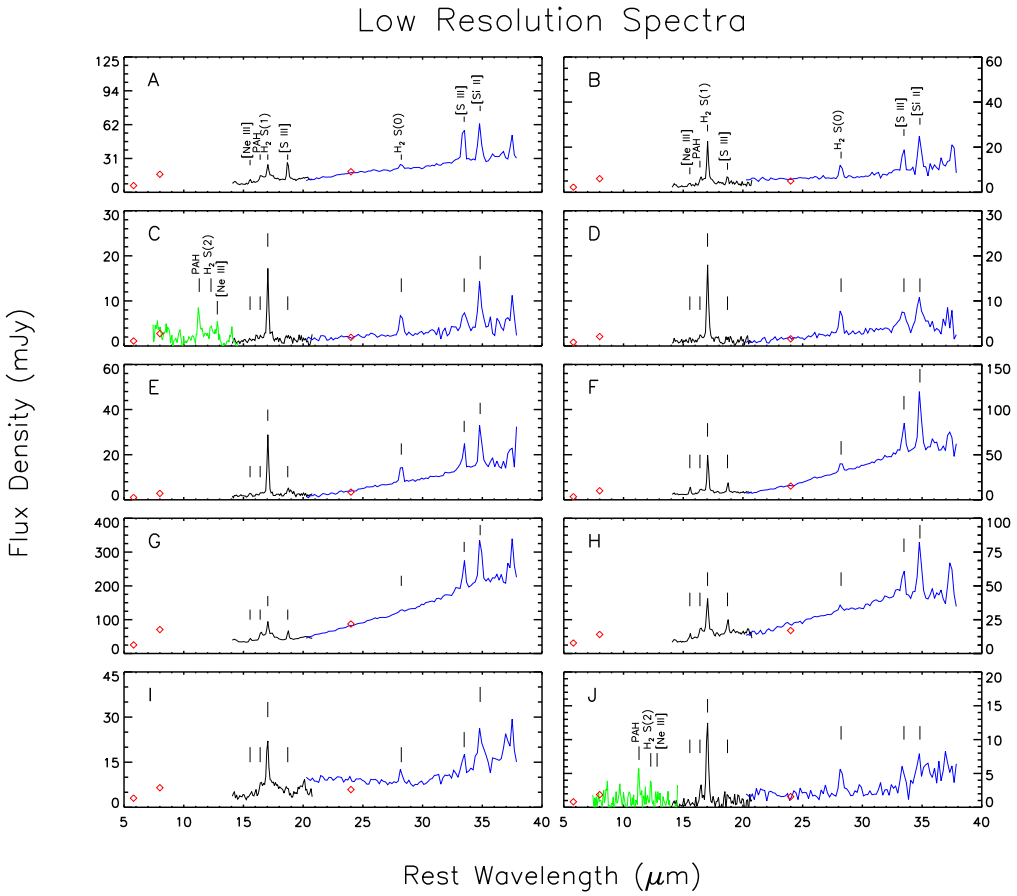

Figure 4.4 Low resolution spectra from IRS LL1 (blue), LL2 (black), SL1 (green, where available) modules extracted from bridge regions A–J. The SL1 data have been scaled up to the same aperture size as the LL1 assuming a uniform distribution over the aperture. Photometric data points from IRAC and MIPS are shown as red diamonds.

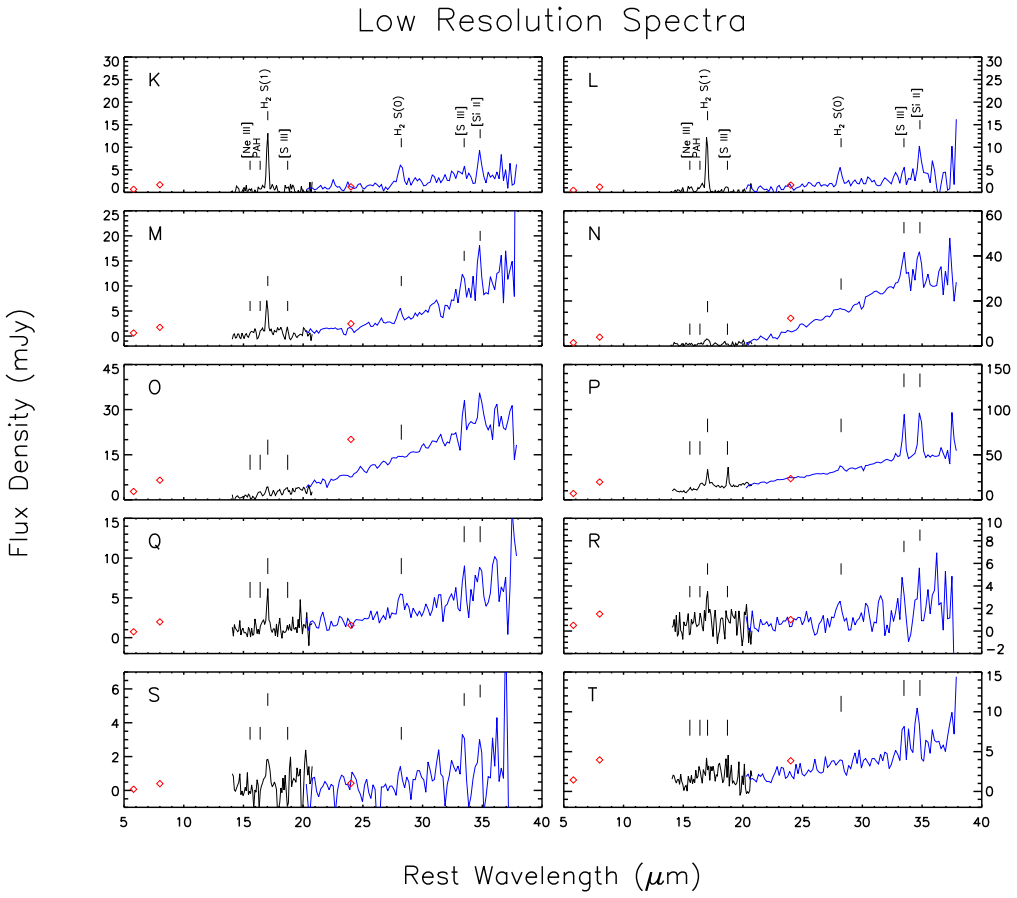

Figure 4.5 Low resolution spectra from IRS low resolution extraction regions K–T. Symbols are as in Figure 4.4.

4.4.2 H_2 distribution

The low resolution spectra contain information on the spatial distribution of the emission. In Figure 4.6 we show cross sections of the LL1 and LL2 slits which cut through the two galaxies and the bridge at positions indicated in Figure 4.2. In position 2, the slits are just south of UGC 12915. The locations of the galaxies at each position are shown in the top panels. No significant emission was detected as position 4, so it is not shown.

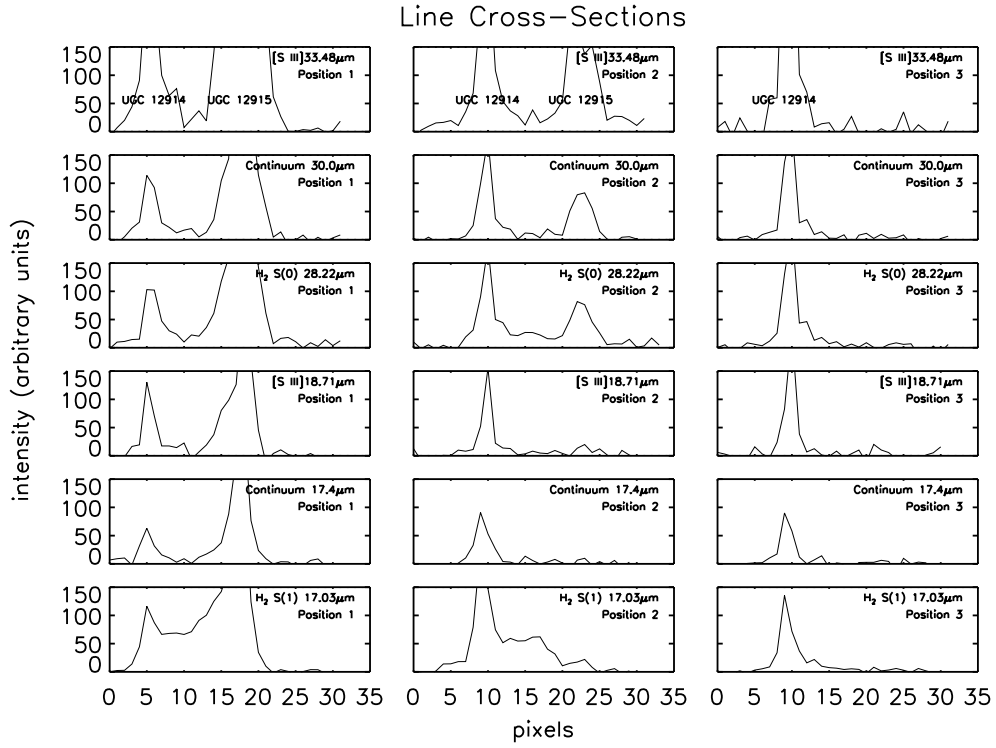

Figure 4.6 Cross sections through the LL1 and LL2 slits at the wavelengths of [S III]33.48μm, 30 μm continuum, H_2 S(0) 28.22 μm, [S III]18.71μm, 17.4 μm continuum, and H_2 S(1) 17.03 μm. The two continuum profiles give a sense of the the galaxy widths at wavelengths near the lines of interest. The positions are indicated in Figure 4.2. In position 2, the slit is slightly south of UGC 12915. These plots, particularly of the H_2 S(1) line, demonstrate that H_2 emission is extended across the full width of the Taffy bridge.

The right panels of Figure 4.6 show that the emission is much weaker outside of UGC 12914

at position 3 than at position 2 (see also Figures 4.4 and 4.5), indicating that either the gas density or temperature drops significantly south of a line connecting the nuclei, though the data gap between positions 2 and 3 makes it unclear how rapidly this change occurs.

The low emission levels east of the galaxy at position 3 give some sense of the contamination level in the bridge due to the galaxies, which appears to be minimal. This is confirmed by the continuum, which is shown at wavelengths of 30 μm and 17.4 μm to indicate the spatial extent of the emission at wavelengths near the emission lines of interest. [§III]33.48μm emission is concentrated in the galaxies, with little originating in the bridge. The H_2 S(0) line shows more emission in the bridge compared to the galaxies, particularly along position 2. The H_2 S(1) line is even stronger in the bridge compared to the galaxies, and actually drops significantly just south of UGC 12915.

To provide the reader with a better visualization of the results we also provide a map for both the S(0) and S(1) data superimposed on the IRAC 8 μm greyscale image of the Taffy. Although the Taffy system was not fully mapped, sufficient long-slit low-res spectra were made to allow the construction of sparse LL spectral maps using CUBISM. Figure 4.7 shows both the 20 cm radio continuum map (Condon et al., 1993) and a visualization of the 0–0 S(0) and S(1) maps. Although these sparse maps must not be over-interpreted, it is apparent that the H_2 emission is highly extended between the galaxies, into the bridge region. This is quite similar to the distribution of radio continuum from the bridge. The results show that extended H_2 emission is present in the bridge region, and has many similarities with the extended emission seen in the intergalactic shock feature in Stephan's Quintet (Appleton et al., 2006; Cluver et al., 2010).

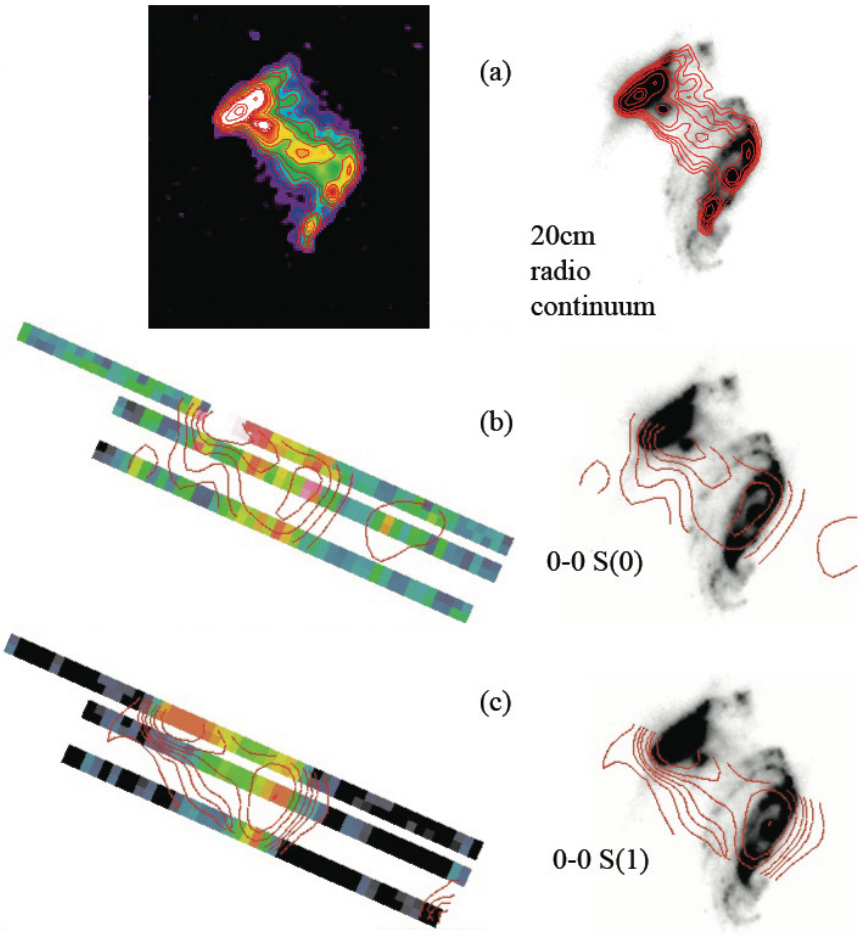

Figure 4.7 (a) Radio contours from Condon et al. (1993), overlaid on IRAC 8.0 μm image. (b) Sparse spectral map of H_2 0–0 S(0) and (b) S(1) lines constructed from IRS LL data.

4.4.3 Excitation diagram and H_2 mass surface densities

Although we do not have full spectral coverage of the whole bridge, we can explore the variation of H_2 properties as a function of position in the bridge where we have useful data. These extraction regions are restricted mainly to the LL module of the IRS, and so cover the 0–0 S(0) and S(1) lines. In two regions we have good overlap of the SL module with the same spatial region and for these we were able to detect the S(2) and S(3) lines at 12.3 and 9.66 μm. These measurements are sufficient to allow us to make a preliminary exploration of the excitation properties of the warm H_2 across the bridge, subject to several constraints and assumptions discussed later.

We have constructed H_2 excitation diagrams for the regions A–U as defined in Figure 2. These diagrams plot the column density ($N_{\rm u}$) of H_2 in the upper level of each transition, normalized by its statistical weight, versus the upper level energy ($E_{\rm u}$; e.g., Rigopoulou et al., 2002), which we derived from the measured fluxes assuming local thermodynamic equilibrium (LTE) for each position observed. Since most of the excitation diagrams consist of two points only, corresponding to the 0–0 S(0) and S(1) lines, we do not show them here, but rather present in Table C.3 the results for a single-temperature fit through the two points. These provide a baseline measurement, and allow us to explore how the ratio of the S(0) and S(1) lines might vary as a function of position in the bridge. We will show later, with appropriate assumptions, other extractions which include the detection of the 0–0 S(2) and S(3) and lines. However, for the moment we restrict the discussion to the S(0) and S(1) lines only. For regions N, O, and S only an upper limit was obtained for the S(0) line and so no temperature was derived, and for region U, no H_2 lines were detected.

From this analysis (see Table C.3), most of the regions in the bridge have the same temperature (slope in the excitation diagram) in the range 157–175 K, with only two regions Q and R, having lower temperatures of 130–133 K. The nuclei of both galaxies (regions G and H) show a higher temperature–especially the center of UGC 12914, with a H_2 temperature of 195$\pm$12 K, some 30 K warmer than the average bridge region. The warm H_2 surface density derived from these measurements (also given in Table C.3) range from 10 $M_\odot$ pc^{-2} at position F (containing

a star forming knot), to the lowest value of 2.4 $M_\odot$ pc^{-2} at region P. The mid-bridge regions D, K, and R have similar H_2 surface densities of 5–6.6 $M_\odot$ pc^{-2}. Excluding the regions obviously on the disk of the galaxies (A, G, H, P, and T), and region F (which contains the star forming knot) the average and median value of the surface density over regions between the galaxies is 5.0 ± 1.6 and 5.5 $M_\odot$ pc^{-2} respectively. Taking these values as representative of the whole bridge region we obtain a total H_2 mass $\sim 9 \times 10^8$ $M_\odot$, assuming a bridge area of 170 kpc^2.

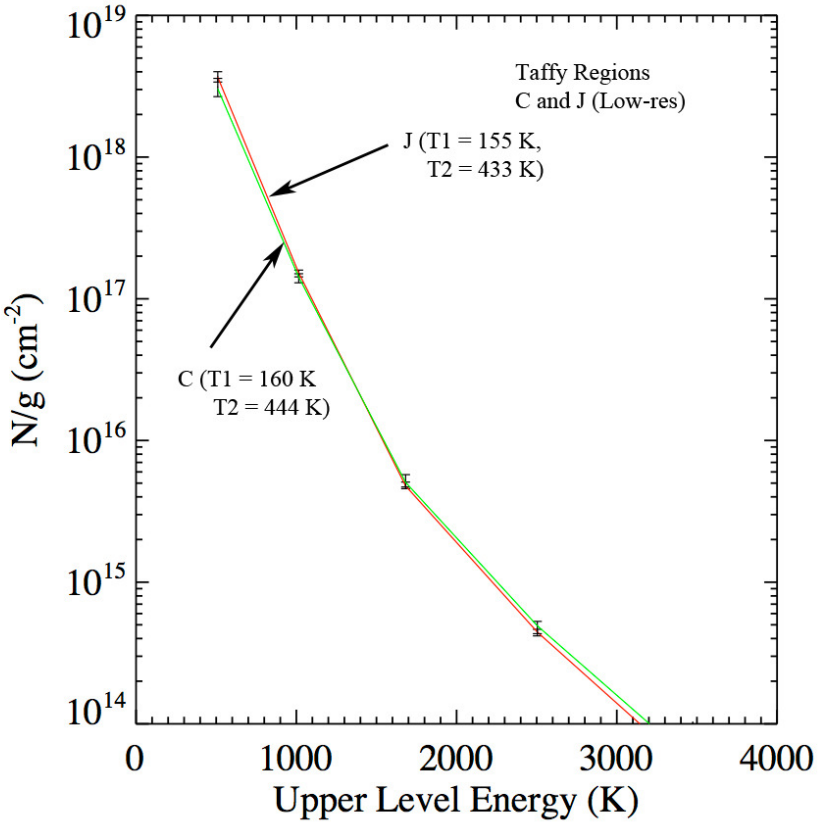

Figure 4.8 Excitation diagrams with multi-temperature fits of low resolution regions C (green) and J (red). The fit parameters are shown in Table C.3.

There are several simplifying assumptions we have made in estimating the H_2 surface density from these data. Firstly we have assumed a thermalized equilibrium value for the ortho-to-para ratio. For temperatures above 300 K, this ratio is 3, but for temperatures in the range 130–180 K this value varies from 2.3–2.8 respectively (see Equation 4 of **?**). Under

most circumstances we might expect the lower-J transitions to be in equilibrium. Normally, the ortho-to-para ratio would be investigated by looking for systematic differences in the odd and even transitions in the excitation diagram. However, because we have so few points (in most cases only two) we must simply assume equilibrium values. This obviously introduces an unknown uncertainty in the final derived properties of the gas. Deviations from LTE would lead to uncertainties in the assumed excitation temperature of the gas and thus the final total column densities. In regions C and J where 4 lines are detected (discussed below) we do not see any obvious deviations in the odd and even values for N/g versus upper-level energy, but we cannot be sure for all points. For Stephan's Quintet, where many more transitions were detected, and which seems to have strong similarities with our current data, we find no obvious deviations from LTE (see Cluver et al. 2010).

A second assumption is that the 0–0 S(0) and S(1) transitions can be fitted by a single temperature component. Excitation diagrams for H_2 observations in Stephan's Quintet (Appleton et al., 2006; Cluver et al., 2010) and Arp 143 (Beirão et al., 2009), for gas in which shocks are suspected, are usually fitted by more than one temperature component. To explore this assumption we use the two regions (C and J) where the low-res spectra overlapped, and the high-res data in the bridge to investigate how this assumption will affect the results. For C and J, we present in Table C.3 the resultant fit through the data for the four lines. We find that in addition to a cool component, a warmer component ($\sim$430–440 K) is needed to explain the S(2) and S(3) measurements. The fits for these regions are shown in Figure 4.8. However, the effect on the temperature of the coolest component (which dominates the mass surface density) is quite small. For the high-res spectrum which falls somewhere between region B and C in Figure 4.2, we also confirm that a higher temperature component is consistent with these data (although in this case, because of the restricted wavelength coverage, only three lines are used).

For the hi-res data we derive a two-temperature fit of $T_1 = 102$ K for the coolest component, and $T_2 = 310$ K for the warmer one. However, these results are less reliable than those for the low-res module where four lines are detected. With only three observed points there

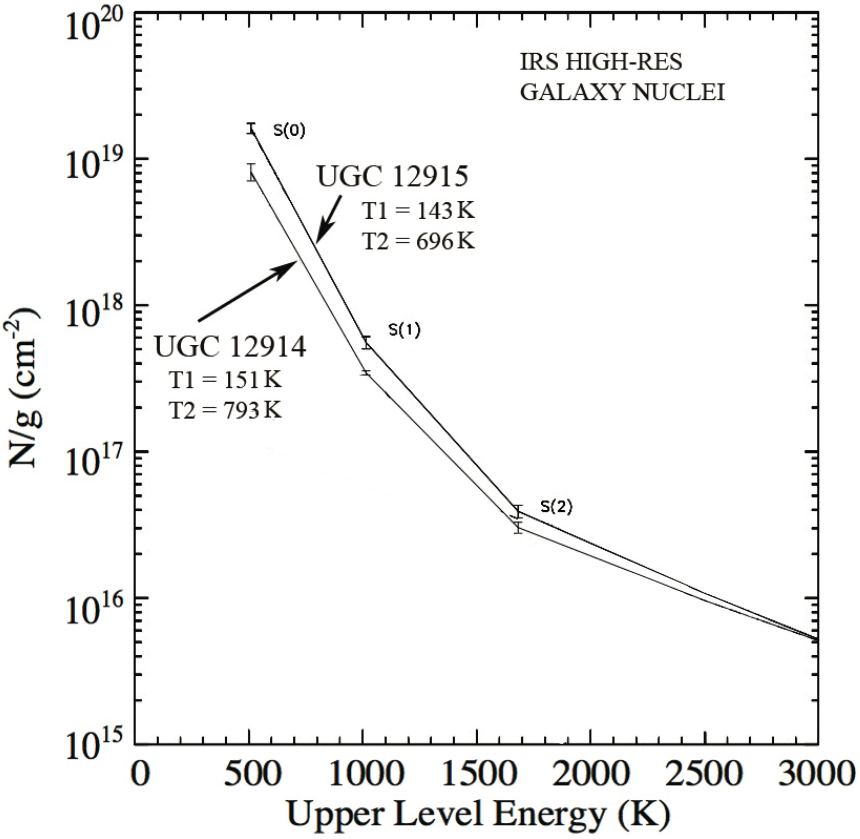

Figure 4.9 Excitation diagrams with multi-temperature fits of high resolution nuclei. The fit parameters are shown in Table C.3.

is significant degeneracy between the temperature and the column density, and so the results should be taken as very approximate and poorly constrained. Adopting the above temperatures, the column density in the cooler component (15 $M_{\odot}$ pc^{-2}) would be 2.5 times the value derived from the low-res data, and are probably unrealistic. We consider them as strict upper limits only.

We also tabulate the measured H_2 line fluxes for the 0–0 S(0)–S(2) lines for the nucleus and outer disk positions of UGC 12914, and the UGC 12915 nucleus as measured from the hi-res spectra. The derived H_2 properties for these systems are also given in Table C.3. Figure 4.9 shows the fits to the excitation diagrams for the two nuclei. In both systems it was necessary to fit a two-temperature model to the points. The warmer component in these cases is warmer

than in the case for the bridge, perhaps indicating an increased excitation from star formation. This is consistent with the view, presented in the next section, that the excitation mechanism for the H_2 changes as one proceeds from the galaxy disks to the mid-bridge, transitioning from PDR heating to likely shock excitation.

4.5 Discussion

4.5.1 H_2 heating sources

4.5.1.1 UV heating

To quantify the strength of the H_2 emission, we compare the total flux in the H_2 0–0 S(0) and S(1) lines with the 7.7 μm PAH line. The PAH7.7μm strength is estimated using the method of Helou et al. (2004), in which the flux from the starlight-dominated 3.6 μm band, scaled by a factor 0.232, is subtracted from the flux in the 8.0 μm band. Following Ogle et al. (2010), we plot the luminosity ratio $L(H_2)/L(\mathrm{PAH7.7}\mu\mathrm{m})$ against the 24 μm luminosity νL_ν, for both the low and high resolution extraction regions in Figure 4.10. The 24 μm luminosity is determined from the MIPS measurements for all of the data points, except for the high-res apertures. For the high-res apertures associated with the galaxies, the MIPS measurements are very sensitive to the exact centering of the extraction box, and so we self-consistently used the average flux over the range 22.5–25.0 μm from the spectrum to form the 24 μm continuum. This also ensures that any bias introduced by assuming the lines come from a point source rather than an extended source extraction do not somehow influence the results since the slit correction factor for point sources would disappear in the ratio. In addition to the Taffy regions, we show star forming galaxies, LINERS, and Seyferts from the SINGS sample (Roussel et al., 2007). We also show the SQ shock sub-region (Cluver et al., 2010) and Arp 143 knot G, which had the highest $L(H_2)/L(\mathrm{PAH7.7}\mu\mathrm{m})$ ratio of any part of the Arp 143 system (Beirão et al., 2009). $F(\mathrm{PAH7.7}\mu\mathrm{m})$ has been determined in the same way for all data points.

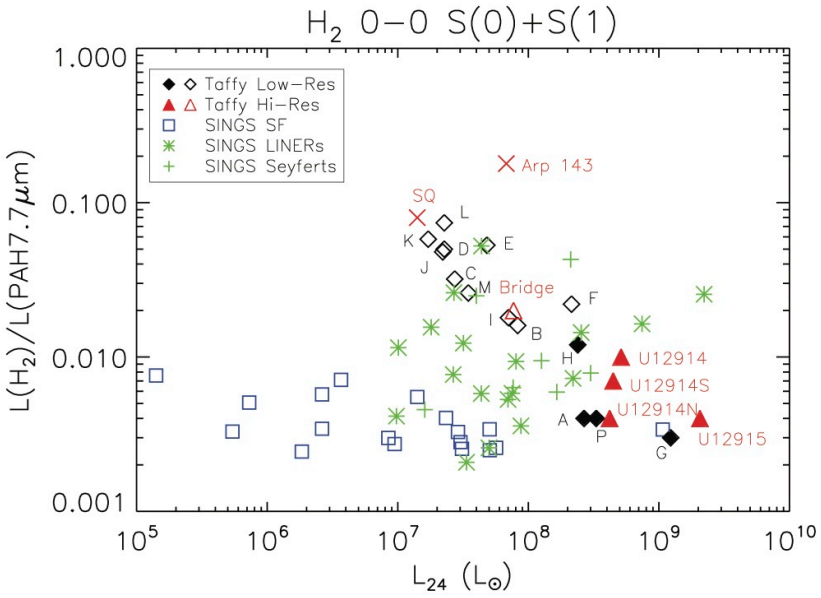

Figure 4.10 Total luminosity in H_2 0–0 S(0) and S(1) lines relative to 7.7 μm PAH emission. Extraction regions which fall on the disks or their nuclei have filled symbols. The PAH emission was determined using rectangular apertures matched to the spectral extraction apertures in the IRAC 8.0 μm band, which was Gaussian-convolved to match the resolution of the MIPS 24 μm band and corrected for stellar contamination (see text). Luminosities at 24 μm were determined using MIPS 24μm photometry, except for the high resolution Taffy apertures, for which an average of the spectrum over 22.5–25.0 μm was used (see text). For comparison, we show galaxies from the SINGS sample (Roussel et al., 2007), Arp 143 knot G (Beirão et al., 2009), and the SQ shock sub-region (Cluver et al., 2010).

In Figure 4.10 we have distinguished between spectra taken on the bright parts of the galaxy disks compared with spectra taken between the galaxies in the bridge. The spectra centered close to bright disk regions (or the nuclei themselves) show $L(\mathrm{H_2})/L(\mathrm{PAH7.7}\mu\mathrm{m})$ ratios typical of star-forming galaxies and likely associated with UV-excited photodissociation regions (PDRs) around young stars. The $L(\mathrm{H_2})/L$ PAH7.7μm) ratio in the Taffy bridge regions are much larger than in the bright disks, and are generally higher than those of the SINGS AGNs. As we will show later, these ratios are too high to be easily explained by PDR excitation, and we will argue that they are elevated by turbulent dissipation of energy, probably via shocks. We note that Region F, which includes the giant extraplanar H II region, shows a higher $L(\mathrm{H_2})/L(\mathrm{PAH7.7}\mu\mathrm{m})$ ratio than is typical of star forming galaxies. This is not surprising, since it lies in the bridge and may have both bridge and PDR-type heating present along the line of sight.

There is generally good agreement between the high and low resolution data in the emission regions within the galaxies. The high resolution spectra of the UGC 12915 nucleus cover the same part of the system as region G, the UGC 12914 nucleus is comparable to region H, the northern clump of UGC 12914 is comparable to region A, and the UGC 12914 southern knot is not far from region P. These regions have $L(\mathrm{H_2})/L(\mathrm{PAH7.7}\mu\mathrm{m})$ ratios on the high end of the star forming galaxy distribution which, along with their positions within the galaxies, suggests that the excitation mechanism may be the same as that of the SINGS galaxies, namely UV-excitation due to PDRs.

A similar conclusion is reached by examining Figure 4.11, which shows the ratio $L(\mathrm{H_2})/L_{24}$, as in Ogle et al. (2010). In addition to the SQ shock sub-region and Arp 143 knot G, we also plot here 3C 326 N (Ogle et al., 2007). Emission at 24 μm is mostly due to warm dust heated by young stars. The relative $\mathrm{H_2}$ emission in the Taffy bridge regions is considerably stronger than that in the star forming galaxies, and is also stronger than most of the AGNs. The bridge regions are generally comparable to 3C 326 N and Arp 143 knot G, but somewhat weaker than the SQ shock sub-region.

The two galaxies are not exceptionally strong $\mathrm{H_2}$ emitters compared to the SINGS star

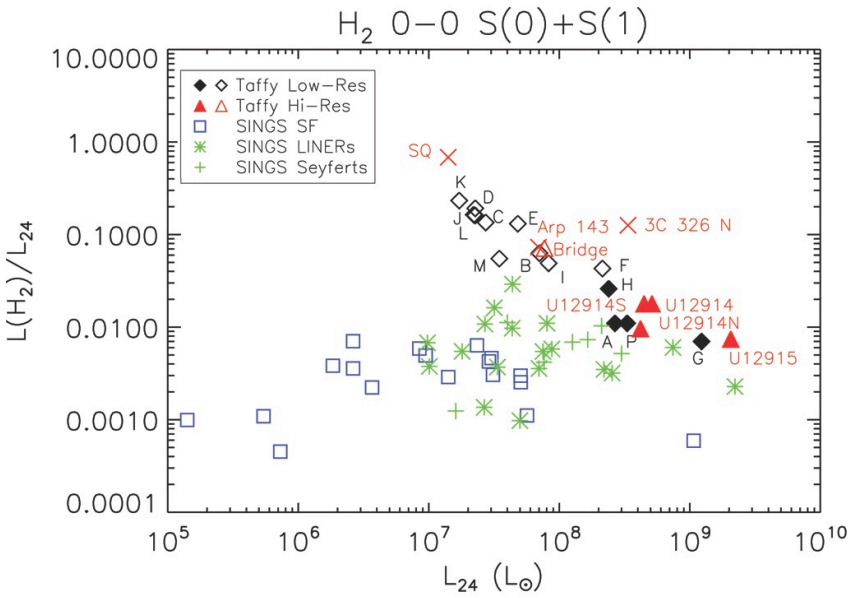

Figure 4.11 Total luminosity in H_2 0–0 S(0) and S(1) lines relative to 24 μm emission. Other objects are shown as in Figure 4.10. In addition, we include 3C 326N (Ogle et al., 2007).

forming galaxies, with emission levels only slightly above the most H_2-bright star forming galaxies . In contrast to most of the bridge, the two galaxies both host star formation. UGC 12915 seems to be in an early starburst phase (Jarrett et al., 1999), so much of the H_2 emission is likely to have a PDR origin. Star formation in UGC 12914 does not appear to be as strongly enhanced (Jarrett et al., 1999), but the H_2 emission is consistent with star forming galaxies.

To rule out the possibility that the bridge gas is heated in extended PDRs, we compare to the Meudon PDR models of Le Petit et al. et al. (2006) using parameters from Habart et al. (2011). Four different models were used, with $n_{\rm H} = 100$ and 1000 cm^{-3} and UV radiation scaling factor $G_{\rm UV} = 1$ and 10. The radiation scaling factor is defined relative to the UV field of Habing et al. (1968). The models predict a flux ratio of the H_2 S(0)–S(2) lines to the CO(1–0) line $F(H_2)/F(CO) \approx 2.5$–30. Using the CO(1–0) data of Gao et al. (2003), we find $F(CO) = 1.24 \times 10^{-18}$ W m^{-2} over the entire bridge. Scaling the H_2 flux measured in the high resolution bridge spectrum to the full area of the bridge, $F(H_2) = 4.5 \times 10^{-16}$ W m^{-2}. This gives$F(H_2)/F(CO) \approx 360$, over an order of magnitude above what could be produced by a

PDR. We note that this is a conservative value for the H_2 flux since this region of the bridge has a lower-than-average H_2 flux and does not take into account higher-order H_2 transitions which would add power to the H_2 signal. Nevertheless, the result is very much in line with other similar observations in Stephan's Quintet (Cluver et al., 2010) and the MOHEG systems (Ogle et al., 2010) which occupy a similar phase-space in the diagrams shown in Figures 4.10 and 4.11. In these cases, shocks are presented as the likely heating source for the warm H_2.

It is worth making a comparison between the properties of the Taffy bridge and that seen in the large-scale shocked filaments in the Stephan's Quintet system (Appleton et al., 2006; Cluver et al., 2010). Taking regions C, D, E, F, J, K, L, M, Q and R as bridge spectra, we can estimate the mean surface brightness of the summed 0-0 S(0) and S(1) H_2 lines to be 1.5×10^{34} W over a projected area of 87.6 kpc^2. The mean surface brightness over these apertures is 1.7×10^{32} W kpc^{-2}. Individual regions in the bridge are sometimes higher (region F) and lower (region R) by factors of 2, but on average the surface brightness of the observed line luminosity is brighter by almost a factor of two than the equivalent emission averaged over the main shocked region in Stephan's Quintet, which we estimate to be $\sim 10^{32}$ W kpc^{-2} for the S(0) and S(1) lines over 476 kpc^2. Thus the surface luminosity in the Taffy is much more intense, reflecting a larger mass of excited gas than in the case of SQ. If shocks are responsible for the heating, then the degree to which shocks permeate the available gas mass may lead to variations in the observed H_2 luminosity. Powerful, likely extended H_2 emission is seen in some (but not all) ULIRGS (Higdon et al., 2006; Zakamska, 2010), which would make sense if galaxy collision geometry and available gas mass plays a role in how much cold molecular gas is shocked.

We note that the luminosities calculated above are for observed lines only, but in most cases the low H_2 temperatures lead to a correction of only 10-20% upwards for unobserved lines given that we have little knowledge of any hot component which would be observable as strong ro-vibrational transitions. We cannot rule out a substantial underestimate of the total warm H_2 luminosity in the bridge if such a component were present. Models suggest that J-shocks are more efficient at heating gas to these higher temperatures than magnetic C-shocks

(**?**), but this is beyond the scope of the present paper. *Herschel Space Telescope* observations have been granted (PI: P. Appleton) which may provide further diagnostics of the importance of J-shocks in the Taffy via detection of strong [OI]63 μm emission.

4.5.1.2 Cosmic ray heating

Given the relatively strong radio emission from the bridge region, we consider whether cosmic ray (CR) heating could be responsible for the excitation of the warm H_2 emission. Low-energy cosmic rays (1–10 MeV) can ionize some of the gas, and the resulting primary and secondary electrons heat the gas, which excites the H_2 through collisions (Dalgarno et al., 1999). Radio continuum observations of the bridge can provide some clues as to the energy density of cosmic rays. We caution, however, that the CRs that are expected to excite H_2 are the very low energy tail of the CRs that give rise to the radio continuum emission.

Based on the VLA 20 cm radio continuum flux in the mid-range bridge $\sim$1.1 mJy per $5''$ beam (Condon et al., 1993), and assuming a plasma depth of 12 kpc (roughly the scale of the bridge), a spectral index α ($\nu^{-\alpha}$) of 1.2 over the range 1.49–4.96 GHz, the minimum equipartition magnetic field is found to be 6.4 μG (e.g., Govoni & Feretti, 2004) for a lower spectral cut-off at 10 MHz. This is close to the value obtained by Condon et al. (1993) under similar assumptions. The corresponding magnetic energy density is 3.8×10^{-13} J m^{-3}. This energy density is uncertain to within at least a factor of two because of uncertainties in the value of the proton/electron energy ratio (assumed unity), as well as uncertainties in the volume filling factor of the magnetic field (also assumed to be unity), and the true depth of the plasma column.

If the energy density in the cosmic rays $< U_{\rm CR} > \sim < U_B >_{\rm min}$, then we can estimate the power available for heating $L_{\rm heat} = < U_{\rm CR} > \times \eta/\tau$ where η is the efficiency of the CR heating of H_2, and τ is the characteristic deposition timescale. For the mid-bridge region this corresponds to a luminosity surface density $L_{\rm CR} = 4.5 \times 10^{32} (\eta/\tau_7)$ W kpc^{-2}, if τ_7 is the deposition timescale in units of 10 Myr – the approximate expansion timescale of the bridge. We can estimate η by approximating the energy deposited by a typical MeV cosmic ray from

its specific stopping power measured in MeV per unit column density. A value of 3.5 MeV g^{-1} cm^{-2} is quoted for typical MeV cosmic rays in the ISM (Yusef-Zadeh et al., 2007), where the column density is that of the target material, in this case a mixture of molecular hydrogen and H I. With the H_2 column densities in the Taffy bridge of $\sim 2 \times 10^{20}$ molecules cm^{-2}, the stopping power liberated by the passage of these CRs through this medium would be of order 3.5×10^{-3} MeV per particle. Even allowing for the existence of more cold H_2 material, this implies $\eta < 0.01$. Since the H_2 luminosity seen in the S(0)–S(2) lines in the LH IRS slit is L_{H_2} $= 2.7 \times 10^{33}$ W (and probably larger because of unobserved lines), which corresponds to line surface luminosity $> 1.2 \times 10^{32}$ W kpc^{-2}, then in order to power the H_2 for the lifetime of the bridge (τ_7=1), a cosmic ray energy density of at least 100 times that derived from equipartition arguments would be required. Alternatively, CRs could heat the H_2 if we are observing the system during a deposition burst ($\tau_7 \sim 0.01$). Such a process would have to be global, perhaps a sudden injection of CRs streaming from the galactic disks, but this seems unlikely.

Another approach to evaluating the influence of cosmic rays, which is independent of assumptions about equipartition, is to estimate the ionization rate ζ_{CR} needed to balance the H_2 line cooling if CRs were the primary heating source. By assuming a canonical value for the H_2 line luminosity-density across the bridge and integrating only the 0–0 S(0)–(1) lines we estimate an H_2 cooling rate of $\sim 5.6 \times 10^{-32}$ W $molecule^{-1}$ (assuming an average 5 $M_\odot$ pc^{-2} over the bridge) and a luminosity density of 1.7×10^{26} W pc^{-2}. The heating rate by CR ionization has been estimated by various authors. Yusef-Zadeh et al. (2007) estimate the CR heating per molecule to be $2 \times (4 \times 10^{-18} \zeta_{H_2})$ W, where ζ_{H_2} is the H_2 ionization rate. Under these assumptions, for CR heating to balance the H_2 cooling would require an ionization rate of at least 10^{-14} s^{-1}. Under the same assumptions, Ogle et al. (2010) and Nesvadba et al. (2010) infer similar values for the ionization rate in the MOHEG radio galaxy 3C 326, where shocks were implicated.

This ionization rate is significantly higher than that measured in the molecular clouds in the Galactic Center (see Oka et al. 2005). Thus on purely comparative grounds a CR ionization rate in the Taffy bridge would again require an unusually high CR energy density, perhaps 10

times that of the unusual Galactic Center regions and ∼100 times the galactic neighborhood. Based on these arguments we can conclude that cosmic rays cannot be responsible for heating the H_2 in the Taffy bridge.

4.5.1.3 Heating by magnetic reconnection

This process is closely related to the previous one. In the previous subsection we estimated that the magnetic energy density in the bridge plasma was about 3.8×10^{-13} W m^{-3}. Again assuming a bridge depth of about 12 kpc, the energy column density is about 1.4×10^{47} J kpc^{-2}. Supposing that this magnetic energy is extracted on the bridge expansion timescale of about 10^7 yr (Condon et al., 1993), we expect a surface luminosity of about, $F_{\rm rec} = 4.4 \times 10^{32} \tau_7$ W kpc^{-2}.

This is comparable to the corresponding cosmic ray surface luminosity, as would be expected from the equipartition approximation of the previous subsection. Like the cosmic ray luminosity, this estimate must be corrected for an efficiency factor, representing the fraction of the reconnection energy used to excite H_2. This should include both direct excitation from the radiation from reconnection regions, and indirect processes, like broader ambient heating from reconnection. In either case we expect a very low efficiency, since the plasma will be transparent to most wavebands of the broad radiation spectrum produced directly or indirectly in reconnection events.

Note that the surface luminosity estimate above assumes the extraction of all of the magnetic energy on the adopted timescale, and so is an overestimate. On the other hand, it does not account for additional field generation in turbulent dynamos. This process may be locally important, but it is hard to see how it could have a global effect in the short time available. With the magnetic field estimate above, and mass density 10^7 $M_\odot$ kpc^{-2} estimated from Gao et al. (2003) the Alfvén velocity $v_{\rm A} \sim 20$ km s^{-1}, an order of magnitude less than the bridge expansion velocity of 450 km s^{-1} (Condon et al., 1993), so even the propagation of magnetic effects must be very localized. To create significant power over the whole bridge would require some organized triggering of many localized reconnection events. One possible

mechanism might be a consequence of the large-scale turbulence, to be discussed in the next section. Turbulence could, in principal, create locally tangled magnetic fields which could then be stretched by the galaxies moving apart, creating the conditions for possible reconnection. If the turbulence continued to be present over a long period of time, new events could continue to be created which might heat the H_2. Thus, although unlikely, we cannot completely rule out magnetic reconnection as another source of H_2 heating.

Specifically, if the typical reconnection scale relative to the bridge size is much less than the ratio of the Alfvén speed to the bridge expansion speed, then the reconnection timescale is much less than the age of the bridge. In that case, with a short timescale for reconnection, the reconnection luminosity is likely to decay on a similar timescale, yielding less luminosity than at earlier times.

4.5.1.4 Turbulence and/or shock heating

A more likely source for H_2 heating is turbulence, created in the wake of the collision between the two galaxies. We estimate turbulent heating rate $\Gamma_{\rm turb}$ using

$$\Gamma_{\rm turb} = \frac{3}{2} \times \frac{2 m_{\rm H} (v/2.36)^2}{t_{\rm dis}},$$

where v is the velocity width over a length scale l, the factor 2.36 converts the line width to the rms velocity of the gas, and $t_{\rm dis} = l/(v/2.36)$ is the energy dissipation timescale (e.g., Mac Low, 1999; Tielens, 2005). From the CO observations of Gao et al. (2003), we take $v \approx 200$ km s^{-1} over a beam of 14 arcsec, or $l \approx 4$ kpc. This yields $t_{\rm dis} \approx 5 \times 10^7$ yr. The heating rate is then $\Gamma_{\rm turb} \approx 2.5 \times 10^{-32}$ W molecule^{-1}, about 60% of the observed cooling rate of 4×10^{-32} W molecule^{-1}. Turbulence on this scale could contribute significantly to the gas heating, provided that it is relatively efficient.

A related possibility is heating by shocks. We may obtain a crude estimate of the energy available in shocks by examining the bulk mechanical energy associated with the post-shock gas. The CO velocity dispersion, which should roughly track the velocity dispersion of the cold H_2, is (200/2.36) km s^{-1} (Gao et al., 2003). Zhu et al. (2007) found the H_2 mass to be $M_{\rm H_2} \sim 1.3 \times 10^9\ M_\odot$, so over the 20 Myr since the collision the average heating rate is

1.5×10^{34} W. This is comparable to the bridge H_2 luminosity of 2×10^{34} W, assuming a bridge area of 170 kpc^2.

This estimate can be checked against an upper limit to the available power estimated using the bulk kinetic energy of the H I and H_2 gas in the bridge. A re-analysis of the radio data of Condon et al. (1993) by Gao et al. (2003) determined that the H I mass in the bridge is $M_{\rm HI} \sim 6 \times 10^9\ M_\odot$. We take this mass as the pre-shock H I mass, and a collision velocity of 450 km s^{-1} (Condon et al., 1993) in the shock frame. The time since the collision is ~ 20 Myr, so the total available power from the H I is 1.9×10^{36} W, about 2 orders of magnitude higher than the H_2 luminosity.

The recent models of Lisenfeld & Völk (2010) also required the presence of strong shocks in the bridge. In the model, the shocks accelerate charged particles to ultrarelativistic energies, which then produce the synchrotron emission observed in the radio continuum.

We conclude that the largest heating source is probably shocks, as in the model presented by Guillard et al. (2009) which was developed to explain the powerful H_2 emission detected in the giant intergalactic shock wave in Stephan's Quintet. The essential ingredients of this model are that a high-speed shock wave is driven into a multi-phase medium leading to the collapse and shock-heating of denser material. Molecules form rapidly on dust grains which survive in the denser clumps of material, and strong H_2 emission results. Models fitted to the H_2 excitation diagrams in Stephan's Quintet show that the emission is consistent with several low and medium velocity C-shocks, although more destructive J-shocks cannot be ruled out. Our observations do not provide enough points on the excitation diagram to justify extensive shock-modeling, but the similarities between the spectra seen in the Taffy bridge (powerful H_2 with only low-excitation metal lines) and the approximately similar low-J temperature fits suggest a common origin for the H_2 excitation.

By analogy with Stephan's Quintet, a distribution of shock velocities, related to the density distribution in the shocked gas, is likely to be present (Guillard et al., 2009). In the gas that is less dense than the molecular gas, shock velocities > 100 km s^{-1} are likely, which will ionize the medium. These shock velocities can be estimated using the observed ratio [Ne III]15.56

μm/ [Ne III]12.81 μm. These lines can also originate with star formation, and the observed line ratio [Ne III]/[Ne II] ≈ 0.62 is within the range typical of star forming regions (Dale et al., 2006), but there is no evidence of significant star formation in the Taffy bridge. We use the MAPPINGS shock models of Allen et al. (2008) for a magnetic field of 5 μG and a pre-shock gas density between 0.1–100 cm^{-3}, as shown in Figure 4.12. The shock velocity for the Taffy bridge falls in the range 100–300 km s^{-1}, comparable to the SQ shock (Cluver et al., 2010).

Figures 4.10 and 4.11 may provide some insight into the location of the strongest shocks. Figure 4.10 shows a spatial trend in $L(\mathrm{H_2})/L(\mathrm{PAH})$, with values close to those of the galaxies at the bridge/galaxy interface growing to become comparable to the SQ shock near the center of the bridge. A similar trend is found in $L(\mathrm{H_2})/L_{24}$ (Figure 4.11). This suggests that the shocks in the Taffy bridge are strongest near its center.

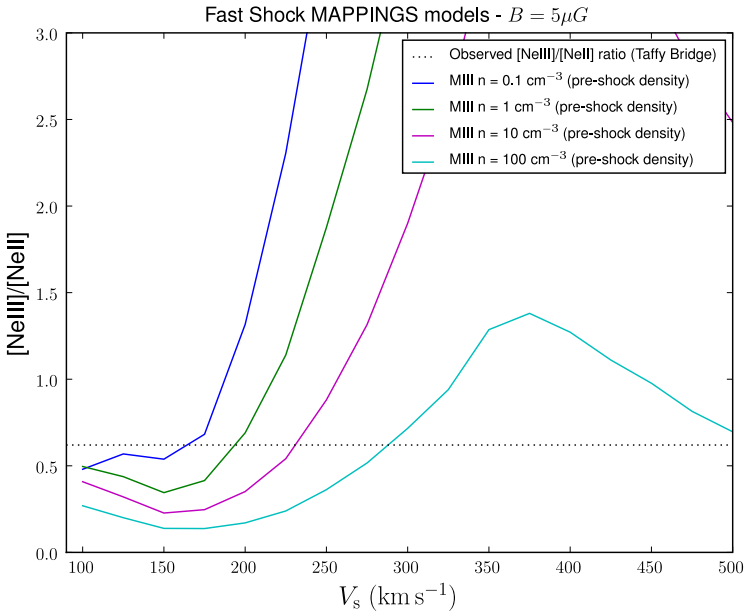

Figure 4.12 MAPPINGS shock velocity models (Allen et al., 2008) for magnetic field $B = 5\mu$G. The dotted line indicates [Ne III]/[Ne II] = 0.62, as measured in the bridge using the IRS SH module. The curves correspond to different values for the pre-shock density.

4.5.2 Comparison with CO data

One of the most remarkable features of the Taffy system is the fact that the peak H I concentration is in the bridge between the two galaxies (Condon et al., 1993). In contrast, the CO (1–0) map of Gao et al. (2003) shows that the cold molecular gas has its highest concentrations in the galaxies. However, the molecular gas is present throughout the bridge, so that the total cold H_2 mass in the bridge appears to be comparable to that of the galaxies.

The estimated cold H_2 mass depends on the conversion factor $X = N_{H_2}/I_{CO}$, which is unknown. Zhu et al. (2007) fit large velocity gradient models to CO line ratios and determined that $X = 2.6 \times 10^{19}$ cm^{-2}/(K km s^{-1}) in the bridge, which implies $M_{H_2,cold} = 1.3 \times 10^9\ M_\odot$. The warm H_2 mass is estimated to be $9 \times 10^8\ M_\odot$ based on the S(0) and S(1) lines (see Section 4.4.3), implying $M_{H_2,warm}/M_{H_2,cold} = 0.7$.

Zhu et al. (2007) also provide an estimate of $X = N_{H_2}/I_{CO}$ for the two galaxies in the Taffy system which is systematically lower by almost a factor of three than the average value of 2.3×10^{20} cm^{-2}/(K km s^{-1}) assumed by Roussel et al. (2007) for the SINGs galaxies. If we rescale the Zhu et al. (2007) values to allow a more direct comparison with SINGs, then the mass in the cold component in the bridge would increase, bringing warm to cold ratio in the bridge to 0.26. This is on the upper end of the distribution for SINGS galaxies. However it is not clear that such a normalization is justified given that peculiar nature of the Taffy galaxies. Additionally, since the Taffy bridge (unlike SINGs galaxies) does not contain an obvious source of heating, the bracketted range of $M_{H_2,warm}/M_{H_2,cold}$= 0.28–0.7 suggests an active heat source from shocks. We note that in the case of Stephan's Quintet, recent measurements with the IRAM 30 m telescope (**?**) suggest comparable values along the main intergalactic shock $M_{H_2,warm}/M_{H_2,cold}$ = 0.19–0.28 after correction to a common CO to H_2.

4.6 Summary and Future Work

We have reported on the detection of powerful mid-IR emission lines of H_2 in the Taffy galaxies. Our main results are:

1. The mid-IR spectrum of the Taffy bridge bears a striking similarity to the spectrum of the group-wide shock in Stephan's Quintet (Appleton et al., 2006; Cluver et al., 2010). In particular, the $L(H_2)/L(PAH)$ ratio is unusually high, exceeding by an order of magnitude that found in SINGS star forming galaxies (Roussel et al., 2007).

2. The warm H_2 is distributed throughout the bridge between the two galaxies. This is similar to the cold H_2 component detected previously using sub-mm observations of CO. The warm H_2 emission peaks in the galaxies, which is also similar to the CO, but differs from the neutral H I gas, which peaks in the bridge.

3. Single-temperature fits to the two H_2 lines measured throughout the bridge indicate a nearly uniform temperature of 150–175 K. We also estimate a mass density of $\sim 5\ M_\odot\ \mathrm{pc}^{-2}$. Two-temperature fits in regions where we measure three lines suggest the total mass may be higher by a factor of 3.

4. The H_2 gas is probably heated by shocks produced during the collision, similar to the shock in Stephan's Quintet and also by continuing cloud collisions in the bridge. In the SQ shock model of Guillard et al. (2009), the galaxy interaction drives shocks in a multiphase medium. The shock velocity, the post-shock temperature and the gas cooling timescales depend on the pre-shock gas density. The H_2 gas is formed from gas that is shocked to velocities sufficiently low ($v_s < 200$ km s^{-1}) for dust to survive.

We have determined that the H_2 molecule provides an important cooling channel for the warm gas in the Taffy bridge. Other molecules may also be important. The ability of the *Herschel Space Observatory* to observe emission lines of CO, H_2O, and OH will provide further insight into cooling in the Taffy bridge. In particular, CO line fluxes could shed further light on the heating mechanism by allowing us to distinguish between C- and J-type shocks.

CHAPTER 5. SUMMARY AND DISCUSSION

5.1 Super star clusters

5.1.1 Summary and discussion

In both the Arp 284 and Arp 261 systems, we were able to fit broadband photometric colors to STARBURST99 to confirm the existence of large populations of young star clusters. In Arp 284, we detected a total of 174 clusters. When sample completeness was considered, the sample was reduced to 53 or 63 clusters for luminosity and mass cuts, respectively. This left too few clusters to comment reliably on the possibility of infant mortality in the system. The sample showed little variation across the tidal features of NGC 7714, although the intergalactic bridge connecting this galaxy to NGC 7715 showed some indications of having an older cluster population. This result is uncertain due to the small number of clusters involved and the limited spatial coverage of the bridge in the important F380W filter. If the bridge population is in fact older than that in the tidal features of NGC 7714, it implies that clusters last longer in the bridge than in the galaxies. This environmental dependence would support the mass-dependent cluster disruption model over mass-independent disruption.

The other key result in Arp 284 was the discovery that the giant H II regions in which the star clusters reside tend to be older than the detected clusters they contain. We also found that the majority of the flux from these H II regions originates outside the clusters. This indicates that there is a significant background population of stars below our detection threshold, either because they are in old, faint clusters or because they are field stars whose clusters have already dissolved. We refer to these young clusters embedded in older populations as "jewels in the crown."

The results for the Arp 261 system are less clear. It is certain that there is a large population of young clusters in the system, but the age and relative size of an intermediate age population ($\geq$ 100 Myr), is unknown due to the unknown metallicity of the system. Despite these limitations, we detect active star formation in the northern bridge and, on a smaller scale, the central bridge, suggesting that the long-held assumption that Arp 261 is a Taffy-like system is probably not entirely correct. Accurate ages of the clusters in the northern bridge could help to constrain the collision timescale and thereby provide some clues about the dynamical timescale of the interaction.

5.1.2 Future work

The Arp 261 project will benefit tremendously from a determination of the metallicity of the system. We have optical spectra obtained at the Lick Observatory which will allow the us to determine the metallicity of each galaxy. The spectra also cover the bridge region, but the emission is sufficiently faint that we will likely only be able to measure upper limits to line fluxes in this region. The bridge metallicity should be quite similar to the galaxies, possibly a bit lower if the collision was a flyby in which the bridge formed primarily from material in the outer disks of the galaxies.

The best way to determine the nature of the Arp 261 collision would be to obtain radial velocity measurements of the 21 cm H I line. This would permit detailed dynamical models of the collision, which be useful in determining how the northern bridge formed and thus what cluster ages are expected there.

It would be helpful in both Arp 284 and Arp 261 to get additional UV data in the bridges. This would allow accurate ages to be determined for significantly more clusters in the most interesting parts of the systems. Most of the limitations on our conclusions are the result of the use of archival data. The use of archival data was necessary, since time on *HST* is extremely difficult to get. (For observation Cycle 19, from October 2011 – September 2012, guest observers requested 18,000 orbits of observations, compared to 2,600 available orbits). However, the nonuniform coverage, both spatially and in terms of data quality, limits the our

ability to get accurate age estimates in the most interesting parts of the system. Dedicated observations with full, multi-band coverage down to a limiting magnitude just outside the range of contamination by bright stars, is essential if this field is to move forward.

5.2 Star formation suppression

5.2.1 Summary and discussion

Using mid-IR spectra obtained with the *Spitzer* IRS instrument, we have found emission from purely rotational lines of H_2 in the bridge between the Taffy galaxies. Although we do not have a full spectral map, the available data demonstrate that the emission is extended across the entire bridge region. The H_2 could be heated by a number of different processes, but the most likely is a combination of shocks and turbulence.

Most detected extragalactic H_2 emission is found in photodissociation regions (PDRs), UV-excited regions surrounding young starts. There is little evidence of star formation in the Taffy bridge, and a comparison of the Taffy bridge to SINGS normal galaxy sample values of $L(H_2)/L(\mathrm{PAH7.7}\mu\mathrm{m})$ and $L(H_2)/L_{24}$, where L_{24} is the continuum luminosity at 24 μm, indicate that the Taffy bridge emission is stronger than that typically found in star forming galaxies. We also used PDR models to further establish, based on the ratio of $L(H_2)/L(\mathrm{CO})$, that UV heating cannot explain the observed H_2 emission.

The strong magnetic fields in the Taffy bridge also made heating by cosmic rays and magnetic reconnection plausible. However, an analysis of the energetics indicates that both of these processes would have to be unrealistically efficient to make a significant contribution to the H_2 heating.

We are left with shock and turbulence as likely heating sources. A shock heating scenario is suggested by the high collision velocity of the galaxies ($\sim$450 km s^{-1}), as well as the striking similarity between the Taffy spectrum and that of the group-wide shock in Stephan's Quintet. More quantitatively, the bulk kinetic energy of the gas due to the collision is sufficient heat the gas. This scenario is also supported by the CO velocity dispersion.

This result is interesting because H_2 is typically destroyed by shocks. In the case of

Stephan's Quintet, models indicate that H_2 was able to survive the shock due to the multiphase nature of the intergalactic medium, in which regions of higher-than-average density, where the shock velocity decreased, allowed H_2 to be excited but not destroyed.

The Taffy bridge is one of very few extragalactic sources of strong, resolved H_2 emission. Although there are many types of galaxies which strong H_2 line emission, the emission region is generally unresolved. This system therefore presents a rare opportunity to understand the cooling of shock-heated gas.

5.2.2 Future work

Having established that the H_2 molecule provides an important cooling mechanism for the molecular gas in the Taffy bridge, the next logical step is to determine what other atoms and molecules are important cooling channels. This will be explored with spectral maps obtained from *Herschel Space Observatory* program, "Charting Cooling Pathways in High-Speed Extragalactic Shocks" (PI: Appleton). *Herschel* will allow us to observe emission from several additional species of atoms and molecules that can reveal more about the shocks responsible for the heating. Models of the shock in Stephan's Quintet predict that the ratios of CO lines depend on whether the shocks are strong, dissociative J-shocks or weaker, magnetic C-shocks, with J-shocks showing stronger emission in higher-J transitions (here, J is the total rotational angular momentum quantum number). Other potentially important coolants include [O I], [C II], H_2O, OH, and NH_3. The observations will cover the entire Taffy bridge, so we will also be able to see the spatial distribution of the coolants. The program also includes Stephan's Quintet, for which more ancillary data (including full *Spitzer* spectral maps) are available, which will aid in the interpretation of the results.

It would also be useful to obtain X-ray data of the system. The nature of the H_2 emission in Stephan's Quintet was determined much more clearly than that in the Taffy partly because pre-existing X-ray data had already established the presence of an enormous shock at the same position as the H_2 emission (Trinchieri et al., 2005). The shock is shown in *Chandra* X-ray alongside the *Spitzer* spectral map of the H_2 S(1) line in Figure 5.1. The Taffy bridge probably

consists of a large number of small shocks rather than a single large one, but X-rays could still be helpful in characterizing the shocks and their spatial distribution.

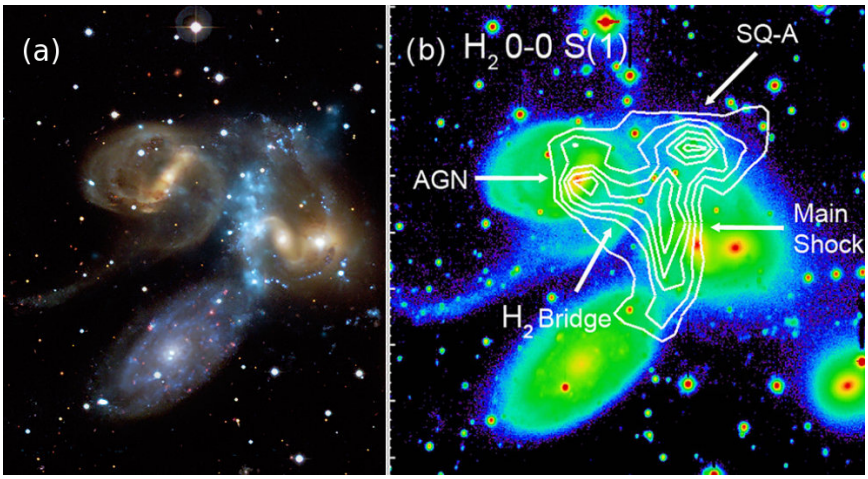

Figure 5.1 (a) Optical image of Stephan's Quintet, with *Chandra* X-ray image in blue (from http://chandra.harvard.edu/photo/2009/stephq/). (b) H_2 0–0 S(1) line contours over *R*-band image from Cluver et al. (2010).

HST observations of the Taffy system would provide a much more comprehensive view of star formation in the system. *Spitzer* has largely explained why the bridge lacks young stars, but the galaxies should have significant cluster populations. Characterizing these clusters would provide a much more complete picture of star formation in the Taffy galaxies.

Another direction this project could go is simply to look for H_2 emission in more systems. The Taffy project began as a mid-IR survey of collisional ring galaxies, with the Taffy added as an afterthought as an example of a ring seen from the side. Despite being a late addition to the sample, I reduced its spectrum first, and it turned out to be interesting enough that most of the 6 month fellowship was spent working on the Taffy. It is not unlikely that (other) collisional ring galaxies will also show H_2 emission, but only Arp 143 has been studied in detail (Beirão et al., 2009), with some H_2 emission found. Completion of the original project could thus be very useful.

5.3 Final remarks

The study of galaxy interactions and their effect on star formation has progressed considerably since Larson & Tinsley (1978). *HST* has enabled imaging of individual star forming regions in interacting systems, while *Spitzer* has provided a new avenue for suppressed star formation to be explored. Together, these sorts of studies can provide complete pictures of the star formation in a particular system, which can then be generalized and refined through studies of additional systems,

To date, only Stephan's Quintet has such comprehensive coverage. It is also an extremely complex system, making the star formation history very difficult to untangle. Further studies involving simpler interacting systems can serve to broaden our understanding of large-scale star formation, the circumstances under which it can arise, and the fate of the star clusters that form as a result.

APPENDIX A. Additional data tables for Arp 284

Table A.1 Cluster magnitudes and age estimates

ID	F380W mag	F555W mag	F606W mag	F814W mag	Age ($Z_\odot$) Myr	Age ($0.4Z_\odot$) Myr	Age ($0.2Z_\odot$) Myr
1	22.46±0.06	–	22.64±0.03	22.18±0.05	15^{+1}_{-1}	15^{+3}_{-6}	15^{+3}_{-1}
2	23.30±0.14	–	22.84±0.06	23.10±0.15	4^{+2}_{-2}	5^{+2}_{-2}	5^{+4}_{-1}
3	22.33±0.07	–	21.23±0.03	21.67±0.07	1^{+1}_{-1}	2^{+2}_{-2}	3^{+1}_{-2}
4	22.46±0.08	–	22.02±0.04	22.09±0.08	6^{+1}_{-2}	6^{+1}_{-1}	7^{+8}_{-2}
5	21.25±0.04	–	20.86±0.02	21.06±0.04	5^{+1}_{-1}	5^{+1}_{-1}	6^{+1}_{-1}
6	22.18±0.06	–	22.04±0.03	22.28±0.09	5^{+1}_{-2}	5^{+1}_{-1}	6^{+1}_{-1}
7	21.00±0.03	–	21.30±0.02	21.07±0.03	5^{+1}_{-1}	14^{+1}_{-1}	15^{+1}_{-1}
8	22.80±0.11	–	21.78±0.04	21.89±0.05	3^{+1}_{-1}	4^{+1}_{-1}	4^{+2}_{-1}
9	20.84±0.03	–	20.82±0.04	20.74±0.07	5^{+1}_{-1}	14^{+1}_{-3}	15^{+1}_{-2}
10	21.13±0.04	–	21.43±0.03	21.07±0.05	15^{+1}_{-1}	14^{+1}_{-2}	15^{+1}_{-1}
11	22.89±0.11	–	22.27±0.05	21.94±0.13	32^{+94}_{-27}	21^{+109}_{-15}	20^{+102}_{-12}
12	23.39±0.17	–	22.97±0.09	22.71±0.16	35^{+74}_{-30}	20^{+79}_{-15}	20^{+75}_{-13}
13	21.41±0.05	–	21.51±0.03	21.17±0.07	6^{+1}_{-1}	14^{+2}_{-2}	15^{+1}_{-2}
14	22.30±0.10	–	21.62±0.07	21.89±0.22	3^{+3}_{-2}	4^{+3}_{-2}	5^{+4}_{-3}
15	21.89±0.07	–	21.73±0.04	21.04±0.06	15^{+13}_{-4}	21^{+3}_{-5}	20^{+4}_{-4}
16	20.53±0.03	–	20.15±0.02	20.67±0.07	3^{+1}_{-1}	4^{+1}_{-1}	5^{+1}_{-1}
17	23.44±0.18	–	23.10±0.07	22.52±0.15	15^{+13}_{-5}	21^{+23}_{-13}	20^{+129}_{-11}
18	21.45±0.05	–	21.26±0.03	21.03±0.08	6^{+1}_{-1}	14^{+3}_{-5}	15^{+2}_{-2}
19	22.25±0.06	–	21.26±0.02	21.68±0.10	1^{+2}_{-1}	3^{+1}_{-2}	3^{+1}_{-1}
20	22.24±0.05	–	21.46±0.02	21.94±0.10	2^{+2}_{-2}	3^{+1}_{-1}	3^{+2}_{-1}
21	23.84±0.23	–	22.17±0.05	22.30±0.11	1^{+2}_{-1}	3^{+1}_{-3}	3^{+1}_{-3}
22	22.73±0.09	–	21.68±0.04	22.01±0.11	2^{+2}_{-2}	3^{+1}_{-2}	3^{+2}_{-1}
23	21.46±0.03	–	21.38±0.02	21.49±0.07	4^{+1}_{-1}	5^{+1}_{-1}	6^{+1}_{-1}
24	26.42±1.97	24.65±0.17	24.42±0.15	24.09±0.27	550^{+3250}_{-547}	288^{+9812}_{-284}	80^{+10020}_{-76}
25	23.69±0.17	23.68±0.08	23.57±0.08	23.00±0.12	15^{+14}_{-7}	21^{+24}_{-14}	20^{+143}_{-11}
26	24.32±0.29	24.42±0.14	24.38±0.14	23.81±0.25	15^{+41}_{-10}	20^{+190}_{-15}	20^{+191}_{-14}
27	22.94±0.09	–	22.75±0.05	22.07±0.09	15^{+1}_{-1}	21^{+5}_{-12}	20^{+5}_{-11}
28	23.46±0.18	–	22.7±0.08	22.49±0.15	98^{+297}_{-95}	111^{+250}_{-107}	89^{+63}_{-84}
29	22.12±0.06	–	21.9±0.04	21.62±0.07	6^{+1}_{-1}	15^{+4}_{-6}	16^{+3}_{-2}
30	23.93±0.22	–	23.34±0.06	23.04±0.13	35^{+250}_{-30}	20^{+276}_{-15}	20^{+129}_{-14}

Table A.1 (Continued)

ID	F380W mag	F555W mag	F606W mag	F814W mag	Age ($Z_\odot$) Myr	Age ($0.4Z_\odot$) Myr	Age ($0.2Z_\odot$) Myr
31	24.04±0.24	23.27±0.07	22.88±0.05	23.30±0.15	3^{+2}_{-2}	4^{+2}_{-1}	4^{+2}_{-1}
32	21.64±0.06	–	21.21±0.03	21.07±0.05	6^{+1}_{-1}	17^{+4}_{-9}	18^{+3}_{-6}
33	22.69±0.08	–	22.57±0.05	22.90±0.21	4^{+1}_{-1}	5^{+1}_{-1}	5^{+2}_{-1}
34	23.16±0.12	23.24±0.06	22.95±0.05	22.27±0.06	15^{+1}_{-7}	21^{+8}_{-13}	20^{+7}_{-11}
35	23.04±0.11	–	22.70±0.06	21.99±0.10	15^{+1}_{-1}	21^{+9}_{-12}	20^{+129}_{-11}
36	20.52±0.02	–	20.40±0.01	20.48±0.02	5^{+1}_{-1}	13^{+2}_{-1}	14^{+1}_{-1}
37	23.39±0.14	23.54±0.08	23.33±0.07	23.11±0.12	6^{+9}_{-1}	10^{+15}_{-2}	15^{+8}_{-6}
38	23.08±0.11	22.93±0.05	22.72±0.04	22.07±0.05	15^{+1}_{-7}	21^{+10}_{-13}	20^{+210}_{-11}
39	23.43±0.13	23.32±0.06	22.99±0.05	22.88±0.09	5^{+2}_{-2}	5^{+21}_{-1}	10^{+17}_{-6}
40	22.34±0.06	22.51±0.05	22.41±0.07	22.19±0.10	5^{+2}_{-2}	14^{+3}_{-5}	15^{+2}_{-2}
41	23.01±0.12	22.71±0.07	22.70±0.08	21.93±0.07	15^{+6}_{-7}	21^{+16}_{-13}	222^{+58}_{-213}
42	24.21±0.29	24.05±0.11	23.66±0.09	22.84±0.09	15^{+21}_{-7}	21^{+543}_{-16}	260^{+219}_{-252}
43	23.32±0.22	22.78±0.12	22.65±0.14	21.96±0.12	18^{+215}_{-13}	21^{+623}_{-16}	221^{+524}_{-215}
44	20.57±0.03	20.44±0.03	20.18±0.03	20.25±0.05	5^{+1}_{-2}	5^{+1}_{-1}	5^{+1}_{-1}
45	21.59±0.04	–	21.53±0.02	21.71±0.05	4^{+2}_{-1}	5^{+1}_{-1}	6^{+1}_{-1}
46	22.12±0.08	22.00±0.05	21.79±0.07	21.50±0.09	13^{+23}_{-8}	10^{+16}_{-2}	18^{+7}_{-9}
47	23.33±0.14	–	23.28±0.08	22.40±0.13	15^{+1}_{-1}	21^{+9}_{-12}	20^{+9}_{-11}
48	23.70±0.17	–	23.71±0.11	23.28±0.23	15^{+16}_{-10}	14^{+10}_{-6}	15^{+6}_{-4}
49	21.52±0.06	21.45±0.05	21.13±0.03	20.96±0.06	6^{+1}_{-1}	10^{+9}_{-2}	15^{+6}_{-6}
50	23.80±0.17	–	23.52±0.07	22.96±0.10	15^{+10}_{-4}	21^{+17}_{-13}	20^{+145}_{-11}
51	21.02±0.05	21.05±0.04	20.63±0.03	20.54±0.05	5^{+1}_{-2}	5^{+1}_{-1}	5^{+1}_{-1}
52	24.66±0.38	24.02±0.13	24.04±0.13	24.10±0.32	7^{+589}_{-4}	78^{+365}_{-74}	8^{+188}_{-4}
53	22.89±0.10	22.87±0.05	22.71±0.05	22.46±0.09	6^{+30}_{-1}	10^{+14}_{-2}	17^{+6}_{-8}
54	24.10±0.24	24.05±0.13	23.84±0.10	22.88±0.10	15^{+9}_{-7}	21^{+30}_{-14}	266^{+92}_{-251}
55	21.58±0.04	21.58±0.02	21.41±0.02	20.88±0.02	15^{+1}_{-1}	21^{+2}_{-3}	20^{+3}_{-2}
56	21.06±0.03	21.10±0.02	20.88±0.02	20.29±0.03	15^{+1}_{-1}	21^{+2}_{-12}	20^{+2}_{-2}
57	22.04±0.05	22.04±0.05	21.85±0.05	21.40±0.07	15^{+1}_{-1}	10^{+13}_{-1}	19^{+4}_{-10}
58	23.98±0.24	24.38±0.18	23.74±0.12	23.16±0.12	15^{+15}_{-7}	10^{+44}_{-5}	10^{+207}_{-2}
59	23.19±0.14	23.58±0.09	23.23±0.07	23.12±0.14	5^{+2}_{-3}	5^{+15}_{-2}	15^{+5}_{-11}
60	22.34±0.08	22.35±0.08	22.02±0.07	21.43±0.08	15^{+1}_{-1}	10^{+19}_{-2}	20^{+8}_{-11}
61	23.70±0.20	24.09±0.16	23.78±0.13	22.64±0.09	15^{+1}_{-7}	21^{+18}_{-13}	267^{+66}_{-50}
62	23.53±0.15	24.23±0.15	23.69±0.11	23.62±0.22	2^{+3}_{-2}	4^{+2}_{-3}	4^{+2}_{-3}
63	23.64±0.18	24.47±0.19	24.16±0.16	24.74±0.61	2^{+3}_{-2}	4^{+2}_{-4}	5^{+1}_{-5}
64	24.38±0.35	23.91±0.14	23.90±0.15	24.04±0.31	6^{+462}_{-3}	6^{+369}_{-2}	8^{+141}_{-4}
65	22.77±0.08	22.72±0.04	22.59±0.04	21.87±0.05	15^{+1}_{-1}	21^{+5}_{-12}	20^{+5}_{-11}
66	22.30±0.18	21.88±0.14	21.09±0.09	20.79±0.07	3^{+3}_{-2}	4^{+2}_{-1}	5^{+1}_{-2}
67	23.85±0.23	23.22±0.07	23.90±0.14	23.32±0.18	148^{+309}_{-142}	111^{+339}_{-103}	122^{+95}_{-113}
68	23.51±0.16	23.37±0.08	22.97±0.06	22.62±0.09	12^{+35}_{-8}	10^{+38}_{-5}	10^{+36}_{-2}
69	21.10±0.04	21.28±0.04	20.87±0.03	21.34±0.11	2^{+2}_{-1}	4^{+1}_{-1}	4^{+1}_{-1}

Table A.1 (Continued)

ID	F380W	F555W	F606W	F814W	Age ($Z_\odot$)	Age ($0.4Z_\odot$)	Age ($0.2Z_\odot$)
	mag	mag	mag	mag	Myr	Myr	Myr
70	20.80±0.03	20.95±0.03	20.56±0.03	20.55±0.05	5^{+1}_{-2}	5^{+1}_{-1}	5^{+1}_{-1}
71	23.53±0.16	23.94±0.13	23.64±0.12	23.36±0.20	6^{+23}_{-3}	10^{+15}_{-6}	15^{+7}_{-11}
72	23.46±0.16	23.53±0.09	23.15±0.07	22.69±0.09	15^{+15}_{-7}	10^{+29}_{-3}	10^{+29}_{-2}
73	22.51±0.11	22.01±0.05	21.57±0.05	21.32±0.07	4^{+2}_{-1}	5^{+1}_{-1}	5^{+2}_{-1}
74	23.22±0.12	23.26±0.07	23.14±0.07	22.56±0.08	15^{+6}_{-1}	21^{+13}_{-13}	20^{+12}_{-11}
75	22.72±0.09	22.64±0.05	22.37±0.04	21.93±0.06	15^{+13}_{-5}	10^{+18}_{-2}	10^{+17}_{-1}
76	20.03±0.02	20.08±0.01	19.85±0.01	19.73±0.02	6^{+1}_{-1}	10^{+3}_{-1}	15^{+1}_{-1}
77	24.31±0.31	24.08±0.13	23.85±0.11	22.98±0.11	15^{+21}_{-7}	21^{+777}_{-15}	262^{+206}_{-254}
78	24.65±0.45	23.39±0.09	22.37±0.05	22.08±0.07	2^{+2}_{-2}	3^{+1}_{-1}	3^{+2}_{-1}
79	22.66±0.09	22.24±0.04	21.64±0.03	21.57±0.06	3^{+1}_{-1}	4^{+1}_{-1}	4^{+1}_{-1}
80	22.90±0.10	22.54±0.05	21.73±0.03	21.93±0.07	1^{+1}_{-1}	3^{+1}_{-2}	3^{+1}_{-1}
81	21.12±0.03	21.41±0.02	21.22±0.02	21.29±0.05	4^{+1}_{-1}	5^{+1}_{-1}	5^{+1}_{-1}
82	24.53±0.65	24.32±0.30	24.60±0.56	24.20±0.58	13^{+1387}_{-13}	18^{+1482}_{-17}	18^{+2482}_{-16}
83	22.85±0.10	22.87±0.06	22.91±0.06	22.38±0.08	15^{+6}_{-3}	21^{+9}_{-12}	20^{+7}_{-11}
84	21.40±0.04	21.50±0.03	21.28±0.03	20.93±0.03	15^{+1}_{-3}	10^{+1}_{-1}	18^{+2}_{-4}
85	21.71±0.05	21.53±0.03	21.32±0.03	20.87±0.04	15^{+10}_{-3}	21^{+4}_{-12}	20^{+5}_{-11}
86	22.67±0.08	22.61±0.05	22.42±0.04	21.85±0.05	15^{+1}_{-1}	21^{+5}_{-12}	20^{+6}_{-11}
87	20.86±0.03	20.87±0.02	20.41±0.02	20.78±0.04	2^{+1}_{-1}	4^{+1}_{-1}	4^{+1}_{-1}
88	20.03±0.02	20.37±0.02	20.35±0.02	20.02±0.02	6^{+1}_{-1}	14^{+1}_{-1}	15^{+1}_{-1}
89	23.17±0.14	23.33±0.12	22.66±0.08	23.09±0.19	1^{+3}_{-1}	2^{+2}_{-2}	3^{+2}_{-3}
90	22.25±0.06	22.07±0.03	21.77±0.02	22.35±0.08	3^{+1}_{-1}	4^{+1}_{-1}	4^{+2}_{-1}
91	24.34±0.36	23.74±0.12	23.11±0.08	22.84±0.16	3^{+3}_{-2}	4^{+2}_{-1}	5^{+2}_{-2}
92	22.18±0.09	22.26±0.05	21.99±0.08	22.09±0.10	5^{+1}_{-2}	5^{+1}_{-1}	5^{+2}_{-1}
93	21.83±0.04	21.61±0.02	21.36±0.02	20.74±0.02	15^{+1}_{-1}	21^{+2}_{-12}	20^{+3}_{-3}
94	23.56±0.19	23.47±0.12	22.80±0.09	23.13±0.19	1^{+3}_{-1}	3^{+2}_{-3}	3^{+2}_{-3}
95	23.02±0.19	22.71±0.06	22.19±0.05	22.52±0.21	3^{+1}_{-2}	4^{+1}_{-2}	4^{+1}_{-1}
96	22.21±0.06	21.97±0.03	21.69±0.03	21.24±0.04	19^{+8}_{-10}	10^{+16}_{-2}	10^{+16}_{-1}
97	23.27±0.20	22.07±0.09	22.56±0.11	22.06±0.11	28^{+400}_{-23}	21^{+510}_{-16}	150^{+395}_{-144}
98	23.85±0.25	23.66±0.16	23.40±0.16	22.76±0.14	15^{+30}_{-8}	21^{+484}_{-16}	20^{+484}_{-14}
99	22.40±0.09	22.13±0.05	21.88±0.05	21.85±0.08	5^{+2}_{-2}	5^{+15}_{-1}	6^{+15}_{-2}
100	23.17±0.12	22.93±0.05	22.79±0.05	22.31±0.07	19^{+13}_{-10}	21^{+17}_{-13}	20^{+132}_{-11}
101	24.49±0.36	24.12±0.15	23.82±0.12	23.82±0.25	5^{+458}_{-3}	5^{+375}_{-2}	6^{+155}_{-3}
102	22.76±0.09	22.84±0.06	22.41±0.05	21.99±0.06	15^{+10}_{-7}	10^{+15}_{-2}	10^{+15}_{-1}
103	23.34±0.16	23.29±0.12	23.11±0.13	22.39±0.12	15^{+11}_{-7}	21^{+27}_{-14}	20^{+206}_{-12}
104	23.64±0.18	23.38±0.08	23.17±0.07	22.94±0.12	6^{+176}_{-2}	10^{+146}_{-5}	10^{+107}_{-5}
105	24.07±0.27	23.40±0.08	22.96±0.06	22.17±0.07	9^{+249}_{-4}	10^{+897}_{-5}	10^{+808}_{-5}
106	24.31±0.36	23.64±0.14	23.64±0.18	23.81±0.38	7^{+688}_{-4}	79^{+418}_{-75}	8^{+210}_{-4}
107	22.94±0.09	22.51±0.04	22.78±0.04	22.16±0.06	15^{+13}_{-4}	21^{+17}_{-7}	140^{+37}_{-26}
108	23.02±0.10	23.14±0.06	23.07±0.06	22.55±0.09	15^{+1}_{-1}	20^{+8}_{-12}	19^{+6}_{-10}

Table A.1 (Continued)

ID	F380W	F555W	F606W	F814W	Age ($Z_\odot$)	Age ($0.4Z_\odot$)	Age ($0.2Z_\odot$)
	mag	mag	mag	mag	Myr	Myr	Myr
109	22.99±0.11	22.69±0.05	22.60±0.06	21.98±0.07	15^{+8}_{-1}	21^{+15}_{-13}	20^{+192}_{-11}
110	23.32±0.12	23.62±0.09	23.58±0.09	22.54±0.08	15^{+1}_{-1}	21^{+8}_{-12}	249^{+54}_{-234}
111	23.58±0.16	23.63±0.08	23.55±0.08	23.02±0.13	15^{+15}_{-5}	21^{+22}_{-14}	20^{+14}_{-11}
112	23.65±0.19	24.48±0.19	24.25±0.17	23.87±0.25	4^{+23}_{-3}	14^{+12}_{-11}	15^{+7}_{-11}
113	23.17±0.13	22.71±0.06	22.38±0.04	21.86±0.06	10^{+31}_{-5}	10^{+38}_{-4}	10^{+37}_{-2}
114	23.70±0.18	24.06±0.12	23.89±0.12	23.38±0.16	15^{+14}_{-7}	10^{+26}_{-2}	16^{+13}_{-8}
115	23.69±0.18	23.97±0.12	23.80±0.11	23.64±0.21	6^{+8}_{-3}	14^{+12}_{-10}	15^{+7}_{-11}
116	23.24±0.14	23.09±0.07	22.81±0.05	22.45±0.08	13^{+27}_{-4}	10^{+33}_{-3}	10^{+31}_{-2}
117	24.05±0.23	24.02±0.13	24.09±0.16	23.52±0.19	15^{+30}_{-7}	21^{+124}_{-16}	20^{+173}_{-13}
118	23.36±0.14	22.99±0.07	22.96±0.07	22.58±0.10	13^{+139}_{-3}	21^{+124}_{-14}	21^{+134}_{-13}
119	23.49±0.16	23.24±0.07	23.20±0.08	22.79±0.12	13^{+36}_{-4}	21^{+45}_{-14}	20^{+118}_{-12}
120	23.03±0.10	22.98±0.06	22.84±0.06	22.25±0.07	15^{+5}_{-1}	21^{+11}_{-13}	20^{+10}_{-11}
121	22.05±0.05	22.36±0.04	22.09±0.03	22.42±0.08	4^{+1}_{-2}	4^{+1}_{-1}	5^{+1}_{-1}
122	24.27±0.28	23.51±0.08	22.98±0.05	22.88±0.09	3^{+3}_{-1}	4^{+2}_{-1}	5^{+1}_{-2}
123	23.44±0.14	23.29±0.06	22.71±0.03	22.69±0.08	3^{+1}_{-1}	4^{+1}_{-1}	4^{+1}_{-1}
124	24.67±0.39	24.42±0.13	24.07±0.1	23.96±0.22	5^{+430}_{-3}	5^{+366}_{-2}	5^{+156}_{-2}
125	–	23.62±0.06	23.38±0.06	22.97±0.08	7^{+1093}_{-2}	9^{+470}_{-4}	11^{+1089}_{-6}
126	–	23.93±0.08	24.16±0.10	24.22±0.21	6^{+81}_{-2}	14^{+106}_{-9}	13^{+67}_{-8}
127	23.69±0.13	23.33±0.06	23.7±0.09	22.96±0.09	15^{+11}_{-4}	21^{+24}_{-12}	144^{+78}_{-129}
128	23.81±0.15	23.84±0.08	23.71±0.08	23.10±0.09	15^{+7}_{-1}	21^{+17}_{-13}	20^{+135}_{-11}
129	23.79±0.14	23.45±0.07	23.54±0.08	22.73±0.07	15^{+7}_{-1}	21^{+19}_{-13}	231^{+94}_{-107}
130	22.53±0.06	22.32±0.03	22.17±0.03	21.85±0.04	13^{+22}_{-1}	21^{+5}_{-12}	20^{+5}_{-11}
131	–	24.52±0.14	24.40±0.14	23.25±0.10	15^{+10085}_{-9}	504^{+9596}_{-498}	263^{+4437}_{-254}
132	23.26±0.10	23.29±0.06	23.3±0.06	22.72±0.07	15^{+1}_{-1}	21^{+9}_{-12}	20^{+8}_{-11}
133	23.97±0.15	23.57±0.07	23.64±0.08	23.3±0.11	35^{+185}_{-30}	21^{+165}_{-14}	22^{+126}_{-15}
134	–	23.19±0.05	23.06±0.05	22.77±0.07	36^{+509}_{-31}	21^{+360}_{-15}	107^{+27}_{-100}
135	–	23.23±0.05	23.76±0.08	23.16±0.09	13^{+19}_{-2}	403^{+82}_{-390}	140^{+50}_{-33}
136	24.71±0.33	24.23±0.11	24.16±0.12	23.21±0.10	15^{+25}_{-7}	21^{+959}_{-15}	266^{+198}_{-257}
137	–	24.85±0.17	25.12±0.27	23.68±0.14	15^{+10085}_{-10}	497^{+9603}_{-491}	264^{+4836}_{-256}
138	–	22.88±0.04	22.71±0.04	22.34±0.06	30^{+652}_{-25}	357^{+70}_{-351}	121^{+46}_{-114}
139	21.98±0.04	21.93±0.02	21.82±0.02	21.93±0.04	5^{+1}_{-1}	6^{+1}_{-2}	14^{+2}_{-9}
140	26.00±0.87	24.79±0.16	24.36±0.13	24.15±0.20	4^{+1296}_{-3}	5^{+519}_{-2}	5^{+1195}_{-2}
141	24.08±0.17	23.87±0.08	24.13±0.11	23.31±0.10	15^{+8}_{-1}	21^{+25}_{-13}	150^{+140}_{-141}
142	23.31±0.10	23.33±0.05	23.06±0.05	23.15±0.09	5^{+1}_{-2}	5^{+1}_{-1}	5^{+11}_{-1}
143	24.01±0.16	23.65±0.07	23.43±0.06	22.68±0.06	15^{+12}_{-7}	21^{+22}_{-13}	235^{+136}_{-226}
144	23.43±0.11	23.38±0.06	23.48±0.07	22.77±0.07	15^{+1}_{-1}	21^{+10}_{-12}	20^{+10}_{-11}
145	22.26±0.05	22.32±0.03	21.92±0.02	22.05±0.04	3^{+1}_{-1}	4^{+1}_{-1}	5^{+1}_{-1}
146	24.45±0.24	24.07±0.09	24.86±0.22	23.74±0.15	15^{+19}_{-7}	21^{+581}_{-14}	244^{+178}_{-235}
147	21.75±0.04	21.57±0.02	21.40±0.01	21.01±0.02	13^{+2}_{-1}	21^{+2}_{-12}	20^{+3}_{-3}

Table A.1 (Continued)

ID	F380W	F555W	F606W	F814W	Age ($Z_\odot$)	Age ($0.4Z_\odot$)	Age ($0.2Z_\odot$)
	mag	mag	mag	mag	Myr	Myr	Myr
148	24.35±0.20	24.42±0.14	24.58±0.18	23.83±0.16	15^{+16}_{-7}	21^{+40}_{-14}	20^{+171}_{-12}
149	24.16±0.17	24.13±0.11	24.08±0.14	23.65±0.15	15^{+33}_{-10}	19^{+45}_{-12}	19^{+45}_{-11}
150	22.56±0.06	22.26±0.03	22.17±0.03	21.68±0.03	19^{+6}_{-8}	21^{+5}_{-7}	20^{+5}_{-6}
151	24.39±0.22	24.08±0.11	24.14±0.13	23.58±0.13	15^{+125}_{-7}	21^{+415}_{-15}	20^{+223}_{-13}
152	23.93±0.15	23.82±0.08	23.70±0.08	22.81±0.07	15^{+1}_{-1}	21^{+15}_{-13}	252^{+75}_{-39}
153	23.58±0.13	23.16±0.05	23.35±0.06	22.48±0.05	15^{+1}_{-1}	21^{+15}_{-8}	242^{+58}_{-30}
154	–	24.33±0.11	24.20±0.13	22.63±0.06	15^{+221}_{-7}	501^{+1299}_{-492}	265^{+172}_{-158}
155	25.18±0.50	24.33±0.14	24.32±0.15	23.45±0.12	15^{+2485}_{-10}	503^{+4897}_{-498}	264^{+3936}_{-258}
156	–	24.45±0.14	24.15±0.12	23.63±0.14	6^{+2394}_{-3}	8^{+2292}_{-4}	9^{+9291}_{-4}
157	–	23.71±0.08	23.80±0.10	23.45±0.13	35^{+592}_{-30}	21^{+429}_{-15}	110^{+84}_{-103}
158	–	23.90±0.10	24.04±0.12	23.56±0.15	13^{+726}_{-7}	390^{+172}_{-384}	135^{+90}_{-127}
n01	18.85±0.01	18.77±0.01	18.68±0.01	18.59±0.02	6^{+1}_{-1}	14^{+1}_{-2}	15^{+1}_{-1}
n02	19.26±0.02	19.44±0.02	19.35±0.03	19.14±0.02	5^{+1}_{-1}	14^{+1}_{-3}	15^{+1}_{-1}
n03	19.54±0.02	19.47±0.02	19.27±0.03	18.96±0.02	13^{+1}_{-1}	10^{+1}_{-1}	17^{+2}_{-3}
n04	19.21±0.02	19.11±0.02	18.75±0.02	18.64±0.02	6^{+1}_{-1}	10^{+2}_{-1}	15^{+2}_{-1}
n05	19.36±0.07	19.10±0.05	18.69±0.04	18.51±0.04	5^{+2}_{-2}	5^{+6}_{-1}	5^{+19}_{-1}
n06	18.38±0.01	18.19±0.01	18.02±0.01	17.95±0.02	6^{+1}_{-1}	12^{+3}_{-3}	15^{+1}_{-1}
n07	20.32±0.05	19.82±0.03	19.53±0.03	18.61±0.02	15^{+1}_{-1}	21^{+3}_{-5}	268^{+24}_{-22}
n08	18.50±0.04	18.10±0.04	17.81±0.04	17.74±0.04	5^{+2}_{-2}	6^{+4}_{-2}	6^{+9}_{-1}
n09	18.68±0.08	18.76±0.10	18.68±0.12	17.88±0.08	15^{+1}_{-1}	21^{+11}_{-13}	20^{+8}_{-11}
n10	20.15±0.04	19.51±0.03	19.22±0.03	19.11±0.02	5^{+1}_{-2}	5^{+1}_{-1}	6^{+1}_{-1}
n11	20.11±0.05	19.54±0.04	19.30±0.05	18.32±0.04	15^{+1}_{-1}	21^{+4}_{-12}	265^{+31}_{-23}
n12	18.89±0.06	18.62±0.07	18.36±0.08	18.01±0.06	13^{+26}_{-3}	10^{+29}_{-3}	10^{+21}_{-2}
n13	19.09±0.08	18.26±0.06	18.21±0.07	17.47±0.04	30^{+156}_{-21}	21^{+609}_{-13}	239^{+161}_{-128}
n14	17.21±0.01	16.56±0.01	16.96±0.02	15.75±0.01	15^{+1}_{-1}	21^{+1}_{-2}	257^{+9}_{-7}
n15	19.38±0.02	18.94±0.02	18.61±0.02	18.58±0.03	5^{+1}_{-2}	5^{+1}_{-1}	5^{+1}_{-1}
n16	18.46±0.06	17.80±0.04	17.66±0.04	17.07±0.03	29^{+12}_{-19}	21^{+20}_{-13}	205^{+21}_{-190}

Table A.2 Cluster $E(B-V)$ and mass estimates

ID	$E(B-V)$ $Z_\odot$	$E(B-V)$ $0.4Z_\odot$	$E(B-V)$ $0.2Z_\odot$	$M(10^6 M_\odot)$ $Z_\odot$	$M(10^6 M_\odot)$ $0.4Z_\odot$	$M(10^6 M_\odot)$ $0.2Z_\odot$
1	0^{+0}_{-0}	0^{+0}_{-0}	$0^{+0.04}_{-0}$	0.029	0.029	0.029
2	$0.16^{+0.12}_{-0.16}$	$0.12^{+0.12}_{-0.12}$	$0.12^{+0.12}_{-0.12}$	0.012	0.012	0.013
3	$0.24^{+0.06}_{-0.06}$	$0.22^{+0.1}_{-0.08}$	$0.24^{+0.06}_{-0.1}$	0.047	0.053	0.061
4	$0^{+0.18}_{-0}$	$0^{+0.06}_{-0}$	$0^{+0.18}_{-0}$	0.013	0.013	0.013
5	$0.06^{+0.06}_{-0.04}$	$0.1^{+0.04}_{-0.04}$	$0.06^{+0.04}_{-0.04}$	0.042	0.074	0.065
6	$0^{+0.08}_{-0}$	$0^{+0.04}_{-0}$	$0^{+0.04}_{-0}$	0.011	0.017	0.017
7	0^{+0}_{-0}	0^{+0}_{-0}	0^{+0}_{-0}	0.081	0.074	0.051
8	$0.4^{+0.08}_{-0.08}$	$0.38^{+0.08}_{-0.08}$	$0.34^{+0.08}_{-0.08}$	0.075	0.086	0.067
9	0^{+0}_{-0}	0^{+0}_{-0}	0^{+0}_{-0}	0.110	0.100	0.070
10	0^{+0}_{-0}	0^{+0}_{-0}	0^{+0}_{-0}	0.081	0.074	0.081
11	$0^{+0.24}_{-0}$	$0.08^{+0.18}_{-0.08}$	$0.08^{+0.22}_{-0.08}$	0.063	0.067	0.074
12	$0^{+0.22}_{-0}$	$0^{+0.22}_{-0}$	$0^{+0.26}_{-0}$	0.024	0.024	0.039
13	0^{+0}_{-0}	0^{+0}_{-0}	0^{+0}_{-0}	0.074	0.067	0.031
14	$0.18^{+0.22}_{-0.14}$	$0.18^{+0.16}_{-0.16}$	$0.22^{+0.12}_{-0.22}$	0.053	0.043	0.031
15	$0^{+0.06}_{-0}$	$0.06^{+0.08}_{-0.06}$	$0.08^{+0.08}_{-0.08}$	0.145	0.142	0.083
16	$0^{+0.04}_{-0}$	$0^{+0.04}_{-0}$	$0.04^{+0.04}_{-0.04}$	0.085	0.069	0.05
17	$0^{+0.1}_{-0}$	$0.08^{+0.22}_{-0.08}$	$0.08^{+0.24}_{-0.08}$	0.037	0.039	0.021
18	0^{+0}_{-0}	0^{+0}_{-0}	$0^{+0.04}_{-0}$	0.084	0.077	0.035
19	$0.18^{+0.14}_{-0.04}$	$0.22^{+0.06}_{-0.1}$	$0.2^{+0.06}_{-0.06}$	0.040	0.043	0.049
20	$0.18^{+0.06}_{-0.14}$	$0.12^{+0.04}_{-0.06}$	$0.08^{+0.1}_{-0.04}$	0.021	0.024	0.036
21	$0.54^{+0.14}_{-0.14}$	$0.54^{+0.14}_{-0.14}$	$0.54^{+0.14}_{-0.14}$	0.076	0.076	0.099
22	$0.32^{+0.08}_{-0.16}$	$0.26^{+0.08}_{-0.1}$	$0.24^{+0.1}_{-0.08}$	0.034	0.037	0.055
23	$0^{+0.04}_{-0}$	0^{+0}_{-0}	0^{+0}_{-0}	0.023	0.035	0.032
24	$0^{+0.98}_{-0}$	$0.06^{+0.86}_{-0.06}$	$0.18^{+0.76}_{-0.18}$	0.036	0.055	0.062
25	$0^{+0.1}_{-0}$	$0.08^{+0.26}_{-0.08}$	$0.1^{+0.26}_{-0.1}$	0.026	0.025	0.014
26	$0^{+0.22}_{-0}$	$0^{+0.38}_{-0}$	$0^{+0.42}_{-0}$	0.009	0.009	0.006
27	$0^{+0.04}_{-0}$	$0.02^{+0.14}_{-0.02}$	$0.04^{+0.14}_{-0.04}$	0.049	0.048	0.032
28	$0^{+0.54}_{-0}$	$0.02^{+0.46}_{-0.02}$	$0.04^{+0.44}_{-0.04}$	0.103	0.107	0.094
29	$0^{+0.06}_{-0}$	$0^{+0.04}_{-0}$	$0^{+0.08}_{-0}$	0.051	0.049	0.020
30	$0^{+0.32}_{-0}$	$0.08^{+0.24}_{-0.08}$	$0.08^{+0.26}_{-0.08}$	0.023	0.023	0.029

Table A.2 (Continued)

ID	$E(B-V)$ $Z_\odot$	$E(B-V)$ $0.4Z_\odot$	$E(B-V)$ $0.2Z_\odot$	$M(10^6 M_\odot)$ $Z_\odot$	$M(10^6 M_\odot)$ $0.4Z_\odot$	$M(10^6 M_\odot)$ $0.2Z_\odot$
31	$0.2^{+0.18}_{-0.18}$	$0.2^{+0.18}_{-0.18}$	$0.14^{+0.26}_{-0.14}$	0.010	0.012	0.009
32	$0.04^{+0.06}_{-0.04}$	$0^{+0.1}_{-0}$	$0^{+0.12}_{-0}$	0.095	0.090	0.039
33	$0^{+0.06}_{-0}$	$0^{+0.04}_{-0}$	$0^{+0.04}_{-0}$	0.010	0.010	0.009
34	$0^{+0.12}_{-0}$	$0.22^{+0.18}_{-0.12}$	$0.24^{+0.18}_{-0.14}$	0.082	0.08	0.027
35	$0^{+0.08}_{-0}$	$0.12^{+0.16}_{-0.1}$	$0.14^{+0.18}_{-0.14}$	0.074	0.073	0.035
36	0^{+0}_{-0}	0^{+0}_{-0}	0^{+0}_{-0}	0.127	0.118	0.089
37	$0^{+0.14}_{-0}$	$0^{+0.12}_{-0}$	$0^{+0.16}_{-0}$	0.012	0.007	0.005
38	$0.02^{+0.1}_{-0.02}$	$0.24^{+0.16}_{-0.1}$	$0.26^{+0.18}_{-0.26}$	0.105	0.103	0.035
39	$0.26^{+0.2}_{-0.26}$	$0.3^{+0.12}_{-0.3}$	$0^{+0.42}_{-0}$	0.009	0.028	0.024
40	$0^{+0.08}_{-0}$	$0^{+0.04}_{-0}$	$0^{+0.04}_{-0}$	0.029	0.026	0.018
41	$0.06^{+0.12}_{-0.06}$	$0.22^{+0.2}_{-0.14}$	$0^{+0.44}_{-0}$	0.272	0.109	0.045
42	$0.18^{+0.24}_{-0.18}$	$0.42^{+0.28}_{-0.38}$	$0^{+0.72}_{-0}$	0.130	0.094	0.030
43	$0.12^{+0.42}_{-0.12}$	$0.3^{+0.3}_{-0.3}$	$0^{+0.62}_{-0}$	0.264	0.140	0.063
44	$0.08^{+0.14}_{-0.06}$	$0.12^{+0.06}_{-0.06}$	$0.12^{+0.06}_{-0.04}$	0.167	0.167	0.145
45	$0^{+0.04}_{-0}$	0^{+0}_{-0}	0^{+0}_{-0}	0.019	0.028	0.026
46	$0^{+0.14}_{-0}$	$0^{+0.14}_{-0}$	$0^{+0.18}_{-0}$	0.064	0.032	0.046
47	$0^{+0.08}_{-0}$	$0.06^{+0.18}_{-0.06}$	$0.08^{+0.2}_{-0.08}$	0.041	0.041	0.024
48	$0^{+0.1}_{-0}$	$0^{+0.1}_{-0}$	$0^{+0.12}_{-0}$	0.011	0.010	0.011
49	$0.04^{+0.08}_{-0.04}$	$0^{+0.08}_{-0}$	$0.04^{+0.1}_{-0.04}$	0.103	0.053	0.043
50	$0^{+0.08}_{-0}$	$0.12^{+0.18}_{-0.12}$	$0.12^{+0.22}_{-0.12}$	0.028	0.030	0.014
51	$0.14^{+0.16}_{-0.08}$	$0.18^{+0.08}_{-0.08}$	$0.18^{+0.08}_{-0.06}$	0.158	0.158	0.137
52	$0^{+0.48}_{-0}$	$0^{+0.4}_{-0}$	$0^{+0.48}_{-0}$	0.002	0.019	0.002
53	$0.02^{+0.12}_{-0.02}$	$0^{+0.12}_{-0}$	$0^{+0.16}_{-0}$	0.025	0.013	0.010
54	$0.2^{+0.18}_{-0.18}$	$0.42^{+0.28}_{-0.18}$	$0^{+0.56}_{-0}$	0.127	0.091	0.031
55	0^{+0}_{-0}	$0.1^{+0.06}_{-0.04}$	$0.12^{+0.06}_{-0.06}$	0.192	0.189	0.096
56	0^{+0}_{-0}	$0.04^{+0.12}_{-0.04}$	$0.06^{+0.06}_{-0.06}$	0.27	0.266	0.166
57	0^{+0}_{-0}	$0.02^{+0.08}_{-0.02}$	$0^{+0.14}_{-0}$	0.074	0.038	0.060
58	$0^{+0.18}_{-0}$	$0.22^{+0.24}_{-0.22}$	$0.16^{+0.34}_{-0.16}$	0.012	0.015	0.012
59	$0.02^{+0.26}_{-0.02}$	$0.06^{+0.18}_{-0.06}$	$0^{+0.22}_{-0}$	0.012	0.010	0.008
60	$0^{+0.06}_{-0}$	$0.14^{+0.12}_{-0.14}$	$0.08^{+0.2}_{-0.08}$	0.101	0.055	0.058
61	$0.2^{+0.2}_{-0.2}$	$0.42^{+0.26}_{-0.22}$	$0^{+0.2}_{-0}$	0.160	0.114	0.038
62	$0^{+0.16}_{-0}$	$0^{+0.16}_{-0}$	$0^{+0.16}_{-0}$	0.005	0.005	0.004
63	$0^{+0.1}_{-0}$	$0^{+0.1}_{-0}$	$0^{+0.12}_{-0}$	0.002	0.002	0.001
64	$0^{+0.52}_{-0}$	$0^{+0.44}_{-0}$	$0^{+0.46}_{-0}$	0.002	0.002	0.002
65	$0^{+0.08}_{-0}$	$0.2^{+0.12}_{-0.1}$	$0.2^{+0.16}_{-0.1}$	0.102	0.108	0.039
66	$0.7^{+0.18}_{-0.3}$	$0.66^{+0.18}_{-0.22}$	$0.6^{+0.22}_{-0.16}$	0.552	0.637	0.535
67	$0^{+0.2}_{-0}$	$0^{+0.28}_{-0}$	$0^{+0.28}_{-0}$	0.048	0.046	0.054
68	$0^{+0.5}_{-0}$	$0.18^{+0.16}_{-0.18}$	$0.1^{+0.26}_{-0.1}$	0.016	0.021	0.015
69	$0^{+0.04}_{-0}$	$0^{+0.04}_{-0}$	0^{+0}_{-0}	0.037	0.037	0.033

Table A.2 (Continued)

ID	$E(B-V)$ $Z_\odot$	$E(B-V)$ $0.4Z_\odot$	$E(B-V)$ $0.2Z_\odot$	$M(10^6 M_\odot)$ $Z_\odot$	$M(10^6 M_\odot)$ $0.4Z_\odot$	$M(10^6 M_\odot)$ $0.2Z_\odot$
70	$0^{+0.16}_{-0}$	$0.04^{+0.06}_{-0.04}$	$0.06^{+0.06}_{-0.06}$	0.103	0.096	0.083
71	$0^{+0.28}_{-0}$	$0^{+0.2}_{-0}$	$0^{+0.16}_{-0}$	0.010	0.006	0.004
72	$0^{+0.08}_{-0}$	$0.18^{+0.16}_{-0.18}$	$0.1^{+0.26}_{-0.1}$	0.015	0.020	0.018
73	$0.54^{+0.12}_{-0.2}$	$0.5^{+0.1}_{-0.12}$	$0.5^{+0.12}_{-0.12}$	0.238	0.238	0.256
74	$0^{+0.06}_{-0}$	$0.08^{+0.2}_{-0.08}$	$0.08^{+0.24}_{-0.08}$	0.036	0.038	0.021
75	$0^{+0.06}_{-0}$	$0.16^{+0.1}_{-0.16}$	$0.08^{+0.2}_{-0.08}$	0.028	0.038	0.037
76	0^{+0}_{-0}	0^{+0}_{-0}	0^{+0}_{-0}	0.280	0.164	0.117
77	$0.18^{+0.26}_{-0.18}$	$0.42^{+0.3}_{-0.42}$	$0^{+0.7}_{-0}$	0.116	0.084	0.026
78	$0.92^{+0.18}_{-0.16}$	$0.94^{+0.16}_{-0.16}$	$0.94^{+0.16}_{-0.22}$	0.376	0.376	0.424
79	$0.48^{+0.1}_{-0.1}$	$0.46^{+0.1}_{-0.1}$	$0.42^{+0.1}_{-0.1}$	0.133	0.153	0.120
80	$0.36^{+0.1}_{-0.1}$	$0.38^{+0.1}_{-0.1}$	$0.36^{+0.12}_{-0.1}$	0.056	0.060	0.073
81	0^{+0}_{-0}	0^{+0}_{-0}	0^{+0}_{-0}	0.042	0.042	0.039
82	0^{+1}_{-0}	$0^{+0.94}_{-0}$	$0^{+0.94}_{-0}$	0.005	0.005	0.004
83	$0^{+0.04}_{-0}$	$0^{+0.16}_{-0}$	$0^{+0.2}_{-0}$	0.032	0.034	0.024
84	0^{+0}_{-0}	$0^{+0.06}_{-0}$	$0^{+0.08}_{-0}$	0.108	0.054	0.092
85	0^{+0}_{-0}	$0.08^{+0.14}_{-0.08}$	$0.08^{+0.16}_{-0.08}$	0.170	0.179	0.098
86	$0^{+0.04}_{-0}$	$0.12^{+0.16}_{-0.08}$	$0.14^{+0.18}_{-0.1}$	0.085	0.083	0.040
87	$0.06^{+0.06}_{-0.04}$	$0.06^{+0.06}_{-0.04}$	$0.02^{+0.04}_{-0.02}$	0.067	0.077	0.068
88	0^{+0}_{-0}	0^{+0}_{-0}	0^{+0}_{-0}	0.213	0.194	0.089
89	$0^{+0.22}_{-0}$	$0^{+0.22}_{-0}$	$0^{+0.2}_{-0}$	0.005	0.007	0.007
90	$0.02^{+0.08}_{-0.02}$	$0.02^{+0.08}_{-0.02}$	$0^{+0.1}_{-0}$	0.015	0.016	0.011
91	$0.66^{+0.26}_{-0.3}$	$0.64^{+0.26}_{-0.26}$	$0.62^{+0.26}_{-0.24}$	0.089	0.089	0.070
92	$0^{+0.2}_{-0}$	$0.02^{+0.14}_{-0.02}$	$0.04^{+0.12}_{-0.04}$	0.023	0.022	0.020
93	$0.02^{+0.04}_{-0.02}$	$0.24^{+0.1}_{-0.04}$	$0.26^{+0.08}_{-0.06}$	0.359	0.353	0.118
94	$0.14^{+0.3}_{-0.14}$	$0.16^{+0.24}_{-0.16}$	$0.14^{+0.24}_{-0.14}$	0.009	0.009	0.011
95	$0.26^{+0.18}_{-0.24}$	$0.26^{+0.18}_{-0.26}$	$0.18^{+0.18}_{-0.18}$	0.024	0.032	0.023
96	$0^{+0.06}_{-0}$	$0.2^{+0.06}_{-0.14}$	$0.12^{+0.18}_{-0.08}$	0.062	0.081	0.086
97	$0.08^{+0.4}_{-0.08}$	$0.2^{+0.3}_{-0.2}$	$0^{+0.52}_{-0}$	0.176	0.091	0.078
98	$0.02^{+0.28}_{-0.02}$	$0.2^{+0.36}_{-0.2}$	$0.22^{+0.36}_{-0.22}$	0.048	0.048	0.018
99	$0.2^{+0.18}_{-0.2}$	$0.24^{+0.12}_{-0.24}$	$0.2^{+0.12}_{-0.2}$	0.033	0.059	0.051
100	$0^{+0.1}_{-0}$	$0.12^{+0.2}_{-0.1}$	$0.14^{+0.2}_{-0.14}$	0.055	0.055	0.032
101	$0.26^{+0.42}_{-0.26}$	$0.3^{+0.34}_{-0.3}$	$0.26^{+0.38}_{-0.26}$	0.007	0.012	0.010
102	$0^{+0.04}_{-0}$	$0.14^{+0.1}_{-0.14}$	$0.06^{+0.2}_{-0.06}$	0.025	0.033	0.035
103	$0^{+0.18}_{-0}$	$0.14^{+0.28}_{-0.14}$	$0.14^{+0.3}_{-0.14}$	0.051	0.054	0.024
104	$0.12^{+0.28}_{-0.12}$	$0.08^{+0.22}_{-0.08}$	$0^{+0.38}_{-0}$	0.009	0.011	0.009
105	$0.18^{+0.58}_{-0.12}$	$0.56^{+0.24}_{-0.56}$	$0.48^{+0.44}_{-0.48}$	0.092	0.121	0.028
106	$0^{+0.62}_{-0}$	$0^{+0.54}_{-0}$	$0.02^{+0.56}_{-0.02}$	0.003	0.025	0.003
107	$0^{+0.08}_{-0}$	$0.1^{+0.14}_{-0.1}$	$0^{+0.04}_{-0}$	0.153	0.058	0.03
108	$0^{+0.04}_{-0}$	$0^{+0.16}_{-0}$	$0^{+0.18}_{-0}$	0.026	0.027	0.021

Table A.2 (Continued)

ID	$E(B-V)$ $Z_\odot$	$E(B-V)$ $0.4Z_\odot$	$E(B-V)$ $0.2Z_\odot$	$M(10^6 M_\odot)$ $Z_\odot$	$M(10^6 M_\odot)$ $0.4Z_\odot$	$M(10^6 M_\odot)$ $0.2Z_\odot$
109	$0^{+0.12}_{-0}$	$0.18^{+0.18}_{-0.12}$	$0.2^{+0.2}_{-0.2}$	0.093	0.091	0.035
110	$0.02^{+0.16}_{-0.02}$	$0.2^{+0.2}_{-0.14}$	$0^{+0.34}_{-0}$	0.167	0.058	0.022
111	$0^{+0.08}_{-0}$	$0^{+0.26}_{-0}$	$0.02^{+0.26}_{-0.02}$	0.019	0.019	0.013
112	$0^{+0.24}_{-0}$	$0^{+0.2}_{-0}$	$0^{+0.16}_{-0}$	0.006	0.006	0.004
113	$0.02^{+0.4}_{-0.02}$	$0.32^{+0.12}_{-0.18}$	$0.24^{+0.24}_{-0.18}$	0.053	0.070	0.025
114	$0^{+0.08}_{-0}$	$0^{+0.2}_{-0}$	$0^{+0.24}_{-0}$	0.010	0.006	0.010
115	$0^{+0.28}_{-0}$	$0^{+0.22}_{-0}$	$0^{+0.14}_{-0}$	0.008	0.007	0.003
116	$0^{+0.1}_{-0}$	$0.16^{+0.14}_{-0.16}$	$0.08^{+0.24}_{-0.08}$	0.018	0.023	0.019
117	$0^{+0.16}_{-0}$	$0^{+0.36}_{-0}$	$0.02^{+0.36}_{-0.02}$	0.012	0.012	0.009
118	$0^{+0.12}_{-0}$	$0.06^{+0.22}_{-0.06}$	$0.06^{+0.26}_{-0.06}$	0.035	0.035	0.017
119	$0^{+0.1}_{-0}$	$0.04^{+0.24}_{-0.04}$	$0.04^{+0.28}_{-0.04}$	0.025	0.027	0.014
120	$0^{+0.06}_{-0}$	$0.12^{+0.18}_{-0.12}$	$0.12^{+0.22}_{-0.12}$	0.055	0.058	0.027
121	$0^{+0.04}_{-0}$	0^{+0}_{-0}	0^{+0}_{-0}	0.015	0.014	0.014
122	$0.56^{+0.16}_{-0.16}$	$0.54^{+0.16}_{-0.16}$	$0.5^{+0.16}_{-0.16}$	0.056	0.061	0.047
123	$0.42^{+0.12}_{-0.12}$	$0.4^{+0.12}_{-0.12}$	$0.36^{+0.12}_{-0.12}$	0.038	0.044	0.035
124	$0.32^{+0.4}_{-0.32}$	$0.36^{+0.3}_{-0.36}$	$0.36^{+0.3}_{-0.36}$	0.013	0.013	0.011
125	$0.26^{+0.18}_{-0.26}$	$0.2^{+0.28}_{-0.2}$	$0.22^{+0.38}_{-0.22}$	0.020	0.014	0.014
126	$0^{+0.1}_{-0}$	$0^{+0.1}_{-0}$	$0^{+0.12}_{-0}$	0.004	0.004	0.002
127	$0^{+0.12}_{-0}$	$0.12^{+0.22}_{-0.12}$	$0^{+0.26}_{-0}$	0.075	0.030	0.014
128	$0^{+0.1}_{-0}$	$0.12^{+0.22}_{-0.12}$	$0.14^{+0.24}_{-0.14}$	0.027	0.026	0.012
129	$0.08^{+0.14}_{-0.08}$	$0.26^{+0.2}_{-0.14}$	$0^{+0.16}_{-0}$	0.134	0.060	0.023
130	0^{+0}_{-0}	$0.02^{+0.14}_{-0.02}$	$0.04^{+0.16}_{-0.04}$	0.060	0.059	0.034
131	$0.42^{+0.5}_{-0.42}$	$0.4^{+0.58}_{-0.4}$	$0.24^{+0.74}_{-0.24}$	0.209	0.514	0.047
132	$0^{+0.04}_{-0}$	$0.04^{+0.18}_{-0.04}$	$0.06^{+0.2}_{-0.06}$	0.029	0.028	0.018
133	$0^{+0.22}_{-0}$	$0.02^{+0.24}_{-0.02}$	$0^{+0.3}_{-0}$	0.015	0.015	0.023
134	$0^{+0.26}_{-0}$	$0.06^{+0.2}_{-0.06}$	$0^{+0.3}_{-0}$	0.075	0.029	0.038
135	$0^{+0.06}_{-0}$	$0^{+0.22}_{-0}$	$0^{+0.06}_{-0}$	0.061	0.127	0.010
136	$0.22^{+0.28}_{-0.2}$	$0.46^{+0.32}_{-0.46}$	$0.02^{+0.68}_{-0.02}$	0.101	0.077	0.024
137	$0.52^{+0.6}_{-0.52}$	$0.52^{+0.7}_{-0.52}$	$0.34^{+0.82}_{-0.34}$	0.198	0.519	0.044
138	$0^{+0.32}_{-0}$	$0^{+0.32}_{-0}$	$0^{+0.36}_{-0}$	0.119	0.251	0.048
139	$0.04^{+0.06}_{-0.04}$	$0^{+0.1}_{-0}$	$0^{+0.06}_{-0}$	0.033	0.015	0.027
140	$0.6^{+0.36}_{-0.6}$	$0.54^{+0.36}_{-0.54}$	$0.56^{+0.36}_{-0.56}$	0.022	0.020	0.023
141	$0^{+0.18}_{-0}$	$0.16^{+0.26}_{-0.16}$	$0^{+0.42}_{-0}$	0.056	0.025	0.010
142	$0.08^{+0.2}_{-0.08}$	$0.1^{+0.12}_{-0.1}$	$0.12^{+0.12}_{-0.12}$	0.012	0.011	0.010
143	$0.12^{+0.14}_{-0.12}$	$0.34^{+0.2}_{-0.14}$	$0^{+0.54}_{-0}$	0.141	0.083	0.028
144	$0^{+0.06}_{-0}$	$0.1^{+0.16}_{-0.1}$	$0.1^{+0.2}_{-0.1}$	0.031	0.033	0.017
145	$0.16^{+0.06}_{-0.08}$	$0.14^{+0.06}_{-0.06}$	$0.14^{+0.06}_{-0.06}$	0.034	0.032	0.025
146	$0.08^{+0.28}_{-0.08}$	$0.22^{+0.34}_{-0.22}$	$0^{+0.48}_{-0}$	0.054	0.021	0.009
147	0^{+0}_{-0}	$0.08^{+0.08}_{-0.04}$	$0.08^{+0.08}_{-0.06}$	0.150	0.158	0.073

Table A.2 (Continued)

ID	$E(B-V)$ $Z_\odot$	$E(B-V)$ $0.4Z_\odot$	$E(B-V)$ $0.2Z_\odot$	$M(10^6 M_\odot)$ $Z_\odot$	$M(10^6 M_\odot)$ $0.4Z_\odot$	$M(10^6 M_\odot)$ $0.2Z_\odot$
148	$0^{+0.16}_{-0}$	$0.02^{+0.34}_{-0.02}$	$0.04^{+0.36}_{-0.04}$	0.010	0.009	0.006
149	$0^{+0.16}_{-0}$	$0^{+0.26}_{-0}$	$0^{+0.28}_{-0}$	0.009	0.009	0.008
150	$0^{+0.06}_{-0}$	$0.12^{+0.12}_{-0.06}$	$0.14^{+0.14}_{-0.08}$	0.099	0.097	0.057
151	$0^{+0.22}_{-0}$	$0.12^{+0.32}_{-0.12}$	$0.14^{+0.34}_{-0.14}$	0.017	0.017	0.008
152	$0.12^{+0.14}_{-0.12}$	$0.34^{+0.2}_{-0.14}$	$0^{+0.1}_{-0}$	0.131	0.074	0.025
153	$0.1^{+0.12}_{-0.1}$	$0.3^{+0.18}_{-0.1}$	$0^{+0.06}_{-0}$	0.173	0.087	0.031
154	$0.72^{+0.32}_{-0.16}$	$0.72^{+0.5}_{-0.34}$	$0.54^{+0.46}_{-0.18}$	1.043	2.718	0.23
155	$0.2^{+0.58}_{-0.2}$	$0.14^{+0.68}_{-0.14}$	$0^{+0.82}_{-0}$	0.075	0.172	0.018
156	$0.42^{+0.5}_{-0.42}$	$0.26^{+0.58}_{-0.26}$	$0.32^{+0.56}_{-0.32}$	0.012	0.008	0.014
157	$0^{+0.26}_{-0}$	$0.02^{+0.28}_{-0.02}$	$0^{+0.34}_{-0}$	0.041	0.013	0.020
158	$0^{+0.3}_{-0}$	$0^{+0.4}_{-0}$	$0^{+0.4}_{-0}$	0.041	0.086	0.007
n01	0^{+0}_{-0}	0^{+0}_{-0}	0^{+0}_{-0}	0.795	0.725	0.333
n02	0^{+0}_{-0}	0^{+0}_{-0}	0^{+0}_{-0}	0.479	0.437	0.304
n03	0^{+0}_{-0}	$0^{+0.04}_{-0}$	$0^{+0.08}_{-0}$	0.627	0.332	0.480
n04	$0^{+0.04}_{-0}$	0^{+0}_{-0}	$0^{+0.04}_{-0}$	0.758	0.444	0.317
n05	$0.34^{+0.16}_{-0.26}$	$0.38^{+0.08}_{-0.38}$	$0.4^{+0.08}_{-0.4}$	2.22	2.07	1.80
n06	0^{+0}_{-0}	0^{+0}_{-0}	$0^{+0.04}_{-0}$	1.44	1.09	0.601
n07	$0.24^{+0.06}_{-0.06}$	$0.44^{+0.1}_{-0.06}$	$0^{+0.06}_{-0}$	6.54	4.99	1.80
n08	$0.28^{+0.12}_{-0.24}$	$0.12^{+0.26}_{-0.12}$	$0.26^{+0.08}_{-0.26}$	1.82	1.11	2.98
n09	$0^{+0.08}_{-0}$	$0^{+0.22}_{-0}$	$0.02^{+0.24}_{-0.02}$	2.16	2.12	1.53
n10	$0.38^{+0.14}_{-0.06}$	$0.42^{+0.06}_{-0.04}$	$0.36^{+0.06}_{-0.04}$	0.730	1.38	1.20
n11	$0.26^{+0.08}_{-0.08}$	$0.4^{+0.12}_{-0.08}$	$0^{+0.06}_{-0}$	8.46	5.67	2.51
n12	$0^{+0.06}_{-0}$	$0.1^{+0.12}_{-0.1}$	$0.02^{+0.24}_{-0.02}$	0.853	1.13	1.15
n13	$0.28^{+0.14}_{-0.14}$	$0.38^{+0.2}_{-0.38}$	$0^{+0.28}_{-0}$	17.4	11.6	11.4
n14	$0.28^{+0.02}_{-0.04}$	$0.34^{+0.02}_{-0.04}$	0^{+0}_{-0}	89.0	49.4	28.9
n15	$0.28^{+0.14}_{-0.04}$	$0.32^{+0.04}_{-0.04}$	$0.34^{+0.04}_{-0.04}$	1.699	1.584	1.376
n16	$0.16^{+0.1}_{-0.1}$	$0.28^{+0.14}_{-0.1}$	$0^{+0.4}_{-0}$	22.7	11.9	10.5

Table A.3 H II region photometry

Region	FUV[a]	NUV[a]	F380W[a]	F555W[a]	F606W[a]	F814W[a]
A	2080±95	1890±81	549 ± 4	396 ± 1	459 ± 1	276 ± 1
B	1130±110	474±63	468 ± 4	–	202 ± 2	110 ± 2
C	1550±80	551±40	–	–	–	153 ± 1
D	500±91	236±58	258 ± 3	–	140 ± 1	86.2 ± 1.7
E	$\leq$ 218±25	$\leq$ 64.8±21.2	15.8 ± 3.0	–	11.2 ± 0.7	–
F	13600±100	6220±110	13200 ± 100	9080 ± 10	8610 ± 10	5690 ± 10
G	$\leq$ 70.3±11.2	$\leq$ 22.4±8.3	–	17.2 ± 0.4	16.9 ± 0.4	8.32 ± 0.28
H	$\leq$ 93.2±10.4	$\leq$ 43.2±6.5	–	27.6 ± 0.4	25.2 ± 0.4	10.9 ± 0.3
I	$\leq$ 39.2±7.3	$\leq$ 32.0±5.9	–	14.9 ± 0.4	14.8 ± 0.4	9.73 ± 0.27
J	$\leq$ 41.0±6.3	$\leq$ 34.8±5.7	–	10.4 ± 0.4	13.0 ± 0.4	5.07 ± 0.28

[a]FUV, NUV, F380W, F555W, F606W, F814W in units of 10^{-18} erg s^{-1} cm^{-2} Å^{-1}

Table A.3 (Continued)

Region	Hα[a]	3.6 μm[b]	4.5 μm[b]	5.8 μm[b]	8.0 μm[b]
A	139 ± 14	2.56 ± 0.07	1.58 ± 0.04	8.48 ± 0.12	24.9 ± 0.3
B	92.9 ± 9.4	0.431 ± 0.010	0.391 ± 0.006	1.01 ± 0.05	2.69 ± 0.23
C	52.8 ± 5.3	0.235 ± 0.019	0.235 ± 0.010	0.553 ± 0.034	1.20 ± 0.10
D	32.0 ± 3.5	0.357 ± 0.061	0.255 ± 0.048	0.980 ± 0.119	2.42 ± 0.34
E	7.32 ± 0.79	$\leq 0.141 \pm 0.011$	$\leq 0.0851 \pm 0.0150$	$\leq 0.365 \pm 0.050$	$\leq 1.37 \pm 0.09$
F	1140 ± 110	14.5 ± 0.1	12.9 ± 0.1	40.2 ± 0.2	114 ± 1
G	2.8 ± 0.3	0.0152 ± 0.0034	–	0.0552 ± 0.0127	0.105 ± 0.015
H	4.87 ± 0.51	0.0305 ± 0.0035	0.0193 ± 0.003	0.0804 ± 0.0101	0.154 ± 0.011
I	2.02 ± 0.23	0.0259 ± 0.0032	0.0186 ± 0.003	0.0665 ± 0.0107	0.221 ± 0.015
J	3.50 ± 0.36	0.0211 ± 0.0033	0.0111 ± 0.005	0.0609 ± 0.0108	0.159 ± 0.012

[a]Hα in units of 10^{-15} erg s^{-1} cm^{-2}
[b]3.6, 4.5, 5.8, 8.0 μm in units of mJy

Table A.4 H II region ages (Myr)

Region	Age (inst)[a] $0.4Z_\odot$	Age (inst)[a] $0.2Z_\odot$	Age (cont)[a] $0.4Z_\odot$	Age (cont)[a] $0.2Z_\odot$	Med. Age[b] $0.4Z_\odot$	Med Age[b] $0.2Z_\odot$
A	10^{+1}_{-1}	10^{+1}_{-1}	1^{+1}_{-1}	1^{+1}_{-1}	5^{+1}_{-1}	5^{+2}_{-2}
B	273^{+65}_{-96}	88^{+16}_{-18}	489^{+273}_{-207}	128^{+1272}_{-42}	14^{+1}_{-3}	15^{+1}_{-2}
C	–	–	–	–	–	–
D	292^{+135}_{-234}	87^{+84}_{-82}	497^{+1103}_{-435}	1200^{+900}_{-1195}	16^{+4}_{-8}	17^{+3}_{-4}
E	–	–	–	–	–	–
F	222^{+6}_{-6}	86^{+1}_{-1}	421^{+12}_{-11}	2600^{+100}_{-100}	10^{+16}_{-2}	15^{+1}_{-1}
G	6^{+2}_{-1}	6^{+2}_{-1}	1^{+15}_{-1}	1^{+19}_{-1}	21^{+959}_{-15}	266^{+198}_{-257}
H	6^{+1}_{-1}	6^{+2}_{-1}	1^{+8}_{-1}	2^{+8}_{-2}	182^{+36}_{-177}	68^{+24}_{-62}
I	7^{+376}_{-2}	8^{+1092}_{-2}	1^{+3799}_{-1}	2^{+4298}_{-2}	13^{+12}_{-7}	120^{+74}_{-114}
J	4^{+1}_{-1}	4^{+1}_{-1}	1^{+7}_{-1}	1^{+8}_{-1}	4^{+1}_{-1}	5^{+1}_{-1}

[a]Ages in Myr from large-aperture broadband photometry for instantaneous starburst (inst) and continuous star formation (cont) models

[b]Median age of *HST*-resolved clusters in the region. These are useful only for regions A, B, D, F; see text for explanation.

Table A.4 (Continued)

Region	EW(Hα) Å	EW(Hα) $0.4Z_\odot$	Lit. Age[a] $0.2Z_\odot$	f_c[b]	$L_{\mathrm{H}\alpha}/L_{\mathrm{X}}$[c]	
A	29.8 ± 3.3	10^{+0}_{-1}	11^{+0}_{-0}	5 ± 0.5	0.18	22
B	39.6 ± 5	9^{+0}_{-0}	10^{+0}_{-0}	3.5 ± 0.5	0.26	11
C	27.3 ± 3	10^{+0}_{-1}	11^{+1}_{-0}	4.5 ± 0.5	–	6.1
D	22.4 ± 3.4	11^{+1}_{-0}	12^{+1}_{-1}	–	0.17	≥ 23
E	56.2 ± 21	8^{+2}_{-1}	9^{+1}_{-1}	–	–	3.1
F	15 ± 1.6	12^{+0}_{-0}	14^{+1}_{-1}	$5; 15-50$	0.25	1.5
G	28.5 ± 7	10^{+1}_{-1}	11^{+1}_{-1}	–	0.06	–
H	27.3 ± 4.4	10^{+0}_{-1}	11^{+1}_{-0}	–	0.27	–
I	12.1 ± 2.1	13^{+1}_{-1}	16^{+0}_{-1}	–	0.15	–
J	113 ± 82	6^{+3}_{-0}	7^{+3}_{-1}	–	0.31	–

[a]Ages determined by photoionization modeling. A, B, C from García-Vargas et al. (1997); F from González Delgado et al. (1995) and González Delgado et al. (1999)

[b]Fraction of H II region luminosity contained in sample clusters in F814W

[c]From Smith et al. (2005a)

Table A.5 H II region extinctions

Region	$E(B-V)$ (inst) $0.4Z_\odot$	$E(B-V)$ (inst) $0.2Z_\odot$	$E(B-V)$ (cont) $0.4Z_\odot$	$E(B-V)$ (cont) $0.2Z_\odot$	Lit. $E(B-V)^a$
A	$0.22^{+0.02}_{-0.02}$	$0.14^{+0.02}_{-0.02}$	$0.36^{+0.02}_{-0.02}$	$0.34^{+0.02}_{-0.02}$	0.25
B	$0^{+0.06}_{-0}$	$0.12^{+0.08}_{-0.08}$	$0.12^{+0.08}_{-0.10}$	$0.18^{+0.08}_{-0.18}$	0.28
C	–	–	–	–	0.34
D	$0.10^{+0.14}_{-0.10}$	$0.20^{+0.08}_{-0.20}$	$0.18^{+0.12}_{-0.18}$	$0^{+0.48}_{-0}$	–
E	–	–	–	–	–
F	$0.18^{+0.02}_{-0.18}$	$0.28^{+0.02}_{-0.02}$	$0.26^{+0.02}_{-0.02}$	0^{+0}_{-0}	0.22; 0.08
G	$0.24^{+0.08}_{-0.24}$	$0.42^{+0.08}_{-0.20}$	$0.22^{+0.14}_{-0.08}$	$0.20^{+0.16}_{-0.08}$	–
H	$0.12^{+0.06}_{-0.06}$	$0.28^{+0.06}_{-0.18}$	$0.08^{+0.14}_{-0.06}$	$0.08^{+0.12}_{-0.06}$	–
I	$0.24^{+0.30}_{-0.16}$	$0.44^{+0.14}_{-0.44}$	$0.44^{+0.16}_{-0.44}$	$0.44^{+0.44}_{-0.44}$	–
J	$0.42^{+0.12}_{-0.12}$	$0.38^{+0.12}_{-0.12}$	$0.14^{+0.16}_{-0.12}$	$0.12^{+0.16}_{-0.12}$	–

[a]A,B, C from González Delgado et al. (1995); F from González Delgado et al. (1995) (Balmer decrement) and González Delgado et al. (1999) (UV continuum)

APPENDIX B. Complete cluster data tables for Arp 261

Table B.1 Cluster magnitudes and EW(Hα)

ID	F300W mag	F555W mag	F625W mag	F814W mag	log[EW(Hα)/Å]
1	–	–	–	–	$1.39^{+0.22}_{-0.21}$
2	–	–	–	–	$0.61^{+0.40}_{-0.37}$
3	–	21.564±0.362	22.999±0.488	21.691±0.282	$1.13^{+0.07}_{-0.07}$
4	–	23.219±0.416	22.956±0.483	22.407±0.328	$0.35^{+0.10}_{-0.11}$
5	–	24.714±0.581	24.364±0.739	24.021±0.565	$1.18^{+0.46}_{-0.44}$
6	–	24.137±0.51	23.742±0.618	23.587±0.499	–
7	–	22.857±0.398	21.757±0.394	20.877±0.251	$0.89^{+0.44}_{-0.44}$
8	–	24.461±0.541	24.368±0.740	–	$2.61^{+1.31}_{-1.28}$
9	–	23.699±0.450	22.476±0.438	21.493±0.272	$0.51^{+0.28}_{-0.29}$
10	–	24.63±0.565	24.282±0.718	24.448±0.673	$0.51^{+0.42}_{-0.39}$
11	–	25.046±0.685	23.641±0.581	22.731±0.362	–
12	–	24.511±0.547	24.211±0.700	23.825±0.521	–
13	–	23.528±0.436	23.29±0.525	23.195±0.414	–
14	–	24.093±0.489	23.154±0.507	22.265±0.316	$1.11^{+0.18}_{-0.17}$
15	–	22.975±0.402	22.647±0.452	22.467±0.332	–
16	–	24.488±0.542	24.309±0.724	23.817±0.519	$0.16^{+0.34}_{-0.31}$
17	–	24.500±0.545	24.036±0.658	24.046±0.569	–
18	–	24.361±0.535	23.332±0.531	22.719±0.362	–
19	–	24.404±0.533	23.979±0.647	23.723±0.509	–
20	–	24.298±0.515	23.224±0.516	22.343±0.322	$1.09^{+0.06}_{-0.05}$
21	–	24.303±0.516	24.29±0.719	24.718±0.786	$1.63^{+0.55}_{-0.53}$
22	–	24.310±0.517	24.068±0.666	24.118±0.588	$1.31^{+0.48}_{-0.46}$
23	–	24.576±0.557	24.593±0.804	24.704±0.762	$1.69^{+0.74}_{-0.71}$
24	24.069±1.827	24.595±0.562	23.662±0.584	21.900±0.292	$1.54^{+0.30}_{-0.29}$
25	–	23.348±0.423	22.204±0.418	20.313±0.239	$1.31^{+0.22}_{-0.21}$
26	–	25.257±0.750	24.073±0.735	23.676±0.529	$0.99^{+0.26}_{-0.24}$
27	21.753±0.755	20.747±0.353	19.88±0.351	19.632±0.23	–
28	–	24.303±0.553	23.963±0.707	24.017±0.604	–
29	22.371±0.898	20.587±0.347	19.665±0.34	18.92±0.218	–
30	–	23.380±0.420	22.128±0.403	21.053±0.247	$0.22^{+0.29}_{-0.29}$

Table B.1 (Continued)

ID	F300W	F555W	F625W	F814W	log[EW(Hα)/Å]
	mag	mag	mag	mag	
31	20.171±0.553	24.074±0.496	20.743±0.363	20.829±0.249	$2.22^{+0.49}_{-0.50}$
32	–	24.522±0.550	23.997±0.650	23.335±0.433	$1.14^{+0.35}_{-0.34}$
33	–	24.306±0.518	24.007±0.652	24.069±0.571	–
34	23.862±1.712	–	24.998±0.943	–	$2.44^{+1.37}_{-1.32}$
35	24.087±1.756	22.325±0.373	20.995±0.358	19.926±0.226	–
36	23.969±1.787	24.198±0.502	24.08±0.669	23.881±0.536	–
37	–	24.246±0.509	23.766±0.603	23.519±0.463	–
38	–	24.919±0.622	24.055±0.663	26.766±2.486	$2.33^{+0.98}_{-0.95}$
39	–	24.495±0.544	24.120±0.678	23.667±0.49	$0.97^{+0.34}_{-0.32}$
40	–	24.834±0.601	23.988±0.648	24.036±0.567	$1.96^{+0.59}_{-0.58}$
41	–	–	23.427±0.546	23.493±0.472	$0.98^{+0.17}_{-0.16}$
42	22.772±1.053	24.029±0.483	23.510±0.558	23.944±0.546	$2.42^{+0.90}_{-0.89}$
43	23.441±1.387	23.185±0.414	22.968±0.485	22.845±0.369	–
44	22.736±1.045	23.803±0.460	23.394±0.540	23.127±0.403	–
45	–	23.634±0.445	23.16±0.508	23.692±0.5	$2.39^{+0.81}_{-0.80}$
46	–	24.47±0.539	24.175±0.691	23.493±0.459	–
47	–	23.855±0.465	23.456±0.550	23.019±0.389	–
48	–	–	20.776±0.354	19.815±0.225	$0.62^{+0.77}_{-0.69}$
49	23.868±1.738	24.364±0.527	23.742±0.599	23.452±0.456	–
50	22.631±1.007	22.943±0.402	23.943±0.640	23.427±0.466	$1.53^{+0.59}_{-0.56}$
51	–	24.371±0.529	23.861±0.623	23.038±0.393	$0.65^{+0.32}_{-0.30}$
52	–	21.083±0.356	19.992±0.352	18.375±0.223	$1.25^{+0.47}_{-0.45}$
53	22.711±1.035	24.187±0.503	23.582±0.570	23.798±0.522	$2.32^{+0.86}_{-0.85}$
54	–	23.179±0.413	21.797±0.396	20.822±0.249	$0.9^{+0.49}_{-0.48}$
55	–	23.957±0.477	23.537±0.563	23.787±0.527	$1.38^{+0.23}_{-0.21}$
56	–	22.986±0.402	21.886±0.400	20.983±0.253	$0.95^{+0.40}_{-0.40}$
57	–	24.489±0.546	23.569±0.568	24.724±0.759	$2.43^{+0.94}_{-0.92}$
58	23.458±1.382	24.462±0.540	23.972±0.646	23.164±0.410	$1.21^{+0.44}_{-0.41}$
59	–	24.523±0.548	24.124±0.679	23.292±0.426	$1.53^{+0.55}_{-0.53}$
60	–	23.322±0.433	22.948±0.497	22.266±0.325	$0.96^{+0.09}_{-0.09}$

Table B.1 (Continued)

ID	F300W mag	F555W mag	F625W mag	F814W mag	log[EW(Hα)/Å]
61	–	24.112±0.526	23.640±0.636	23.622±0.520	$0.82^{+0.10}_{-0.10}$
62	–	25.418±0.794	24.285±0.794	23.400±0.478	–
63	–	22.010±0.365	22.609±0.449	21.975±0.298	$0.88^{+0.13}_{-0.14}$
64	–	25.138±0.771	24.168±0.715	22.827±0.379	$0.51^{+0.51}_{-0.46}$
65	–	23.278±0.421	23.202±0.514	23.343±0.436	–
66	–	24.493±0.543	24.051±0.663	24.206±0.610	$1.86^{+0.68}_{-0.66}$
67	–	24.243±0.510	24.325±0.730	24.088±0.583	$1.19^{+0.57}_{-0.54}$
68	–	25.116±0.680	24.390±0.770	23.413±0.460	$0.90^{+0.62}_{-0.59}$
69	–	24.457±0.538	23.910±0.631	23.848±0.529	$0.54^{+0.28}_{-0.26}$
70	–	24.352±0.530	23.93±0.637	23.314±0.432	–
71	22.687±1.066	24.460±0.553	23.839±0.637	25.191±1.041	–
72	23.177±1.284	23.835±0.476	23.541±0.580	23.162±0.421	–
73	–	25.351±0.724	24.617±0.812	23.244±0.420	$1.96^{+0.86}_{-0.82}$
74	–	26.533±1.270	24.318±0.728	23.057±0.398	$0.10^{+0.54}_{-0.55}$
75	–	25.019±0.640	24.754±0.856	24.083±0.579	$1.84^{+0.84}_{-0.81}$
76	–	24.312±0.519	23.860±0.622	23.536±0.465	–
77	–	25.023±0.643	24.526±0.785	–	$2.42^{+1.19}_{-1.15}$
78	23.019±1.166	24.217±0.506	24.095±0.672	23.855±0.532	–
79	–	22.366±0.386	21.946±0.414	22.086±0.312	$2.12^{+0.35}_{-0.46}$
80	–	23.469±0.443	23.019±0.506	22.798±0.378	$2.14^{+0.61}_{-0.63}$
81	22.167±0.855	23.533±0.438	23.204±0.514	24.376±0.673	$2.57^{+1}_{-0.99}$
82	–	23.315±0.432	22.743±0.475	22.386±0.335	$1.89^{+0.81}_{-0.81}$
83	–	24.125±0.496	25.023±0.953	23.760±0.510	$1.87^{+1.10}_{-1.04}$
84	–	25.119±0.767	24.018±0.680	22.751±0.371	$2.08^{+0.64}_{-0.65}$
85	–	23.620±0.455	23.248±0.535	23.272±0.440	$1.53^{+0.48}_{-0.47}$
86	–	23.567±0.434	23.257±0.506	23.411±0.436	$1.02^{+0.62}_{-0.61}$
87	–	23.894±0.485	23.373±0.554	23.458±0.470	$0.20^{+0.12}_{-0.11}$
88	–	24.043±0.499	23.589±0.589	24.108±0.601	$1.38^{+0.36}_{-0.36}$
89	–	23.095±0.417	22.681±0.469	21.994±0.306	–
90	–	23.794±0.470	23.479±0.570	23.207±0.426	$1.52^{+0.30}_{-0.31}$

Table B.1 (Continued)

ID	F300W mag	F555W mag	F625W mag	F814W mag	log[EW(Hα)/Å]
91	–	23.228±0.426	22.957±0.498	22.735±0.368	$0.43^{+0.04}_{-0.03}$
92	–	23.571±0.451	22.780±0.479	22.730±0.368	$1.30^{+0.19}_{-0.19}$
93	22.845±1.090	24.373±0.529	24.061±0.666	24.144±0.601	–
94	–	22.714±0.399	22.270±0.435	22.679±0.363	$2.41^{+0.71}_{-0.77}$
95	21.533±0.712	22.989±0.404	22.882±0.476	23.094±0.409	$1.58^{+0.59}_{-0.57}$
96	–	23.191±0.424	22.562±0.458	22.733±0.370	$2.02^{+0.62}_{-0.66}$
97	23.017±1.172	–	23.385±0.540	23.586±0.472	$2.54^{+1.20}_{-1.17}$
98	21.269±0.667	22.064±0.371	21.578±0.387	22.023±0.301	$2.50^{+0.80}_{-0.81}$
99	22.699±1.038	22.541±0.385	22.051±0.409	22.487±0.337	$2.64^{+0.98}_{-0.98}$
100	23.099±1.247	23.716±0.465	23.173±0.525	22.843±0.383	$1.52^{+0.30}_{-0.31}$
101	20.422±0.571	20.947±0.355	20.594±0.360	21.160±0.259	$2.55^{+0.86}_{-0.87}$
102	22.070±0.914	23.386±0.456	22.565±0.481	23.787±0.571	$2.56^{+0.91}_{-1.00}$
103	22.977±1.152	23.353±0.424	23.070±0.497	22.851±0.372	–
104	23.552±1.454	23.208±0.418	23.113±0.503	22.695±0.362	$1.36^{+0.57}_{-0.54}$
105		24.594±0.577	24.278±0.740	24.977±0.908	$2.55^{+1.31}_{-1.28}$
106	–	25.370±0.724	25.475±1.149	23.696±0.494	$2.08^{+1.28}_{-1.20}$
107	–	25.292±0.726	24.759±0.888	25.305±1.021	$2.59^{+1.56}_{-1.50}$
108	22.663±1.015	23.422±0.430	22.632±0.451	23.369±0.446	$2.56^{+0.96}_{-0.95}$
109	–	23.745±0.454	23.706±0.592	24.089±0.579	$2.69^{+1.18}_{-1.16}$
110	–	23.046±0.406	22.057±0.409	20.349±0.239	$1.09^{+0.34}_{-0.33}$
111	–	24.413±0.532	23.848±0.619	23.781±0.512	$1.33^{+0.39}_{-0.37}$
112	–	24.313±0.516	23.369±0.536	22.821±0.367	$1.24^{+0.13}_{-0.12}$
113	22.686±1.030	24.094±0.499	23.342±0.533	22.733±0.359	$1.45^{+0.29}_{-0.27}$
114	20.181±0.555	21.700±0.369	21.209±0.379	21.467±0.274	$2.26^{+1.15}_{-1.11}$
115	20.651±0.594	22.043±0.377	21.446±0.385	21.598±0.282	$2.41^{+1.14}_{-1.11}$
116	22.258±0.916	24.410±0.560	24.521±0.814	23.879±0.570	$2.19^{+1.29}_{-1.21}$
117	–	23.962±0.482	23.505±0.558	22.988±0.391	–
118	–	23.410±0.428	22.049±0.409	21.542±0.273	$0.63^{+0.30}_{-0.30}$
119	21.409±0.690	22.098±0.375	21.667±0.391	21.219±0.262	$0.25^{+0.24}_{-0.26}$
120	–	25.115±0.711	24.157±0.688	23.435±0.458	$1.35^{+0.68}_{-0.64}$

Table B.1 (Continued)

ID	F300W mag	F555W mag	F625W mag	F814W mag	log[EW(Hα)/Å]
121	21.447±0.698	21.897±0.368	21.472±0.383	21.157±0.260	$1.03^{+0.14}_{-0.13}$
122	23.404±1.356	22.841±0.400	22.336±0.428	22.114±0.311	$0.45^{+0.05}_{-0.06}$
123	–	21.558±0.356	20.454±0.349	18.788±0.217	$1.10^{+0.57}_{-0.42}$
124	21.749±0.760	22.365±0.384	21.797±0.397	21.750±0.294	$2.11^{+0.67}_{-0.65}$
125	–	–	23.266±0.522	22.946±0.381	–
126	–	24.721±0.582	23.908±0.631	23.619±0.482	–
127	–	–	25.866±1.555	22.695±0.375	$2.37^{+2.49}_{-1.98}$
128	–	–	24.248±0.716	24.851±0.989	$2.12^{+1.26}_{-1.19}$
129	–	22.464±0.382	21.488±0.383	19.825±0.232	$1.22^{+0.38}_{-0.37}$
130	23.643±1.546	23.241±0.431	22.390±0.431	22.212±0.318	–
131	–	24.609±0.564	24.130±0.681	23.858±0.525	$1.42^{+0.48}_{-0.46}$
132	21.321±0.697	21.736±0.373	21.336±0.389	21.038±0.266	–
133	19.919±0.538	21.160±0.357	20.610±0.360	21.115±0.259	$2.46^{+0.76}_{-0.77}$
134	–	26.178±1.089	24.559±0.794	21.878±0.290	$1.87^{+0.87}_{-0.84}$
135	–	–	24.253±0.758	–	$2.71^{+2.01}_{-1.87}$
136	22.385±0.974	22.392±0.391	21.834±0.409	21.508±0.282	–
137	21.584±0.745	22.327±0.387	22.175±0.429	22.078±0.319	$0.50^{+0.11}_{-0.09}$
138	21.448±0.721	22.643±0.403	22.362±0.443	22.062±0.325	–
139	–	23.426±0.429	23.059±0.495	22.854±0.371	$0.81^{+0.11}_{-0.11}$
140	22.474±0.952	23.894±0.483	22.882±0.477	23.505±0.480	$2.38^{+1.03}_{-1.00}$
141	21.251±0.692	22.449±0.397	22.159±0.429	21.624±0.288	–
142	22.204±0.997	22.504±0.419	22.125±0.430	21.710±0.304	$1.91^{+0.86}_{-0.82}$
143	21.625±0.730	22.910±0.401	22.191±0.418	22.727±0.361	$2.44^{+0.87}_{-0.86}$
144	20.934±0.648	22.365±0.405	21.627±0.401	21.851±0.329	$2.45^{+1.09}_{-1.07}$
145	–	23.847±0.463	23.210±0.514	23.016±0.389	$0.56^{+0.01}_{-0.02}$
146	20.786±0.607	22.469±0.392	21.805±0.398	22.731±0.415	$2.23^{+0.9}_{-0.88}$
147	19.470±0.525	20.928±0.363	20.518±0.368	20.385±0.250	$2.20^{+0.63}_{-0.62}$
148	20.658±0.592	22.676±0.402	22.307±0.427	22.758±0.398	$2.06^{+0.82}_{-0.79}$
149	–	22.041±0.365	21.241±0.365	21.824±0.279	$2.51^{+0.82}_{-0.98}$
150	–	23.724±0.446	22.674±0.442	21.565±0.267	$1.23^{+0.14}_{-0.17}$

Table B.1 (Continued)

ID	F300W	F555W	F625W	F814W	log[EW(Hα)/Å]
	mag	mag	mag	mag	
151	22.339±0.905	23.103±0.410	22.703±0.458	22.444±0.338	–
152	20.143±0.566	21.550±0.373	21.153±0.383	20.777±0.261	$0.29^{+0.14}_{-0.13}$
153	22.670±1.019	23.787±0.465	23.462±0.551	22.99±0.393	–
154	19.337±0.523	20.792±0.362	20.436±0.368	20.241±0.247	$1.28^{+0.20}_{-0.20}$
155	18.513±0.514	20.370±0.369	19.804±0.370	19.613±0.25	$1.13^{+0.02}_{-0.05}$
156	20.448±0.587	21.850±0.379	21.601±0.400	21.564±0.312	$1.69^{+0.55}_{-0.54}$
157	21.791±0.765	23.224±0.419	22.988±0.488	23.196±0.426	$2.30^{+1.00}_{-0.98}$
158	22.561±0.978	24.279±0.525	24.367±0.743	–	$1.86^{+1.05}_{-1.00}$
159	18.904±0.525	20.306±0.368	20.047±0.373	19.850±0.253	$1.07^{+0.18}_{-0.15}$
160	–	24.600±0.562	24.354±0.737	25.221±0.977	–
161	20.588±0.617	21.562±0.375	21.368±0.390	20.874±0.272	$1.03^{+0.02}_{-0.01}$
162	19.017±0.511	20.594±0.359	20.343±0.366	20.155±0.244	–
163	–	24.466±0.545	23.752±0.601	23.277±0.429	$1.26^{+0.48}_{-0.45}$
164	19.633±0.524	21.471±0.36	21.219±0.374	21.217±0.261	$1.94^{+0.27}_{-0.28}$
165	17.693±0.484	19.090±0.347	18.742±0.345	18.382±0.223	–
166	23.008±1.368	23.268±0.453	22.592±0.464	21.530±0.284	–
167	20.019±0.543	21.852±0.367	21.713±0.392	21.474±0.272	$0.89^{+0.32}_{-0.30}$
168	–	21.531±0.361	24.283±0.717	23.685±0.494	$0.74^{+0.41}_{-0.39}$
169	19.026±0.511	20.688±0.359	20.48±0.368	20.443±0.249	$0.73^{+0.10}_{-0.09}$
170	22.464±1.084	23.034±0.442	22.51±0.457	22.454±0.384	$1.79^{+0.74}_{-0.71}$
171	–	24.623±0.566	24.262±0.712	23.825±0.519	$1.75^{+0.66}_{-0.64}$
172	–	25.016±0.638	24.182±0.693	23.142±0.405	–
173	22.242±0.881	23.170±0.416	22.162±0.416	22.490±0.339	–
174	20.863±0.631	22.722±0.405	22.644±0.467	22.250±0.329	–
175	22.534±0.968	24.119±0.497	23.478±0.554	23.164±0.417	$2.34^{+0.93}_{-0.90}$
176	21.199±0.659	22.921±0.406	22.793±0.468	23.029±0.411	$2.34^{+1.15}_{-1.12}$
177	22.524±0.987	23.039±0.413	23.135±0.508	22.623±0.359	$1.39^{+0.41}_{-0.37}$
178	22.659±1.016	22.791±0.393	22.477±0.438	22.330±0.321	–
179	22.568±0.979	23.799±0.459	23.465±0.551	23.673±0.493	$1.85^{+0.49}_{-0.48}$
180	23.786±1.622	24.525±0.547	23.855±0.620	23.797±0.512	–

Table B.1 (Continued)

ID	F300W mag	F555W mag	F625W mag	F814W mag	log[EW(Hα)/Å]
181	23.703±1.566	23.415±0.428	22.671±0.454	22.721±0.356	$2.28^{+0.63}_{-0.64}$
182	23.512±1.430	25.506±0.768	24.401±0.749	23.321±0.431	–
183	–	24.621±0.572	24.266±0.715	23.529±0.471	–
184	19.513±0.519	21.037±0.356	20.581±0.36	20.639±0.246	$1.76^{+0.61}_{-0.60}$
185	–	23.656±0.446	22.661±0.454	20.403±0.240	$1.44^{+0.06}_{-0.05}$
186	21.391±0.688	22.744±0.393	22.328±0.427	22.906±0.385	$2.26^{+0.92}_{-0.91}$
187	–	–	–	–	$2.23^{+0.06}_{-0.05}$
188	22.094±0.856	23.885±0.562	23.688±0.624	23.708±0.633	–
189	22.800±1.066	24.110±0.492	23.450±0.549	23.981±0.553	$1.93^{+0.48}_{-0.48}$
190	21.336±0.677	22.82±0.396	22.199±0.418	21.857±0.290	$1.04^{+0.04}_{-0.04}$
191	19.060±0.512	20.738±0.359	20.507±0.368	20.538±0.251	$1.64^{+0.40}_{-0.42}$
192	–	25.642±0.821	24.385±0.745	23.780±0.512	$1.19^{+0.67}_{-0.63}$
193	20.220±0.568	21.909±0.376	21.804±0.410	21.610±0.293	$2.03^{+1.04}_{-1.02}$
194	–	23.067±0.407	22.619±0.450	22.631±0.348	$1.40^{+0.09}_{-0.09}$
195	–	23.775±0.457	23.469±0.552	23.126±0.403	$0.59^{+0.12}_{-0.1}$
196	22.991±1.171	24.148±0.502	23.758±0.602	23.132±0.407	$1.55^{+0.45}_{-0.43}$
197	21.624±0.73	23.220±0.420	23.001±0.490	22.808±0.375	$0.87^{+0.90}_{-0.87}$
198	22.389±0.918	23.695±0.449	23.481±0.532	23.776±0.514	$2.25^{+0.72}_{-0.71}$
199	23.659±1.532	24.352±0.524	24.127±0.68	24.198±0.605	$1.39^{+0.54}_{-0.52}$
200	–	26.172±1.014	24.657±0.826	25.061±0.909	$2.51^{+1.35}_{-1.30}$
201	21.835±0.776	22.887±0.399	22.154±0.415	22.529±0.339	$2.52^{+0.92}_{-0.91}$
202	–	24.619±0.566	23.924±0.635	23.557±0.469	$0.95^{+0.38}_{-0.36}$
203	23.425±1.394	24.534±0.553	24.163±0.688	24.377±0.670	–
204	–	23.544±0.439	23.094±0.5	22.579±0.342	–
205	22.381±0.921	24.074±0.492	23.443±0.548	23.853±0.542	–
206	–	23.696±0.455	23.04±0.495	23.530±0.474	$2.32^{+1.06}_{-1.03}$
207	–	24.189±0.508	23.775±0.605	24.365±0.654	$2.50^{+1.08}_{-1.06}$
208	–	24.740±0.592	24.379±0.746	23.960±0.555	$2.39^{+1.31}_{-1.26}$
209	–	23.143±0.405	21.891±0.389	20.844±0.241	$0.80^{+0.42}_{-0.37}$
210	23.405±1.386	23.788±0.465	23.038±0.494	23.605±0.491	$2.40^{+0.96}_{-0.94}$

Table B.1 (Continued)

ID	F300W mag	F555W mag	F625W mag	F814W mag	log[EW(Hα)/Å]
211	–	23.411±0.433	22.870±0.475	23.394±0.452	–
212	23.678±1.538	23.526±0.436	23.197±0.513	23.001±0.389	–
213	–	24.498±0.544	23.765±0.604	23.134±0.406	$2.37^{+0.93}_{-0.91}$
214	–	23.966±0.475	23.746±0.600	23.172±0.411	$1.19^{+0.31}_{-0.30}$
215	–	23.339±0.423	22.946±0.482	22.793±0.365	$2.09^{+0.57}_{-0.57}$
216	22.770±1.058	24.212±0.514	23.985±0.651	23.254±0.427	–
217	–	23.469±0.431	22.882±0.475	22.538±0.338	–
218	22.935±1.132	23.230±0.416	22.91±0.478	22.834±0.371	–
219	–	25.059±0.696	23.928±0.637	24.281±0.640	$2.35^{+1.13}_{-1.09}$
220	23.580±1.495	24.513±0.546	24.340±0.733	24.076±0.579	$1.01^{+0.51}_{-0.48}$
221	22.230±0.875	22.852±0.397	22.286±0.424	21.816±0.288	–
222	21.492±0.704	22.567±0.386	22.221±0.419	22.028±0.300	$0.31^{+0.21}_{-0.21}$
223	–	24.603±0.607	24.066±0.734	23.434±0.485	$0.49^{+0.36}_{-0.35}$
224	–	24.012±0.498	23.404±0.559	23.021±0.404	$2.16^{+0.87}_{-0.86}$
225	22.682±1.029	23.570±0.441	23.141±0.506	23.048±0.398	$1.68^{+0.44}_{-0.43}$
226	23.291±1.454	23.879±0.499	23.626±0.634	23.506±0.498	–
227	23.400±1.364	24.129±0.497	23.445±0.548	23.100±0.401	–
228	–	25.419±0.767	24.719±0.871	23.430±0.461	$1.13^{+0.79}_{-0.76}$
229	21.304±0.675	22.687±0.392	22.358±0.429	22.478±0.338	–
230	–	23.589±0.453	23.026±0.506	23.657±0.513	$2.55^{+0.97}_{-0.99}$
231	–	24.101±0.491	23.655±0.582	23.372±0.439	–
232	24.03±1.915	27.001±1.944	25.113±0.996	23.613±0.491	$0.9^{+1.06}_{-0.97}$
233	23.461±1.425	23.607±0.443	23.117±0.503	23.074±0.397	–
234	22.602±1.047	23.182±0.424	22.476±0.451	22.664±0.363	$2.36^{+0.85}_{-0.88}$
235	–	24.372±0.540	23.718±0.613	23.509±0.474	–
236	22.845±1.152	24.181±0.550	23.272±0.542	23.118±0.426	$2.55^{+1.46}_{-1.42}$
237	–	25.440±0.780	24.066±0.667	23.420±0.453	$1.07^{+0.52}_{-0.49}$
238	–	23.004±0.403	22.105±0.412	21.545±0.273	$-0.23^{+0.37}_{-0.38}$
239	22.522±0.972	23.925±0.478	23.244±0.520	22.292±0.321	–
240	22.410±0.953	23.932±0.499	24.515±0.796	24.670±0.878	$1.72^{+1.20}_{-1.10}$

Table B.1 (Continued)

ID	F300W	F555W	F625W	F814W	log[EW(Hα)/Å]
	mag	mag	mag	mag	
241	22.682±1.032	24.450±0.545	23.698±0.591	23.079±0.400	$1.27^{+0.46}_{-0.44}$
242	23.278±1.289	23.626±0.444	23.405±0.542	23.044±0.393	$0.96^{+0.23}_{-0.21}$
243	–	24.551±0.558	24.231±0.706	23.664±0.491	$1.41^{+0.67}_{-0.63}$
244	22.844±1.113	23.450±0.431	23.239±0.519	22.822±0.372	–
245	23.281±1.312	24.485±0.553	24.495±0.779	22.769±0.362	$1.79^{+0.96}_{-0.90}$
246	–	25.105±0.680	24.178±0.693	23.357±0.439	–
247	–	22.773±0.402	22.656±0.467	22.782±0.377	$1.56^{+0.30}_{-0.30}$
248	23.205±1.260	23.072±0.407	22.651±0.453	22.269±0.316	$1.39^{+0.08}_{-0.07}$
249	22.930±1.209	25.553±0.835	24.458±0.807	23.440±0.490	$1.50^{+0.77}_{-0.73}$
250	22.597±1.037	23.801±0.479	23.390±0.559	23.789±0.552	$2.49^{+1.29}_{-1.25}$
251	–	24.410±0.543	24.014±0.656	23.301±0.436	$1.15^{+0.57}_{-0.54}$
252	20.760±0.603	22.341±0.379	22.014±0.407	21.612±0.278	–
253	22.958±1.139	24.035±0.484	23.433±0.547	23.908±0.544	$2.45^{+1.04}_{-1.02}$
254	23.509±1.447	24.024±0.492	21.776±0.395	23.229±0.431	$0.99^{+0.18}_{-0.19}$
255	22.760±1.060	23.491±0.434	22.956±0.484	23.425±0.45	$2.49^{+0.92}_{-0.91}$
256	22.419±0.927	23.660±0.447	23.237±0.518	23.568±0.473	–
257	23.336±1.377	24.022±0.484	23.608±0.577	23.191±0.414	$1.75^{+0.78}_{-0.74}$
258	22.314±0.898	23.370±0.426	22.895±0.477	23.948±0.564	$2.46^{+0.85}_{-0.85}$
259	–	23.991±0.480	23.511±0.559	22.586±0.344	–
260	21.097±0.643	22.352±0.379	22.345±0.428	22.082±0.304	$1.16^{+0.07}_{-0.06}$
261	22.900±1.119	24.151±0.502	23.309±0.529	23.626±0.489	$2.08^{+0.75}_{-0.74}$
262	24.868±2.839	–	23.851±0.620	23.379±0.441	$1.34^{+0.48}_{-0.46}$
263	–	23.916±0.472	23.907±0.631	24.109±0.606	–
264	21.888±0.793	22.625±0.392	22.122±0.414	21.638±0.279	$1.72^{+0.42}_{-0.41}$
265	–	24.104±0.529	23.875±0.689	23.275±0.463	$1.27^{+0.38}_{-0.35}$
266	23.652±1.514	24.476±0.542	24.284±0.718	23.510±0.461	$0.41^{+0.36}_{-0.34}$
267	22.264±0.884	23.598±0.444	23.015±0.490	23.636±0.490	$1.92^{+0.62}_{-0.61}$
268	–	23.963±0.511	23.565±0.623	23.235±0.457	$0.45^{+0.20}_{-0.17}$
269	23.057±1.188	24.958±0.628	23.865±0.622	23.388±0.442	–
270	21.688±0.743	23.034±0.407	22.443±0.436	22.581±0.345	$2.06^{+0.48}_{-0.48}$

Table B.1 (Continued)

ID	F300W mag	F555W mag	F625W mag	F814W mag	log[EW(Hα)/Å]
271	–	24.377±0.531	24.017±0.655	23.798±0.520	–
272	21.52±0.734	22.742±0.420	22.275±0.438	22.489±0.363	$2.55^{+1.29}_{-1.26}$
273	22.987±1.164	23.906±0.475	23.486±0.555	23.390±0.450	$1.29^{+0.41}_{-0.39}$
274	22.870±1.101	–	24.525±0.785	25.336±1.061	$2.37^{+1.21}_{-1.17}$
275	22.958±1.129	24.157±0.498	23.489±0.555	23.54±0.466	$0.24^{+0.11}_{-0.1}$
276	22.030±0.849	22.347±0.386	21.946±0.414	22.429±0.345	$2.55^{+0.8}_{-0.88}$
277	19.884±0.567	20.670±0.370	19.996±0.372	20.710±0.267	$2.45^{+0.66}_{-0.82}$
278	18.826±0.521	19.782±0.366	19.898±0.371	20.217±0.257	$2.48^{+0.69}_{-0.86}$
279	–	23.274±0.420	22.779±0.465	22.461±0.332	–
280	21.078±0.639	22.427±0.381	22.017±0.407	22.850±0.376	$2.44^{+0.78}_{-0.78}$
281	21.267±0.667	21.881±0.367	21.490±0.383	21.238±0.262	$1.22^{+0.26}_{-0.25}$
282	20.555±0.624	20.943±0.373	20.201±0.374	21.354±0.291	$2.57^{+0.81}_{-0.95}$
283	22.902±1.124	23.534±0.441	23.041±0.495	22.752±0.363	–
284	21.429±0.692	22.630±0.387	22.270±0.423	21.912±0.292	$1.04^{+0.07}_{-0.07}$
285	22.387±0.919	23.991±0.480	23.485±0.554	24.019±0.566	$2.43^{+0.93}_{-0.91}$
286	21.548±0.746	21.576±0.370	21.399±0.390	21.601±0.296	$2.45^{+0.74}_{-0.80}$
287	–	24.169±0.504	23.482±0.554	24.075±0.582	$2.40^{+0.94}_{-0.92}$
288	21.389±0.708	22.307±0.386	22.087±0.423	22.345±0.334	$2.43^{+0.93}_{-0.96}$
289	21.901±0.786	22.485±0.383	22.083±0.411	21.944±0.295	–
290	–	23.969±0.491	23.380±0.555	22.751±0.374	–
291	23.910±1.738	24.756±0.599	24.431±0.759	23.368±0.441	–
292	21.814±0.767	23.446±0.431	23.211±0.514	23.067±0.398	$1.99^{+0.55}_{-0.54}$
293	22.877±1.176	23.525±0.454	23.764±0.622	22.878±0.411	$2.25^{+1.03}_{-1.02}$
294	–	23.827±0.486	23.587±0.589	23.112±0.423	$2.00^{+0.89}_{-0.88}$
295	22.131±0.856	23.197±0.420	22.886±0.478	23.839±0.541	$2.54^{+1.34}_{-1.31}$
296	–	23.355±0.426	22.787±0.466	22.223±0.313	–
297	22.079±0.837	23.003±0.406	22.666±0.455	23.202±0.417	$2.53^{+1.13}_{-1.12}$
298	22.623±1.004	23.504±0.436	23.229±0.517	22.707±0.356	$0.10^{+0.07}_{-0.06}$
299	–	24.688±0.583	24.021±0.657	22.756±0.360	$0.86^{+0.76}_{-0.72}$
300	24.050±1.834	24.193±0.504	23.918±0.634	24.163±0.606	–

Table B.1 (Continued)

ID	F300W	F555W	F625W	F814W	log[EW(Hα)/Å]
	mag	mag	mag	mag	
301	21.657±0.733	22.906±0.400	22.237±0.421	21.779±0.286	$1.62^{+0.08}_{-0.08}$
302	18.234±0.496	20.064±0.356	19.794±0.360	19.926±0.240	$0.68^{+0.18}_{-0.18}$
303	–	26.170±1.028	24.597±0.806	23.729±0.500	–
304	–	23.538±0.439	23.160±0.508	23.034±0.396	–
305	–	24.172±0.500	–	22.813±0.367	$0.74^{+0.36}_{-0.33}$
306	19.083±0.505	20.301±0.351	19.965±0.352	20.478±0.242	$2.29^{+0.57}_{-0.58}$
307	22.646±1.004	24.272±0.513	24.119±0.677	23.804±0.515	–
308	19.005±0.511	20.266±0.356	19.962±0.361	20.499±0.249	$2.20^{+0.48}_{-0.59}$
309	24.075±1.824	24.125±0.495	23.632±0.579	23.967±0.551	$1.90^{+0.61}_{-0.59}$
310	23.570±1.472	24.662±0.574	24.082±0.669	23.492±0.458	$1.86^{+0.86}_{-0.83}$
311	–	24.443±0.537	23.878±0.625	23.820±0.518	–
312	22.036±0.826	23.159±0.414	22.725±0.460	22.760±0.363	$2.32^{+0.78}_{-0.78}$
313	–	23.863±0.469	23.066±0.497	24.060±0.584	$2.25^{+0.78}_{-0.77}$
314	22.356±0.910	23.833±0.465	23.196±0.513	23.018±0.391	–
315	23.627±1.530	24.531±0.552	24.069±0.668	24.665±0.752	–
316	–	24.645±0.581	23.925±0.635	23.329±0.435	$1.17^{+0.62}_{-0.59}$
317	22.627±0.999	23.971±0.480	23.686±0.589	23.193±0.414	–
318	–	25.449±0.760	24.496±0.776	23.608±0.488	–
319	21.740±0.752	22.995±0.404	22.642±0.452	22.433±0.331	$0.94^{+0.18}_{-0.19}$
320	21.578±0.718	20.894±0.354	20.289±0.356	20.012±0.234	–
321	22.321±0.933	23.924±0.485	23.496±0.574	22.805±0.376	$0.99^{+0.22}_{-0.21}$
322	23.665±1.530	24.362±0.525	23.971±0.646	23.481±0.461	$1.14^{+0.37}_{-0.35}$
323	22.516±0.964	23.793±0.462	23.361±0.536	22.759±0.363	$0.85^{+0.07}_{-0.05}$
324	23.774±1.608	24.617±0.567	24.283±0.717	24.475±0.682	$2.06^{+0.90}_{-0.88}$
325	–	26.040±1.052	25.118±0.992	23.666±0.489	$1.68^{+1.04}_{-0.98}$
326	–	24.489±0.541	24.625±0.814	24.127±0.590	$1.40^{+0.62}_{-0.59}$
327	23.108±1.258	23.737±0.464	23.465±0.568	23.156±0.419	–
328		24.800±0.603	23.973±0.646	24.218±0.620	–
329	–	24.728±0.591	24.182±0.695	24.150±0.602	$1.81^{+0.84}_{-0.80}$
330	23.994±0.476	23.994±0.481	23.519±0.561	23.413±0.447	$0.54^{+0.16}_{-0.14}$

Table B.1 (Continued)

ID	F300W mag	F555W mag	F625W mag	F814W mag	log[EW(Hα)/Å]
331	22.940±1.134	23.433±0.430	22.910±0.478	22.959±0.384	$1.49^{+0.07}_{-0.07}$
332	22.548±0.974	22.933±0.400	22.604±0.448	22.266±0.316	–
333	23.164±1.254	25.089±0.660	24.329±0.731	23.375±0.441	$1.31^{+0.77}_{-0.74}$
334	–	24.229±0.510	23.483±0.554	22.461±0.332	$0.53^{+0.24}_{-0.22}$
335	22.025±0.844	23.451±0.441	23.027±0.506	23.209±0.427	$1.41^{+0.34}_{-0.35}$
336	–	25.62±0.820	25.266±1.057	23.647±0.491	–
337	22.510±1.003	23.703±0.462	23.478±0.571	24.120±0.603	$1.18^{+0.34}_{-0.33}$
338	23.489±1.418	23.937±0.474	23.500±0.557	23.787±0.519	$0.42^{+0.22}_{-0.21}$
339	24.074±1.881	23.975±0.477	23.324±0.53	22.794±0.364	$1.20^{+0.17}_{-0.16}$
340	–	23.716±0.456	22.741±0.461	22.897±0.376	–
341	22.135±0.934	23.588±0.471	22.809±0.507	23.24±0.454	–
342	23.275±1.292	24.707±0.579	23.671±0.586	24.372±0.652	$2.35^{+0.82}_{-0.81}$
343	–	25.503±0.765	24.737±0.851	23.558±0.468	$1.46^{+0.85}_{-0.80}$
344	24.112±1.886	24.447±0.534	23.884±0.626	23.729±0.504	–
345	–	21.773±0.365	20.687±0.362	19.002±0.226	$1.17^{+0.52}_{-0.50}$
346	21.651±0.732	23.315±0.422	22.995±0.488	22.991±0.388	$1.62^{+0.27}_{-0.26}$
347	22.920±1.252	23.57±0.47	23.375±0.588	23.289±0.462	–
348	–	25.009±0.654	27.143±2.505	23.559±0.472	$2.43^{+2.71}_{-2.11}$
349	22.792±1.092	23.782±0.459	23.400±0.542	23.293±0.429	$0.25^{+0.12}_{-0.10}$
350	23.340±1.485	24.428±0.577	24.118±0.748	24.351±0.696	–
351	23.392±1.364	23.595±0.442	22.949±0.482	23.560±0.471	$2.5^{+0.91}_{-0.91}$
352	23.336±1.331	23.997±0.480	23.414±0.543	24.288±0.625	$2.44^{+0.91}_{-0.90}$
353	–	24.884±0.612	23.883±0.626	24.664±0.738	$2.49^{+1.03}_{-1.01}$
354	22.826±1.098	24.313±0.524	23.227±0.517	22.921±0.384	–
355	23.074±1.195	24.673±0.583	23.814±0.614	23.899±0.548	$2.23^{+0.98}_{-0.95}$
356	24.198±1.956	22.700±0.390	21.699±0.391	20.935±0.252	–
357	–	24.240±0.509	23.841±0.618	23.444±0.449	$0.57^{+0.26}_{-0.24}$
358	22.230±0.882	23.559±0.441	23.344±0.534	23.002±0.391	$1.43^{+0.55}_{-0.52}$
359	–	24.601±0.576	23.963±0.644	23.024±0.395	–
360	23.287±1.304	22.912±0.399	22.32±0.426	21.733±0.283	–

Table B.1 (Continued)

ID	F300W	F555W	F625W	F814W	log[EW(Hα)/Å]
	mag	mag	mag	mag	
361	23.021±1.186	24.274±0.522	24.320±0.731	24.666±0.791	$2.65^{+1.57}_{-1.52}$
362	22.739±1.051	23.095±0.409	22.713±0.458	22.769±0.363	$0.14^{+0.01}_{-0.02}$
363	20.909±0.635	22.035±0.377	21.506±0.394	22.122±0.315	$2.5^{+0.68}_{-0.80}$
364	–	24.080±0.489	23.735±0.597	22.693±0.354	$1.22^{+0.37}_{-0.36}$
365	22.521±0.967	23.616±0.445	23.257±0.521	23.087±0.404	$0.44^{+0.14}_{-0.12}$
366	22.580±1.022	23.978±0.495	23.467±0.569	24.155±0.637	$2.61^{+1.17}_{-1.16}$
367	23.832±1.664	25.108±0.667	24.657±0.826	23.441±0.452	–
368	20.811±0.611	21.830±0.367	21.224±0.375	21.925±0.293	$2.45^{+0.86}_{-0.86}$
369	20.457±0.574	21.604±0.362	21.088±0.371	21.219±0.262	$2.22^{+0.72}_{-0.72}$
370	22.032±0.843	23.405±0.430	22.590±0.447	23.233±0.424	$2.46^{+0.83}_{-0.84}$
371	22.308±0.894	23.76±0.459	22.975±0.486	23.631±0.485	$2.34^{+0.85}_{-0.83}$
372	23.622±1.517	24.404±0.532	23.588±0.571	24.647±0.737	$2.36^{+0.84}_{-0.83}$
373	23.339±1.381	24.190±0.351	23.598±0.591	22.82±0.376	–
374	–	21.574±0.362	20.457±0.358	18.771±0.225	$1.14^{+0.55}_{-0.54}$
375	–	25.349±0.740	24.847±0.916	23.796±0.525	$1.41^{+0.74}_{-0.70}$
376	–	–	–	–	$2.42^{+0.55}_{-0.54}$
377	21.011±0.631	22.051±0.371	21.606±0.388	22.067±0.302	$2.48^{+0.84}_{-0.85}$
378	24.005±1.788	24.207±0.507	23.487±0.555	24.344±0.653	$2.60^{+1.18}_{-1.15}$
379	22.471±0.952	23.797±0.467	22.935±0.482	23.082±0.403	$2.38^{+1.01}_{-0.99}$
380	–	–	–	–	$0.88^{+1.18}_{-1.15}$
381	21.755±0.757	23.498±0.436	23.044±0.494	23.641±0.494	$2.30^{+0.84}_{-0.83}$
382	23.174±1.249	24.709±0.580	23.989±0.648	24.194±0.609	$1.89^{+0.56}_{-0.55}$
383	–	23.581±0.442	23.021±0.492	23.083±0.403	$1.89^{+0.71}_{-0.69}$
384	20.799±0.607	22.210±0.375	21.629±0.389	22.195±0.313	$2.46^{+0.84}_{-0.84}$
385	23.456±1.398	24.173±0.501	23.922±0.635	23.421±0.452	$1.31^{+0.34}_{-0.32}$
386	23.550±1.440	23.611±0.441	23.199±0.500	22.934±0.384	–
387	21.739±0.781	22.522±0.393	22.147±0.427	22.333±0.334	–
388	–	–	23.170±0.509	21.558±0.274	$1.21^{+0.05}_{-0.04}$
389	22.036±0.821	23.079±0.408	22.564±0.445	22.648±0.350	$2.01^{+0.40}_{-0.40}$
390	–	22.762±0.396	22.214±0.419	22.685±0.362	$2.30^{+0.81}_{-0.80}$

Table B.1 (Continued)

ID	F300W mag	F555W mag	F625W mag	F814W mag	log[EW(Hα)/Å]
391	22.129±0.892	23.459±0.451	22.848±0.486	22.350±0.332	–
392	–	21.267±0.358	20.775±0.363	21.300±0.264	$2.45^{+0.74}_{-0.76}$
393	21.633±0.753	23.093±0.418	22.976±0.501	22.805±0.378	$1.76^{+0.45}_{-0.45}$
394	20.870±0.616	22.380±0.381	22.175±0.417	22.022±0.304	$1.62^{+0.39}_{-0.37}$
395	–	25.939±1.611	24.944±0.995	24.949±1.181	–
396	–	24.209±0.535	23.561±0.586	24.029±0.596	$2.22^{+1.14}_{-1.11}$
397	22.212±0.864	23.345±0.424	22.865±0.473	23.366±0.440	$2.44^{+0.85}_{-0.84}$
398	–	24.451±0.575	24.228±0.778	24.323±0.689	$1.38^{+0.53}_{-0.51}$
399	23.210±1.411	23.727±0.484	23.060±0.539	22.958±0.413	$1.40^{+0.24}_{-0.27}$
400	21.802±0.797	23.262±0.434	22.991±0.503	23.583±0.518	$1.50^{+0.69}_{-0.67}$
401	22.393±0.958	23.472±0.455	22.903±0.480	23.050±0.414	–
402	22.100±0.840	23.208±0.415	22.752±0.462	23.108±0.403	$2.35^{+0.72}_{-0.72}$
403	22.208±0.866	23.681±0.449	23.180±0.511	23.297±0.426	$2.41^{+0.82}_{-0.81}$
404	22.050±0.832	23.909±0.477	23.635±0.581	23.041±0.394	$1.92^{+0.86}_{-0.83}$
405	22.206±0.820	23.193±0.408	22.439±0.423	23.423±0.440	$2.49^{+0.85}_{-0.98}$
406	21.291±0.675	23.092±0.413	22.875±0.477	22.845±0.374	$1.11^{+0.79}_{-0.76}$
407	21.787±0.788	23.731±0.469	23.184±0.527	23.498±0.481	$0.95^{+0.30}_{-0.28}$
408	–	25.074±0.656	23.904±0.630	23.147±0.408	–
409	22.011±0.812	23.297±0.42	22.879±0.475	22.998±0.387	$1.76^{+0.24}_{-0.24}$
410	–	23.255±0.420	22.417±0.434	22.160±0.311	$1.70^{+0.35}_{-0.33}$
411	–	24.443±0.537	24.034±0.658	23.985±0.555	–
412	–	24.210±0.526	23.259±0.523	23.004±0.399	$2.08^{+0.99}_{-0.95}$
413	22.433±1.042	24.396±0.574	23.453±0.602	24.187±0.669	$2.43^{+1.13}_{-1.12}$
414	–	26.687±1.314	25.051±0.964	23.690±0.494	$1.11^{+0.84}_{-0.78}$
415	20.838±0.610	22.391±0.380	21.900±0.401	22.120±0.306	$2.10^{+0.53}_{-0.53}$
416	23.789±1.841	24.773±0.655	23.667±0.643	23.438±0.488	$2.41^{+1.12}_{-1.11}$
417	23.009±1.172	23.965±0.486	23.428±0.547	23.374±0.457	$1.71^{+0.67}_{-0.64}$
418	22.561±0.984	23.222±0.416	22.762±0.463	22.512±0.338	$0.69^{+0.02}_{-0.01}$
419	–	24.026±0.491	23.731±0.600	24.939±0.989	$2.25^{+1.10}_{-1.06}$
420	22.696±1.028	24.120±0.499	21.859±0.399	22.947±0.384	–

Table B.1 (Continued)

ID	F300W mag	F555W mag	F625W mag	F814W mag	log[EW(Hα)/Å]
421	21.819±0.845	23.420±0.458	22.822±0.509	22.246±0.342	–
422	–	24.560±0.555	23.943±0.639	23.079±0.398	–
423	22.260±0.978	23.317±0.450	22.756±0.501	22.336±0.348	–
424	21.639±0.734	23.067±0.411	22.642±0.453	22.501±0.340	–
425	–	24.940±0.621	24.446±0.762	23.485±0.458	$0.72^{+0.49}_{-0.46}$
426	23.097±1.207	23.193±0.414	22.479±0.438	22.116±0.305	–
427	22.850±1.093	23.908±0.473	23.482±0.554	23.110±0.405	–
428	22.604±1.014	23.425±0.431	22.996±0.488	22.867±0.376	$1.21^{+0.30}_{-0.29}$
429	22.292±0.897	22.956±0.403	22.63±0.451	22.817±0.37	$1.84^{+0.41}_{-0.39}$
430	–	23.478±0.436	23.005±0.489	23.009±0.393	$0.31^{+0.11}_{-0.09}$
431	21.653±0.733	22.481±0.382	22.125±0.414	22.229±0.313	–
432	–	–	24.522±0.784	23.656±0.491	$0.83^{+0.63}_{-0.60}$
433	21.695±0.741	22.920±0.399	22.619±0.450	22.355±0.324	–
434	22.719±1.032	24.629±0.567	24.355±0.737	24.584±0.715	$0.89^{+0.52}_{-0.49}$
435	21.790±0.725	23.289±0.415	22.849±0.459	22.681±0.343	–
436	23.652±1.538	24.802±0.594	25.429±1.128	25.259±0.964	–
437	22.759±1.054	24.519±0.550	24.459±0.765	24.548±0.706	–
438	23.910±1.911	25.215±0.740	23.738±0.656	23.334±0.469	–
439	23.306±1.321	23.972±0.479	23.475±0.553	23.075±0.399	–
440	23.627±1.500	24.999±0.640	24.083±0.669	24.45±0.672	$2.39^{+1.00}_{-0.98}$
441	–	24.324±0.519	23.137±0.505	20.791±0.248	$1.48^{+0.15}_{-0.15}$
442	–	25.753±0.912	24.978±1.039	23.657±0.525	$1.02^{+0.79}_{-0.76}$
443	21.875±0.780	23.872±0.467	23.396±0.541	23.954±0.558	$1.97^{+0.60}_{-0.59}$
444	22.925±1.131	26.060±0.962	23.738±0.598	24.505±0.692	$1.98^{+0.58}_{-0.57}$
445	23.001±1.159	21.619±0.362	20.634±0.361	19.852±0.232	$0.23^{+0.95}_{-0.95}$
446	–	26.782±1.383	25.015±0.948	23.917±0.539	–
447	22.024±0.778	22.501±0.377	22.109±0.401	22.825±0.357	$2.53^{+0.88}_{-1.01}$
448	22.064±0.828	23.97±0.477	23.407±0.543	23.886±0.545	$2.43^{+1.01}_{-0.99}$
449	22.666±1.017	24.557±0.554	24.343±0.733	23.766±0.508	–
450	23.271±1.283	23.742±0.454	23.408±0.543	23.422±0.451	$1.47^{+0.22}_{-0.21}$

Table B.1 (Continued)

ID	F300W mag	F555W mag	F625W mag	F814W mag	log[EW(Hα)/Å]
451	–	25.007±0.638	24.805±0.875	23.968±0.556	$1.99^{+1.16}_{-1.11}$
452	21.293±0.670	22.554±0.385	22.126±0.414	22.814±0.367	$2.52^{+0.84}_{-0.84}$
453	–	24.090±0.489	23.674±0.586	23.406±0.448	–
454	–	24.781±0.592	24.032±0.658	23.527±0.464	–
455	–	24.672±0.581	23.83±0.616	23.558±0.477	$1.74^{+0.58}_{-0.56}$
456	–	26.159±1.005	24.711±0.842	23.287±0.427	–
457	23.061±1.192	24.613±0.562	24.535±0.788	24.278±0.622	–
458	–	25.120±0.666	24.527±0.785	23.660±0.486	$1.54^{+0.74}_{-0.70}$
459	23.708±1.550	24.323±0.519	23.655±0.583	23.376±0.441	$1.57^{+0.48}_{-0.47}$
460	23.054±1.192	24.124±0.494	23.484±0.554	24.208±0.608	$2.49^{+0.95}_{-0.94}$
461	23.473±1.437	22.460±0.381	21.182±0.373	20.328±0.239	$-0.29^{+0.80}_{-0.81}$
462	24.188±1.954	23.605±0.443	23.171±0.509	23.251±0.420	$0.5^{+0.13}_{-0.14}$
463	–	26.188±1.038	25.090±0.980	23.844±0.523	$1.19^{+0.82}_{-0.76}$
464	–	24.221±0.501	22.698±0.444	21.495±0.265	$0.64^{+0.12}_{-0.12}$
465	–	24.251±0.509	23.583±0.570	23.073±0.397	–
466	23.391±1.360	–	18.387±0.344	–	$0.15^{+1.45}_{-1.31}$
467	–	25.088±0.655	25.609±1.217	23.150±0.407	$2.23^{+1.46}_{-1.38}$
468	–	23.358±0.424	22.462±0.437	21.602±0.276	$1.10^{+0.24}_{-0.23}$
469	–	23.495±0.433	22.874±0.475	22.431±0.329	$0.57^{+0.16}_{-0.17}$

Table B.2 Cluster age estimates

				Color-based			EW(Hα)		
ID	Clump	Hα?	N	Age (Myr)	Age (Myr)	Age (Myr)	Age (Myr)	Age (Myr)	Age (Myr)
				$Z = 0.004$	$Z = 0.008$	$Z = 0.020$	$Z = 0.004$	$Z = 0.008$	$Z = 0.020$
1	–	yes	–	–	–	–	12^{+0}_{-0}	11^{+0}_{-0}	8^{+0}_{-0}
2	–	yes	–	–	–	–	20^{+1}_{-0}	18^{+1}_{-0}	14^{+0}_{-0}
3	–	yes	–	–	–	–	15^{+1}_{-0}	13^{+0}_{-0}	9^{+0}_{-0}
4	–	yes	2	259^{+10041}_{-248}	486^{+13614}_{-479}	16^{+10384}_{-10}	24^{+3}_{-2}	21^{+3}_{-2}	17^{+2}_{-1}
5	–	yes	2	259^{+13841}_{-253}	489^{+13611}_{-484}	16^{+14084}_{-11}	14^{+1}_{-1}	12^{+1}_{-1}	9^{+1}_{-1}
6	–	yes	2	259^{+13841}_{-253}	489^{+13611}_{-484}	16^{+14084}_{-11}	–	–	–
7	–	yes	2	259^{+10041}_{-248}	482^{+13618}_{-475}	16^{+14084}_{-10}	17^{+0}_{-0}	15^{+0}_{-0}	11^{+0}_{-0}
8	–	yes	–	–	–	–	6^{+0}_{-0}	5^{+0}_{-0}	5^{+0}_{-0}
9	–	yes	2	259^{+12241}_{-251}	482^{+13618}_{-476}	16^{+14084}_{-11}	21^{+1}_{-1}	19^{+1}_{-1}	15^{+1}_{-1}
10	–	yes	2	247^{+13853}_{-242}	465^{+13635}_{-460}	16^{+14084}_{-12}	21^{+11}_{-3}	19^{+10}_{-3}	15^{+8}_{-3}
11	–	yes	2	259^{+13841}_{-253}	482^{+13618}_{-477}	16^{+14084}_{-11}	–	–	–
12	–	yes	2	259^{+13841}_{-253}	488^{+13612}_{-483}	16^{+14084}_{-11}	–	–	–
13	–	yes	2	257^{+10243}_{-249}	488^{+13612}_{-483}	16^{+14084}_{-11}	–	–	–
14	–	yes	2	258^{+13842}_{-251}	483^{+13617}_{-478}	16^{+14084}_{-11}	15^{+1}_{-0}	13^{+1}_{-1}	10^{+0}_{-0}
15	–	yes	2	259^{+10041}_{-248}	488^{+13612}_{-481}	16^{+10284}_{-10}	–	–	–
16	–	yes	2	259^{+13841}_{-253}	487^{+13613}_{-482}	16^{+14084}_{-11}	–	–	–
17	–	yes	2	256^{+13844}_{-250}	490^{+13610}_{-485}	16^{+14084}_{-11}	–	–	–
18	–	yes	2	259^{+13841}_{-253}	485^{+13615}_{-480}	16^{+14084}_{-11}	–	–	–
19	–	yes	2	259^{+13841}_{-253}	489^{+13611}_{-484}	16^{+14084}_{-11}	–	–	–
20	–	yes	2	259^{+13841}_{-252}	484^{+13616}_{-479}	16^{+14084}_{-11}	15^{+0}_{-1}	13^{+0}_{-0}	10^{+0}_{-0}
21	–	yes	2	15^{+14085}_{-10}	16^{+14084}_{-12}	13^{+14087}_{-10}	10^{+0}_{-0}	9^{+0}_{-0}	7^{+0}_{-0}
22	–	yes	2	250^{+13850}_{-244}	472^{+13628}_{-467}	16^{+14084}_{-11}	13^{+1}_{-1}	11^{+1}_{-1}	8^{+1}_{-0}
23	–	yes	2	150^{+13950}_{-145}	18^{+14082}_{-14}	16^{+14084}_{-12}	10^{+0}_{-0}	8^{+0}_{-0}	7^{+0}_{-0}
24	–	yes	3	261^{+13839}_{-254}	21^{+14079}_{-16}	16^{+14084}_{-9}	11^{+0}_{-0}	9^{+0}_{-0}	7^{+0}_{-0}
25	–	yes	2	261^{+1539}_{-146}	520^{+13580}_{-413}	16^{+14084}_{-8}	13^{+0}_{-0}	11^{+0}_{-0}	8^{+0}_{-0}
26	–	yes	2	259^{+13841}_{-254}	485^{+13615}_{-481}	16^{+14084}_{-13}	16^{+1}_{-1}	14^{+1}_{-1}	10^{+1}_{-1}
27	–	no	3	260^{+260}_{-251}	21^{+10279}_{-15}	16^{+154}_{-9}	–	–	–
28	–	no	2	252^{+13848}_{-247}	479^{+13621}_{-474}	16^{+14084}_{-11}	–	–	–
29	–	yes	3	260^{+186}_{-251}	21^{+10279}_{-15}	16^{+27}_{-8}	–	–	–
30	–	yes	2	259^{+10141}_{-250}	482^{+13618}_{-476}	16^{+14084}_{-10}	26^{+3}_{-2}	23^{+3}_{-2}	18^{+2}_{-2}
31	–	yes	3	20^{+46}_{-12}	20^{+42}_{-14}	16^{+16}_{-8}	7^{+0}_{-0}	6^{+0}_{-0}	6^{+0}_{-0}
32	–	yes	2	259^{+13841}_{-253}	486^{+13614}_{-481}	16^{+14084}_{-11}	15^{+1}_{-1}	13^{+1}_{-1}	9^{+0}_{-1}
33	–	no	2	251^{+13849}_{-245}	476^{+13624}_{-471}	16^{+14084}_{-11}	–	–	–
34	–	yes	–	–	–	–	6^{+0}_{-0}	6^{+0}_{-0}	5^{+0}_{-0}
35	–	yes	3	260^{+9940}_{-251}	490^{+13610}_{-485}	16^{+252}_{-9}	–	–	–

Table B.2 (Continued)

				Color-based			EW(Hα)		
ID	Clump	Hα?	N	Age (Myr)	Age (Myr)	Age (Myr)	Age (Myr)	Age (Myr)	Age (Myr)
				$Z = 0.004$	$Z = 0.008$	$Z = 0.020$	$Z = 0.004$	$Z = 0.008$	$Z = 0.020$
36	–	yes	3	250^{+12150}_{-245}	21^{+14079}_{-16}	16^{+10384}_{-11}	–	–	–
37	–	yes	2	259^{+13841}_{-253}	488^{+13612}_{-483}	16^{+14084}_{-11}	–	–	–
38	–	yes	2	13^{+14087}_{-10}	14^{+14086}_{-12}	6^{+14094}_{-5}	6^{+0}_{-0}	6^{+0}_{-0}	5^{+0}_{-0}
39	–	yes	2	259^{+13841}_{-253}	487^{+13613}_{-482}	16^{+14084}_{-11}	16^{+1}_{-1}	14^{+1}_{-1}	11^{+1}_{-1}
40	–	yes	2	259^{+13841}_{-254}	489^{+13611}_{-484}	16^{+14084}_{-11}	8^{+0}_{-0}	6^{+0}_{-0}	6^{+0}_{-0}
41	–	yes	–	–	–	–	16^{+1}_{-1}	14^{+1}_{-0}	10^{+1}_{-0}
42	–	yes	3	15^{+350}_{-10}	15^{+322}_{-11}	16^{+204}_{-13}	6^{+0}_{-0}	6^{+0}_{-0}	5^{+0}_{-0}
43	–	yes	3	255^{+10045}_{-248}	473^{+10027}_{-468}	16^{+10084}_{-11}	–	–	–
44	–	yes	3	21^{+595}_{-15}	21^{+556}_{-16}	16^{+158}_{-11}	–	–	–
45	–	yes	2	149^{+12351}_{-143}	433^{+13667}_{-428}	16^{+10484}_{-11}	6^{+0}_{-0}	6^{+0}_{-0}	5^{+0}_{-0}
46	–	yes	2	259^{+13841}_{-253}	487^{+13613}_{-482}	16^{+14084}_{-11}	–	–	–
47	–	yes	2	259^{+12241}_{-252}	488^{+13612}_{-483}	16^{+14084}_{-11}	–	–	–
48	–	yes	2	259^{+9941}_{-243}	484^{+13616}_{-477}	16^{+10484}_{-10}	20^{+0}_{-0}	18^{+0}_{-0}	14^{+0}_{-0}
49	–	yes	3	258^{+10242}_{-253}	21^{+14079}_{-16}	16^{+10184}_{-11}	–	–	–
50	–	yes	3	19^{+393}_{-14}	20^{+277}_{-15}	16^{+71}_{-11}	11^{+0}_{-0}	9^{+1}_{-0}	7^{+0}_{-0}
51	–	yes	2	259^{+13841}_{-252}	485^{+13615}_{-480}	16^{+14084}_{-11}	20^{+3}_{-2}	17^{+3}_{-2}	13^{+3}_{-2}
52	–	yes	2	258^{+366}_{-152}	485^{+13615}_{-468}	16^{+908}_{-8}	13^{+0}_{-0}	12^{+0}_{-0}	8^{+0}_{-0}
53	–	yes	3	15^{+344}_{-10}	15^{+271}_{-11}	16^{+154}_{-12}	6^{+0}_{-0}	6^{+0}_{-0}	5^{+0}_{-0}
54	–	yes	2	258^{+10242}_{-249}	483^{+13617}_{-477}	16^{+14084}_{-10}	17^{+0}_{-0}	15^{+0}_{-0}	11^{+0}_{-0}
55	A	yes	2	246^{+13854}_{-240}	465^{+13635}_{-460}	16^{+14084}_{-11}	12^{+0}_{-0}	11^{+0}_{-0}	8^{+0}_{-0}
56	–	yes	2	259^{+10041}_{-248}	481^{+13619}_{-474}	16^{+14084}_{-10}	17^{+0}_{-0}	14^{+0}_{-0}	11^{+0}_{-0}
57	–	no	2	14^{+14086}_{-10}	15^{+14085}_{-11}	50^{+14050}_{-47}	6^{+0}_{-0}	6^{+0}_{-0}	5^{+0}_{-0}
58	–	yes	3	259^{+9941}_{-253}	21^{+10279}_{-16}	16^{+197}_{-11}	14^{+1}_{-1}	12^{+1}_{-1}	9^{+1}_{-1}
59	–	yes	2	259^{+13841}_{-253}	485^{+13615}_{-480}	16^{+14084}_{-11}	11^{+0}_{-0}	9^{+0}_{-0}	7^{+0}_{-0}
60	A	yes	2	259^{+10141}_{-250}	486^{+13614}_{-479}	16^{+14084}_{-10}	16^{+1}_{-1}	14^{+1}_{-0}	11^{+1}_{-0}
61	–	yes	2	257^{+13843}_{-251}	489^{+13611}_{-484}	16^{+14084}_{-11}	18^{+1}_{-1}	16^{+1}_{-1}	12^{+1}_{-1}
62	–	yes	2	259^{+13841}_{-254}	483^{+13617}_{-479}	16^{+14084}_{-12}	–	–	–
63	–	yes	2	259^{+9941}_{-245}	486^{+13614}_{-479}	16^{+971}_{-8}	17^{+1}_{-0}	15^{+1}_{-0}	11^{+0}_{-0}
64	A	yes	2	259^{+13841}_{-253}	481^{+13619}_{-476}	16^{+14084}_{-11}	21^{+20}_{-4}	19^{+17}_{-3}	15^{+14}_{-3}
65	A	yes	2	246^{+10154}_{-239}	463^{+13637}_{-458}	16^{+10284}_{-11}	–	–	–
66	A	yes	2	250^{+13850}_{-245}	474^{+13626}_{-469}	16^{+14084}_{-11}	9^{+0}_{-0}	7^{+0}_{-0}	6^{+0}_{-0}
67	–	yes	2	253^{+13847}_{-247}	477^{+13623}_{-472}	16^{+14084}_{-11}	14^{+1}_{-1}	12^{+1}_{-1}	9^{+1}_{-1}
68	–	yes	2	259^{+13841}_{-254}	483^{+13617}_{-478}	16^{+14084}_{-11}	17^{+3}_{-2}	15^{+3}_{-2}	11^{+3}_{-2}
69	–	yes	2	259^{+13841}_{-253}	489^{+13611}_{-484}	16^{+14084}_{-11}	21^{+5}_{-2}	18^{+4}_{-2}	14^{+4}_{-2}
70	A	yes	2	259^{+13841}_{-253}	487^{+13613}_{-482}	16^{+14084}_{-11}	–	–	–

Table B.2 (Continued)

				Color-based			EW(Hα)		
ID	Clump	Hα?	N	Age (Myr)	Age (Myr)	Age (Myr)	Age (Myr)	Age (Myr)	Age (Myr)
				$Z = 0.004$	$Z = 0.008$	$Z = 0.020$	$Z = 0.004$	$Z = 0.008$	$Z = 0.020$
71	–	yes	3	15^{+149}_{-12}	14^{+184}_{-11}	4^{+180}_{-3}	–	–	–
72	–	yes	3	254^{+9946}_{-248}	21^{+10179}_{-16}	16^{+296}_{-11}	–	–	–
73	–	yes	2	258^{+13842}_{-252}	482^{+13618}_{-477}	16^{+14084}_{-11}	8^{+0}_{-0}	6^{+0}_{-0}	6^{+0}_{-0}
74	–	yes	2	260^{+13840}_{-254}	841^{+13259}_{-836}	–	28^{+3}_{-2}	25^{+2}_{-1}	20^{+2}_{-1}
75	–	yes	2	259^{+13841}_{-254}	486^{+13614}_{-481}	16^{+14084}_{-11}	9^{+0}_{-0}	7^{+0}_{-0}	6^{+0}_{-0}
76	–	yes	2	259^{+13841}_{-253}	487^{+13613}_{-482}	16^{+14084}_{-11}	–	–	–
77	–	yes	–	–	–	16^{+14084}_{-11}	6^{+0}_{-0}	6^{+0}_{-0}	5^{+0}_{-0}
78	–	yes	3	18^{+573}_{-13}	18^{+536}_{-13}	16^{+224}_{-11}	–	–	–
79	B	yes	2	256^{+10044}_{-247}	489^{+13611}_{-482}	16^{+10184}_{-10}	7^{+0}_{-0}	6^{+0}_{-0}	6^{+0}_{-0}
80	B	yes	2	259^{+10241}_{-251}	487^{+13613}_{-481}	16^{+14084}_{-11}	7^{+0}_{-0}	6^{+0}_{-0}	6^{+0}_{-0}
81	–	yes	3	15^{+106}_{-11}	14^{+126}_{-10}	6^{+141}_{-3}	6^{+0}_{-0}	5^{+0}_{-0}	5^{+0}_{-0}
82	B	yes	2	259^{+10141}_{-250}	487^{+13613}_{-481}	16^{+14084}_{-10}	26^{+19}_{-4}	23^{+16}_{-4}	19^{+12}_{-3}
83	–	yes	2	259^{+13841}_{-253}	489^{+13611}_{-484}	16^{+14084}_{-11}	9^{+0}_{-0}	7^{+1}_{-0}	6^{+0}_{-0}
84	B	yes	2	258^{+13842}_{-252}	481^{+13619}_{-476}	16^{+14084}_{-11}	–	–	–
85	B	yes	2	256^{+13844}_{-249}	488^{+13612}_{-483}	16^{+14084}_{-11}	7^{+0}_{-0}	6^{+0}_{-0}	6^{+0}_{-0}
86	B	yes	2	251^{+10249}_{-244}	474^{+13626}_{-469}	16^{+10484}_{-11}	16^{+2}_{-1}	14^{+2}_{-2}	10^{+2}_{-1}
87	B	yes	2	256^{+13844}_{-250}	490^{+13610}_{-485}	16^{+14084}_{-11}	11^{+0}_{-0}	9^{+0}_{-0}	7^{+0}_{-0}
88	B	yes	2	148^{+13952}_{-143}	19^{+14081}_{-14}	16^{+14084}_{-11}	12^{+1}_{-1}	11^{+0}_{-0}	8^{+0}_{-0}
89	–	yes	2	259^{+10041}_{-248}	486^{+13614}_{-479}	16^{+10484}_{-10}	–	–	–
90	–	yes	2	259^{+13841}_{-252}	488^{+13612}_{-483}	16^{+14084}_{-11}	11^{+0}_{-0}	9^{+0}_{-0}	7^{+0}_{-0}
91	–	yes	2	259^{+10141}_{-250}	488^{+13612}_{-482}	16^{+14084}_{-10}	23^{+3}_{-2}	20^{+3}_{-2}	16^{+2}_{-2}
92	B	yes	2	259^{+13841}_{-252}	489^{+13611}_{-484}	16^{+14084}_{-11}	13^{+0}_{-0}	11^{+0}_{-0}	8^{+0}_{-0}
93	–	yes	3	15^{+343}_{-11}	15^{+289}_{-11}	16^{+178}_{-13}	–	–	–
94	B	yes	2	244^{+10156}_{-237}	465^{+10035}_{-460}	16^{+10284}_{-11}	6^{+0}_{-0}	6^{+0}_{-0}	5^{+0}_{-0}
95	C	yes	3	15^{+96}_{-10}	15^{+82}_{-10}	16^{+37}_{-11}	$10^{+0.3}_{-0.32}$	9^{+0}_{-0}	7^{+0}_{-0}
96	B	yes	2	257^{+10243}_{-250}	489^{+13611}_{-484}	16^{+14084}_{-11}	7^{+0}_{-0}	6^{+0}_{-0}	6^{+0}_{-0}
97	C	yes	–	–	–	–	6^{+0}_{-0}	5^{+0}_{-0}	5^{+0}_{-0}
98	C	yes	3	20^{+260}_{-14}	20^{+174}_{-15}	16^{+55}_{-11}	6^{+0}_{-0}	5^{+0}_{-0}	5^{+0}_{-0}
99	C	yes	3	149^{+10051}_{-143}	21^{+10179}_{-16}	16^{+757}_{-11}	6^{+0}_{-0}	5^{+0}_{-0}	5^{+0}_{-0}
100	–	yes	3	256^{+9944}_{-250}	21^{+10179}_{-16}	16^{+226}_{-11}	11^{+0}_{-0}	9^{+0}_{-0}	7^{+0}_{-0}
101	–	no	3	21^{+252}_{-15}	20^{+187}_{-15}	16^{+119}_{-11}	$6^{+0.08}_{-0}$	5^{+0}_{-0}	5^{+0}_{-0}
102	–	yes	3	15^{+149}_{-11}	14^{+174}_{-10}	6^{+185}_{-3}	$6^{+0.08}_{-0}$	5^{+0}_{-0}	5^{+0}_{-0}
103	E	yes	3	253^{+9847}_{-247}	21^{+10179}_{-16}	16^{+277}_{-11}	–	–	–
104	C	yes	3	259^{+10041}_{-252}	491^{+13609}_{-486}	16^{+961}_{-11}	$12^{+0.7}_{-0.7}$	11^{+1}_{-0}	8^{+0}_{-0}
105	–	yes	2	15^{+14085}_{-11}	15^{+14085}_{-11}	13^{+14087}_{-10}	6^{+0}_{-0}	5^{+0}_{-0}	5^{+0}_{-0}

Table B.2 (Continued)

				Color-based			EW(Hα)		
ID	Clump	Hα?	N	Age (Myr)	Age (Myr)	Age (Myr)	Age (Myr)	Age (Myr)	Age (Myr)
				$Z = 0.004$	$Z = 0.008$	$Z = 0.020$	$Z = 0.004$	$Z = 0.008$	$Z = 0.020$
106	–	yes	2	258^{+13842}_{-253}	482^{+13618}_{-477}	16^{+14084}_{-12}	$7^{+0.21}_{-0.21}$	6^{+0}_{-0}	6^{+0}_{-0}
107	–	yes	2	146^{+13954}_{-142}	18^{+14082}_{-14}	16^{+14084}_{-13}	6^{+0}_{-0}	5^{+0}_{-0}	5^{+0}_{-0}
108	–	yes	3	18^{+481}_{-13}	18^{+466}_{-13}	16^{+285}_{-12}	6^{+0}_{-0}	5^{+0}_{-0}	5^{+0}_{-0}
109	–	yes	2	146^{+10354}_{-141}	17^{+10483}_{-12}	16^{+10384}_{-11}	6^{+0}_{-0}	5^{+0}_{-0}	4^{+1}_{-0}
110	–	yes	2	258^{+9942}_{-156}	490^{+13610}_{-475}	16^{+14084}_{-8}	15^{+0}_{-0}	13^{+0}_{-0}	10^{+0}_{-0}
111	–	yes	2	259^{+13841}_{-253}	487^{+13613}_{-482}	16^{+14084}_{-11}	13^{+1}_{-1}	11^{+1}_{-0}	8^{+0}_{-0}
112	–	yes	2	259^{+13841}_{-253}	485^{+13615}_{-480}	16^{+14084}_{-11}	14^{+0}_{-0}	12^{+0}_{-0}	9^{+0}_{-0}
113	E	yes	3	256^{+290}_{-250}	21^{+558}_{-16}	16^{+28}_{-9}	11^{+0}_{-0}	10^{+0}_{-0}	7^{+0}_{-0}
114	D	yes	3	15^{+44}_{-8}	15^{+42}_{-10}	16^{+18}_{-8}	7^{+0}_{-0}	6^{+0}_{-0}	6^{+0}_{-0}
115	D	yes	3	18^{+114}_{-11}	16^{+53}_{-11}	16^{+19}_{-8}	6^{+0}_{-0}	6^{+0}_{-0}	5^{+0}_{-0}
116	–	yes	3	15^{+137}_{-11}	14^{+110}_{-10}	15^{+44}_{-12}	7^{+0}_{-0}	6^{+0}_{-0}	6^{+0}_{-0}
117	E	yes	2	259^{+13841}_{-252}	487^{+13613}_{-482}	16^{+14084}_{-11}	–	–	–
118	–	yes	2	259^{+13841}_{-252}	484^{+13616}_{-479}	16^{+14084}_{-11}	20^{+1}_{-1}	18^{+1}_{-1}	14^{+1}_{-0}
119	D	yes	3	255^{+142}_{-247}	21^{+187}_{-15}	16^{+18}_{-8}	25^{+3}_{-2}	22^{+3}_{-2}	18^{+2}_{-1}
120	E	yes	2	258^{+13842}_{-253}	483^{+13617}_{-478}	16^{+14084}_{-11}	12^{+1}_{-1}	11^{+1}_{-1}	8^{+1}_{-0}
121	D	yes	3	255^{+158}_{-247}	21^{+508}_{-15}	16^{+21}_{-8}	16^{+1}_{-0}	14^{+1}_{-0}	10^{+1}_{-0}
122	–	yes	3	260^{+10040}_{-253}	21^{+14079}_{-16}	16^{+674}_{-11}	22^{+3}_{-2}	19^{+2}_{-1}	16^{+1}_{-2}
123	–	yes	2	259^{+223}_{-149}	490^{+13610}_{-470}	16^{+851}_{-8}	15^{+0}_{-0}	13^{+0}_{-0}	10^{+0}_{-0}
124	D	yes	3	250^{+220}_{-243}	21^{+464}_{-16}	16^{+31}_{-9}	7^{+0}_{-0}	6^{+0}_{-0}	6^{+0}_{-0}
125	–	yes	2	259^{+12141}_{-252}	488^{+13612}_{-483}	16^{+14084}_{-11}	–	–	–
126	–	yes	2	259^{+13841}_{-253}	487^{+13613}_{-482}	16^{+14084}_{-11}	–	–	–
127	–	yes	–	–	–	–	6^{+1}_{-1}	6^{+0}_{-1}	5^{+0}_{-1}
128	D	yes	–	–	–	–	7^{+0}_{-0}	6^{+0}_{-0}	6^{+0}_{-0}
129	–	yes	2	258^{+9842}_{-154}	485^{+13615}_{-470}	16^{+14084}_{-8}	$14^{+0.2}_{-0}$	12^{+0}_{-0}	9^{+0}_{-0}
130	–	yes	3	260^{+10140}_{-253}	21^{+14079}_{-16}	16^{+674}_{-11}	–	–	–
131	–	yes	2	259^{+13841}_{-253}	488^{+13612}_{-483}	16^{+14084}_{-11}	12^{+1}_{-1}	10^{+0}_{-0}	8^{+0}_{-0}
132	–	yes	3	254^{+167}_{-246}	21^{+516}_{-15}	16^{+22}_{-8}	–	–	–
133	–	yes	3	16^{+55}_{-9}	15^{+50}_{-10}	16^{+23}_{-9}	6^{+0}_{-0}	5^{+0}_{-0}	5^{+0}_{-0}
134	–	yes	2	268^{+13832}_{-163}	13700^{+400}_{-13488}	10700^{+3400}_{-10692}	$9^{+0.25}_{-0.24}$	7^{+0}_{-0}	6^{+0}_{-0}
135	–	yes	–	–	–	–	6^{+0}_{-0}	5^{+0}_{-0}	4^{+1}_{-0}
136	–	yes	3	260^{+351}_{-252}	21^{+10179}_{-16}	16^{+34}_{-9}	–	–	–
137	–	yes	3	21^{+389}_{-15}	21^{+249}_{-16}	16^{+38}_{-9}	21^{+3}_{-2}	19^{+3}_{-2}	16^{+2}_{-2}
138	–	yes	3	20^{+316}_{-13}	21^{+134}_{-16}	16^{+23}_{-8}	–	–	–
139	–	yes	2	259^{+10141}_{-250}	489^{+13611}_{-483}	16^{+14084}_{-10}	18^{+1}_{-1}	16^{+1}_{-0}	12^{+1}_{-0}
140	–	yes	3	15^{+262}_{-10}	15^{+231}_{-11}	16^{+141}_{-12}	6^{+0}_{-0}	6^{+0}_{-0}	5^{+0}_{-0}

Table B.2 (Continued)

				Color-based			EW(Hα)		
ID	Clump	Hα?	N	Age (Myr)	Age (Myr)	Age (Myr)	Age (Myr)	Age (Myr)	Age (Myr)
				$Z = 0.004$	$Z = 0.008$	$Z = 0.020$	$Z = 0.004$	$Z = 0.008$	$Z = 0.020$
141	F	yes	3	21^{+343}_{-14}	21^{+122}_{-15}	16^{+18}_{-8}	–	–	–
142	F	yes	3	259^{+322}_{-251}	21^{+974}_{-16}	16^{+33}_{-9}	8^{+0}_{-0}	7^{+0}_{-0}	6^{+0}_{-0}
143	–	yes	3	15^{+156}_{-10}	15^{+118}_{-10}	16^{+46}_{-11}	6^{+0}_{-0}	6^{+0}_{-0}	5^{+0}_{-0}
144	F	yes	3	16^{+135}_{-10}	15^{+67}_{-10}	16^{+23}_{-9}	6^{+0}_{-0}	6^{+0}_{-0}	5^{+0}_{-0}
145	–	yes	2	259^{+13841}_{-252}	486^{+13614}_{-481}	16^{+14084}_{-11}	21^{+2}_{-1}	18^{+2}_{-1}	14^{+2}_{-1}
146	F	yes	3	15^{+20}_{-10}	14^{+41}_{-10}	16^{+35}_{-13}	7^{+0}_{-0}	6^{+0}_{-0}	6^{+0}_{-0}
147	F	yes	3	18^{+41}_{-10}	16^{+40}_{-10}	16^{+14}_{-8}	7^{+0}_{-0}	6^{+0}_{-0}	6^{+0}_{-0}
148	F	yes	3	15^{+16}_{-10}	14^{+30}_{-9}	15^{+21}_{-10}	8^{+0}_{-0}	6^{+0}_{-0}	6^{+0}_{-0}
149	–	yes	2	245^{+10155}_{-238}	477^{+10023}_{-471}	16^{+10284}_{-10}	6^{+0}_{-0}	5^{+0}_{-0}	5^{+0}_{-0}
150	–	yes	2	258^{+10142}_{-249}	483^{+13617}_{-477}	16^{+14084}_{-10}	14^{+1}_{-1}	12^{+0}_{-0}	9^{+0}_{-0}
151	–	yes	3	251^{+289}_{-245}	21^{+559}_{-16}	16^{+38}_{-9}	–	–	–
152	F	yes	3	20^{+233}_{-12}	20^{+41}_{-14}	16^{+14}_{-8}	25^{+10}_{-4}	22^{+9}_{-3}	17^{+7}_{-3}
153	–	yes	3	21^{+576}_{-15}	21^{+546}_{-16}	16^{+127}_{-11}	–	–	–
154	F	yes	3	19^{+40}_{-11}	20^{+36}_{-14}	16^{+13}_{-8}	13^{+1}_{-0}	12^{+0}_{-0}	8^{+0}_{-0}
155	F	yes	3	16^{+28}_{-8}	10^{+36}_{-4}	15^{+12}_{-7}	15^{+1}_{-0}	13^{+0}_{-0}	9^{+0}_{-0}
156	F	yes	3	16^{+56}_{-9}	15^{+51}_{-10}	16^{+19}_{-8}	10^{+0}_{-0}	8^{+0}_{-0}	7^{+0}_{-0}
157	–	yes	3	15^{+143}_{-10}	15^{+109}_{-10}	16^{+43}_{-11}	7^{+0}_{-0}	6^{+0}_{-0}	6^{+0}_{-0}
158	–	yes	–	–	–	–	9^{+1}_{-0}	7^{+1}_{-0}	6^{+0}_{-0}
159	F	yes	3	19^{+43}_{-11}	20^{+38}_{-14}	16^{+14}_{-8}	16^{+0}_{-0}	13^{+0}_{-0}	10^{+0}_{-0}
160	–	yes	2	14^{+14086}_{-10}	15^{+14085}_{-11}	7^{+14093}_{-4}	–	–	–
161	F	no	3	21^{+343}_{-13}	21^{+118}_{-15}	16^{+17}_{-8}	16^{+0}_{-0}	14^{+0}_{-0}	10^{+0}_{-0}
162	F	yes	3	16^{+34}_{-8}	16^{+35}_{-10}	16^{+12}_{-8}	–	–	–
163	–	yes	2	259^{+13841}_{-253}	486^{+13614}_{-481}	16^{+14084}_{-11}	13^{+1}_{-1}	12^{+1}_{-1}	8^{+1}_{-0}
164	–	yes	3	15^{+23}_{-7}	15^{+29}_{-8}	15^{+14}_{-7}	8^{+0}_{-0}	6^{+0}_{-0}	6^{+0}_{-0}
165	F	yes	3	20^{+34}_{-12}	20^{+32}_{-14}	16^{+10}_{-8}	–	–	–
166	F	yes	3	261^{+252}_{-253}	21^{+10179}_{-16}	16^{+25}_{-8}	–	–	–
167	F	yes	3	15^{+27}_{-7}	15^{+32}_{-8}	16^{+12}_{-8}	17^{+1}_{-1}	15^{+1}_{-1}	11^{+1}_{-1}
168	–	yes	2	15^{+10185}_{-9}	15^{+686}_{-10}	16^{+804}_{-11}	19^{+3}_{-2}	16^{+3}_{-2}	13^{+3}_{-2}
169	F	yes	3	15^{+29}_{-7}	15^{+33}_{-8}	16^{+13}_{-8}	19^{+1}_{-1}	16^{+1}_{-1}	13^{+1}_{-1}
170	F	yes	3	251^{+726}_{-245}	21^{+903}_{-16}	16^{+226}_{-11}	9^{+0}_{-0}	7^{+0}_{-0}	6^{+0}_{-0}
171	–	yes	2	259^{+13841}_{-253}	489^{+13611}_{-484}	16^{+14084}_{-11}	9^{+0}_{-0}	8^{+0}_{-0}	6^{+0}_{-0}
172	–	yes	2	259^{+13841}_{-253}	481^{+13619}_{-476}	16^{+14084}_{-11}	–	–	–
173	F	yes	3	21^{+447}_{-15}	21^{+393}_{-16}	16^{+131}_{-11}	–	–	–
174	F	yes	3	15^{+42}_{-7}	15^{+42}_{-10}	16^{+17}_{-8}	–	–	–
175	–	yes	3	20^{+379}_{-14}	20^{+237}_{-15}	16^{+38}_{-11}	6^{+0}_{-0}	6^{+0}_{-0}	5^{+0}_{-0}

Table B.2 (Continued)

				Color-based			EW(Hα)		
ID	Clump	Hα?	N	Age (Myr)	Age (Myr)	Age (Myr)	Age (Myr)	Age (Myr)	Age (Myr)
				$Z = 0.004$	$Z = 0.008$	$Z = 0.020$	$Z = 0.004$	$Z = 0.008$	$Z = 0.020$
176	F	yes	3	15^{+46}_{-10}	14^{+48}_{-9}	16^{+27}_{-11}	6^{+0}_{-0}	6^{+0}_{-0}	5^{+0}_{-0}
177	F	yes	3	252^{+381}_{-245}	21^{+754}_{-16}	16^{+183}_{-10}	12^{+1}_{-1}	11^{+0}_{-0}	8^{+0}_{-0}
178	–	yes	3	254^{+598}_{-247}	21^{+10079}_{-16}	16^{+235}_{-11}	–	–	–
179	–	yes	3	16^{+334}_{-11}	15^{+272}_{-10}	16^{+164}_{-11}	$9^{+0.12}_{-0.13}$	7^{+0}_{-0}	6^{+0}_{-0}
180	–	yes	3	252^{+10248}_{-247}	21^{+10479}_{-17}	16^{+10084}_{-12}	–	–	–
181	–	yes	3	259^{+10241}_{-253}	21^{+14079}_{-16}	16^{+10284}_{-11}	7^{+0}_{-0}	6^{+0}_{-0}	6^{+0}_{-0}
182	–	yes	3	260^{+9940}_{-255}	21^{+10179}_{-16}	15^{+143}_{-10}	–	–	–
183	–	yes	2	259^{+13841}_{-253}	486^{+13614}_{-481}	16^{+14084}_{-11}	–	–	–
184	G	yes	3	16^{+37}_{-8}	15^{+38}_{-9}	16^{+14}_{-8}	9^{+0}_{-0}	8^{+0}_{-0}	6^{+0}_{-0}
185	–	yes	2	263^{+1537}_{-130}	841^{+13259}_{-508}	16^{+14084}_{-8}	11^{+0}_{-0}	10^{+0}_{-0}	7^{+0}_{-0}
186	G	yes	3	15^{+89}_{-10}	14^{+84}_{-9}	16^{+45}_{-11}	7^{+0}_{-0}	6^{+0}_{-0}	6^{+0}_{-0}
187	G	yes	–	–	–	–	7^{+0}_{-0}	6^{+0}_{-0}	6^{+0}_{-0}
188	G	yes	3	15^{+143}_{-11}	14^{+124}_{-10}	16^{+65}_{-13}	–	–	–
189	–	yes	3	15^{+342}_{-11}	15^{+318}_{-11}	16^{+206}_{-13}	8^{+0}_{-0}	6^{+0}_{-0}	6^{+0}_{-0}
190	G	yes	3	21^{+283}_{-14}	21^{+55}_{-15}	16^{+17}_{-8}	16^{+1}_{-0}	14^{+0}_{-0}	10^{+0}_{-0}
191	G	yes	3	15^{+27}_{-7}	15^{+32}_{-8}	16^{+13}_{-8}	10^{+0}_{-0}	8^{+0}_{-0}	7^{+0}_{-0}
192	–	yes	2	259^{+13841}_{-254}	485^{+13615}_{-481}	16^{+14084}_{-13}	14^{+2}_{-2}	12^{+1}_{-1}	9^{+1}_{-1}
193	G	yes	3	15^{+36}_{-7}	15^{+38}_{-9}	16^{+15}_{-8}	8^{+0}_{-0}	6^{+0}_{-0}	6^{+0}_{-0}
194	–	yes	3	21^{+365}_{-15}	21^{+231}_{-16}	16^{+41}_{-10}	12^{+0}_{-0}	10^{+0}_{-0}	8^{+0}_{-0}
195	–	yes	2	259^{+12041}_{-252}	487^{+13613}_{-482}	16^{+14084}_{-11}	21^{+2}_{-2}	18^{+2}_{-2}	14^{+2}_{-1}
196	–	yes	3	254^{+602}_{-248}	21^{+836}_{-16}	16^{+163}_{-11}	11^{+0}_{-0}	9^{+0}_{-0}	7^{+0}_{-0}
197	G	yes	3	15^{+146}_{-9}	15^{+82}_{-10}	16^{+25}_{-9}	17^{+132}_{-3}	15^{+102}_{-3}	12^{+77}_{-2}
198	–	yes	3	15^{+230}_{-10}	15^{+199}_{-10}	16^{+138}_{-12}	$7^{+0.1}_{-0}$	6^{+0}_{-0}	6^{+0}_{-0}
199	–	yes	3	20^{+10380}_{-15}	20^{+10280}_{-16}	16^{+886}_{-12}	12^{+1}_{-1}	11^{+0}_{-1}	8^{+0}_{-0}
200	–	yes	2	258^{+13842}_{-255}	489^{+13611}_{-486}	16^{+14084}_{-15}	6^{+0}_{-0}	5^{+0}_{-0}	5^{+0}_{-0}
201	G	yes	3	20^{+295}_{-14}	20^{+193}_{-15}	16^{+51}_{-11}	6^{+0}_{-0}	5^{+0}_{-0}	5^{+0}_{-0}
202	–	no	2	259^{+13841}_{-253}	487^{+13613}_{-482}	16^{+14084}_{-11}	17^{+1}_{-1}	14^{+1}_{-1}	11^{+1}_{-1}
203	–	yes	3	16^{+10184}_{-12}	16^{+678}_{-12}	16^{+460}_{-13}	–	–	–
204	–	yes	2	259^{+10141}_{-250}	485^{+13615}_{-479}	16^{+14084}_{-10}	–	–	–
205	G	yes	3	15^{+167}_{-10}	14^{+148}_{-10}	16^{+90}_{-13}	–	–	–
206	G	yes	2	153^{+13947}_{-147}	460^{+13640}_{-455}	16^{+14084}_{-11}	6^{+0}_{-0}	6^{+0}_{-0}	5^{+0}_{-0}
207	–	yes	2	144^{+13956}_{-139}	17^{+14083}_{-12}	16^{+14084}_{-12}	6^{+0}_{-0}	5^{+0}_{-0}	5^{+0}_{-0}
208	–	yes	3	254^{+12646}_{-249}	21^{+14079}_{-17}	16^{+10284}_{-12}	6^{+0}_{-0}	6^{+0}_{-0}	5^{+0}_{-0}
209	–	yes	2	258^{+10142}_{-247}	483^{+13617}_{-476}	16^{+14084}_{-10}	18^{+0}_{-0}	16^{+0}_{-0}	12^{+0}_{-0}
210	–	yes	3	138^{+10162}_{-133}	21^{+10179}_{-17}	16^{+932}_{-12}	6^{+0}_{-0}	6^{+0}_{-0}	5^{+0}_{-0}

Table B.2 (Continued)

				Color-based			EW(Hα)		
ID	Clump	Hα?	N	Age (Myr)	Age (Myr)	Age (Myr)	Age (Myr)	Age (Myr)	Age (Myr)
				$Z = 0.004$	$Z = 0.008$	$Z = 0.020$	$Z = 0.004$	$Z = 0.008$	$Z = 0.020$
211	–	yes	3	15^{+101}_{-10}	14^{+94}_{-10}	16^{+50}_{-12}	–	–	–
212	–	yes	3	257^{+10143}_{-251}	21^{+14079}_{-16}	16^{+10184}_{-11}	–	–	–
213	–	yes	2	259^{+13841}_{-253}	485^{+13615}_{-480}	16^{+14084}_{-11}	6^{+0}_{-0}	6^{+0}_{-0}	5^{+0}_{-0}
214	–	yes	2	259^{+13841}_{-252}	488^{+13612}_{-483}	16^{+14084}_{-11}	14^{+1}_{-1}	12^{+1}_{-0}	9^{+0}_{-1}
215	–	yes	3	21^{+555}_{-15}	21^{+531}_{-16}	16^{+148}_{-11}	7^{+0}_{-0}	6^{+0}_{-0}	6^{+0}_{-0}
216	–	yes	3	21^{+491}_{-16}	21^{+468}_{-16}	16^{+57}_{-11}	–	–	–
217	–	yes	2	259^{+10141}_{-250}	488^{+13612}_{-482}	16^{+14084}_{-10}	–	–	–
218	–	yes	3	251^{+9949}_{-245}	21^{+10079}_{-16}	16^{+332}_{-11}	–	–	–
219	–	yes	3	15^{+330}_{-11}	10^{+271}_{-7}	15^{+154}_{-12}	6^{+0}_{-0}	6^{+0}_{-0}	5^{+0}_{-0}
220	–	yes	3	21^{+10279}_{-16}	21^{+10179}_{-17}	16^{+588}_{-12}	16^{+1}_{-1}	14^{+2}_{-1}	10^{+1}_{-1}
221	–	yes	3	258^{+193}_{-250}	21^{+626}_{-15}	16^{+23}_{-8}	–	–	–
222	H	yes	3	21^{+329}_{-14}	21^{+143}_{-15}	16^{+23}_{-8}	24^{+3}_{-2}	21^{+3}_{-1}	17^{+2}_{-1}
223	–	yes	2	259^{+13841}_{-253}	486^{+13614}_{-481}	16^{+14084}_{-11}	22^{+10}_{-3}	19^{+9}_{-3}	16^{+7}_{-3}
224	–	yes	2	259^{+13841}_{-252}	485^{+13615}_{-480}	16^{+14084}_{-11}	7^{+0}_{-0}	6^{+0}_{-0}	6^{+0}_{-0}
225	–	yes	3	21^{+627}_{-15}	21^{+575}_{-16}	16^{+182}_{-11}	10^{+0}_{-0}	8^{+0}_{-0}	7^{+0}_{-0}
226	–	yes	3	247^{+10153}_{-242}	21^{+10279}_{-16}	16^{+746}_{-11}	–	–	–
227	–	yes	3	258^{+10042}_{-252}	21^{+10279}_{-16}	16^{+242}_{-11}	–	–	–
228	–	yes	2	258^{+13842}_{-253}	482^{+13618}_{-477}	16^{+14084}_{-12}	15^{+2}_{-2}	13^{+2}_{-1}	9^{+2}_{-1}
229	H	yes	3	16^{+140}_{-10}	15^{+82}_{-10}	16^{+26}_{-11}	–	–	–
230	–	yes	2	147^{+13953}_{-142}	19^{+14081}_{-14}	16^{+10484}_{-11}	6^{+0}_{-0}	5^{+0}_{-0}	5^{+0}_{-0}
231	–	yes	2	259^{+13841}_{-252}	488^{+13612}_{-483}	16^{+14084}_{-11}	–	–	–
232	–	yes	3	262^{+13838}_{-258}	21^{+14079}_{-18}	15^{+14085}_{-12}	–	–	–
233	–	yes	3	254^{+10146}_{-248}	21^{+10379}_{-16}	16^{+897}_{-11}	–	–	–
234	–	yes	3	246^{+9854}_{-240}	21^{+735}_{-16}	16^{+240}_{-11}	6^{+0}_{-0}	6^{+0}_{-0}	5^{+0}_{-0}
235	–	no	2	259^{+13841}_{-253}	489^{+13611}_{-484}	16^{+14084}_{-11}	15^{+2}_{-2}	13^{+2}_{-1}	9^{+2}_{-1}
236	–	yes	3	21^{+793}_{-16}	21^{+636}_{-16}	16^{+163}_{-11}	6^{+0}_{-0}	5^{+0}_{-0}	5^{+0}_{-0}
237	–	yes	2	258^{+13842}_{-253}	484^{+13616}_{-480}	16^{+14084}_{-12}	16^{+1}_{-1}	13^{+1}_{-1}	10^{+1}_{-1}
238	–	yes	2	259^{+10041}_{-248}	484^{+13616}_{-477}	16^{+14084}_{-10}	36^{+19}_{-6}	31^{+15}_{-5}	25^{+11}_{-4}
239	H	yes	3	258^{+193}_{-250}	21^{+535}_{-16}	16^{+20}_{-8}	–	–	–
240	H	yes	3	15^{+158}_{-11}	14^{+166}_{-10}	16^{+153}_{-13}	9^{+1}_{-1}	8^{+1}_{-1}	7^{+0}_{-0}
241	–	yes	3	21^{+440}_{-15}	21^{+266}_{-16}	15^{+33}_{-8}	13^{+1}_{-1}	12^{+1}_{-1}	8^{+1}_{-0}
242	–	yes	3	255^{+9945}_{-249}	21^{+10279}_{-16}	16^{+382}_{-11}	16^{+1}_{-1}	14^{+1}_{-1}	11^{+1}_{-1}
243	–	yes	3	15^{+283}_{-10}	15^{+164}_{-11}	15^{+43}_{-10}	12^{+1}_{-1}	10^{+1}_{-1}	8^{+0}_{-0}
244	–	yes	3	254^{+617}_{-248}	21^{+937}_{-16}	16^{+202}_{-11}	–	–	–
245	–	yes	3	260^{+639}_{-254}	21^{+10179}_{-16}	16^{+132}_{-11}	9^{+0}_{-0}	7^{+0}_{-0}	6^{+0}_{-0}

Table B.2 (Continued)

				Color-based			EW(Hα)		
ID	Clump	Hα?	N	Age (Myr)	Age (Myr)	Age (Myr)	Age (Myr)	Age (Myr)	Age (Myr)
				$Z = 0.004$	$Z = 0.008$	$Z = 0.020$	$Z = 0.004$	$Z = 0.008$	$Z = 0.020$
246	–	yes	2	259^{+13841}_{-254}	483^{+13617}_{-478}	16^{+14084}_{-11}	–	–	–
247	–	yes	2	250^{+10150}_{-242}	473^{+10027}_{-467}	16^{+10184}_{-10}	10^{+0}_{-0}	9^{+0}_{-0}	7^{+0}_{-0}
248	I	no	3	260^{+9940}_{-252}	21^{+10379}_{-16}	16^{+231}_{-10}	12^{+0}_{-0}	11^{+0}_{-0}	8^{+0}_{-0}
249	–	yes	3	20^{+500}_{-15}	20^{+444}_{-16}	15^{+52}_{-10}	11^{+1}_{-1}	10^{+1}_{-1}	7^{+0}_{-0}
250	–	yes	3	15^{+346}_{-10}	15^{+320}_{-11}	16^{+206}_{-12}	6^{+0}_{-0}	5^{+0}_{-0}	5^{+0}_{-0}
251	–	yes	2	259^{+13841}_{-253}	486^{+13614}_{-481}	16^{+14084}_{-11}	15^{+1}_{-1}	13^{+1}_{-1}	9^{+1}_{-1}
252	I	yes	3	19^{+134}_{-11}	20^{+41}_{-14}	16^{+14}_{-8}	–	–	–
253	–	yes	3	16^{+498}_{-11}	16^{+480}_{-12}	16^{+269}_{-12}	6^{+0}_{-0}	6^{+0}_{-0}	5^{+0}_{-0}
254	H	yes	3	10^{+10490}_{-8}	7^{+10293}_{-5}	8^{+10292}_{-7}	16^{+0}_{-0}	14^{+0}_{-0}	10^{+0}_{-0}
255	–	yes	3	19^{+573}_{-14}	20^{+530}_{-15}	16^{+288}_{-11}	$6^{+0}_{-0.08}$	5^{+0}_{-0}	5^{+0}_{-0}
256	–	yes	3	15^{+277}_{-10}	15^{+233}_{-10}	16^{+145}_{-11}	–	–	–
257	–	yes	3	256^{+10044}_{-250}	21^{+10279}_{-16}	16^{+292}_{-11}	9^{+0}_{-0}	8^{+0}_{-0}	6^{+0}_{-0}
258	H	yes	3	15^{+175}_{-11}	14^{+207}_{-10}	13^{+213}_{-10}	6^{+0}_{-0}	5^{+0}_{-0}	5^{+0}_{-0}
259	J	yes	3	256^{+238}_{-249}	21^{+535}_{-16}	16^{+24}_{-9}	–	–	–
260	I	yes	3	19^{+236}_{-12}	20^{+89}_{-14}	16^{+20}_{-8}	15^{+0}_{-0}	13^{+0}_{-0}	9^{+0}_{-0}
261	H	yes	3	19^{+512}_{-14}	20^{+483}_{-16}	16^{+206}_{-11}	7^{+0}_{-0}	6^{+0}_{-0}	6^{+0}_{-0}
262	–	yes	–	$-^{+}_{-}$	–	–	13^{+1}_{-1}	11^{+1}_{-0}	8^{+0}_{-0}
263	–	yes	2	149^{+13951}_{-144}	18^{+14082}_{-13}	16^{+10484}_{-11}	–	–	–
264	–	yes	3	256^{+165}_{-248}	21^{+515}_{-15}	16^{+20}_{-8}	9^{+0}_{-0}	8^{+0}_{-0}	7^{+0}_{-0}
265	I	yes	2	259^{+13841}_{-253}	487^{+13613}_{-482}	16^{+14084}_{-11}	13^{+1}_{-1}	12^{+1}_{-1}	8^{+1}_{-0}
266	–	yes	3	257^{+10143}_{-252}	21^{+10379}_{-16}	16^{+441}_{-11}	23^{+18}_{-4}	20^{+15}_{-3}	16^{+12}_{-3}
267	–	yes	3	15^{+184}_{-10}	14^{+173}_{-10}	16^{+130}_{-12}	8^{+0}_{-0}	7^{+0}_{-0}	6^{+0}_{-0}
268	I	yes	2	259^{+13841}_{-253}	487^{+13613}_{-482}	16^{+14084}_{-11}	22^{+5}_{-2}	19^{+5}_{-2}	16^{+3}_{-2}
269	–	yes	3	21^{+613}_{-16}	21^{+575}_{-16}	15^{+56}_{-10}	–	–	–
270	I	yes	3	18^{+240}_{-12}	16^{+125}_{-11}	16^{+30}_{-11}	8^{+0}_{-0}	6^{+0}_{-0}	6^{+0}_{-0}
271	–	yes	2	259^{+13841}_{-253}	489^{+13611}_{-484}	16^{+14084}_{-11}	–	–	–
272	K	yes	3	18^{+234}_{-12}	16^{+138}_{-11}	16^{+37}_{-11}	6^{+0}_{-0}	5^{+0}_{-0}	5^{+0}_{-0}
273	H	yes	3	21^{+10079}_{-16}	21^{+660}_{-16}	16^{+239}_{-11}	13^{+1}_{-1}	11^{+1}_{-0}	8^{+1}_{-0}
274	I	yes	–	–	–	–	6^{+0}_{-0}	6^{+0}_{-0}	5^{+0}_{-0}
275	–	yes	3	20^{+593}_{-15}	21^{+543}_{-16}	16^{+198}_{-11}	25^{+13}_{-4}	22^{+11}_{-3}	18^{+8}_{-2}
276	K	yes	3	135^{+446}_{-129}	21^{+528}_{-16}	16^{+282}_{-11}	6^{+0}_{-0}	5^{+0}_{-0}	5^{+0}_{-0}
277	K	yes	3	18^{+169}_{-12}	18^{+129}_{-13}	16^{+57}_{-11}	6^{+0}_{-0}	6^{+0}_{-0}	5^{+0}_{-0}
278	K	yes	3	17^{+135}_{-10}	16^{+72}_{-11}	16^{+27}_{-8}	6^{+0}_{-0}	5^{+0}_{-0}	5^{+0}_{-0}
279	J	yes	2	259^{+10141}_{-250}	488^{+13612}_{-482}	16^{+14084}_{-10}	–	–	–
280	H	yes	3	15^{+62}_{-10}	14^{+62}_{-9}	16^{+48}_{-12}	6^{+0}_{-0}	6^{+0}_{-0}	5^{+0}_{-0}

Table B.2 (Continued)

				Color-based			EW(Hα)		
ID	Clump	Hα?	N	Age (Myr)	Age (Myr)	Age (Myr)	Age (Myr)	Age (Myr)	Age (Myr)
				$Z = 0.004$	$Z = 0.008$	$Z = 0.020$	$Z = 0.004$	$Z = 0.008$	$Z = 0.020$
281	H	yes	3	252^{+155}_{-244}	21^{+215}_{-15}	16^{+21}_{-8}	14^{+0}_{-0}	12^{+0}_{-0}	9^{+0}_{-0}
282	K	yes	3	18^{+210}_{-13}	18^{+259}_{-13}	13^{+231}_{-9}	6^{+0}_{-0}	5^{+0}_{-0}	5^{+0}_{-0}
283	H	yes	3	255^{+633}_{-249}	21^{+961}_{-16}	16^{+189}_{-11}	–	–	–
284	–	yes	3	21^{+323}_{-14}	21^{+120}_{-15}	16^{+19}_{-8}	16^{+1}_{-0}	14^{+0}_{-0}	10^{+0}_{-0}
285	J	yes	3	15^{+158}_{-11}	14^{+149}_{-10}	16^{+112}_{-13}	6^{+0}_{-0}	6^{+0}_{-0}	5^{+0}_{-0}
286	K	yes	3	147^{+433}_{-140}	21^{+609}_{-16}	16^{+266}_{-11}	6^{+0}_{-0}	6^{+0}_{-0}	5^{+0}_{-0}
287	L	yes	2	150^{+13950}_{-145}	437^{+13663}_{-432}	16^{+14084}_{-11}	6^{+0}_{-0}	6^{+0}_{-0}	5^{+0}_{-0}
288	K	yes	3	18^{+261}_{-12}	18^{+168}_{-13}	16^{+50}_{-11}	6^{+0}_{-0}	6^{+0}_{-0}	5^{+0}_{-0}
289	–	yes	3	251^{+224}_{-244}	21^{+510}_{-16}	16^{+32}_{-9}	–	–	–
290	L	yes	2	259^{+13841}_{-252}	486^{+13614}_{-481}	16^{+14084}_{-11}	–	–	–
291	J	yes	3	261^{+10239}_{-256}	21^{+14079}_{-16}	16^{+428}_{-11}	–	–	–
292	J	yes	3	15^{+148}_{-9}	15^{+96}_{-10}	16^{+29}_{-11}	8^{+0}_{-0}	6^{+0}_{-0}	6^{+0}_{-0}
293	K	yes	3	255^{+726}_{-249}	21^{+976}_{-16}	16^{+222}_{-11}	7^{+0}_{-0}	6^{+0}_{-0}	6^{+0}_{-0}
294	K	yes	2	259^{+13841}_{-252}	486^{+13614}_{-481}	16^{+14084}_{-11}	8^{+0}_{-0}	6^{+0}_{-0}	6^{+0}_{-0}
295	K	yes	3	15^{+162}_{-10}	14^{+180}_{-10}	13^{+191}_{-10}	6^{+0}_{-0}	5^{+0}_{-0}	5^{+0}_{-0}
296	L	yes	2	259^{+10141}_{-250}	486^{+13614}_{-480}	16^{+14084}_{-10}	–	–	–
297	K	yes	3	16^{+253}_{-11}	16^{+233}_{-11}	16^{+166}_{-11}	6^{+0}_{-0}	5^{+0}_{-0}	5^{+0}_{-0}
298	IL	yes	3	253^{+346}_{-247}	21^{+620}_{-16}	16^{+119}_{-9}	28^{+32}_{-5}	25^{+26}_{-4}	20^{+19}_{-3}
299	H	yes	2	259^{+13841}_{-253}	482^{+13618}_{-477}	16^{+14084}_{-11}	18^{+7}_{-3}	15^{+6}_{-2}	12^{+6}_{-2}
300	–	yes	3	145^{+13955}_{-140}	21^{+12379}_{-17}	16^{+10384}_{-13}	–	–	–
301	L	yes	3	21^{+365}_{-14}	21^{+129}_{-15}	16^{+18}_{-8}	10^{+0}_{-0}	9^{+0}_{-0}	7^{+0}_{-0}
302	K	yes	3	15^{+19}_{-7}	14^{+27}_{-7}	15^{+13}_{-7}	19^{+2}_{-1}	17^{+2}_{-1}	13^{+2}_{-1}
303	–	yes	2	258^{+13842}_{-254}	483^{+13617}_{-479}	16^{+14084}_{-13}	–	–	–
304	–	yes	3	18^{+283}_{-12}	16^{+156}_{-11}	16^{+35}_{-11}	0^{+0}_{-0}	0^{+0}_{-0}	0^{+0}_{-0}
305	–	yes	–	–	–	–	19^{+3}_{-2}	16^{+2}_{-1}	13^{+2}_{-1}
306	K	yes	3	15^{+49}_{-8}	15^{+46}_{-10}	16^{+22}_{-8}	7^{+0}_{-0}	6^{+0}_{-0}	6^{+0}_{-0}
307	–	yes	3	15^{+319}_{-10}	15^{+228}_{-11}	16^{+104}_{-11}	–	–	–
308	K	yes	3	15^{+46}_{-8}	15^{+45}_{-10}	16^{+23}_{-11}	7^{+0}_{-0}	6^{+0}_{-0}	6^{+0}_{-0}
309	–	yes	3	148^{+13952}_{-143}	21^{+14079}_{-17}	16^{+10384}_{-12}	8^{+0}_{-0}	7^{+0}_{-0}	6^{+0}_{-0}
310	–	yes	3	257^{+10043}_{-252}	21^{+10279}_{-16}	16^{+277}_{-11}	9^{+0}_{-0}	7^{+0}_{-0}	6^{+0}_{-0}
311	–	yes	2	259^{+13841}_{-253}	488^{+13612}_{-483}	16^{+14084}_{-11}	–	–	–
312	K	yes	3	20^{+340}_{-14}	20^{+211}_{-15}	16^{+42}_{-11}	6^{+0}_{-0}	6^{+0}_{-0}	6^{+0}_{-0}
313	–	yes	3	15^{+398}_{-11}	15^{+420}_{-11}	13^{+354}_{-10}	7^{+0}_{-0}	6^{+0}_{-0}	6^{+0}_{-0}
314	–	yes	3	20^{+357}_{-14}	20^{+212}_{-15}	16^{+35}_{-11}	–	–	–
315	J	yes	3	15^{+10285}_{-11}	15^{+898}_{-11}	16^{+818}_{-13}	–	–	–

Table B.2 (Continued)

				Color-based			EW(Hα)		
ID	Clump	Hα?	N	Age (Myr)	Age (Myr)	Age (Myr)	Age (Myr)	Age (Myr)	Age (Myr)
				$Z = 0.004$	$Z = 0.008$	$Z = 0.020$	$Z = 0.004$	$Z = 0.008$	$Z = 0.020$
316	L	yes	2	259^{+13841}_{-253}	485^{+13615}_{-480}	16^{+14084}_{-11}	15^{+1}_{-1}	12^{+1}_{-1}	9^{+1}_{-1}
317	–	yes	3	21^{+439}_{-15}	21^{+356}_{-16}	16^{+52}_{-11}	–	–	–
318	–	yes	2	259^{+13841}_{-254}	482^{+13618}_{-477}	16^{+14084}_{-12}	–	–	–
319	L	yes	3	20^{+308}_{-14}	20^{+139}_{-15}	16^{+25}_{-9}	17^{+0}_{-0}	14^{+0}_{-0}	11^{+0}_{-0}
320	–	yes	3	260^{+207}_{-251}	21^{+10179}_{-15}	16^{+31}_{-8}	–	–	–
321	–	yes	3	21^{+382}_{-15}	21^{+212}_{-16}	16^{+28}_{-9}	16^{+1}_{-1}	14^{+1}_{-1}	10^{+1}_{-1}
322	–	yes	3	256^{+10144}_{-251}	21^{+10379}_{-16}	16^{+576}_{-11}	15^{+1}_{-1}	13^{+1}_{-1}	9^{+0}_{-1}
323	–	yes	3	21^{+486}_{-15}	21^{+466}_{-16}	16^{+31}_{-9}	18^{+1}_{-1}	15^{+1}_{-1}	12^{+1}_{-1}
324	–	yes	3	18^{+10382}_{-14}	18^{+10282}_{-14}	16^{+10084}_{-13}	8^{+0}_{-0}	6^{+0}_{-0}	6^{+0}_{-0}
325	L	yes	2	259^{+13841}_{-254}	482^{+13618}_{-478}	16^{+14084}_{-12}	10^{+1}_{-1}	8^{+1}_{-1}	7^{+0}_{-0}
326	–	yes	2	257^{+13843}_{-251}	489^{+13611}_{-484}	16^{+14084}_{-11}	12^{+1}_{-1}	11^{+0}_{-1}	8^{+0}_{-0}
327	–	yes	3	252^{+9948}_{-246}	21^{+10179}_{-16}	16^{+305}_{-11}	–	–	–
328	–	yes	2	256^{+13844}_{-251}	488^{+13612}_{-483}	16^{+14084}_{-12}	–	–	–
329	–	yes	2	258^{+13842}_{-253}	489^{+13611}_{-484}	16^{+14084}_{-11}	9^{+0}_{-0}	7^{+0}_{-0}	6^{+0}_{-0}
330	–	yes	2	259^{+13841}_{-252}	489^{+13611}_{-484}	16^{+14084}_{-11}	21^{+3}_{-2}	19^{+3}_{-2}	15^{+2}_{-2}
331	–	yes	3	249^{+9951}_{-243}	21^{+946}_{-16}	16^{+291}_{-11}	11^{+0}_{-0}	10^{+0}_{-0}	7^{+0}_{-0}
332	–	yes	3	256^{+356}_{-248}	21^{+911}_{-16}	16^{+154}_{-9}	–	–	–
333	–	yes	3	21^{+759}_{-16}	21^{+653}_{-16}	15^{+123}_{-10}	13^{+2}_{-1}	11^{+1}_{-1}	8^{+1}_{-0}
334	–	yes	2	259^{+13841}_{-252}	482^{+13618}_{-477}	16^{+14084}_{-11}	21^{+4}_{-2}	19^{+4}_{-2}	15^{+4}_{-2}
335	–	yes	3	15^{+222}_{-10}	15^{+151}_{-10}	16^{+53}_{-11}	12^{+0}_{-1}	10^{+0}_{-0}	8^{+0}_{-0}
336	–	yes	2	258^{+13842}_{-253}	481^{+13619}_{-476}	16^{+14084}_{-12}	0^{+0}_{-0}	0^{+0}_{-0}	0^{+0}_{-0}
337	–	yes	3	15^{+228}_{-11}	14^{+259}_{-10}	16^{+215}_{-13}	14^{+1}_{-1}	12^{+1}_{-0}	9^{+0}_{-1}
338	–	yes	3	141^{+10159}_{-136}	21^{+10179}_{-16}	16^{+855}_{-12}	23^{+7}_{-3}	20^{+7}_{-2}	16^{+5}_{-3}
339	–	yes	3	260^{+10240}_{-254}	21^{+14079}_{-16}	16^{+948}_{-11}	14^{+0}_{-1}	12^{+0}_{-0}	9^{+0}_{-1}
340	–	yes	2	259^{+13841}_{-253}	489^{+13611}_{-484}	16^{+14084}_{-11}	–	–	–
341	–	yes	3	15^{+263}_{-10}	15^{+209}_{-11}	16^{+115}_{-11}	–	–	–
342	–	yes	3	15^{+550}_{-11}	15^{+509}_{-11}	16^{+313}_{-13}	6^{+0}_{-0}	6^{+0}_{-0}	5^{+0}_{-0}
343	–	yes	2	259^{+13841}_{-254}	483^{+13617}_{-478}	16^{+14084}_{-12}	11^{+1}_{-1}	10^{+1}_{-1}	7^{+0}_{-0}
344	–	yes	3	256^{+13844}_{-251}	21^{+14079}_{-17}	16^{+10384}_{-11}	–	–	–
345	–	yes	2	258^{+376}_{-149}	491^{+13609}_{-472}	16^{+10484}_{-8}	14^{+0}_{-0}	12^{+0}_{-0}	9^{+0}_{-0}
346	–	yes	3	15^{+109}_{-9}	15^{+70}_{-10}	16^{+27}_{-11}	10^{+0}_{-0}	9^{+0}_{-0}	7^{+0}_{-0}
347	–	yes	3	144^{+10056}_{-139}	21^{+946}_{-16}	16^{+402}_{-11}	–	–	–
348	–	yes	–	–	–	–	6^{+1}_{-1}	6^{+1}_{-1}	5^{+0}_{-2}
349	–	yes	3	21^{+642}_{-16}	21^{+579}_{-16}	16^{+197}_{-11}	25^{+12}_{-4}	22^{+10}_{-3}	18^{+8}_{-2}
350	–	no	3	16^{+10184}_{-12}	16^{+886}_{-12}	16^{+593}_{-13}	–	–	–

Table B.2 (Continued)

				Color-based			EW(Hα)		
ID	Clump	Hα?	N	Age (Myr)	Age (Myr)	Age (Myr)	Age (Myr)	Age (Myr)	Age (Myr)
				$Z = 0.004$	$Z = 0.008$	$Z = 0.020$	$Z = 0.004$	$Z = 0.008$	$Z = 0.020$
351	–	yes	3	139^{+10161}_{-134}	21^{+10179}_{-16}	16^{+10084}_{-12}	6^{+0}_{-0}	5^{+0}_{-0}	5^{+0}_{-0}
352	–	yes	3	15^{+10085}_{-11}	15^{+633}_{-11}	13^{+651}_{-10}	6^{+0}_{-0}	6^{+0}_{-0}	5^{+0}_{-0}
353	–	yes	2	148^{+13952}_{-144}	425^{+13675}_{-421}	16^{+14084}_{-13}	6^{+0}_{-0}	5^{+0}_{-0}	5^{+0}_{-0}
354	–	yes	3	21^{+625}_{-15}	21^{+592}_{-16}	15^{+36}_{-8}	–	–	–
355	–	yes	3	18^{+520}_{-13}	16^{+490}_{-12}	16^{+193}_{-12}	7^{+0}_{-0}	6^{+0}_{-0}	6^{+0}_{-0}
356	–	yes	3	260^{+10040}_{-252}	489^{+13611}_{-484}	16^{+626}_{-10}	–	–	–
357	–	yes	2	259^{+13841}_{-253}	487^{+13613}_{-482}	16^{+14084}_{-11}	21^{+4}_{-2}	18^{+4}_{-2}	14^{+3}_{-2}
358	–	yes	3	20^{+350}_{-14}	20^{+210}_{-15}	16^{+37}_{-11}	11^{+1}_{-0}	10^{+0}_{-1}	8^{+0}_{-0}
359	–	yes	2	259^{+13841}_{-253}	483^{+13617}_{-478}	16^{+14084}_{-11}	–	–	–
360	–	yes	3	260^{+437}_{-252}	21^{+12279}_{-16}	16^{+169}_{-9}	–	–	–
361	–	yes	3	15^{+381}_{-11}	14^{+405}_{-10}	16^{+290}_{-13}	6^{+0}_{-0}	5^{+0}_{-0}	5^{+0}_{-1}
362	–	yes	3	248^{+9852}_{-242}	21^{+891}_{-16}	16^{+288}_{-11}	27^{+12}_{-4}	24^{+11}_{-4}	19^{+8}_{-3}
363	m	yes	3	15^{+127}_{-9}	15^{+97}_{-10}	16^{+42}_{-11}	6^{+0}_{-0}	5^{+0}_{-0}	5^{+0}_{-0}
364	–	yes	2	259^{+13841}_{-252}	483^{+13617}_{-477}	16^{+14084}_{-11}	14^{+1}_{-1}	12^{+1}_{-1}	9^{+1}_{-1}
365	–	yes	3	21^{+452}_{-15}	21^{+421}_{-16}	16^{+136}_{-11}	22^{+5}_{-2}	20^{+4}_{-2}	16^{+3}_{-2}
366	m	yes	3	15^{+219}_{-11}	14^{+242}_{-10}	16^{+195}_{-13}	6^{+0}_{-0}	5^{+0}_{-0}	5^{+0}_{-0}
367	–	yes	3	260^{+10140}_{-255}	21^{+12479}_{-16}	16^{+275}_{-11}	–	–	–
368	m	yes	3	16^{+134}_{-10}	15^{+104}_{-10}	16^{+47}_{-11}	6^{+0}_{-0}	6^{+0}_{-0}	5^{+0}_{-0}
369	m	yes	3	20^{+158}_{-13}	20^{+57}_{-14}	16^{+20}_{-8}	7^{+0}_{-0}	6^{+0}_{-0}	6^{+0}_{-0}
370	m	yes	3	15^{+178}_{-10}	15^{+153}_{-10}	16^{+91}_{-12}	6^{+0}_{-0}	5^{+0}_{-0}	5^{+0}_{-0}
371	N	yes	3	15^{+180}_{-10}	14^{+166}_{-10}	16^{+117}_{-13}	6^{+0}_{-0}	6^{+0}_{-0}	5^{+0}_{-0}
372	–	yes	3	15^{+10185}_{-11}	15^{+776}_{-11}	13^{+944}_{-10}	6^{+0}_{-0}	6^{+0}_{-0}	5^{+0}_{-0}
373	–	yes	2	259^{+11941}_{-251}	486^{+13614}_{-480}	16^{+14084}_{-11}	–	–	–
374	–	yes	2	258^{+368}_{-149}	492^{+13608}_{-472}	16^{+10484}_{-8}	15^{+0}_{-0}	13^{+0}_{-0}	9^{+0}_{-0}
375	–	yes	2	258^{+13842}_{-253}	483^{+13617}_{-478}	16^{+14084}_{-12}	12^{+1}_{-1}	10^{+1}_{-1}	8^{+0}_{-0}
376	N	yes	–	–	–	–	6^{+0}_{-0}	6^{+0}_{-0}	5^{+0}_{-0}
377	m	yes	3	17^{+159}_{-11}	16^{+112}_{-11}	16^{+37}_{-11}	6^{+0}_{-0}	5^{+0}_{-0}	5^{+0}_{-0}
378	m	yes	3	18^{+10482}_{-14}	18^{+10382}_{-14}	13^{+10387}_{-10}	6^{+0}_{-0}	5^{+0}_{-0}	5^{+0}_{-0}
379	m	yes	3	20^{+390}_{-15}	20^{+269}_{-15}	16^{+63}_{-11}	6^{+0}_{-0}	6^{+0}_{-0}	5^{+0}_{-0}
380	N	yes	–	–	–	–	17^{+1}_{-1}	15^{+1}_{-1}	11^{+1}_{-1}
381	m	yes	3	15^{+67}_{-10}	14^{+69}_{-10}	16^{+46}_{-13}	7^{+0}_{-0}	6^{+0}_{-0}	6^{+0}_{-0}
382	–	yes	3	16^{+531}_{-12}	15^{+500}_{-11}	16^{+237}_{-13}	8^{+0}_{-0}	7^{+0}_{-0}	6^{+0}_{-0}
383	N	yes	2	258^{+13842}_{-251}	490^{+13610}_{-485}	16^{+14084}_{-11}	8^{+0}_{-0}	7^{+0}_{-0}	6^{+0}_{-0}
384	N	yes	3	15^{+56}_{-9}	14^{+54}_{-9}	16^{+28}_{-11}	6^{+0}_{-0}	5^{+0}_{-0}	5^{+0}_{-0}
385	–	yes	3	254^{+10046}_{-248}	21^{+10279}_{-16}	16^{+394}_{-11}	13^{+1}_{-0}	11^{+0}_{-0}	8^{+0}_{-0}

Table B.2 (Continued)

				Color-based			EW(Hα)		
ID	Clump	Hα?	N	Age (Myr)	Age (Myr)	Age (Myr)	Age (Myr)	Age (Myr)	Age (Myr)
				$Z = 0.004$	$Z = 0.008$	$Z = 0.020$	$Z = 0.004$	$Z = 0.008$	$Z = 0.020$
386	m	yes	3	258^{+10042}_{-252}	21^{+10479}_{-16}	16^{+759}_{-11}	–	–	–
387	N	yes	3	21^{+373}_{-15}	21^{+259}_{-16}	16^{+120}_{-11}	–	–	–
388	–	yes	–	–	–	–	14^{+0}_{-0}	12^{+0}_{-0}	9^{+0}_{-0}
389	–	yes	3	20^{+359}_{-14}	21^{+228}_{-16}	16^{+44}_{-11}	8^{+0}_{-0}	6^{+0}_{-0}	6^{+0}_{-0}
390	N	yes	2	242^{+10158}_{-235}	464^{+10036}_{-459}	16^{+10284}_{-11}	7^{+0}_{-0}	6^{+0}_{-0}	6^{+0}_{-0}
391	N	yes	3	21^{+428}_{-15}	21^{+235}_{-16}	16^{+24}_{-9}	–	–	–
392	N	yes	2	242^{+10058}_{-233}	468^{+9832}_{-461}	16^{+929}_{-10}	6^{+0}_{-0}	6^{+0}_{-0}	5^{+0}_{-0}
393	N	yes	3	16^{+173}_{-10}	15^{+111}_{-10}	16^{+29}_{-11}	9^{+0}_{-0}	8^{+0}_{-0}	6^{+0}_{-0}
394	N	yes	3	16^{+56}_{-9}	15^{+51}_{-9}	16^{+18}_{-8}	10^{+0}_{-0}	9^{+0}_{-0}	7^{+0}_{-0}
395	N	yes	2	259^{+13841}_{-257}	487^{+13613}_{-486}	16^{+14084}_{-15}	–	–	–
396	N	yes	2	153^{+13947}_{-148}	455^{+13645}_{-450}	16^{+14084}_{-11}	7^{+0}_{-0}	6^{+0}_{-0}	6^{+0}_{-0}
397	–	yes	3	15^{+239}_{-10}	15^{+208}_{-10}	16^{+141}_{-11}	6^{+0}_{-0}	6^{+0}_{-0}	5^{+0}_{-0}
398	–	yes	2	247^{+13853}_{-242}	465^{+13635}_{-460}	16^{+14084}_{-12}	12^{+1}_{-1}	11^{+0}_{-0}	8^{+0}_{-0}
399	N	yes	3	255^{+10045}_{-249}	21^{+10379}_{-16}	16^{+528}_{-11}	12^{+0}_{-0}	10^{+0}_{-0}	8^{+0}_{-0}
400	–	yes	3	15^{+109}_{-10}	14^{+109}_{-10}	16^{+79}_{-13}	11^{+1}_{-1}	10^{+1}_{-1}	7^{+0}_{-0}
401	N	yes	3	20^{+426}_{-15}	20^{+386}_{-15}	16^{+153}_{-11}	–	–	–
402	–	yes	3	16^{+272}_{-11}	16^{+208}_{-11}	16^{+116}_{-11}	6^{+0}_{-0}	6^{+0}_{-0}	5^{+0}_{-0}
403	–	yes	3	16^{+254}_{-11}	15^{+161}_{-10}	16^{+50}_{-11}	6^{+0}_{-0}	6^{+0}_{-0}	5^{+0}_{-0}
404	N	yes	3	16^{+258}_{-10}	15^{+112}_{-10}	15^{+26}_{-8}	8^{+0}_{-0}	7^{+0}_{-0}	6^{+0}_{-0}
405	–	yes	3	15^{+184}_{-10}	15^{+197}_{-11}	16^{+179}_{-13}	6^{+0}_{-0}	5^{+0}_{-0}	5^{+0}_{-0}
406	N	yes	3	15^{+49}_{-9}	14^{+50}_{-9}	16^{+22}_{-11}	15^{+3}_{-2}	13^{+2}_{-2}	10^{+2}_{-2}
407	N	yes	3	15^{+69}_{-10}	14^{+68}_{-10}	15^{+37}_{-11}	17^{+1}_{-1}	14^{+1}_{-1}	11^{+1}_{-1}
408	O	yes	2	258^{+13842}_{-253}	483^{+13617}_{-478}	16^{+14084}_{-11}	–	–	–
409	–	yes	3	16^{+267}_{-10}	16^{+162}_{-11}	16^{+44}_{-11}	9^{+0}_{-0}	8^{+0}_{-0}	6^{+0}_{-0}
410	–	yes	2	259^{+10141}_{-250}	485^{+13615}_{-479}	16^{+14084}_{-10}	10^{+0}_{-0}	8^{+0}_{-0}	7^{+0}_{-0}
411	–	yes	2	256^{+13844}_{-250}	490^{+13610}_{-485}	16^{+14084}_{-11}	–	–	–
412	O	yes	2	259^{+13841}_{-253}	485^{+13615}_{-480}	16^{+14084}_{-11}	7^{+0}_{-0}	6^{+0}_{-0}	6^{+0}_{-0}
413	O	yes	3	15^{+172}_{-11}	14^{+177}_{-11}	15^{+137}_{-12}	6^{+0}_{-0}	6^{+0}_{-0}	5^{+0}_{-0}
414	–	yes	2	259^{+13841}_{-254}	513^{+13587}_{-509}	16^{+14084}_{-13}	15^{+3}_{-2}	13^{+3}_{-2}	10^{+2}_{-2}
415	O	yes	3	15^{+51}_{-8}	15^{+48}_{-10}	16^{+20}_{-8}	7^{+0}_{-0}	6^{+0}_{-0}	6^{+0}_{-0}
416	O	yes	3	260^{+13840}_{-255}	21^{+14079}_{-17}	16^{+10184}_{-12}	6^{+0}_{-0}	6^{+0}_{-0}	5^{+0}_{-0}
417	O	yes	3	21^{+10079}_{-16}	21^{+669}_{-16}	16^{+238}_{-11}	9^{+0}_{-0}	8^{+0}_{-0}	7^{+0}_{-0}
418	O	yes	3	253^{+370}_{-246}	21^{+665}_{-16}	16^{+152}_{-10}	19^{+1}_{-1}	17^{+1}_{-1}	13^{+1}_{-1}
419	O	yes	2	13^{+10387}_{-9}	14^{+10286}_{-10}	7^{+10393}_{-4}	7^{+0}_{-0}	6^{+0}_{-0}	6^{+0}_{-0}
420	O	yes	3	10^{+404}_{-7}	9^{+330}_{-6}	9^{+170}_{-6}	–	–	–

Table B.2 (Continued)

				Color-based			EW(Hα)		
ID	Clump	Hα?	N	Age (Myr)	Age (Myr)	Age (Myr)	Age (Myr)	Age (Myr)	Age (Myr)
				$Z = 0.004$	$Z = 0.008$	$Z = 0.020$	$Z = 0.004$	$Z = 0.008$	$Z = 0.020$
421	O	no	3	21^{+353}_{-14}	21^{+150}_{-16}	16^{+22}_{-9}	–	–	–
422	O	yes	2	258^{+13842}_{-252}	484^{+13616}_{-479}	16^{+14084}_{-11}	–	–	–
423	–	no	3	254^{+304}_{-248}	21^{+569}_{-16}	16^{+33}_{-9}	–	–	–
424	O	yes	3	19^{+257}_{-13}	20^{+111}_{-15}	16^{+24}_{-9}	–	–	–
425	–	yes	2	258^{+13842}_{-252}	484^{+13616}_{-479}	16^{+14084}_{-11}	19^{+4}_{-2}	17^{+4}_{-2}	13^{+4}_{-2}
426	–	yes	3	261^{+582}_{-253}	21^{+10279}_{-16}	16^{+167}_{-10}	–	–	–
427	O	yes	3	21^{+754}_{-15}	21^{+621}_{-16}	16^{+166}_{-11}	–	–	–
428	O	yes	3	248^{+441}_{-242}	21^{+598}_{-16}	16^{+174}_{-11}	14^{+1}_{-1}	12^{+1}_{-1}	9^{+0}_{-1}
429	–	yes	3	21^{+489}_{-15}	21^{+480}_{-16}	16^{+192}_{-11}	$9^{+0.12}_{-0}$	7^{+0}_{-0}	6^{+0}_{-0}
430	O	yes	2	258^{+10242}_{-251}	487^{+13613}_{-482}	16^{+14084}_{-11}	24^{+8}_{-3}	21^{+8}_{-3}	17^{+6}_{-3}
431	O	yes	3	21^{+351}_{-15}	21^{+216}_{-16}	16^{+39}_{-10}	–	–	–
432	–	yes	–	–	–	–	18^{+5}_{-2}	16^{+4}_{-2}	12^{+4}_{-2}
433	–	yes	3	20^{+315}_{-13}	20^{+138}_{-15}	16^{+24}_{-8}	–	–	–
434	–	yes	3	15^{+178}_{-11}	14^{+176}_{-10}	16^{+131}_{-13}	17^{+2}_{-1}	15^{+2}_{-1}	11^{+2}_{-1}
435	–	yes	3	18^{+236}_{-12}	16^{+102}_{-11}	16^{+23}_{-9}	–	–	–
436	–	yes	3	15^{+10185}_{-11}	15^{+840}_{-12}	16^{+672}_{-14}	–	–	–
437	–	yes	3	15^{+217}_{-11}	14^{+210}_{-10}	16^{+151}_{-13}	–	–	–
438	–	no	3	262^{+13838}_{-257}	21^{+14079}_{-17}	15^{+521}_{-11}	–	–	–
439	–	yes	3	257^{+9943}_{-251}	21^{+10279}_{-16}	16^{+249}_{-11}	–	–	–
440	–	yes	3	18^{+10282}_{-14}	16^{+930}_{-12}	16^{+497}_{-13}	$6^{+0}_{-0.09}$	6^{+0}_{-0}	5^{+0}_{-0}
441	–	yes	2	265^{+4335}_{-133}	841^{+13259}_{-504}	10700^{+3400}_{-10692}	11^{+0}_{-0}	10^{+0}_{-0}	7^{+0}_{-0}
442	–	yes	2	258^{+13842}_{-253}	482^{+13618}_{-478}	16^{+14084}_{-13}	16^{+4}_{-2}	14^{+3}_{-2}	10^{+3}_{-1}
443	–	yes	3	15^{+58}_{-11}	14^{+60}_{-10}	15^{+43}_{-12}	8^{+0}_{-0}	6^{+0}_{-0}	6^{+0}_{-0}
444	–	yes	3	15^{+227}_{-14}	10^{+203}_{-9}	9^{+117}_{-8}	8^{+0}_{-0}	6^{+0}_{-0}	6^{+0}_{-0}
445	–	yes	3	260^{+233}_{-251}	21^{+10279}_{-15}	16^{+29}_{-8}	25^{+1}_{-0}	22^{+1}_{-0}	18^{+0}_{-0}
446	–	yes	2	259^{+13841}_{-255}	480^{+13620}_{-476}	16^{+14084}_{-13}	–	–	–
447	–	yes	3	18^{+344}_{-13}	18^{+352}_{-13}	16^{+241}_{-11}	6^{+0}_{-0}	5^{+0}_{-0}	5^{+0}_{-0}
448	–	yes	3	15^{+82}_{-11}	14^{+84}_{-10}	15^{+51}_{-12}	6^{+0}_{-0}	6^{+0}_{-0}	5^{+0}_{-0}
449	–	yes	3	15^{+316}_{-10}	15^{+206}_{-11}	15^{+60}_{-10}	–	–	–
450	–	yes	3	146^{+10154}_{-141}	21^{+10179}_{-16}	16^{+523}_{-11}	11^{+0}_{-0}	10^{+0}_{-0}	7^{+0}_{-0}
451	–	yes	2	259^{+13841}_{-254}	487^{+13613}_{-482}	16^{+14084}_{-11}	8^{+0}_{-0}	6^{+0}_{-0}	6^{+0}_{-0}
452	–	yes	3	15^{+91}_{-10}	14^{+87}_{-9}	16^{+50}_{-11}	6^{+0}_{-0}	5^{+0}_{-0}	5^{+0}_{-0}
453	–	yes	2	259^{+13841}_{-252}	488^{+13612}_{-483}	16^{+14084}_{-11}	–	–	–
454	–	yes	2	259^{+13841}_{-253}	486^{+13614}_{-481}	16^{+14084}_{-11}	–	–	–
455	–	yes	2	259^{+13841}_{-253}	485^{+13615}_{-480}	16^{+14084}_{-11}	9^{+0}_{-0}	8^{+0}_{-0}	6^{+0}_{-0}

Table B.2 (Continued)

				Color-based			EW(Hα)		
ID	Clump	Hα?	N	Age (Myr)	Age (Myr)	Age (Myr)	Age (Myr)	Age (Myr)	Age (Myr)
				$Z = 0.004$	$Z = 0.008$	$Z = 0.020$	$Z = 0.004$	$Z = 0.008$	$Z = 0.020$
456	–	yes	2	259^{+13841}_{-254}	498^{+13602}_{-493}	16^{+14084}_{-11}	–	–	–
457	–	yes	3	15^{+437}_{-11}	15^{+420}_{-11}	16^{+208}_{-13}	–	–	–
458	–	yes	2	258^{+13842}_{-253}	484^{+13616}_{-479}	16^{+14084}_{-11}	11^{+0}_{-1}	9^{+1}_{-1}	7^{+0}_{-0}
459	–	yes	3	257^{+10143}_{-251}	21^{+10479}_{-16}	16^{+643}_{-11}	10^{+0}_{-0}	9^{+0}_{-0}	7^{+0}_{-0}
460	–	yes	3	15^{+480}_{-11}	15^{+473}_{-11}	16^{+342}_{-13}	6^{+0}_{-0}	5^{+0}_{-0}	5^{+0}_{-0}
461	–	yes	3	260^{+371}_{-252}	21^{+12379}_{-16}	16^{+131}_{-8}	37^{+5}_{-3}	33^{+4}_{-3}	26^{+3}_{-2}
462	–	yes	3	255^{+13845}_{-249}	479^{+13621}_{-474}	16^{+12884}_{-11}	21^{+2}_{-1}	19^{+1}_{-1}	15^{+1}_{-1}
463	–	yes	2	258^{+13842}_{-253}	481^{+13619}_{-477}	16^{+14084}_{-13}	14^{+2}_{-2}	12^{+2}_{-1}	9^{+1}_{-1}
464	–	yes	2	258^{+13842}_{-250}	480^{+13620}_{-474}	16^{+14084}_{-11}	20^{+1}_{-1}	17^{+1}_{-1}	14^{+1}_{-1}
465	–	yes	2	259^{+13841}_{-252}	486^{+13614}_{-481}	16^{+14084}_{-11}	–	–	–
466	–	yes	–	–	–	–	27^{+0}_{-0}	24^{+0}_{-0}	19^{+0}_{-0}
467	–	yes	2	258^{+13842}_{-252}	480^{+13620}_{-475}	16^{+14084}_{-11}	7^{+0}_{-0}	6^{+0}_{-0}	6^{+0}_{-0}
468	–	yes	2	258^{+10142}_{-249}	483^{+13617}_{-476}	16^{+14084}_{-10}	15^{+0}_{-0}	13^{+0}_{-0}	10^{+0}_{-0}
469	–	yes	2	259^{+10141}_{-250}	485^{+13615}_{-479}	16^{+14084}_{-10}	21^{+1}_{-1}	18^{+1}_{-1}	14^{+1}_{-1}

Table B.3 Clump photometry

Clump	F300W	F555W	F625W	F814W	log[EW(Hα)]	f_c(Hα)	f_c(F625W)
A	–	19.84±0.046	–	19.338±0.056	1.85	0.03	0.12
B	–	19.652±0.042	19.229±0.054	19.149±0.051	2.07	0.29	0.30
C	18.218±0.093	18.282±0.023	–	17.517±0.024	–	–	–
D	16.626±0.043	–	–	–	–	–	–
E	19.378±0.167	19.646±0.043	19.12±0.052	18.942±0.049	1.02	0.06	0.06
F	15.723±0.028	16.598±0.01	16.33±0.014	15.972±0.012	1.64	0.18	0.27
G	17.226±0.058	17.996±0.019	17.505±0.024	17.416±0.023	2.17	0.12	0.18
H	–	18.689±0.027	18.389±0.037	18.211±0.033	1.65	0.31	0.21
I	18.190±0.091	18.949±0.031	18.587±0.04	18.317±0.035	1.40	0.18	0.13
J	18.895±0.129	19.639±0.043	19.392±0.058	19.053±0.05	1.39	0.29	0.11
K	16.557±0.042	17.246±0.014	17.003±0.019	17.285±0.021	2.39	0.30	0.34
L	18.638±0.114	19.147±0.034	18.821±0.045	18.537±0.039	1.48	0.15	0.13
M	18.191±0.091	18.845±0.029	18.361±0.036	18.551±0.04	2.26	0.37	0.27
N	17.350±0.061	18.235±0.022	17.875±0.029	17.825±0.027	2.08	0.26	0.21
O	17.775±0.075	18.419±0.024	18.07±0.032	17.824±0.027	1.67	0.16	0.13

Table B.3 (Continued)

Clump	FUV	NUV	3.6 μm	4.5 μm	5.8 μm	8.0 μm
A	18.35±0.08	19.06±0.05	17.241±0.076	17.260±0.081	15.736±0.053	14.200±0.073
B	18.04±0.06	18.95±0.06	16.717±0.059	16.517±0.059	14.903±0.068	13.361±0.058
C	17.39±0.07	18.07±0.05	15.048±0.055	14.902±0.055	13.281±0.075	11.575±0.053
D	16.03±0.05	16.75±0.04	13.979±0.054	13.856±0.054	12.098±0.075	10.486±0.053
E	18.43±0.07	19.3±0.07	16.448±0.058	16.373±0.064	15.966±0.055	15.352±0.127
F	15.02±0.05	15.79±0.03	13.757±0.053	13.670±0.053	12.558±0.071	11.112±0.055
G	16.52±0.07	17.26±0.06	14.938±0.055	14.671±0.055	13.026±0.070	11.433±0.056
H	17.25±0.07	17.99±0.06	16.053±0.061	15.970±0.062	14.612±0.068	13.110±0.055
I	17.44±0.08	18.13±0.06	16.327±0.057	16.347±0.059	15.401±0.054	13.898±0.070
J	18.14±0.12	19.10±0.15	17.233±0.071	17.319±0.082	15.905±0.054	14.602±0.072
K	16.03±0.06	16.84±0.04	14.923±0.054	14.438±0.054	12.962±0.077	11.283±0.053
L	17.94±0.12	18.40±0.09	16.434±0.059	16.456±0.063	15.516±0.053	13.892±0.070
M	17.16±0.06	18.02±0.06	15.580±0.055	15.364±0.055	13.327±0.076	11.647±0.053
N	16.68±0.06	17.39±0.05	15.504±0.054	15.325±0.055	13.681±0.073	12.019±0.054
O	17.06±0.06	17.82±0.04	15.583±0.054	15.503±0.055	13.992±0.074	12.367±0.054

Table B.4 Clump age estimates (Myr)

		Continuous SF			Instantaneous SF					
								EW(Hα)		
Clump	N[a]	$Z = 0.004$	$Z = 0.008$	$Z = 0.020$	$Z = 0.004$	$Z = 0.008$	$Z = 0.020$	$Z = 0.004$	$Z = 0.008$	$Z = 0.020$
A	4	3^{+3}_{-2}	2^{+3}_{-1}	1^{+2}_{-0}	2^{+2}_{-1}	2^{+2}_{-1}	1^{+2}_{-0}	–	–	–
B	6	104^{+31}_{-22}	107^{+56}_{-27}	99^{+38}_{-33}	6^{+1}_{-1}	5^{+1}_{-1}	4^{+1}_{-1}	8	6	6
C	5	2^{+2}_{-1}	2^{+3}_{-1}	3^{+2}_{-2}	1^{+3}_{-0}	1^{+3}_{-0}	3^{+1}_{-2}	–	–	–
D	4	3^{+2}_{-2}	2^{+3}_{-1}	1^{+2}_{-0}	2^{+2}_{-1}	2^{+2}_{-1}	1^{+0}_{-0}	–	–	–
E	7	474^{+626}_{-182}	642^{+658}_{-357}	367^{+448}_{-213}	6^{+1}_{-1}	15^{+4}_{-6}	16^{+1}_{-2}	16	14	10
F	7	1200^{+300}_{-275}	1600^{+200}_{-100}	998^{+302}_{-75}	20^{+1}_{-1}	20^{+2}_{-1}	16^{+1}_{-1}	10	8	7
G	7	934^{+466}_{-294}	1600^{+300}_{-300}	788^{+412}_{-347}	246^{+10}_{-107}	16^{+5}_{-2}	16^{+1}_{-1}	7	6	6
H	6	1000^{+600}_{-332}	951^{+449}_{-261}	739^{+461}_{-256}	247^{+16}_{-17}	469^{+40}_{-35}	16^{+1}_{-1}	10	8	7
I	7	404^{+173}_{-93}	271^{+676}_{-103}	162^{+120}_{-67}	6^{+1}_{-1}	10^{+1}_{-1}	16^{+1}_{-1}	12	10	8
J	7	336^{+187}_{-188}	147^{+147}_{-61}	101^{+62}_{-41}	6^{+1}_{-1}	6^{+1}_{-2}	5^{+1}_{-1}	12	11	8
K	7	611^{+165}_{-110}	887^{+213}_{-118}	591^{+162}_{-120}	15^{+2}_{-1}	16^{+3}_{-2}	16^{+1}_{-1}	6	6	5
L	7	369^{+192}_{-100}	225^{+206}_{-86}	125^{+130}_{-44}	6^{+1}_{-1}	6^{+1}_{-1}	16^{+1}_{-1}	11	10	7
M	7	226^{+184}_{-72}	199^{+138}_{-68}	130^{+137}_{-47}	6^{+1}_{-1}	6^{+1}_{-1}	5^{+1}_{-1}	7	6	6
N	7	523^{+248}_{-124}	943^{+357}_{-177}	320^{+184}_{-103}	15^{+1}_{-1}	15^{+2}_{-2}	16^{+1}_{-1}	7	6	6
O	7	594^{+303}_{-172}	961^{+639}_{-157}	352^{+226}_{-127}	250^{+11}_{-11}	15^{+2}_{-2}	16^{+1}_{-1}	10	8	7

[a]Number of colors fit to SB99 model

APPENDIX C. Data tables for Taffy galaxies

Table C.1 [

H_2 line fluxes (10^{-17} W m^{-2})]H_2 line fluxes (10^{-17} W m^{-2}). 3σ upper limit estimated from the RMS and expected line width.

Region	RA	Dec	H_2 0–0 S(0)	H_2 0–0 S(1)	H_2 0–0 S(2)	H_2 0–0 S(3)	Scaling[a]
	J2000.0)	J2000.0)	$\lambda 28.22\mu$m	$\lambda 17.03\mu$m	$\lambda 12.28\mu$m + $\lambda 25.89\mu$m	$\lambda 9.66\mu$m	
				High Resolution[b]			
UGC 12915 nucleus	0 01 41.89	+23 29 44.0	3.17 ± 0.25	10.41 ± 0.19	3.02 ± 0.09	–	SH; 1.42
UGC 12914 nucleus	0 01 38.09	+23 29 03.3	1.57 ± 0.21	6.57 ± 0.14	2.30 ± 0.10	–	SH; 1.35
UGC 12914 S	0 01 39.02	+23 28 43.0	2.19 ± 0.27	4.89 ± 0.10	1.51 ± 0.08	–	SH; 1.42
UGC 12914 N	0 01 37.37	+23 29 18.5	1.06 ± 0.13	2.53 ± 0.12	0.72 ± 0.10	–	SH; 1.93
Bridge	0 01 38.89	+23 29 30.0	1.26 ± 0.13	3.61 ± 0.09	1.25 ± 0.10	–	SH; 2.81
				Low Resolution[c]			
A	0 01 37.62	+23 29 18.7	0.50 ± 0.16	2.10 ± 0.24	–	–	–
B	0 01 38.29	+23 29 22.9	0.71 ± 0.08	3.21 ± 0.27	–	–	–
C	0 01 38.97	+23 29 27.0	0.63 ± 0.04	2.65 ± 0.16	–	–	–
C (PAHFIT)[d]	0 01 38.97	+23 29 27.0	0.61 ± 0.09	2.74 ± 0.20	0.40±0.03	0.61±0.04	SL1, SL2; 3
D	0 01 39.64	+23 29 31.1	0.68 ± 0.08	3.18 ± 0.17	–	–	–
E	0 01 40.32	+23 29 35.2	0.95 ± 0.12	4.67 ± 0.16	–	–	–
F	0 01 40.99	+23 29 39.3	1.33 ± 0.03	6.88 ± 0.18	–	–	–
G	0 01 42.00	+23 29 45.5	1.03 ± 0.28	6.31 ± 0.22	–	–	–
H	0 01 38.06	+23 29 04.8	0.61 ± 0.16	4.94 ± 0.25	–	–	–
I	0 01 38.74	+23 29 08.9	0.46 ± 0.04	3.18 ± 0.12	–	–	–
J	0 01 39.41	+23 29 13.0	0.51 ± 0.09	2.72 ± 0.13	–	–	–
J (PAHFIT)	0 01 39.41	+23 29 13.0	0.72 ± 0.06	2.9 ± 0.16	0.37±0.02	0.56±0.03	SL1, SL2; 3
K	0 01 40.09	+23 29 17.1	0.72 ± 0.15	2.83 ± 0.21	–	–	–
L	0 01 40.77	+23 29 21.3	0.48 ± 0.08	2.78 ± 0.21	–	–	–
M	0 01 41.44	+23 29 25.4	0.3 ± 0.06	1.41 ± 0.12	–	–	–
N	0 01 42.12	+23 29 29.5	< 0.41	1.02 ± 0.22	–	–	–
O	0 01 42.79	+23 29 33.6	< 0.25	0.65 ± 0.12	–	–	–
P	0 01 39.15	+23 28 43.6	0.65 ± 0.18	2.62 ± 0.21	–	–	–
Q	0 01 40.16	+23 28 49.8	0.50 ± 0.13	0.86 ± 0.16	–	–	–
R	0 01 40.84	+23 28 53.9	0.36 ± 0.10	0.69 ± 0.25	–	–	–
S	0 01 41.51	+23 28 58.0	< 0.16	0.93 ± 0.12	–	–	–
T	0 01 39.60	+23 28 29.7	< 0.25	< 0.46	–	–	–
U	0 01 40.61	+23 28 35.9	< 0.27	< 0.46	–	–	–

[a]Due the different angular size of the IRS modules, some of the spectra were rescaled so that the continua matched. The module and scaling factor are indicated here.

[b]H_2 S(0) measured with *Spitzer* IRS LH module; S(1) and S(2) lines measured with IRS SH module. All fluxes were measured using SMART.

[c]H_2 S(0) line measured in LL1, S(1) in LL2, S(2) and S(3) where available in SL1. Low resolution bridge region apertures were squares 10.15×10.15 arcsec. Fluxes were measured using SMART except where otherwise noted.

[d]Line fluxes measured by fitting the full spectrum using PAHFIT, which requires a smooth continuum. In region J, SL1 and SL2 were both scaled up by a factor of 3 due to their smaller area. Then SL1, SL2, and LL2 were scaled up by a factor 1.86 to match the LL1 continuum. Following the fitting with PAHFIT, the SL1, SL2, and LL2 were scaled down by 1.86. No rescaling was required in region B.

Table C.2 Fine structure line fluxes for high resolution data (10^{-17} W m^{-2}). [Ne II], [Ne III], and [S III]18.71μm measured with IRS SH module; [Fe II] + [O IV], [S III]33.48μm, and [Si II]measured with IRS LH module.The SH line fluxes have been scaled up using the same factors as in Table C.1.

Region	[Ne II] λ12.81μm	[Ne III] λ15.56μm	[S III] λ18.71μm	[Fe II] + [O IV] λ25.99μm + λ25.89μm	[S III] λ33.48μm	[Si II] λ34.82μm
U12915 nuc	27.94±1.08	3.79±0.18	10.25±0.45	1.91±0.53	18.72±1.61	28.06±0.68
U12914 nuc	4.26±0.28	1.52±0.11	1.79±0.15	0.65±0.15	2.89±0.59	8.34±0.37
U12914 S	9.14±0.39	1.42±0.07	5.96±0.17	0.33±0.10	9.95±0.73	10.78±0.43
U12914 N	6.35±0.32	1.53±0.07	4.20±0.20	0.38±0.14	7.93±0.47	9.41±0.54
Bridge	0.58±0.06	0.36±0.14	0.68±0.07	$< 0.23^a$	0.58±0.23	1.63±0.28

[a] 3σ upper limit estimated from the RMS and expected line width.

Table C.3 H_2 properties of regions A–R

Region	Temperature[a b]	Equilibrium o/p[c]	N_{H_2}	Σ_{H_2}
	K		10^{20}molecule cm^{-2})	M$_\odot$ pc^{-2})
A	160 (±10)	2.6 (±0.1)	2.7 (+1.0/-0.9)	4.4 (+1.4/-1.2)
B	163 (±10)	2.6 (±0.1)	3.7 (+1.1/-0.9)	5.9 (+1.5/-1.2)
C	160 (±5)	2.6 (±0.04)	3.4 (±0.4)	5.5 (+0.8/-0.7)
C-multi T_1	160 (±5)	2.6 (±0.04)	3.2 (±0.4)	5.0 (+0.8/-0.7)
C-multi T_2	488 (10/-70)	3.0	0.010 (+0.01/-0.001)	0.020 (+0.020/-0.001)
D	164 (+8/-7)	2.6 (±0.07)	3.5 (+0.8/-0.7)	5.6 (+1.4/-1.2)
E	167 (±2)	2.7 (±0.1)	4.6 (±0.2)	7.5 (±0.3)
F	169 (±2)	2.5 (±0.1)	6.4 (+0.4/-0.3)	10.2 (+0.6/-0.4)
G	178 (±13)	2.7 (±0.1)	4.5 (+2.2/-1.6)	7.16 (+2.8/-2.5)
H	195 (±12)	2.9 (±0.1)	2.2 (+1.0/-0.8)	3.6 (+1.7/-0.7)
I	185 (±5)	2.8 (±0.1)	1.9 (+0.5/-0.4)	3.0 (+0.5/-0.4)
J	165 (±3)	2.6 (±0.1)	2.6 (+0.4/-0.1)	4.2 (+2.0/-0.2)
J-multi T_1	155 (±3)	2.5 (±0.1)	4.1 (+0.4/-0.1)	6.6 (+2.0/-0.2)
J-multi T_2	433 (±3)	3.0 (±0.1)	0.020 (±0.001)	0.020 (±0.001)
K	157 (±10)	2.6 (±0.1)	4.1 (±1.8)	6.6 (+2.7/-0.1)
L	175 (±11)	2.7 (±0.2)	2.1 (±0.7)	3.4 (+1.2/-1.2)
M	165 (±11)	2.6 (±0.1)	1.5 (±0.6)	2.4 (+1.1/-0.8)
N	–	–	–	–
O	–	–	–	–
P	158 (±13)	2.6 (±0.2)	3.1 (±2.0)	5.8 (+3.2/-2.5)
Q	130 (+14/-11)	2.2 (±0.2)	4.6 (+3/-2)	7.3 (+5/-3)
R	133 (+10/-12)	2.3 (+0.1/-0.3)	3.1 (+1/-0.2)	5.0 (+1.8/-1)
UGC 12915 nuc T_1	143 (+5/-6)	2.4 (±0.1)	22 (+4/-3)	36 (+6/-5)
UGC 12915 nuc T_2	696 (+30/-23)	3.0	0.07 (±0.01)	0.11 (±0.02)
UGC 12914 nuc T_1	151 (+8/-6)	2.5 (±0.1)	9.6 (+3.0/-2.0)	15 (+4/-3)
UGC 12914 nuc T_2	793 (+10/-6)	3.0	0.040 (±0.005)	0.060 (±0.008)
UGC 12914 N T_1	135 (+8/-7)	2.3 (±0.1)	8.6 (+3/-2)	14 (+4/-3)
UGC 12914 N T_2	1500 (±10)	3.0	0.010 (±0.005)	0.020 (±0.008)
UGC 12914 S T_1	132 (+4/-3)	2.8 (±0.1)	19 (+4/-3)	30 (+8/-7)
UGC 12914 S T_2	989 (±40)	3.0	0.020 (±0.005)	0.040 (±0.008)
Hi res mid-bridge single-temp fit	157 (+23/-14)	2.6 (±0.2)	2.3 (+1.7/-1.3)	3.6 (+3.0/-1.9)
Hi res mid-bridge 2-temp fit T_1	103 (+27/-3)	1.7 (+0.5/-0.2)	10 (+3/-4)	15 (+5/-6)
Hi res mid-bridge 2-temp fit T_2	310 (±30)	3.0	0.12 (+0.5/-0.7)	0.2 (+0.05/-0.12)

[a] A minimum temperature of 100 K is assumed for all temperature estimates.

[b] Uncertainties in all derived properties are formal uncertainties in fitting and do not include many possible systematic effects

[c] Equilibrium ortho-to-para ratio for H_2 molecules is assumed. Note that this can be significantly less than 3 for $T < 300$ K, though at high temperatures o/p = 3 with no formal uncertainty apart from that in the temperature determination. For Deviations from thermal equilibrium might be possible in shocks and this would further add to the uncertainties in the derived properties.

BIBLIOGRAPHY

Allen, M. G., Groves, B. A., Dopita, M. A., Sutherland, R. S., & Kewley, L. J. (2008). *The Astrophysical Journal*, 178, 20.

Anathpindika, S. (2009a). *Astronomy & Astrophysics*, 504, 437.

Anathpindika, S. (2009b). *Astronomy & Astrophysics*, 504, 451.

Appleton, P. N., Xu, K. C., Reach, W. et al. (2006). *The Astrophysical Journal*, 639, L51.

Arp, H. (1966). *Atlas of Peculiar Galaxies*. Pasadena: Caltech.

Barnes, J. E. & Hernquist, L. (1996). *The Astrophysical Journal*, 471, 115.

Barton, E. J., Geller, M. J., Kenyon, S. J. (2000). *The Astrophysical Journal*, 530, 660.

Barth, A. J., Ho, L. C., Filippenko, A. V., Sargent, W. L. W. (1995). *The Astronomical Journal*, 110, 1009.

Bastian, N., Ercolano, B., Gieles, M., Rosolowsky, E., Scheepmaker, R. A., Gutermuth, R., Efremov Y. (2007). *Monthly Notices of the Royal Astronomical Society*, 379, 1302.

Bastian, N., Goodwin, S. P. (2006). *Monthly Notices of the Royal Astronomical Society*, 369, L9.

Bastian, N., Gieles, M., Lamers, H. J. G. L. M., Scheepmaker, R. A., de Grijs, R. (2005a). *Astronomy & Astrophysics*, 431, 905.

Bastian, N., Hempel, M., Kissler-Patig, M., Homeier, N. L., Trancho, G. (2005b). *Astronomy & Astrophysics*, 435, 65.

Bastian, N., Trancho, G., Konstantopoulos, I. S., Miller, B. W. (2009). *The Astrophysical Journal*, 701, 607.

Bastian, N., Covey, K. R., Meyer, M. R. (2010). *Annual Review of Astronomy & Astrophysics*, 48, 339.

Baumgardt, H., Makino, J. (2003). *Monthly Notices of the Royal Astronomical Society*, 340, 227.

Begelman, M. (2002). *The Astrophysical Journal*, 568, L97.

Beirão, P., Appleton, P. N., Brandl, B. R., Seibert, M., Jarrett, T., & Houck, J. R. (2009). *The Astrophysical Journal*, 693, 1650.

Bernlöhr, K. (1993). *Astronomy & Astrophysics*, 258, 25.

Bigiel, F., Leroy, A., Walter, F. (2010). *Proceedings IAU Symposium No. 270, 2010*, arXiv:1012.3749v1.

Bigiel, F., Leroy, A., Walter, F., Blitz, L., Brinks, E., de Blok, W. J. G., Madore, B. (2010). *The Astronomical Journal*, 140, 1194.

Bigiel, F., Leroy, A., Walter, F., Brinks, E., de Blok, W. J. G., Madore, B., Thornley, M. D. (2008). *The Astronomical Journal*, 136, 2846.

Bik, A., Lamers, H. J. G. L. M., Bastian, N., Panagia, N., Romaniello, M. (2003). *Astronomy & Astrophysics*, 397, 473.

Blanc, G. A., Heiderman, A.,Gebhart, K., Evans, N. J. II, Adams, J. (2009). *The Astrophysical Journal*, 704, 842.

Boutloukos, S. G., Lamers, H. J. G. L. M. (2003). *Monthly Notices of the Royal Astronomical Society*, 338, 717.

Braine, J., Davoust, E., Zhu, M., Lisenfeld, U., Motch, C., Seaquist, E. R. (2003). *Astronomy & Astrophysics*, 408, L13.

Brandl, B. R., Devost, D., Higdon, S. J. U. et al. (2004). *The Astrophysical Journal Supplement Series*, 154, 188.

Bushouse, H. A., Werner, M. W. (1990). *The Astrophysical Journal*, 359, 72.

Calzetti, D., Kinney, A. L., Storchi-Bergmann, T. (1994). *The Astrophysical Journal*, 429, 582.

Cao, C., Wu, H. (2007). *The Astronomical Journal*, 133, 1710.

Carroll, B. W., Ostlie, D. A. (2005). *An Introduction to Modern Astrophysics, 2nd ed.*. Reading, MA: Addison-Wesley.

Cartwright, A., Whitworth, A. P. (2004). *Monthly Notices of the Royal Astronomical Society*, 348, 589.

Chandar, R., Fall, S. M., Whitmore, B. C. (2006). *The Astrophysical Journal*, 650, L111.

Cluver, M. E., Appleton, P. N., Boulonger, F., et al. (2010). *The Astrophysical Journal*, 710, 248.

Colbert, E., Mushotzky, R. (1999). *The Astrophysical Journal*, 519, 89.

Condon, J. J., Cotton, W. D., Greisen, E. W., Yin, Q. F., Perley, R. A., Taylor, G. B., Broderick, J. J. (1998). *The Astronomical Journal*, 115, 1693.

Condon, J. J., Helou, G., Sanders, D. B., Soifer, B. T. (1993). *The Astronomical Journal*, 105, 1730.

Conti, P. S., Vacca, W. D. (1994). *The Astrophysical Journal*, 423, L97.

Crowl, H. H., Kenney, J. D. P. (2008). *The Astrophysical Journal*, 136, 1623.

Cullen, H., Alexander, P., Clemens, M. (2006). *Monthly Notices of the Royal Astronomical Society*, 366, 49.

Dale, D. A., Bendo, G. J., Engelbracht, C. W. et al. (2005). *The Astrophysical Journal*, 633, 857.

Dale, D. A., Smith, J. D. T., Armus, L. (2006). *The Astrophysical Journal*, 646, 161.

Dalgarno, A.,Yan, M., Liu, W. (1999). *The Astrophysical Journal Supplement Series*, 125, 237.

de Gijs, R., Anders, P. (2006). *Monthly Notices of the Royal Astronomical Society*, 366, 295.

de Gijs, R., Bastian, N., Lamers, H. J. G. L. M. (2003). *Monthly Notices of the Royal Astronomical Society*, 340, 197.

de Gijs, R., Goodwin, S. P. (2008). *Monthly Notices of the Royal Astronomical Society*, 383, 1000.

de Gijs, R., Parmentier, G. (2007). *Chinese Journal of Astronomy & Astrophysics*, 7, 155.

Dobbs, C. L., Burkert, A., Pringle, J. E. (2011). *Monthly Notices of the Royal Astronomical Society*, arXiv: 1101.3414v1.

Donahue, M., de Messiéres, G. E., O'Connell, R. W., Voit, G. M., Hoffer, A., McNamara, B. R., Nulsen, P. E. J. (2011). *The Astrophysical Journal*, 732, 40.

Dressler, A. (1980). *The Astrophysical Journal*, 236, 351.

Dressler, A., Smail, I., Poggianti, B. M., Butcher, H., Couch, W. J., Ellis, R. S., Oemler Jr., A. (1999). *The Astrophysical Journal*, 122, 51.

Duarte-Cabral, A., Dobbs, C. L., Peretto, N., Fuller, G. A. (2011). *Astronomy & Astrophysics*, 528, A50.

Egami, E., Rieke, G. H., Fadda, D., Hines, D. C. (2006). *The Astrophysical Journal*, 652, L21.

Elmegreen, B. G. (2000). *The Astrophysical Journal*, 530, 277.

Elmegreen, B. G., Elmegreen, D. M., Fernandez, M. X., Lemoias, J. J. (2009). *The Astrophysical Journal*, 692, 12.

Elmegreen, D. M., Elmegreen, B. G., Kaufman, M., Sheth, K., Struck ,C., Thomasson, M., Brinks, E. (2006). *The Astrophysical Journal*, 642, 158.

Fall, S. M., Chandar, R., Whitmore, B. C. (2005). *The Astrophysical Journal*, 631, L133.

Fanelli, M. N., O'Connell, R. W., Thuan, T. X. (1988). *The Astrophysical Journal*, 334, 665.

Fazio, G. G., Hora, J. L., Allen, L. E. (2004). *The Astrophysical Journal Supplement Series*, 154, 10.

Flagey, N., Boulanger, F., Vrestraete, L., Miville Deschênes, M. A., Noriega Crespo, A., Reach, W. T. (2006). *Astronomy & Astrophysics*, 453, 969.

Gao, Y., Zhu, M., Seaquist, E. R. (2003). *The Astronomical Journal*, 126, 2171.

García-Vargas, M. L., González Delgado, R. M., Pérez, E., Alloin, D., Díaz, A., Terlevich, E. (1997). *The Astrophysical Journal*, 478, 112.

Gieles, M. (2009). *Monthly Notices of the Royal Astronomical Society*, 394, 2126.

Gieles, M., Athanassoula, E., Portegies Zwart, S. F. (2007). *Monthly Notices of the Royal Astronomical Society*, 376, 809.

Gieles, M., Bastian, N., Lamers, H. J. G. L. M., Mout, J. N. (2005). *Astronomy & Astrophysics*, 441, 949.

Gieles, M., Lamers, H. J. G. L. M., Portegies Zwart, S. F. (2007). *The Astrophysical Journal*, 668, 268.

Gieles, M., Larsen, S. S., Bastian, N., Stein, I. T. (2006). *Astronomy & Astrophysics*, 450, 129.

Gieles, M., Portegies Zwart, S. F., Baumgardt, H., Athanassoula, E., Lamers, H. J. G. L. M., Sipior, M., Leenaarts, J. (2006). *Monthly Notices of the Royal Astronomical Society*, 371, 793.

Gil de Paz, A., Boisser, S., Madore, B. et al. (2007). *The Astrophysical Journal Supplement Series*, 173, 185.

Gittins, D. M., Clarke, C. J., Bate, M. R. (2003). *Monthly Notices of the Royal Astronomical Society*, 340, 841.

Gnedin, O. Y., Ostriker, J. P. (1999). *The Astrophysical Journal*, 513, 626.

González Delgado, R. M., Pérez, E., Díaz, Á. I., García-Vargas, M. L., Terlevich, E., Vilchez, J. M. (1995). *The Astrophysical Journal*, 439, 604.

González Delgado, R. M., García-Vargas, M. L., Goldader, J., Leitherer, C., Pasquali, A. (1999). *The Astrophysical Journal*, 513, 707.

Goodwin, S. P., Bastian, N. (2006). *Monthly Notices of the Royal Astronomical Society*, 373, 752.

Govoni, F., Feretti, L. (2004). *International Journal of Modern Physics D*, 13, 1549.

Guillard, P., Boulonger, F., Pineau des Forêts, G., Appleton, P. N. (2009). *Astronomy & Astrophysics*, 502, 515.

Habart, E., Abergel, A.; Boulanger, F., et al. (2011). *Astronomy & Astrophysics*, 527, A122.

Habing, H. J. (2004). *Bulletin of the Astronomical Institutes of the Netherlands*, 19, 421.

Hancock, M., Smith, B. J., Giroux, M. L., Struck, C. (2008). *Monthly Notices of the Royal Astronomical Society*, 289, 1470.

Hancock, M., Smith, B. J., Struck, C., Giroux, M. L., Appleton, P. N., Charmandaris, V., Reach, W. T. (2007). *The Astronomical Journal*, 133, 676.

Hancock, M., Smith, B. J., Struck, C., Giroux, M. L., Hurlock, S. (2009). *The Astronomical Journal*, 137, 4643.

Hatziminaoglou, E., Pérez-Fournon, I., Polletta, M. et al. (2005). *The Astronomical Journal*, 129, 1198.

Helou, G., Roussel, H., Appleton, P. et al. (2004). *The Astrophysical Journal Supplement Series*, 154, 253.

Higdon, S. J. U., Devost, D., Higdon, J. L et al. (2004). *Publications of the Astronomical Society of the Pacific*, 116, 975.

Higdon, S. J. U., Armus, L., Higdon, J. L., Soifer, B. T., Spoon, H. W. W (2006). *The Astrophysical Journal*, 648, 323.

Holmberg, E. (1941). *The Astrophysical Journal*, 94, 385.

Holmberg, E. (1958). *Meddelanden från Lunds Astronomiska Observatorium*, 2, 136.

Holtzman, J. A., Faber, S. M., Shaya, E. J. et al. (1992). *The Astronomical Journal*, 103, 691.

Holtzman, J. A., Hester, J. J., Casertano, S. et al. (1995). *Publications of the Astronomical Society of the Pacific*, 107, 156.

Houck, J. R., Roellig, T. L.;van Cleve, J. et al. (2004). *The Astrophysical Journal Supplement Series*, 154, 18.

Hunter, D. A., O'Connell, R. W., Gallagher III, J. S. (1994). *The Astronomical Journal*, 108, 84.

Hunter, D. A., Elmegreen, B. G., Dupuy, T. J., Mortonson, M. (2003). *The Astronomical Journal*, 126, 1836.

Hwang, N., Lee, M. G. (2008). *The Astronomical Journal*, 135, 1567.

James, P. A., Shane, N. S., Beckman, J. E. et al. (2004). *Astronomy & Astrophysics*, 414, 23.

Jarrett, T. H., Helou, G., Van Buren, D., Valjavec, E., Condon, J. J. (1999). *The Astronomical Journal*, 118, 2132.

Jog, C. J. & Das, M. (1992). *The Astrophysical Journal*, 400, 476.

Jog, C. J. & Solomon, P. M. (1992). *The Astrophysical Journal*, 387, 152.

Keel, W. C. (2004). *The Astronomical Journal*, 127, 1325.

Kennicutt Jr., R. C. (1984). *The Astrophysical Journal*, 287, 116.

Kennicutt Jr., R. C. (1989). *The Astrophysical Journal*, 344, 685.

Kennicutt Jr., R. C. (1998a), in *Galaxies: Interactions and Induced Star Formation*. Berlin: Springer.

Kennicutt Jr., R. C. (1998b). *The Astrophysical Journal*, 598, 541.

Kennicutt Jr., R. C., Armus, L., Bendo, G. et al. (2003). *Publications of the Astronomical Society of the Pacific*, 115, 928.

King, A. R., Davies, M. B., Ward, M. J., Fabbiano, G., Elvis, M. (2001). *The Astrophysical Journal*, 552, L109.

Kitsionas, S., Whitworth, A. P. (2007). *Monthly Notices of the Royal Astronomical Society*, 378, 507.

Knapen, J. H., Beckman, J. E., Cepa, J., van der Hulst, T., Rand, R. J. (1992). *The Astrophysical Journal*, 385, L37.

Koopmann, R. A., Kenney, J. D. P. (2004). *The Astrophysical Journal*, 613, 866.

Kroupa, P. (2002). *Science*, 295, 85.

Le Petit, F., Nehmé, C., Le Bourlot, J., Roueff, E. (2006). *The Astrophysical Journal Supplement Series*, 164, 506.

Lada, C. J. & Lada, E. A. (2003). *Annual Review of Astronomy and Astrophysics*, 41, 57.

Lamers, H. J. G. L. M., Gieles, M. (2006). *Astronomy & Astrophysics*, L17, L20.

Lamers, H. J. G. L. M., Gieles, M., Bastian, N., Baumgardt, H., Kharchenko, N. V., Portegies Zwart, S. (2005). *Astronomy & Astrophysics*, 441, 117.

Lamers, H. J. G. L. M. (2009). *Astrophysics and Space Science*, 324, 183.

Lançon, A., Goldader, J. D., Leitherer, C., González Delgado, R. M. (2001). *The Astronomical Journal*, 552, 150.

Larson, R. B. & Tinsley, B. M. (1978). *The Astrophysical Journal*, 219, 46.

Lee, J. C., Gil de Paz, A., Tremonti, C., et al. (1999). *The Astrophysical Journal*, 706, 599.

Leitherer, C., Heckman, T. (1995). *The Astrophysical Journal Supplement Series*, 96, 9.

Leitherer, C., Schaerer, D., Goldader, J. D. et al. (1999). *The Astrophysical Journal Supplement Series*, 123, 3.

Leitherer, C., Ortiz Otálvaro, P. A., Bresolin, F. et al. (2010). *The Astrophysical Journal Supplement Series*, 189, 309.

Leroy, A. K., Walter, F., Brinks, E., Bigiel, F., de Blok, W. J. G., Madore, B., Thornley, M. D. (2008). *The Astronomical Journal*, 136, 2782.

Lisenfeld, U., Völk, H. (2010). *Astronomy & Astrophysics*, 524, A27.

Lutz, D., Sturn, E., Genzel, R., Spoon, H. W. W., Moorwood, A. F. M., Netzer, H., & Sternberg, A. (2003). *Astronomy & Astrophysics*, 409, 867.

Mac Low, M.-M. (1999). *The Astrophysical Journal*, 524, 169.

Martin, D. C., Fanson, J., Schiminovich, D. et al. (2005). *The Astrophysical Journal*, 619, L1.

Marziani, P., Dultzin-Hacyan, D., D'Onofrio, M., Sulentic, J. W. (2003). *The Astronomical Journal*, 125, 1897.

McKee, C. F., Ostriker, E. C. (2007). *Annual Review of Astronomy and Astrophysics*, 45, 565.

Moran, S. M., Ellis, R. S., Treu, T., Salim, S., Rich, R. M., Smith, G. P., Kneib, J.-P. (2006). *The Astrophysical Journal*, 641, L97.

Mullan, B., Konstantopoulos, I. S., Kepley, A. A. et al. (2011). *The Astrophysical Journal*, 731, 93.

Nesvadba, N. P. H., Boulanger, F., Salome, P., Guillard, P., Lehnert, M. D., Ogle, P., Appleton, P., Falgarone, E., & Pineau des Forêts, G. (2010). *Astronomy & Astrophysics*, (in press).

Ogle, P., Antonucci, R., Appleton, P. N., & Whysong, D. (2007). *The Astrophysical Journal*, 657, 161.

Ogle, P., Boulanger, F., Guillard, P. et al. (2010). *The Astrophysical Journal*, 724, 1193.

O'Halloran, B., Metcalfe, L., Delaney, M. et al. (2000). *Monthly Notices of the Royal Astronomical Society*, 360, 871.

Oka, T., Geballe, T. R., Gioto, M., Usuda, T., McCall, B. J. (2005). *The Astrophysical Journal*, 632, 882.

Olson, K. M. & Kwan, J. (1990). *The Astrophysical Journal*, 349, 480.

Palla, F. (2002), in *Physics of Star Formation in Galaxies*. Berlin: Springer.

Pellerin, A., Meurer, G. R., Bekki, K., Elmegreen, D. M., Wong, O. I., Knezek, P. M. (2010). *The Astronomical Journal*, 139, 1369.

Portegies Zwart, S. F., Dewi, J., Maccarone, T. (2004a). *Monthly Notices of the Royal Astronomical Society*, 355, 413.

Portegies Zwart, S. F., Baumgardt, H., Hut, P., Makino, J., McMillan, S. L. W. (2004b). *Nature*, 428, 724.

Press, W. H., Flannery, B. P., Teukolsky, S. A., Vetterling, W. T. (1986). *Numerical Recipes*. Cambridge: Cambridge University Press.

Rand, R. J. (1993). *The Astrophysical Journal*, 410, 68.

Rappaport, S. A., Fregeau, J. M., Spruit, H. (2004b). *The Astrophysical Journal*, 606, 436.

Rieke, G. H., Young, E. T.,Engelbracht, C. W. et al. (2004). *The Astrophysical Journal Supplement Series*, 154, 25.

Rigopoulou, D., Kunze, D., Lutz, D., Genzel, R., Moorwood, A. F. M. (2002). *Astronomy & Astrophysics*, 389, 374.

Roediger, E., Hensler, G. (2005). *Astronomy & Astrophysics*, 433, 875.

Roman-Duval, J, Jackson, J. M., Heyer, M.; Rathborne, J., Simon, R. (2010). *The Astrophysical Journal*, 723, 49.

Roussel, H., Helou, G. Hollenbach, D. J. et al. (2007). *The Astrophysical Journal*, 669, 959.

Ryden, B. & Peterson, B. M. (2010). *Foundations of Astrophysics*. San Francisco: Addison-Wesley.

Salpeter, E. E. (1955). *The Astrophysical Journal*, 121, 161.

Sánchez, N., Añez, N., Alfaro, E. J., Crone Odekon, M. (2010). *The Astrophysical Journal*, 720, 541.

Sandage, A. (1961). *The Hubble Atlas of Galaxies*. Washington: Carnegie Institution of Washington.

Scheepmaker, R. A., Haas, M. R., Gieles, M., Bastian, N., Larsen, S. S., Lamers, H. J. G. L. M. (2007). *Astronomy & Astrophysics*, 469, 925.

Scheepmaker, R. A., Lamers, H. J. G. L. M., Anders, P., Larsen, S. S. (2009). *Astronomy & Astrophysics*, 494, 81.

Schmidt, M. (1959). *The Astrophysical Journal*, 129, 243.

Schulz, S., Struck, C. (2001). *Monthly Notices of the Royal Astronomical Society*, 328, 185.

Shioya, Y., Bekki, K., Couch, W. J. (2004). *The Astrophyical Journal*, 601, 654.

Schruba, A., Leroy, A. K., Walter, F., Sandstrom, K., Rosolowsky, E. (2010). *The Astrophyical Journal*, 722, 1699.

Sirianni, M., Lee, M. J., Benitez, N. et al. (2010). *Publications of the Astronomical Society of the Pacific*, 117, 1049.

Sivandandam, S., Rieke, M. J., Rieke, G. H. (2009). *The Astrophysical Journal*, 717, 147.

Smith, B. J., Giroux, M. L, Struck, C., Hancock, M. (2010). *The Astronomical Journal*, 139, 1212.

Smith, B. J., Hancock, M. (2009). *The Astronomical Journal*, 138, 130.

Smith, B. J., & Struck, C. (2001). *The Astronomical Journal*, 121, 710.

Smith, B. J. & Struck, C. (2000). *The Astronomical Journal*, 140, 1975.

Smith, B. J., Struck, C., Pogge, R. W. (1997). *The Astrophysical Journal*, 283, 754.

Smith, B. J., Struck, C., Nowak, M. A. (2005a). *The Astronomical Journal*, 129, 1350.

Smith, B. J., Struck, C., Appleton, P. N., Charmandaris, V., Reach, W., Eitter, J. J. (2005b). *The Astronomical Journal*, 130, 2117.

Smith, B. J., Struck, C., Hancock, M., Appleton, P. N., Charmandaris, V., Reach, W. T. (2007). *The Astronomical Journal*, 133, 791.

Smith, B. J., Struck, C., Hancock, M. et al. (2008). *The Astronomical Journal*, 135, 2406.

Smith, B. J., Wallin, J. (1992). *The Astrophysical Journal*, 393, 544.

Smith, J. D. T., Armus, L., Dale, D. A. et al. (2007). *Publications of the Astronomical Society of the Pacific*, 119, 1133.

Smith, J. D. T., Draine, B. T., Dale, D. A. et al. (2007). *The Astrophysical Journal*, 656, 770.

Storchi-Bergmann, S., Calzetti, D., Kinney, A. L. (1994). *The Astrophysical Journal*, 429, 572.

Struck, C. (1997). *The Astrophysical Journal Supplement Series*, 113, 269.

Struck, C. (1999). *Physics Reports*, 321, 1.

Struck, C. (2006), in *Astrophysics Update 2*. Chichester, UK: Springer.

Struck, C., Smith, B. J. (2003). *The Astrophysical Journal*, 289, 157.

Struck-Marcell, C. (1991). *The Astrophysical Journal*, 368, 348.

Takahashi, K., Portegies Zwart, S. F. (2000). *The Astrophysical Journal*, 515, 759.

Tan, J. C. (2000). *The Astrophysical Journal*, 536, 173.

Tasker, E. J., Tan, J. C. (2009). *The Astrophysical Journal*, 700, 358.

Tenorio-Tagle, G. (1981). *Astronomy & Astrophysics*, 94, 338.

Tielens, A. G. G. M. (2005). *The Physics and Chemistry of the Interstellar Medium*. Cambridge, UK: Cambridge University Press.

Toomre A. (1964). *The Astrophysical Journal*, 139, 1217.

Toomre, A., Toomre, J. (1972). *The Astrophysical Journal*, 178, 623.

Tremonti, C. A., Calzetti, D., Leitherer, C., Heckman, T. M. (2001). *The Astrophysical Journal*, 555, 322.

Trinchieri, G., Sulentic, J., Pietsch, W., Breitschwerdt, D. (2001). *Astronomy & Astrophysics*, 444, 697.

Vázquez, G. A., Leitherer, C. (2005). *The Astrophysical Journal*, 621, 695.

Vázquez-Semadeni, E. (2010). *Astronomical Society of the Pacific Conference Series*. arXiv:1009.3962

Vorontsov-Velyaminov, B. A. (1977). *Astronomy & Astrophysics Supplement Series*. 28, 1.

Wallin, J. F. (1990). *The Astronomical Journal*, 100, 1477.

Wallin, J. F., Stuart, B. V. (1992). *The Astrophysical Journal*, 399, 29.

Weedman, D. W., Feldman, F. R., Balzano, V. A., Ramsey, L. W., Sramek, R. A., Wu, C. -C. (1981). *The Astrophysical Journal*, 248, 105.

Weisskopf, M. C., Brinkman, B., Canizares, C., Garmire, G., Murray, S., Van Speybroeck, L. P. (2002). *Publications of the Astronomical Society of the Pacific*, 114, 1.

Werner, M. W., Roellig, T. L., Low, F. J. et al. (2004). *The Astrophysical Journal Supplement Series*, 154, 1.

Whitmore, B. C., Chandar, R., Fall, S. M. (2007). *The Astronomical Journal*, 133, 1067.

Whitmore, B. C., Schwiezer, F. (1995). *The Astronomical Journal*, 109, 960.

Whitmore B. C., Schwiezer F., Leitherer C., Borne K., Robert C. (1993). *The Astronomical Journal*, 106, 1354.

Whitmore, B. C., Zhang, Q., Leitherer, C., Fall, S. M., Schweizer, F., Miller, B. W. (1999). *The Astronomical Journal*, 118, 1551.

Whitney, B. A., Indebetouw, R., Babler, B. L. et al. (2004). *The Astrophysical Journal Supplement Series*, 154, 315.

Yusef-Zadeh, F., Wardle, M., Roy, S. (2007). *The Astrophysical Journal*, 665, L123.

Zakamska, N. L. (2010). *Nature*, 465, 60.

Zhang, Q., Fall, S. M. (1999). *The Astrophysical Journal*, 527, L81.

Zhu, M., Gao, Y., Seaquist, E. R., Dunne, L. (2007). *The Astronomical Journal*, 134, 118.